



Strålsäkerhets  
myndigheten

Swedish Radiation Safety Authority

Research

# Reliability, Feasibility and Significance of Measurements of Conductivity and Transmissivity of the Rock Mass for the Understanding of the Evolution of a Repository of Radioactive Waste

## 2021:14

**Authors:** Meier T.<sup>1)</sup>, Backers T.<sup>2)</sup>, Eberhardt E.<sup>3)</sup>, Fisher B.<sup>3)</sup>, Geier J.<sup>4)</sup>, Kwon S.<sup>5)</sup>, Min K-B.<sup>5)</sup>, Blaheta R.<sup>6)</sup>, Hančilová I.<sup>6)</sup>, Hasal M.<sup>6)</sup>, Říha J.<sup>6)</sup> & Lanaro, F.<sup>7)</sup>

<sup>1)</sup>geomecon GmbH, Germany

<sup>2)</sup>Ruhr-Universität Bochum, Germany

<sup>3)</sup>Fisher Rock Engineering, LLC, United States of America

<sup>4)</sup>Clearwater Hardrock Consulting, United States of America

<sup>5)</sup>Seoul National University, South Korea

<sup>6)</sup>Technical University of Liberec, Czech Republic

<sup>7)</sup>Geosigma, Sweden

**Report number:** 2021:14

**ISSN:** 2000-0456

**Available at:** [www.ssm.se](http://www.ssm.se)



## SSM perspective

### Background

The conducted research was part of the international research project DECOVALEX 2019 (DEvelopment of COupled models and their VALidation against EXperiments). DECOVALEX 2019 consisted of seven different research projects called Task A to G. SSM were involved in Task G, which were composed of three different teams from Technical University of Liberec (TUL), Seoul National University (SNU) and geomecon GmbH (GMC), and focused on the excavation damage zone (EDZ) and its coupling to water flow.

The formation of EDZ and the associated change of rock mass hydraulic conductivity has been a continuous matter of research, not exclusive of, but prominently in former DECOVALEX tasks (Liu et al., 2011; Wang et al., 2011; Rutqvist et al., 2009a; Rutqvist et al., 2009b; Min et al., 2004; Min et al., 2009; Öhman et al., 2005; and many more). Within these studies, many aspects have been covered and among them the changes of boundary conditions affecting the formation and evolution of the EDZ have been analysed. However, the impact that EDZ development have on a repository for radioactive waste, and in particular for spent nuclear fuel, have not been fully analysed and understood. Parameters, such as hydrogeological conditions and rock stresses are important parameters for understanding the evolution of EDZ and have potential effects on the repository performance.

### Results

The conducted research is primarily concerned with the transmissivity evolution throughout the lifetime of a repository for a spent fuel in a sparsely fractured and competent crystalline rock mass. The conducted work includes a review of measurement methods for understanding the status and evolution of a repository for spent nuclear fuel (Appendix 2).

The research project consists of an examination of different codes ability to simulate interference test data from the TASO4 tunnel in Äspö (Sweden). The fractured rock mass is represented by a distributed fracture network model (DFN), which was defined by Clearwater Hardrock Consulting. The model benchmarking is part of the work package 2 (WP 2) and will be described in detail within this report. It builds on a previous work package (WP 1; Appendix 3), which dealt with a comparison of different software packages for this purpose. Three different teams, Seoul National University (SNU), Technical University of Liberec (TUL), and geomecon GmbH (GMC), tried to model the interference test with two commercially available software packages, 3DEC and COMSOL Multiphysics®. SNU using 3DEC modelled the flow between the injector and monitoring wells by applying a stress dependent fracture flow, while TUL and GMC using COMSOL Multiphysics® allowed the fluid to flow through fractures and the matrix.

While different approaches have been applied, it can be summarized that the codes were not able to predict all the in-situ pressure responses,

particularly those with significant pressure differences in different observation holes. Therefore, the numerical models may not be suitable for modelling the evolution of the rock in the vicinity of tunnels and holes. Possible reasons for this are that: a) not all provided data could be implemented; b) the provided data might be incomplete with reference to channels along the fractures (channeling); c) the differences between the regular and irregular tunnel geometry induce stresses that differ from the in-situ stresses. The numerical codes did however represent the inflow into the tunnel quite well. This might suggest that the DFN representation of the fractured rock mass is more suitable at a larger scale than smaller scale.

### **Relevance**

The development of EDZ around deposition tunnels and deposition holes has been a target of attention in the development of radioactive waste disposal concepts in crystalline rocks. The reason for aiming at understanding the formation of an EDZ is not primarily related to rock stability issues. More important for the long-term safety of the repository is the characteristics of the EDZ that changes the hydraulic properties of the rock mass in the vicinity of the excavations. Due to these changes, there is a potential for an increase in fluid-conductive pathways around the disposal canister and buffer. These induced pathways may act as transport channels for radionuclides away from the repository. As the EDZ may enhance the hydraulic conductivity between the excavations and the fractures in the rock mass, this could also impact the radionuclide transport from the spent fuel locations to the biosphere, and the resaturation timescales for the bentonite buffer.

The understanding of the transmissivity evolution after closure of a repository for spent nuclear fuel relies to a large extent on numerical models. Therefore, continuous testing of different models against field data is of great importance. Not only to be able to better understand the post-closure transmissivity evolution of a repository for spent nuclear fuel, but also for a better understanding of what limitations different models have in this regard and of the challenges when implementing field data in numerical models. Thus, this study is important for SSM:s continued review of SKB:s safety analysis reports for the spent nuclear fuel repository in Forsmark.

### **Need for further research**

To what extent a continuation of the performed research, dealing with post-closure processes like the thermal phase, glaciation, and earthquakes, would yield reliable results is questionable. However, the results from such work could indicate relative changes, e.g. whether the transmissivity in the excavation damage zone (EDZ) is going to increase or decrease during the post-closure processes. In this regard, they could yield valuable insights and enhance the understanding of the evolution of the repository after closure.



Another way forward is to focus more on channelized fractured flow, since a local DFN model appears to be unable to represent the complexity of fractured flow on this detailed scale. Which is relevant when considering near-field modelling of flow and transport close to the depositions holes for spend nuclear fuel.

**Project information**

Contact person SSM: Carl-Henrik Pettersson

Reference: SSM 2016-1671 / 3030045-26





Strål  
säkerhets  
myndigheten

Swedish Radiation Safety Authority

**Authors:** Meier T. <sup>1)</sup>, Backers T. <sup>2)</sup>, Eberhardt E. <sup>3)</sup>, Fisher B. <sup>3)</sup>, Geier J. <sup>4)</sup>, Kwon S. <sup>5)</sup>,  
Min K-B. <sup>5)</sup>, Blaheta R. <sup>6)</sup>, Hančilová I. <sup>6)</sup>, Hasal M. <sup>6)</sup>, Říha J. <sup>6)</sup> & Lanaro, F. <sup>7)</sup>

<sup>1)</sup> geomecon GmbH, Germany

<sup>2)</sup> Ruhr-Universität Bochum, Germany

<sup>3)</sup> Fisher Rock Engineering, LLC, United States of America

<sup>4)</sup> Clearwater Hardrock Consulting, United States of America

<sup>5)</sup> Seoul National University, South Korea

<sup>6)</sup> Technical University of Liberec, Czech Republic

<sup>7)</sup> Geosigma, Sweden

# 2021:14

Reliability, Feasibility and Significance  
of Measurements of Conductivity and  
Transmissivity of the Rock Mass for  
the Understanding of the Evolution of  
a Repository of Radioactive Waste

Date: June 2021

Report number: 2021:14 ISSN: 2000-0456

Available at [www.stralsakerhetsmyndigheten.se](http://www.stralsakerhetsmyndigheten.se)

This report concerns a study which has been conducted for the Swedish Radiation Safety Authority, SSM. The conclusions and viewpoints presented in the report are those of the author/authors and do not necessarily coincide with those of the SSM.

# Content

<b>Summary</b> .....	<b>1</b>
<b>1. Introduction</b> .....	<b>2</b>
1.1. Test Case.....	3
1.2. Expected outcome of this project.....	4
1.3. Modelling teams.....	5
<b>2. Summary of Work Package 1</b> .....	<b>6</b>
<b>3. Definition of Work Package 2</b> .....	<b>7</b>
3.1. Aim of activities .....	7
3.1.1. Activity 2.1: Static simulation of inflow into the tunnel .....	7
3.1.2. Activity 2.2: Dynamic simulation of inflow into the tunnel .....	7
3.1.3. Activity 2.3: Dynamic simulation of the true injection data.....	7
3.2. Data and Model Definition.....	8
3.2.1. Tunnel geometry .....	8
3.2.2. Drillholes .....	9
3.2.3. Boundary Conditions.....	11
3.2.4. Material properties .....	11
3.2.5. Fractures .....	12
3.2.6. Reflector data.....	13
3.2.7. Discrete Fracture Network data .....	14
3.2.8. Excavation Damage Zone.....	14
3.2.9. Update on boundary conditions .....	15
3.2.10. Injection rates and pressures.....	15
3.2.11. Reworked reflector data.....	17
3.3. Simulation .....	18
3.3.1. Activities 2.1 and 2.2.....	19
3.3.2. Activity 2.3.....	20
<b>4. Seoul National University</b> .....	<b>21</b>
4.1. Modelling Method Selected.....	21
4.2. Model Implementation.....	22
4.2.1. Model geometry .....	22
4.2.2. Joint model.....	23
4.2.3. Rock properties.....	25
4.2.4. Joint properties .....	25
4.2.5. Boundary conditions .....	27
4.2.6. Interference tests .....	28
<b>5. Technical University of Liberec and Institute of Geonics of the CAS</b> .....	<b>29</b>

5.1. Modelling Method Selected.....	29
5.2. Model Implementation.....	30
5.2.1. Rock and fracture input properties.....	31
5.2.2. Boundary conditions .....	31
5.2.3. Model initialisation.....	32
5.2.4. Representation of injection holes.....	32
5.2.5. Updates for Activity 2.2 .....	33
5.2.6. Sensitivity study .....	33
<b>6. Geomecon GmbH (GMC).....</b>	<b>35</b>
6.1. Modelling Method Selected.....	35
6.2. Model implementation.....	35
6.2.1. Tunnel geometry and boundary conditions.....	36
6.2.2. Open fractures .....	36
6.2.3. Drillholes .....	37
6.2.4. Discrete Fracture Network Data.....	38
6.2.5. Reflectors .....	38
6.2.6. True Injection data .....	38
6.2.7. Inner modelling domain.....	39
6.2.8. Outer modelling domain.....	39
6.2.9. Material properties .....	41
6.2.10. Mesh discretisation .....	41
6.2.11. Solver settings and computing.....	42
<b>7. Results .....</b>	<b>43</b>
7.1. Tunnel stresses (Activity 2.1).....	43
7.1.1. SNU.....	43
7.1.2. TUL-IGN.....	44
7.1.3. GMC.....	46
7.1.4. Discussion.....	49
7.2. Inflow into tunnel prior to any injection test (Activity 2.1).....	50
7.2.1. SNU.....	50
7.2.2. TUL-IGN.....	51
7.2.3. GMC.....	51
7.2.4. Discussion.....	51
7.3. Inflow into the tunnel during injection test (Activity 2.3).....	51
7.3.1. SNU.....	51
7.3.2. TUL-IGN.....	52
7.3.3. GMC.....	52
7.3.4. Discussion.....	52
7.4. Pressure Responses (Activity 2.1).....	52
7.4.1. SNU.....	53
7.4.2. TUL-IGN.....	53
7.4.3. GMC.....	54
7.4.4. Discussion.....	55
7.5. Pressure responses (Activity 2.2) .....	56
7.5.1. SNU.....	56
7.5.2. TUL-IGN.....	57
7.5.3. GMC.....	61
7.5.4. Discussion.....	63
7.6. Pressure responses (Activity 2.3) .....	63

7.6.1. SNU.....	64
7.6.2. TUL-IGN.....	65
7.6.3. GMC.....	67
7.6.4. Discussion.....	69
7.7. General Discussion.....	70
7.8. Outlook.....	75
<b>8. Acknowledgements .....</b>	<b>76</b>
<b>9. Literature.....</b>	<b>77</b>
<b>10. Appendix 1 – Influence of tunnel surface.....</b>	<b>79</b>
<b>11. Appendix 2 - Literature Review of Measurement Methods for Understanding the Status and Evolution of a Repository for Nuclear Reactive Waste .....</b>	<b>81</b>
11.1. Introduction .....	81
11.2. Measurement Accessibility .....	82
11.2.1. Direct Measurements.....	82
11.2.2. Indirect Measurements .....	83
11.3. Rock Stresses.....	83
11.3.1. Detection and Measurement Methods.....	83
11.3.2. State of Practice and Other Considerations .....	84
11.4. Natural Fractures .....	84
11.4.1. Detection and Measurement Methods.....	85
11.4.2. State of Practice and Other Considerations .....	85
11.4.3. Feasibility and Reliability.....	86
11.5. Rock Damage, Fracturing and CDZ/EDZ .....	86
11.5.1. Detection and Measurement Methods.....	87
11.5.2. State of Practice and Other Considerations .....	87
11.5.3. Feasibility and Reliability.....	88
11.6. Excavation Displacements.....	88
11.6.1. Detection and Measurement Methods.....	88
11.7. Temperature .....	89
11.7.1. Detection and Measurement Methods.....	90
11.7.2. State of Practice and Other Considerations .....	90
11.7.3. Feasibility and Reliability.....	90
11.8. Water Inflows, Fracture Transmissivity and Rock Permeability.....	91
11.8.1. Detection and Measurement Methods.....	91
11.8.2. State of Practice and Other Considerations .....	92
11.8.3. Feasibility and Reliability.....	92
11.9. References.....	92
<b>12. Appendix 3 - WP 1: Reliability, Feasibility and Significance of Measurements of Conductivity and Transmissivity of the Rock Mass for the Understanding of the Evolution of a Repository of Radioactive Waste .....</b>	<b>96</b>
12.1. Aim of Activities.....	96
12.1.1. Activity 1.1.1: Simulation of Isotropic Material .....	96
12.1.2. Activity 1.1.2: Definition of DFN for Rock Mass Simulation .....	96
12.1.3. Activity 1.1.3: Simulation of Fractured Rock Mass .....	96
12.2. Introduction .....	97

12.2.1. Purpose of this study .....	97
12.2.2. The KBS-3 Method .....	97
12.2.3. The technical issues treated in this project.....	99
12.2.4. Approach in this Project .....	100
12.2.5. Expected outcome of this Project .....	101
12.3. Definition of Work Package 1.....	101
12.3.1. Simulation of Isotropic Material.....	102
12.3.1.1. Geometry .....	102
12.3.1.2. Constitutive Models and Input Parameters.....	102
12.3.1.3. Boundary Conditions.....	103
12.3.1.4. Monitoring Lines.....	103
12.3.1.5. Results of Interest .....	104
12.3.2. Simulation of Fractured Rock Mass.....	105
12.3.2.1. Discrete Fracture Network .....	105
12.3.2.2. Deterministic Fracture Network .....	106
12.3.2.3. Constitutive Models and Input Parameters.....	107
12.3.2.4. Validation Simulations.....	108
12.4. Results .....	108
12.4.1. Team geomecon (GMC) - roxol .....	108
12.4.1.1. Numerical Approach .....	108
12.4.1.2. Model Implementation including Discussion.....	108
12.4.1.3. Boundary Conditions.....	109
12.4.1.4. Simulation Results .....	112
<b>12.4.2. Team geomecon (GMC) - COMSOL Multiphysics.....</b>	<b>117</b>
12.4.2.1. Numerical Approach .....	117
12.4.2.2. Model Implementation and Discussion .....	117
12.4.2.3. Boundary Conditions.....	118
12.4.2.4. Simulation Results .....	122
12.4.3. Team Seoul National University (SNU) .....	133
12.4.3.1. Numerical Approach .....	133
12.4.3.2. Model Implementation including Discussion.....	133
12.4.3.3. Simulation Results .....	134
12.4.3.4. Discussion of Results.....	135
12.4.4. Team Technical University Liberec (TUL) and UGN .....	138
12.4.4.1. Numerical Approach .....	138
12.4.4.2. Model Implementation including Discussion.....	138
12.4.4.3. Simulation Results .....	139
12.4.4.4. Discussion of Results.....	146
12.5. Summary and Comparison of the Simulation Results .....	147
12.5.1. Activity 1.1.1.....	147
12.5.2. Activity 1.1.3.....	151
12.6. Discussion and Conclusion.....	156
12.7. References.....	158
12.8. Annex.....	161
12.8.1. Specification of Discrete Fracture Network.....	161
12.8.2. Continuous vs. discrete simulation of fracture orientation distribution .....	161
12.8.3. Variations with respect to fracture intensity .....	162
12.8.4. 2D cross-section specification .....	162
12.8.5. Potential influence of 2D cross-section orientation on percolation.....	163
12.8.6. Resulting 2D realizations for base case .....	164
12.8.7. Effect of intensity and orientation variants on 2D percolation.....	169
12.8.8. Specification of hydraulic properties in Äspö Task Force model.....	172
12.8.9. Recommendations for effective hydraulic properties for 2D DFN datasets.....	173
12.8.10. Calculation of Fracture Permeability.....	174





## Summary

Task G in DECOVALEX-2019 is primarily concerned with the evolution of transmissivity throughout the lifetime of a repository for radioactive waste, and in particular of spent nuclear fuel, in sparsely fractured and competent crystalline rock masses, and the representation of these processes via numerical simulation. The numerical simulations were to be evaluated for their suitability, and to be validated. Over the course of the work presented here, not only were transmissivity changes and the best approaches to simulate those changes examined, but also strategies were to be developed on how to monitor transmissivity change. Guidelines on what a control program and a monitoring system for a repository should include and be able to measure, and how this can be done in practice, was a key objective of the research project.

This activity requires testing of numerical codes and models against field measurements. These measurements were performed in the TAS04 tunnel in Äspö (Sweden) by SKB as hydraulic interference tests (Ericsson et al. (2014), Ittner et al. (2014), Ittner et al. (2015), Ittner and Bouvin (2015), Ericsson et al. (2015)). The experimental setup included drilling 42 short drillholes into the tunnel floor with lengths ranging between 1 m and 2 m. Each was used as an injector hole while the neighboring drillholes served as sites for monitoring pore pressure changes. These interference tests were used to determine the transmissivity of the rock and fractures and serve as a validation target to be modelled numerically within work package (WP) 2, which can be considered the main work package in Task G.

Prior to WP2, a comparison of the different codes has been performed and addressed in WP1. This WP laid the basis for the simulations conducted in WP2 and is only summarized in the following report. The full report is given in Appendix B.

Three different teams from Seoul National University (SNU), Technical University of Liberec (TUL), and geomecon GmbH (GMC) tried to model the interference test with two commercially available software packages, 3DEC and COMSOL Multiphysics®. SNU using 3DEC modelled the flow between the injector and monitoring wells by applying a stress dependent fracture flow, while TUL-IGN and GMC using COMSOL Multiphysics® allowed the fluid to flow through fractures and the matrix.

While different approaches have been applied, it can be summarized that the codes were not able to predict all the in-situ pressure responses, particularly those with significant pressure differences in different observation holes. Therefore, the numerical models may be not suitable for modelling the evolution of the rock in the vicinity of tunnels and holes due to the fact that a) not all provided data could be implemented, b) the provided data might be incomplete with reference to channels along the fractures (channeling), and c) the differences between the regular and irregular tunnel geometry induce stresses that differ from the in-situ stresses. Interestingly, the numerical codes did represent the inflow into the tunnel quite well.

To what extent an upcoming work package, which deals with the post-closure processes like thermal phase, glaciation, and earthquakes, will yield reliable results is questionable. However, the results from this work package may indicate relative changes, e.g. whether the transmissivity in the excavation damage zone (EDZ) is going to increase or decrease during the post-closure processes. In this regard, they will bring about valuable insights and will enhance the prediction of the evolution of the repository after closure.

# 1. Introduction

The potential development of an excavation damage zone (EDZ) around the deposition tunnels and holes of a radioactive waste repository has been a target of investigation from the start of radioactive waste disposal concepts. This is primarily because the formation of an EDZ will change the hydraulic properties of the rock mass in the vicinity of the excavations, potentially creating new fluid pathways and connectivity with natural fractures parallel to the excavations. These enhanced pathways may act as transport channels for radionuclides that may connect to the biosphere through either the natural fracture network or the network of repository excavations that connect to surface through the access ramps and/or shafts. Design premises for the excavations in a repository and for the rock mass around it should be set for ensuring the long-term safety after closure and should be verified by measurement, performance monitoring and quality controls.

The formation of the EDZ and the associated change of rock mass permeability has been a continuous matter of research in former DECOVALEX<sup>1</sup> (DEvelopment of COupled models and their VALidation against EXperiments) tasks (Liu *et al.*, 2011; Wang *et al.*, 2011; Rutqvist *et al.*, 2009a; Rutqvist *et al.*, 2009b; Min *et al.*, 2004; Min *et al.*, 2009; Öhman *et al.*, 2005; and many more). Within these studies, many aspects have been covered; among them changes to boundary conditions affecting the formation and evolution of the EDZ have been analyzed. However, the impact of the EDZ development and the related transmissivity changes on a repository for radioactive waste, and in particular for spent nuclear fuel, has not been fully analyzed. Furthermore, it is unclear how to measure rock mass transmissivity during the construction and operational phases of a repository. Other important parameters, such as hydrogeological conditions and rock stresses are important parameters for understanding the evolution of the EDZ and its effects on the repository performance.

Task G in DECOVALEX-2019 is primarily concerned with the evolution of transmissivity throughout the lifetime of a repository for radioactive waste, and in particular of spent nuclear fuel, in sparsely fractured and competent crystalline rock masses, and the representation of these processes via numerical simulation. Over the course of the work presented here, not only were transmissivity changes studied and the best approaches to simulate the change examined, but also strategies were to be developed on how to monitor transmissivity change. Guidelines on what a control program and a monitoring system for a repository should include and be able to measure, and how this can be done in practice was key objective of the research project.

The research project requires testing of the simulations against measured field data to validate the initial transmissivity of the rock mass. This benchmarking is part of the work package 2 (WP 2) and will be described in detail within this report. It builds up on a previous work package (WP 1), which dealt with a comparison of different software packages for this purpose and is published as an SSM Report (Backers *et al.* 2018).

In work package 3 (WP3), which represents upcoming work to be dealt with individually by the modelling teams, the models will be expanded to include (a) heat generated by the deposition holes to simulate the thermal phase after closure, and (b) additional boundary conditions to simulate future glacial loading and unloading events after closure.

Further information on the purpose and motivation of this work can be found in Appendix B 1.1 to B 1.5.

---

<sup>1</sup> “The DECOVALEX project is an international research and model comparison collaboration, initiated in 1992 and currently in its 7th phase, for advancing the understanding and modelling of coupled thermo-hydro-mechanical chemical (THMC) processes in geological systems. Prediction of these coupled effects is an essential part of the performance and safety assessment of geologic disposal systems for radioactive waste and spent nuclear fuel, and also for a range of sub-surface engineering activities.” ([www.decovallex.org](http://www.decovallex.org))

## 1.1. Test Case

The test case requires that the numerical models developed be validated against data from an in-situ experiment. This was done for this project using data produced by SKB for the TAS04 experiment at Äspö, Sweden, and reported in Ericsson *et al.* (2014), Ittner *et al.* (2014), Ittner *et al.* (2015), Ittner and Bouvin (2015) and Ericsson *et al.* (2015). The figures below (Figure 1 and Figure 2) show an overview of the experiment location setup from which the chosen dataset was obtained.

SKB has conducted the TAS04 experiment aiming at defining and developing standards, strategies and methods needed to design and gather sufficient specifications on the EDZ to procure underground construction works for the planned repository for spent nuclear fuel. One part of the experiments focused on verifying the extent of the EDZ around a tunnel excavated by means of drill-and-blast. This included geometrical, geological, geophysical and hydrogeological investigations and studies of the blasting design and resulting rock mass damage (Ericsson *et al.* 2014).

The TAS04 tunnel was excavated approximately parallel to the maximum horizontal stress as a drift from the TASP tunnel (see Figure 1). The lithology is dominated by fine grained granite and diorite/granodiorite. The observed natural fracture sets are described to be approximately parallel and perpendicular to the tunnel axis as well as gently and steeply dipping (Ericsson *et al.* 2015).

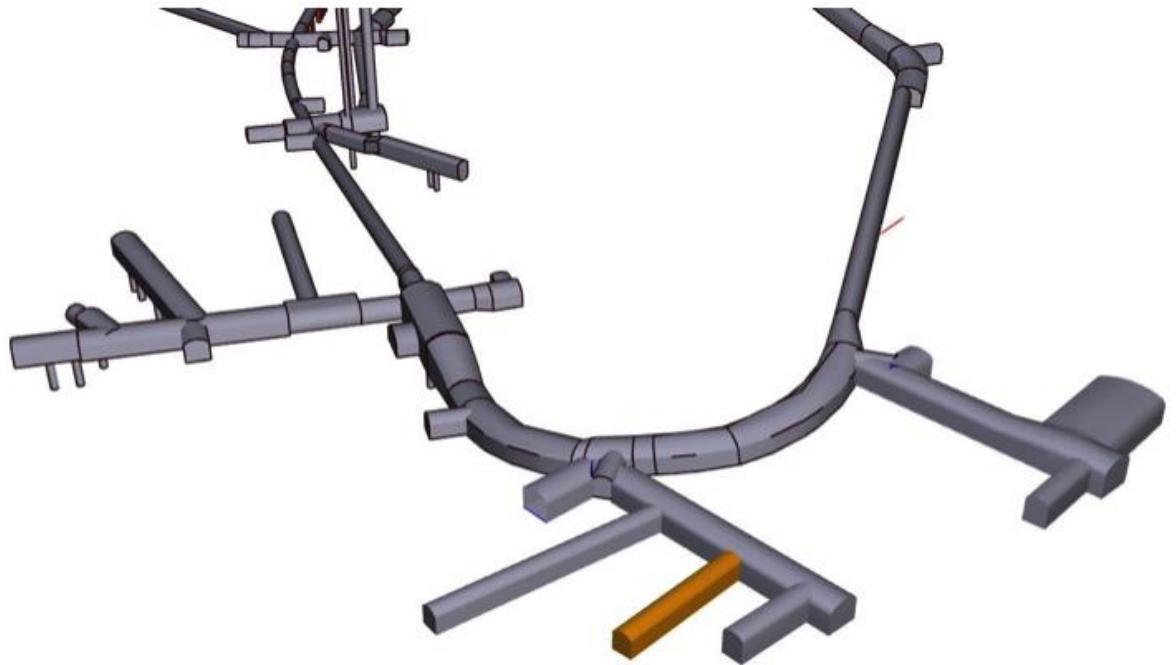


Figure 1. Overview of the location of the TAS04 tunnel (yellow) with respect to the other TAS tunnels taken from Appendix 2 of Ericsson *et al.* (2015).

The experimental setup included drilling 42 short drillholes into the tunnel floor with lengths ranging between 1 m and 2 m as shown in Figure 2. Each drillhole was used as an injector hole while the neighboring drillholes served as sites for monitoring pore pressure changes. These interference tests were used to determine the transmissivity of the rock

and fractures and serve as a validation target to be modelled numerically within this activity.

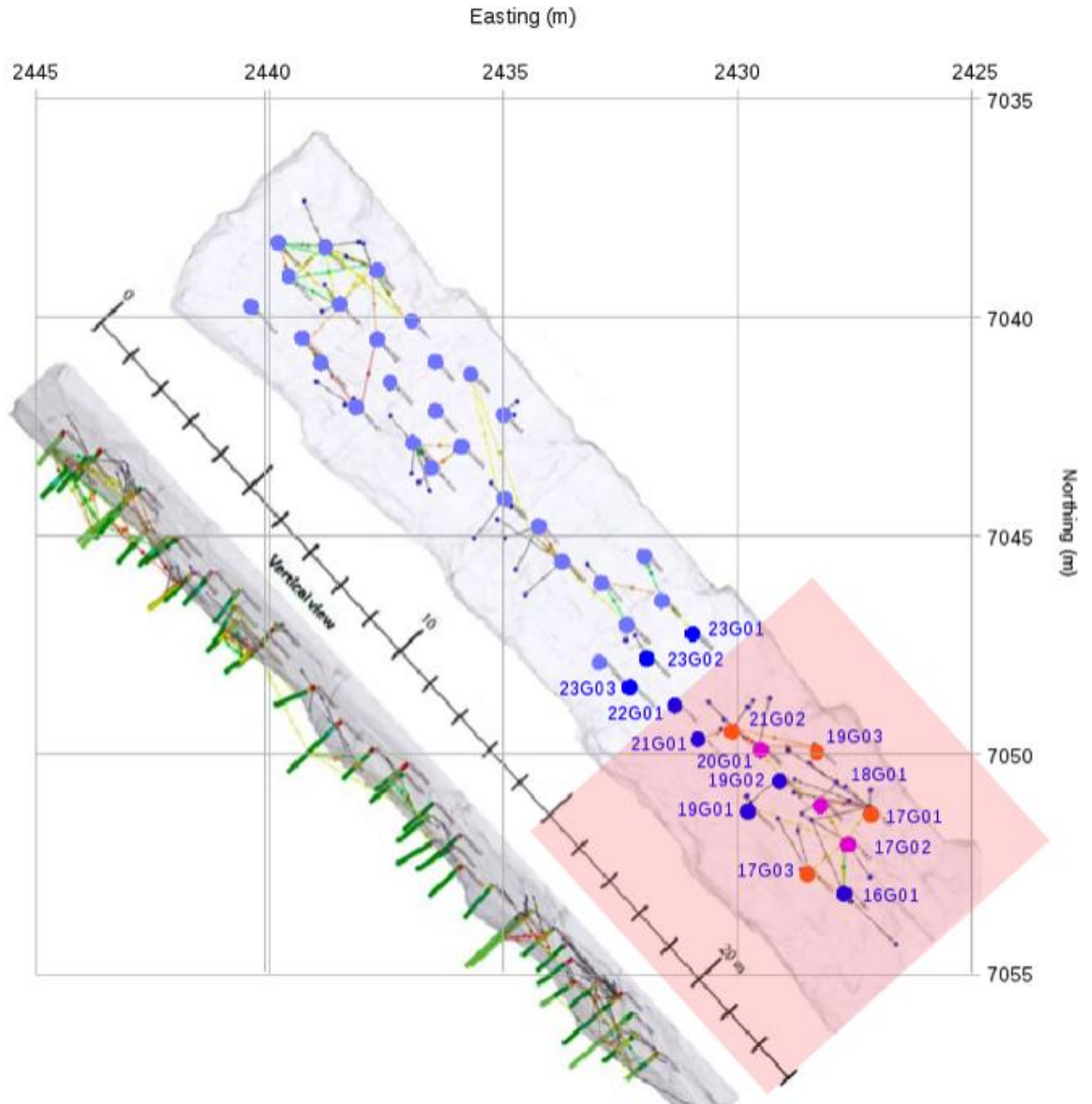


Figure 2. Positions of drillholes in the floor of the TAS04 drift, plotted based on coordinates given in Appendix 1 of Ericsson et al. (2015). Colored dots show the proposed injection holes used for modelling of the interference tests (magenta) and registering hydraulic connections to these injection holes (orange), as well as differentiating those located in the selected test section of TAS04 (dark blue) relative to those outside this section (pale blue). The coordinate axes (easting and northing) are in the local Äspö system. This plot is superimposed on a reoriented version of Ericsson et al. (2015), Figure 8-19, with lines indicating the interpreted hydraulic connections between holes, and to leakage points in the tunnel floor (tiny blue dots). The lower left-hand part of the plot (below the diagonal scale) gives an orthogonal view of the drillholes to indicate their relative lengths and the depths of the interpreted hydraulic connections. Note that the vertical scale in this view is exaggerated.

## 1.2. Expected outcome of this project

The project is expected to deliver the following results:

- Evaluation of suitability of the numerical models and their validation for simulating the evolution of the hydraulic and mechanical rock mass characteristics in the vicinity of deposition tunnels and holes.
- Analysis of representativeness and relevance of the conditions during construction and operations for the evolution of the repository after closure.
- Indication of the importance of sampling/monitoring position for representative measurements. An opinion on the scope of systematic or selective measurements during construction and operation of the repository facility should be provided.
- Strategies to estimate and monitor the transmissivity and its change in the near-field rock mass surrounding the deposition tunnels and holes.
- Validation of the feasibility of the measuring methods with respect to the number of measurements, features to be measured, and significance of the measurements for the long-term safety of a waste repository.

### **1.3. Modelling teams**

Three modelling teams are involved in simulating these interference tests within the Task G of DECOVALEX19 project. The modelling teams are (in alphabetic order):

- geomecon GmbH (GMC), Germany,
- Seoul National University (SNU), South Korea, and
- Technical University of Liberec (TUL), Czech Republic.

The Discrete Fracture Network (DFN) used by the modelling teams was generated by

- Clearwater Hardrock Consulting, United States of America.

## 2. Summary of Work Package 1

The general aim of WP 1 (full report on WP is attached as Appendix 3 starting from pp. 96) is to set up simple, two-dimensional models of the TAS04 cross-section with an isotropic and fractured representation of the rock mass in order to benchmark the employed codes at an early stage of the project and to pinpoint upcoming challenges when considering more complex tunnel geometries, fracture networks, and material laws. A full description of the outcomes of the work package is given in Backers et al. (2018).

Since TUL-IGN and GMC have been using the same code and the same physical interfaces to model the activities, it is not surprising that their simulations yield almost identical results. Some insignificant deviations occur due to different output intervals along monitoring lines or varying mesh refinement but, in general, these are negligible. Only in Activity 1.1.3. (see Backers et al. 2018) the pore pressure distributions show increasing offsets with increasing distance from the start- and end-points of the monitoring lines, i.e., the predefined boundary conditions, which cannot be explained by the aforementioned reasons. This observation was already made during the Stockholm WS and both teams re-evaluated their model set-ups and results with the model definitions, but the differences in pore pressure could not be resolved. Despite the difference in pore pressure in Activity 1.1.3, the remaining values were almost identical.

The results generated by SNU using UDEC (Itasca Consulting Group Inc.) show differences to the other modelling teams' results since the read-out intervals are much coarser and the model domain has been altered to fit the needs of the numerical code. The deviations occur especially for stress and strain and can be observed in Activity 1.1.1 and 1.1.3.

At this point, it is interesting to note that the included deterministic (DTM) and discrete (DFN) fracture networks do not seem to influence the fluid flow results for UDEC. For example: the pore pressure along a monitoring line below the tunnel floor with and without fractures are almost identical for the UDEC code (see Figure 79 in Backers et al., 2018). This is in contrast to the results of the other modelling teams who observed high fluctuations of the pore pressure with and without the fracture network. In particular, significant differences in the fluid flow parameters can be observed when comparing UDEC with the roxol (geomecon GmbH) results. roxol produces almost identical results to the COMSOL results in Activity 1.1.1. However, in Activity 1.1.3, high fluctuations in strain, stress, fluid flow, and pore pressure in the vicinity of the fracture networks are generated due to the mesh-size-dependent fracture flow (see pore pressure distribution in Figure 134) and the "smooth", friction-free fractures (compare with Figure 125 to Figure 132).

From Figure 134 it can also be concluded that percolating fracture networks created by the DTM significantly reduce the pore pressure in the matrix and subsequently increase the affected zone around the tunnel. The extent of the pore-pressure reduction also depends on the effective fracture aperture. The greater the fracture aperture, the greater the fluid withdrawal out of the formation towards the tunnel. Hence, it can be argued that fractures created from a drill-and-blast-procedure will not result in a significant reduction of pore pressure within the excavation damage zone since the created fracture will be too short to form percolating fracture networks and too narrow to increase the drainage area of the tunnel.

## 3. Definition of Work Package 2

The general aim of WP 2 was to simulate the interference tests conducted in the TAS04 tunnel as explained in section 1.1. For this purpose, three modelling activities were defined which gradually increased in modelling complexity. While Activity 2.1 aimed at constructing a 3D subsurface model of the tunnel incorporating the drillholes and a small number of open fractures, Activity 2.2 aimed to embed larger DFNs that include fractures interpreted from geophysical reflector data and the possibility to include an EDZ around the tunnel to established a more realistic subsurface model. For Activities 2.1 and 2.2, the injection was modelled as a continuous 20 min long pressure pulse, whereas for Activity 2.3 the simulation of the interference tests was based on the true injection data.

### 3.1. Aim of activities

The following section describes the aim of each activity in detail.

#### 3.1.1. Activity 2.1: Static simulation of inflow into the tunnel

The goal of this activity was to (a) build a model of the TAS04 experiment and (b) to simulate three interference tests performed by means of HM-coupled simulations. The activity description provided some guidelines for the data to be used but gave the teams a high degree of freedom in how to built their models. However, the teams had to keep in mind that the upcoming activities will require enhanced versions of their initial model.

#### 3.1.2. Activity 2.2: Dynamic simulation of inflow into the tunnel

The goal of this activity was to (a) enhance the initial models developed for the previous activity (Activity 2.1), by including 3D discrete fracture networks, an excavation damage zone and additional information from ground penetrating radar, (b) customize the boundary conditions and model parameters, and (c) perform a parametric back-analysis to obtain the parameters that best reproduce the interference tests. The activity description provided some guidelines regarding the data to be used but gave the teams an even higher degree of freedom in how they enhanced their initial model to achieve the goals of this activity.

#### 3.1.3. Activity 2.3: Dynamic simulation of the true injection data

The goal of this activity was to (a) further enhance the model developed through the previous activities (Activities 2.1 and 2.2), by including the time-dependent injection pressures from the injection holes and the pore pressure responses in the other observation holes. The activity description provided some guidelines regarding the data to be used but gave the teams a high degree of freedom in how to build the necessary capabilities into their model.



### 3.2. Data and Model Definition

The simulations carried out concentrated on a section 15 m to 23 m from the blind end of the TAS04 tunnel (shaded red area in Figure 2). This tunnel interval was chosen because the drillholes are all located in the same rock type, according to the geological mapping, and outside of the main mapped fault zone, which is located 8 to 10 m from the blind end of the tunnel axis. Furthermore, the interference tests performed in this section fulfilled the following key criteria: (a) they lacked indication of anomalies due to leakage either around the packers or through sealing of the drillhole extension but (b) included observations of connectivity of varying magnitudes. It was noted that leakage up to the tunnel floor was possible.

The subsections presented below describe the available data and the interference tests that were chosen for simulation to be used for building the models. The teams were directed, if possible, to re-use the model geometry developed for their previous activities; e.g. use model geometry from Activity 2.1 for Activity 2.2. However, in doing so, it was recognized that the boundary conditions, representation of the rock mass, and fracture flow parameters should be altered to move towards a more realistic model. As with the previous activities, additional required information that is not presented in the reference documents were to be modelled as a first qualified best guess. This means that the parameters and conditions should be chosen from a sensible rock mechanics perspective. All parameters could then be changed by a parametric sweep to gain results that match the interference tests. The teams were to aim at producing the best possible results; however, modelling results within 15% error of the interference test were considered to be acceptable. The 15% error estimate was discussed by all team members to be a reasonable error estimate considering the error in the estimated material properties and the uncertainty of the stress field. For full transparency, objective discussion and comparison of the parameters that yielded the best fit to the interference test, as well as those obtained using other parameters and/or boundary conditions, should be included and discussed. For the visualization of the data provided and better understanding of the work package, the viewer in Appendix 2 from Ericsson *et al.* (2015) was recommended.

**Table 1.** Data provided in the course of WP 2.

Activity	Workshop	Tunnel geometry	Drillholes	Boundary	Material	Open fractures	Reflector data	DFN data	EDZ	Update on boundary conditions	Injection rates and	Reworked reflector data
2.1	4th											
2.2	5th											
2.3	6th											

#### 3.2.1. Tunnel geometry

The contour of the tunnel is shown as a point cloud in Figure 3. The data were given as a tunnel point cloud in \*.TXT and \*.LAS formats. A simplified triangulated tunnel geometry was also provided as an \*.STL file. It was left to each modelling group whether to use part of or the full tunnel surface information. The modelling should concentrate on the section of the tunnel located 15 m to 23 m from the blind end of the tunnel, for which

a high resolution scan of the tunnel floor should be used; however, each modelling team was free to choose the resolution of their model according to their needs and judgement.

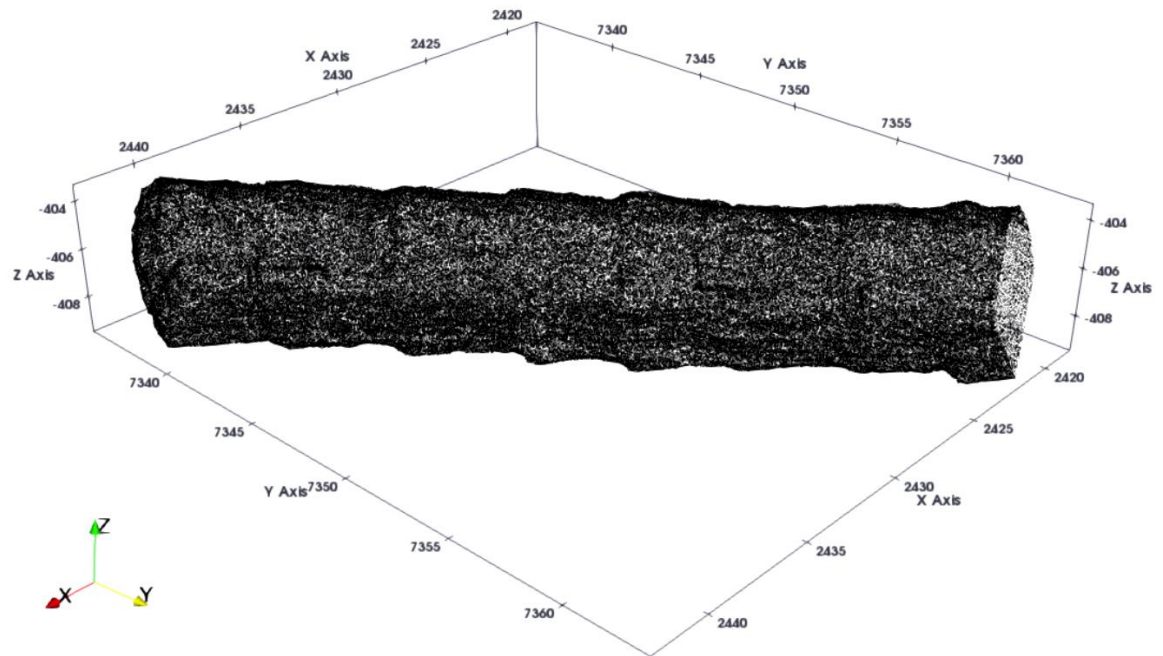


Figure 3. Image of the point cloud describing the tunnel surface data as provided by SKB.

### 3.2.2. Drillholes

In the selected tunnel interval, several drillholes were located as shown in Figure 4. These included drillholes:

- K04016G01
- K04017G01
- K04017G02
- K04017G03
- K04018G01
- K04019G01
- K04019G02
- K04019G03
- K04020G01
- K04021G01
- K04021G02
- K04022G01
- K04023G01
- K04023G02
- K04023G03.

The orientation of each drillhole was given as two points describing the start and end point of the center axis of the drillhole (**Table 2**). Appendix 1 in Ericsson *et al.* (2015) provides additional information on the orientations of the drillholes. The drillholes are 76 mm in diameter.

The complete drillhole was to be modelled as an empty cylinder or line. However, as a minimum requirement, the injection intervals of the interference tests were to be modelled (i.e. K04017G02: 0.4 to 0.6 m below top of drillhole; K04018G01: 0.1 to 0.2 m below top of drillhole; and K04020G01: 0.2 to 0.4 m below top of drillhole).

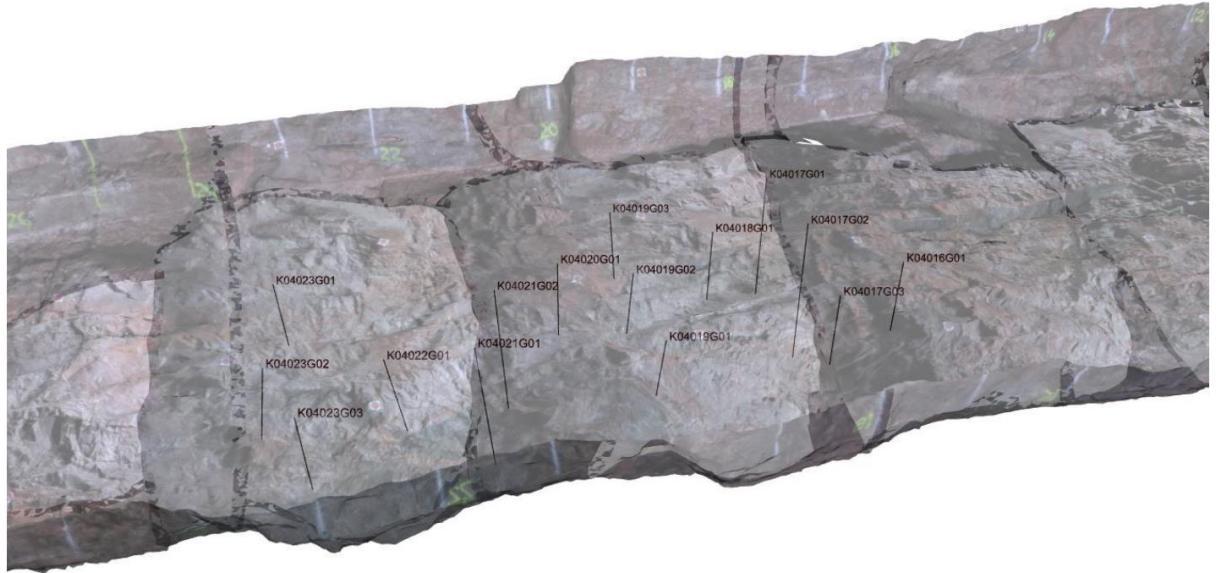


Figure 4. Image of the tunnel floor and the relevant drillholes taken from the Appendix 2 from Ericsson et al. (2015).

**Table 2.** Drillhole name and coordinates of two points describing the orientation and extent of the drillhole central axis.

Drillhole name	Top of drillhole			Bottom of drillhole		
	Easting	Northing	Elevation	Easting	Northing	Elevation
K04016G01	2427.727	7353.1590	-409.019	2427.845	7353.237	-410.015
K04017G01	2427.144	7351.3560	-409.048	2427.144	7351.449	-411.030
K04017G02	2427.64	7352.0420	-409.026	2427.910	7352.231	-410.999
K04017G03	2428.505	7352.7100	-409.011	2428.620	7352.789	-410.006
K04018G01	2428.225	7351.1420	-409.048	2428.327	7351.203	-410.041
K04019G01	2429.772	7351.2810	-409.171	2429.719	7351.195	-410.229
K04019G02	2429.098	7350.5850	-409.141	2429.131	7350.560	-410.141
K04019G03	2428.314	7349.9330	-409.210	2428.348	7350.028	-410.252
K04020G01	2429.501	7349.8810	-408.945	2429.652	7349.961	-409.934
K04021G01	2430.845	7349.6330	-409.024	2430.829	7349.763	-411.068
K04021G02	2430.115	7349.4490	-408.970	2430.115	7349.530	-411.010
K04022G01	2431.338	7348.8620	-409.086	2431.398	7349.060	-410.142
K04023G01	2430.956	7347.2240	-409.157	2430.966	7347.221	-410.191
K04023G02	2431.934	7347.7910	-409.170	2432.163	7347.723	-410.166
K04023G03	2432.302	7348.4440	-409.153	2432.425	7348.553	-410.191

### 3.2.3. Boundary Conditions

The in-situ stress state as described by Christiansson and Jansson (2003) was used. They tested three different methods for stress measurements in two orthogonal drillholes at the 450 m level (i.e., 450 m depth). The major horizontal stress was estimated to be  $24 \pm 5$  MPa, which likely corresponds to the lower range for the 410 m level where the TAS04 tunnel is located. The orientation of the major horizontal stress is NW–SE, nearly parallel to the dominant water-bearing fracture set and the TAS04 tunnel axis. Christiansson and Jansson (2003) reported the vertical component to be in the range of 15–20 MPa and the minor horizontal component to be close to the gravitational stress at 10–13 MPa. There are however other indications that the minor horizontal and vertical stress components are quite similar at around 11–12 MPa (Ericsson *et al.* 2015).

For Activity 2.1, a constant stress and pore pressure field was required as an initial assumption, with the inclusion of a gradient to be simulated for the subsequent activities. Each team could consider the following boundary conditions but were not obligated to include them.

Hydraulic boundary conditions:

- outer boundaries: pore pressure boundary of 5 MPa.
- inner boundaries including drillholes: pore pressure boundary of 0 MPa, except for injection drillholes.

Mechanical boundary conditions:

- vertical stress: normal to boundary with directed load of 12 MPa.
- min. horizontal stress normal to tunnel axis: normal to boundary with directed load of 12 MPa.
- max. horizontal stress parallel to tunnel axis: normal to boundary with directed load of 24 MPa.
- remaining boundary: roller boundary (only boundary-parallel displacement allowed).
- inner boundaries including drillholes: free boundary with load of 0 MPa.

### 3.2.4. Material properties

The bedrock at the Äspö HRL (hard rock laboratory) consists of diorite intersected by granitic and pegmatitic dykes. Typical rock mass properties for the investigation area are given in Table 3 and were provided to be used for the modelling. The use of intact rock properties was judged to be suitable given the massive nature of the rock and the separate, explicit modelling of fractures. Input properties for the injection fluid (i.e. water) are presented in Table 4. The fracture properties were not specified. Instead, each team was left to derive these based on the fracture aperture estimates provided (see Table 5) and assuming a corresponding relationship to normal stress.

**Table 3.** Mechanical and hydraulic properties of the modelled intact (unfractured) granite (assuming isotropic and homogeneous parameters).

Rock Properties	Value	Unit
Young's modulus	76	GPa
Poisson's ratio	0.25	1
Density	2.750	kg m <sup>-3</sup>
Porosity	0.01	%
Permeability	5E-18	m <sup>2</sup>
Biot Coefficient	1	1

**Table 4.** Input parameters for the injection fluid (water).

Water Properties	Value	Unit
Dynamic viscosity	1E-03	Pa s
Compressibility	4.4e-10	Pa <sup>-1</sup>
Density	1000	kg m <sup>-3</sup>

### 3.2.5. Fractures

The open fractures intersecting the tunnel surface and the selected drillholes are shown in Figure 5. They were provided to the modelling teams together with the remaining interpreted fractures in DWG and DGN formats, as produced by SKB/TAS. It was left to the modelling teams to decide whether to explicitly model all of the fractures mapped. The corresponding data can be found in Appendix 6 from Ericsson *et al.* (2015). However, as a minimum, the fractures presented in Figure 5 and Table 5 were to be included. The leak-off from these fractures into the formation should be modelled by the poroelastic material behavior at this stage of modelling.

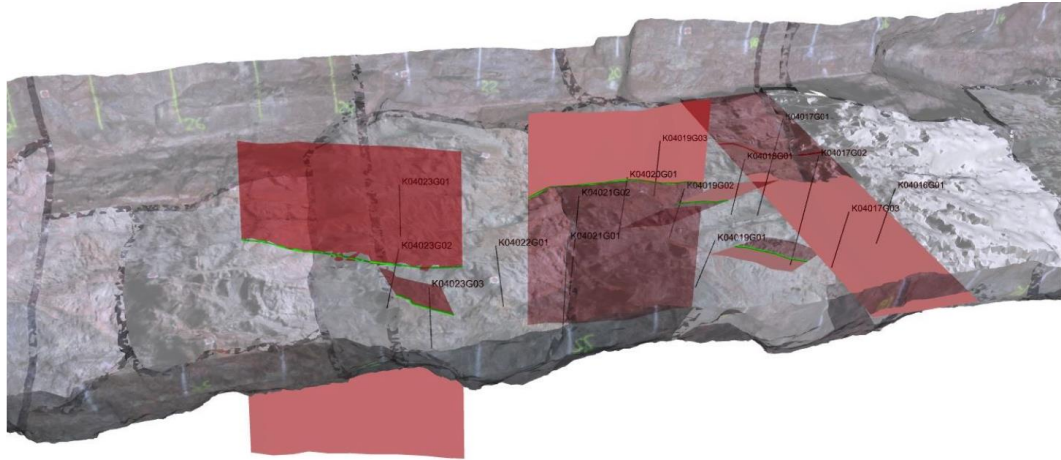


Figure 5. Image of the tunnel floor and the intersecting open fractures taken from the Appendix 2 of Ericsson et al. (2015).

**Table 5.** Data of the interpreted fractures shown in Figure 5.

Drillhole	Fracture	Strike	Dip	Aperture
	#			mm
K04023G03	99	135	66	0.5
K04023G03	94	315	50	0-1
K04021G02	137	300	70	0-0.5
K04019G02	144-c	120	55	0-0.2
K04017G01	143	120	10	0.3
K04017G02	150	170	40	0.2

### 3.2.6. Reflector data

A second set of fractures was derived from mapping carried out using ground penetrating radar (GPR). These reflectors were neglected in Activity 2.1 since they are censored and biased by the limitations of GPR, which restricted detection to fractures that were very shallow (0 to 0.4 m) and mainly sub-horizontal, as shown in Figure 6. However, where the modelling results of Activity 2.1 with the open fractures did not match the measured pressure responses, the reflectors could be implemented in subsequent models to provide additional fluid pathways. Furthermore, these additional fractures increase the potential for open fractures to intersect the drillholes. This is further discussed in Section 3.2.11 for which Figure 11 provides an additional overview of the interpreted reflector data.

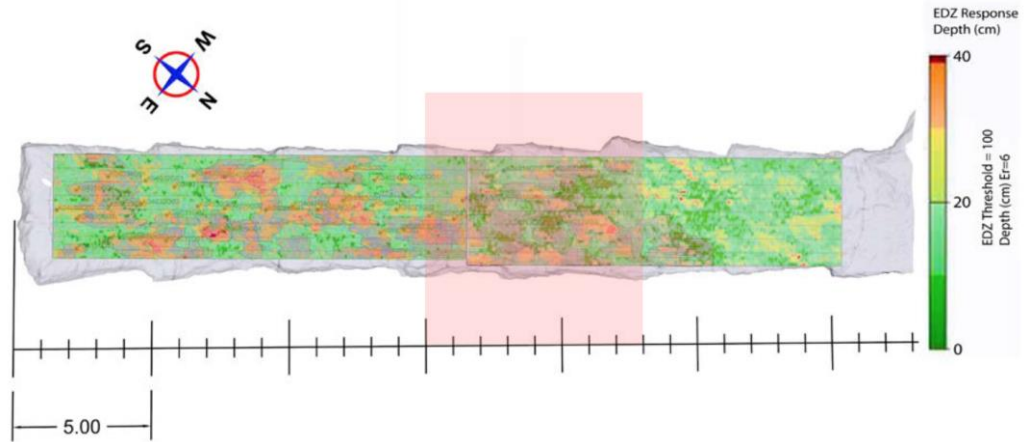


Figure 6. Excavation damage depth from ground penetrating radar measurements (Ericsson et al., 2015). Red highlighted box indicates the modelling area.

### 3.2.7. Discrete Fracture Network data

The third set of fractures considered was derived from conditional stochastic fracture simulations by Dr. Joel Geier. These took the form of Discrete Fracture Network (DFN) models. The data was provided in \*.STL and \*.PAN formats in five subsets. The first three of these represent (1) fractures mapped as “open” that connect to the tunnel floor, (2) fractures mapped as “sealed” that connect to the tunnel floor, and (3) two additional, sub-horizontal fractures just below the tunnel floor that were added to ensure connections between the modelled drillhole sections. The remaining subsets represent stochastically generated fractures in successively larger volumes around the tunnel.

The modelling teams were advised that subset (1) included the “open” fractures that were modelled in the previous activity, based on the same mapped traces in the tunnel floor, but with alternative interpretations of the fracture dip angle. Thus, if they were to use these fractures in combination with the fractures from Activity 2.1, they should remove the duplicated open fractures.

### 3.2.8. Excavation Damage Zone

In cases where the additional fracture sets could not be incorporated into the models, the tunnel geometry could be extended symmetrically by a certain factor around the existing tunnel and used as a boundary for a second material domain to attempt representing the EDZ using an effective medium approach to account for the very small fractures. Figure 7 shows a schematic example of a tunnel surrounded by an EDZ (indicated by the red shading) relative to the undisturbed rock volume (grey shading). The initial input properties to be considered are presented in Table 6; these could however be scaled or modified during a parametric sweep by the modelling teams to achieve fit to the reference data.



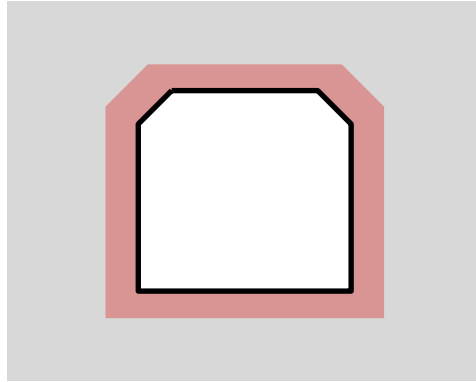


Figure 7. Example of how to introduce an excavation damage zone around a tunnel.

**Table 6.** Petrophysical and geomechanical properties of the granite (isotropic and homogeneous parameters).

Rock Properties	EDZ	Intact rock	Unit
Young's modulus	60	76	GPa
Poisson's ratio	0.3	0.25	-
Density	2600	2750	kg m <sup>-3</sup>
Porosity	0.05	0.01	-
Permeability	5E-14	5E-18	m <sup>2</sup>
Biot Coefficient	1	1	-

### 3.2.9. Update on boundary conditions

Building on Activity 2.1, Activity 2.2 incorporated the use of gradients for the initial stresses and/or pore pressures to yield a more realistic situation. The gradients depended on the density of the fluid and rock. The modelling teams were to consider the following boundary conditions but were not obligated to use them.

Hydraulic boundary conditions:

- Hydrostatic pore pressures with a gradient of 9.81 kPa/m within the rock domain and ambient pore pressures at the inner tunnel boundaries.

Mechanical boundary conditions:

- Gravitational stress conditions in the rock domain so that the vertical and minimum horizontal stresses are equal to 12 MPa at the tunnel mid-level, with a gradient of 29.5 kPa/m.
- The maximum horizontal stress (aligned parallel to the tunnel axis) is equal to 24 MPa at the tunnel mid-level, with a gradient of 29.5 kPa/m + 12 MPa.

### 3.2.10. Injection rates and pressures

In Activity 2.1 and Activity 2.2, the injection was to be modelled by applying an injection pressure for a duration of 1200 s in each of the selected drillholes for the specified injection interval, using pressures of 442 kPa, 92 kPa, and 80 kPa for K04017G02, K04018G01, and K04020G01, respectively (see Table 7).



For Activity 2.3, the true pressure responses in the observation holes were to be modelled. These together with the injection pressure inputs for the interference tests in K04017G02, K04018G01, and K04020G01 are presented in Figure 8, Figure 9, and Figure 10, respectively. In addition, the measured inflow into the tunnel and injection rates are given in the Excel sheet. The presented time information within the excel sheets is a general time (column “Date&Time”) of the measurement in the format Year.Month.Day hh.mm.ss and an additional column (“Time”) of time in seconds. The latter is the synchronized time between the injection hole and observation hole, to be used for the modelling. It was left to the modelling teams whether to use the injection pressures or injection rates. More information on the raw data of the interference tests can be found in Appendix 20 and 21 of Ericsson *et al.* (2015).

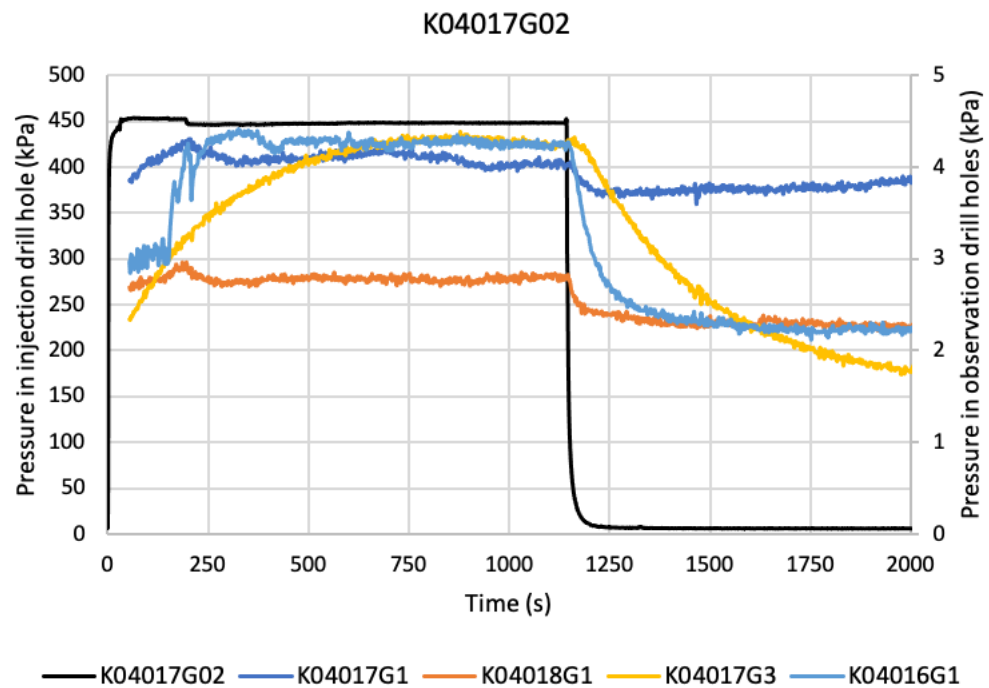


Figure 8. Interference test K04017G02. Black curve (K04017G02) represents the injection pressure (left y-axis).

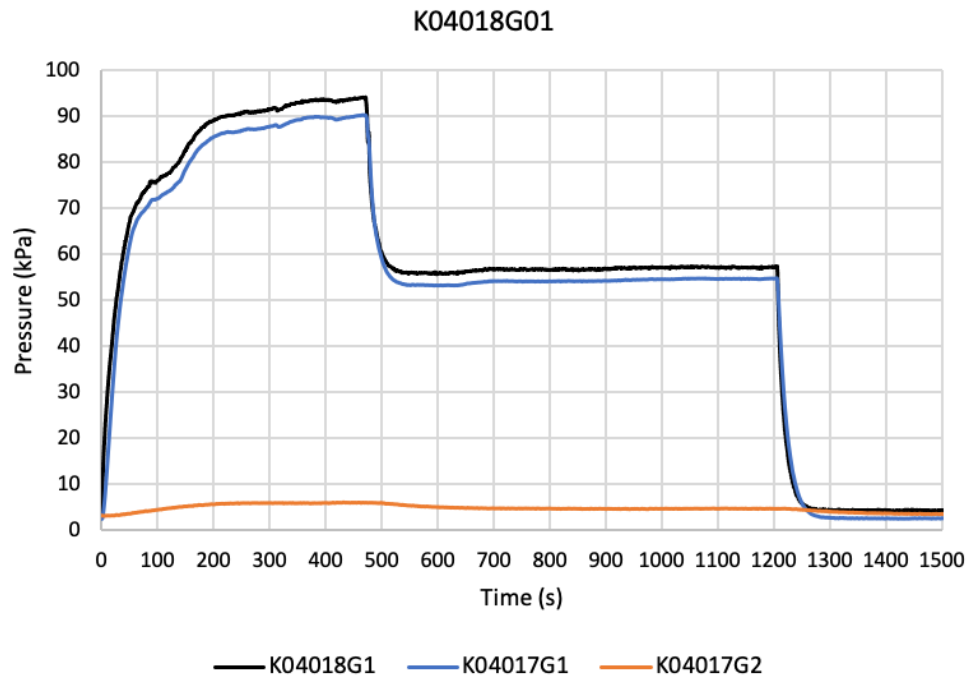


Figure 9. Interference test K04018G01. Black curve (K04018G1) represents the injection pressure (left y-axis).

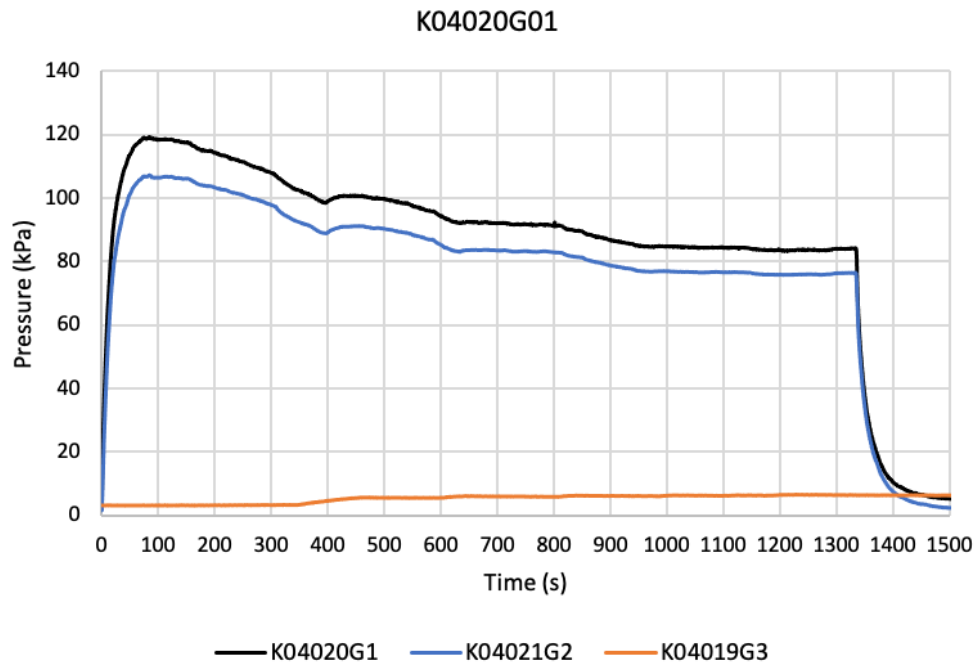


Figure 10. Interference test K04020G01. Black curve (K04020G01) represents the injection pressure (left y-axis).

### 3.2.11. Reworked reflector data

The reflectors previously described in 3.2.6. were included for the modelling groups to use in Activity 2.2 but required further treatment before using due to their irregular shapes. Mesh element reduction, smoothing, and re-triangulations were performed by

GMC on the data set to provide a more robust and easier to handle dataset while still ensuring a sufficiently accurate representation of the geometry. Figure 11 shows the original and reworked data set. Only very small changes can be observed after manipulation of the original data set.

Again, the intention of this dataset was that it could be implemented to provide additional fluid pathways where the modelling results of Activities 2.1 and 2.2 with the open and DFN fractures did not match the measured pressure responses. Furthermore, they might serve to increase connectivity between the drillholes and the open fractures.

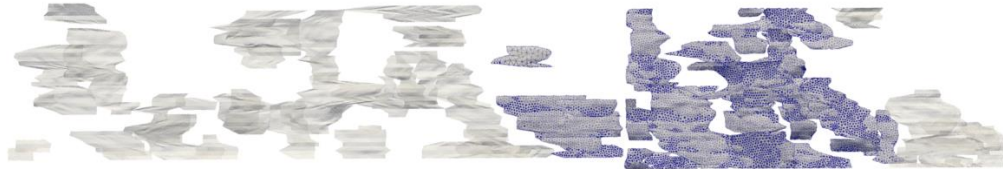


Figure 11. Original (transparent) and reworked (blue) interpreted reflector data.

### 3.3. Simulation

Within the defined set of drillholes (see Section 3.2.2), three injection tests were selected for modelling based on the data presented in Appendix 28 of Ericsson *et al.* (2015), meeting the following key criteria:

- The absence of any indications of irregularities due to leakage either around the packers or through the seal above the drillhole extension;
- Observations of connectivity of varying magnitude.

The following three injection holes and corresponding packed off injection intervals (measured as depths relative to the top of the drillhole) were selected based on these criteria:

- K04017G02 (0.4–0.6 m)
- K04018G01 (0.1–0.2 m)
- K04020G01 (0.2–0.4 m)

Injection tests in all three of these injection holes produced discharge via fractures daylighting into the tunnel floor, as well as measurable pressure responses indicating hydraulic connections with at least two observation holes:

- K04017G02 (0.4–0.6 m): K04016G01, K04017G01, K04017G03, and K04018G01
- K04018G01 (0.1–0.2 m): K04017G01, K04017G02
- K04020G01 (0.2–0.4 m): K04019G03, K04021G02.

The corresponding interference tests are presented in Figure 8, Figure 9, Figure 10 and Table 7. The relative location of each injection and observation hole listed in Table 7 is included in Figure 12.

**Table 7.** Interference tests. See Figure 12 for locations of each hole. Note that depth is measured from the top of the corresponding drillhole.

Injection hole	Depth	Injection pressure	Observation hole	Pressure change in observation hole
	m	kPa		kPa
K04017G02	0.4-0.6	442	K04016G01	1.4
K04017G02	0.4-0.6	442	K04017G01	0.3
K04017G02	0.4-0.6	442	K04017G03	3
K04017G02	0.4-0.6	442	K04018G01	0.4
K04018G01	0.1-0.2	92	K04017G01	88
K04018G01	0.1-0.2	92	K04017G02	4
K04020G01	0.2-0.4	80	K04019G03	4
K04020G01	0.2-0.4	80	K04021G02	21

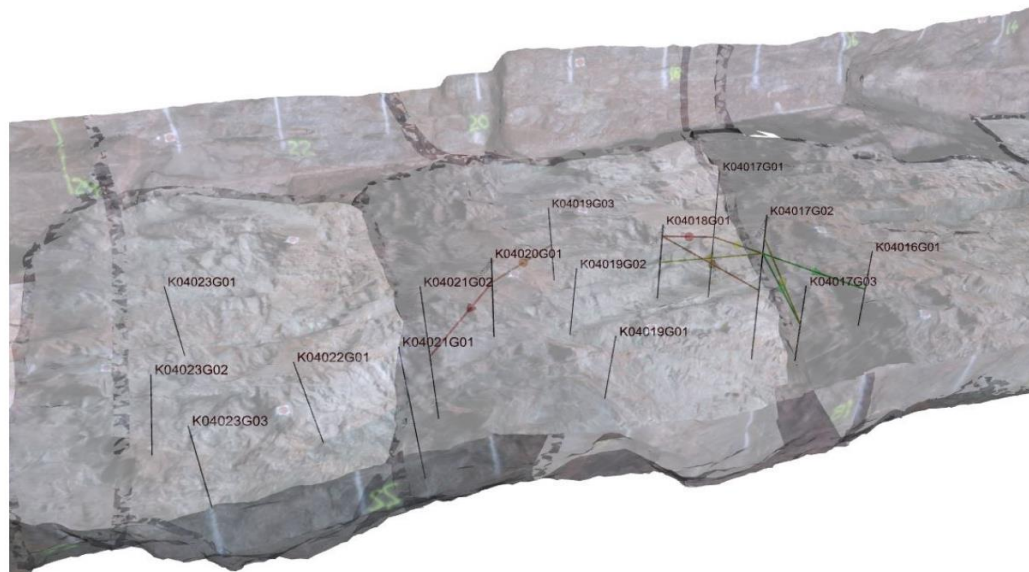


Figure 12. Image of the tunnel floor and the injection tests with direct response in the neighbouring observation holes indicated by arrows taken from the Appendix 2 from Ericsson et al. (2015).

### 3.3.1. Activities 2.1 and 2.2

Each modelling team was directed to apply the corresponding injection pressure in the specified drillhole and injection interval for a period of 1200 s (20 min), and to then monitor the modelled pressure changes in the other drillholes. Since the observation holes were packed off at the top of the drillhole, the complete drillhole would need to be monitored in terms of the maximum change in pressure. Each interference test was to be modelled separately.

### 3.3.2. Activity 2.3

Each modelling team could choose to apply either the time-dependent injection pressure or the time-dependent flow rate (see Figure 8, Figure 9, and Figure 10) in the specified injection drillholes and packed-off intervals. The modelling teams were then to monitor the change in pressure in the other drillholes. Again, since the observation holes were packed off at the top of each drillhole, the complete drillholes would need to be monitored in terms of the maximum change in pressure. Each interference test was to be modelled separately.

In the case of any parametric sweeps performed for the material, fracture, and boundary conditions, those results within 15% error between the numerical result and the measuring campaign should be presented by the modelling team.

## 4. Seoul National University

### 4.1. Modelling Method Selected

Seoul National University (SNU) selected the Discrete Element Method (DEM) to model the mechanical and hydraulic behavior of fractured rock observed in the Äspö interference tests. In WP 1, 2D models were constructed using the commercial program UDEC (ver. 5.0) from Itasca Consulting Group Inc. to simulate the fluid flow through the fractured rock. WP 2 aimed at expanding the previous 2D models to a 3D model using the related commercial program 3DEC (ver. 5.0), also from Itasca Consulting Group Inc. Both UDEC and 3DEC use the same hydro-mechanical formulation and constitutive models.

To build the fractured rock model within 3DEC, a series of joint planes are specified to cut the host rock into discrete blocks. Constitutive models are then assigned, with a selection of models available to model the continuum behavior of the rock blocks and a separate selection of constitutive models applicable to the discontinuum behavior of the block bounding joints. The latter, so-called DEM, can be used to model the joints as different types of fractures.

The motion of every block in DEM follows Newton's second law based on the applied force (Equation 1). The force applied on the contacts of each block is governed by the force-displacement law (Equation 2). The movement of blocks generates the overlap on each contact which induces the contact forces. The iteration of the movement of blocks and contact force continues until every contact force reaches the equilibrium.

$$\frac{d\dot{u}}{dt} = \frac{F}{m} \quad (1)$$

$$F = k \cdot \Delta u \quad (2)$$

Where  $u$  is the displacement,  $t$  is time,  $F$  is force,  $m$  is mass, and  $k$  is the stiffness of the elements. Joints included in the model also deform based on the stress-displacement relationship governed by the joint stiffness (Equation 3). In shear, there is an additional constitutive equation defining the slip of the joint. In this model, the Coulomb slip model is adopted to define the slip of a joint (Equation 4 and 5). During the slip of a joint, joint dilation occurs due to the roughness of the joint surface. The amount of the dilation is proportional to the shear displacement (Equation 6).

$$\Delta\sigma_n = -k_n\Delta u_n^e \quad (3)$$

$$|\tau_s| \leq C + \sigma_n \tan \phi = \tau_{max}, \text{ then } \Delta\tau_s = -k_s\Delta u_s^e \quad (4)$$

$$|\tau_s| \geq \tau_{max}, \text{ then } \tau_s = \text{sign}(\Delta u_s)\tau_{max} \quad (5)$$

$$\Delta u_n^s = \tan(\phi_d) \cdot \Delta u_s, \quad (6)$$

where  $\Delta\sigma_n$  and  $\Delta\tau_s$  are the effective normal and shear stress increment,  $k_n$  and  $k_s$  are the joint normal and shear stiffness,  $\Delta u_n$  and  $\Delta u_s$  are the total incremental normal and shear displacement,  $\Delta u_n^e$  and  $\Delta u_s^e$  are the elastic component of the incremental normal and shear displacement,  $C$  is the cohesion,  $\phi$  is the friction angle and  $\phi_d$  is the dilation angle.

Each joint between the blocks allows for fluid flow based on its transmissivity derived using a cubic law relationship (Witherspoon et al., 1980). This requires assigning apertures and aperture relationships to the joints. A correlation is then drawn between the

normal stress acting on the joint, its corresponding aperture, and its transmissivity. Thus, transmissivity within the model is largely controlled by the modelled deformation of the joints as a function of their normal closure, opening and/or shear dilation (Rutqvist and Stephansson, 2003). These hydraulic constitutive relationships are also dependent on the hydraulic input parameters.

The coupled hydro-mechanical time-stepping procedure used by UDEC and 3DEC alternates between solving for fluid flow and mechanical equilibrium. Fluid flow along each joint is calculated together with the corresponding changes in pore pressure. These locally disturb the effective stresses acting along each joint. In response to the unbalanced stresses that arise, the solution then proceeds to solve for mechanical equilibrium, calculating the corresponding block and joint deformations, which in turn affect the joint apertures and subsequently the hydraulic flow conditions. This cycling between hydraulic and mechanical solutions continues until the goals of the analysis are met (e.g. equilibrium is established, or a specified fluid flow time is reached). It is through this coupling that 3DEC can describe the hydro-mechanical behavior of fractured rock.

Since 3DEC describes the detail and realistic hydro-mechanical behavior of a fracture and fracture networks, the model requires long time to calculate the behavior of blocks and fractures, especially for the hydro-mechanical analysis. Therefore, the size of elements should be coarser than other numerical tools and sometimes it is not able to set enough monitoring points.

## 4.2. Model Implementation

### 4.2.1. Model geometry

A 3D DEM model 50 m in height, 50 m in width and 32 m in length was constructed to represent the host rock describing the Äspö HRL site (Figure 13). The model includes part of the TAS04 tunnel which is parallel to the x-direction. The floor of the tunnel in the model corresponds to an assumed depth of 409 m. To allow increased resolution in the model where the interference tests were performed, the tunnel floor was discretized by minimizing the element size to include a higher concentration of finite-difference elements whose edge size ranges from 0.6 m to 4.2 m and joint contact nodes in comparison to the remaining rock volume.

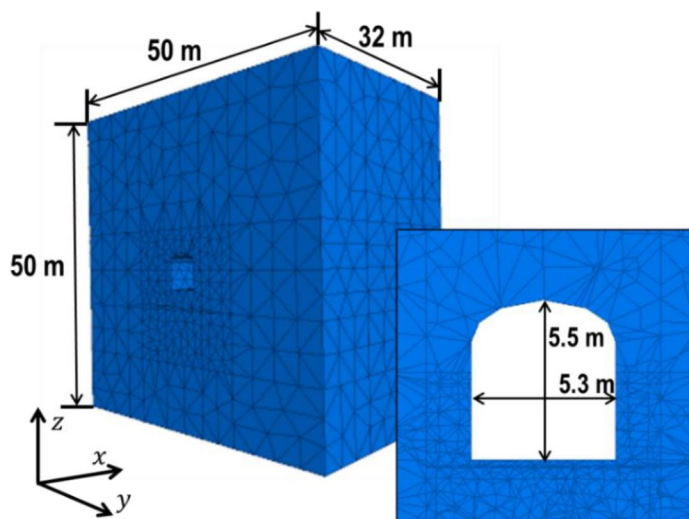


Figure 13. Geometry of 3D DEM model including the tunnel



#### 4.2.2. Joint model

Fractures in the model were embedded as non-persistent circular joints which are deformable and permeable. In WP 2.1, six rectangular open fractures were suggested to serve as fluid pathways (Figure 14 left). The SNU group represented these fractures as circular joints with appropriate radii (Figure 14 right). Each fracture has its own initial aperture based on the values provided in the definition of the activity, as given in Table 8. This initial aperture is applied to the model before the stress re-distribution induced by the excavation of the tunnel.

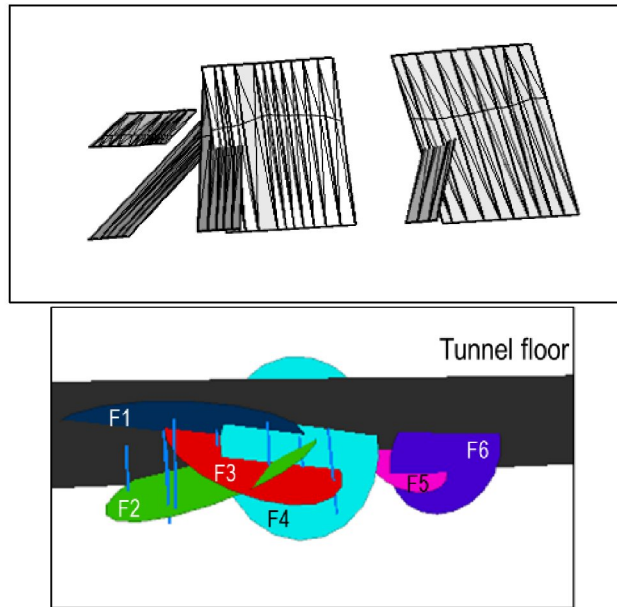


Figure 14. Geometry of fractures (left) suggested in definition of WP 2.1 and (right) assumed as the circular shape in the DEM model

**Table 8.** Attribute information for the open fractures assumed in WP 2.1

Fracture code	Strike (°)	Dip (°)	Origin	Aperture (mm)	Radius (m)
F1 (143, K04017G01)	120	10	(2428.39, 7352.14, -409.00)	0.3	5.3
F2 (150, K04017G02)	170	40	(2429.23, 7352.03, -409.50)	0.2	5
F3 (144-c, K04019G02)	120	55	(2429.04, 7350.72, -409.50)	0.1	3.7
F4 (137, K04021G02)	300	70	(2429.73, 7349.89, -409.50)	0.25	4
F5 (94, K04023G03)	315	50	(2432.43, 7348.51, -409.50)	0.1	3
F6 (99, K04023G03)	135	66	(2432.76, 7347.63, -409.50)	0.5	2

In WP 2.2, the conditional DFN dataset is also implemented in the constructed model. The fractures in the DFN datasets are classified by their connectivity with the drillholes. For instance, Class 1 fractures are those directly connected to the drillholes and the Class 2 fractures are the fractures which are not connected to the drillholes but connected to the Class 1 fractures (see Figure 15). A range of initial apertures were assigned to the fractures and these initial apertures were applied before the stress re-distribution (Table 9).



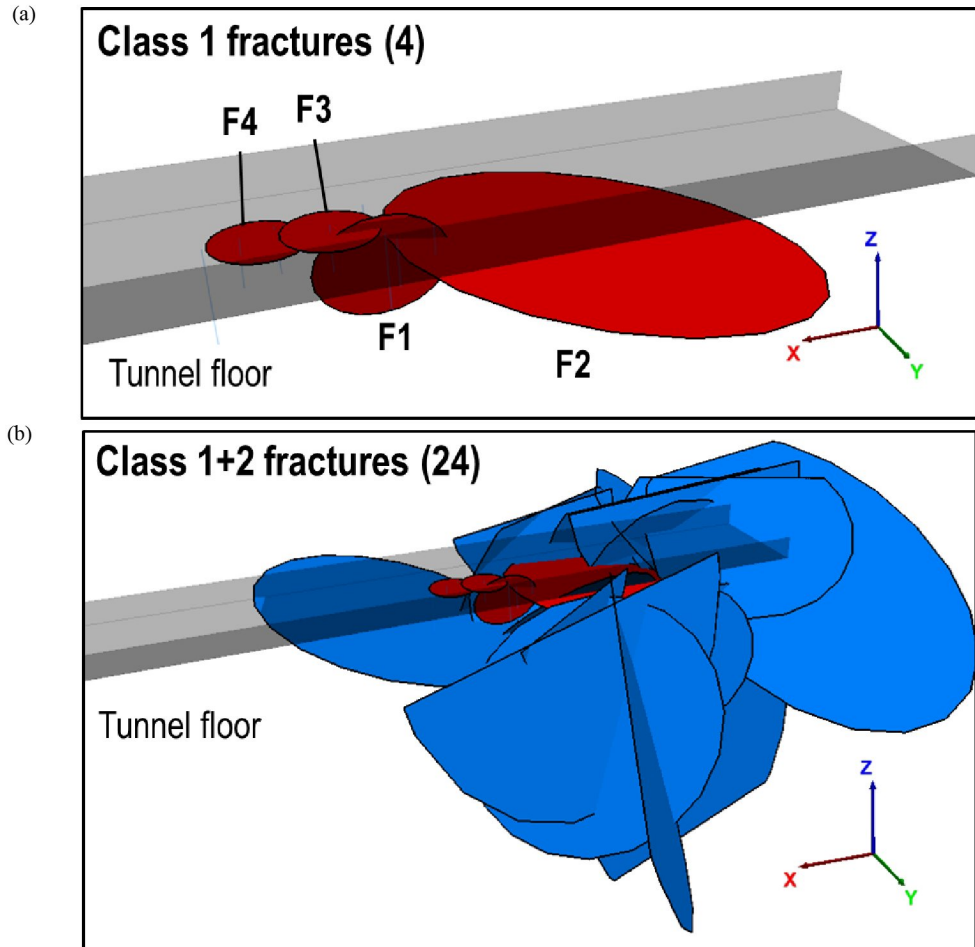


Figure 15. (a) Class 1 and (b) Class 2 fractures from the conditional DFN dataset

**Table 9.** Attribute information for the Class 1 fractures applied in WP 2.2.

Fracture code	Dip direction (°)	Dip (°)	Origin	Aperture (mm)	Radius (m)
F1	182.5	69.4	(2427.4, 7351.9, -410.25)	1	1.47
F2	259.1	9.8	(2424.8, 7355.9, -410.31)	0.4	4.86
F3	0	0	(2428.2, 7351.1, -409.20)	0.046	1.00
F4	0	0	(2428.9, 7349.9, -409.29)	0.046	1.00

In WP 2.3, the model with the same conditional DFN dataset is prepared. In previous WPs, it is assumed that the suggested aperture data is the initial value before the stress re-distribution. However, the suggested aperture data is based on the observation after the excavation of the TAS04 tunnel, so the effects of the stress re-distribution is already considered in the aperture data. Since SNU's DEM model aimed to describe the hydro-mechanical effect of the EDZ as the change of the aperture induced by the stress re-distribution without considering the creation of the new fractures, the model adopted the uniform initial aperture (0.0046 mm) as an aperture before the stress re-distribution and tried to observe that the stress-induced aperture change can describe the hydro-mechanical behavior of the EDZ observed from the TAS04 tunnel.

**Table 10.** Summary of the joint models in each WP.

	WP2.1	WP2.2	WP2.3
Joint geometry	Six open fractures	DFN	DFN
Initial apertures	Diverse	Diverse	Uniform
Description of EDZ	Fracture deformation/slip	Fracture deformation/slip	Fracture deformation/slip

#### 4.2.3. Rock properties

Properties of the host rock were assigned as suggested in the definitions (see Table 3), except for the transmissivity of the rock. This has been ignored because the permeability of the crystalline rock is extremely low relative to that along the fractures. It should also be noted that 3DEC only performs fluid flow calculations along the modelled joint contacts. Pore pressures can be calculated within the modelled blocks to account for effective stresses, however the blocks are otherwise assumed to be impermeable.

#### 4.2.4. Joint properties

The total deformation of the fractures includes both the normal deformation and the shear dilation, which are calculated based on the joint properties and redistributed stresses acting on each joint. The properties for the joints, assuming a Coulomb slip constitutive model, were assumed based on those previously reported for the Äspö HRL (Glamheden *et al.*, 2007; Ericsson *et al.*, 2014; Mas Ivars *et al.*, 2014) (**Table 11**).

**Table 11.** Joint properties in each WP.

Properties	Units	Value		
		WP 2.1	WP 2.2	WP 2.3
Joint normal stiffness	GPa/m	200	200	17.6 ~ 2200
Joint shear stiffness	GPa/m	100	100	100
Dilation angle	Degree	3	3	5 ~ 20
Joint cohesion	MPa	0.9	0.9	0.9
Joint friction angle	Degree	36	36	36
Maximum aperture	mm	10	10	10
Residual aperture	mm	0.005	0.005	0.0045

In Activity 2.1 and 2.2, the joint normal stiffness and the dilation angle were set to remain constant during every simulation procedure, whereas in Activity 2.3 the joint normal stiffness and dilation angle were varied as a function of the normal stress. Glamheden *et al.* (2007) already extracted the ranges of some joint properties subject to the applied normal stress from laboratory tests using rock samples from the Forsmark site. Particularly, the joint normal stiffness and the dilation angle were shown to be highly dependent on the applied normal stress. Since both properties are critical parameters influencing aperture evolution (and therefore transmissivity), the

corresponding input values were carefully examined before the simulation for Activity 2.3.

Walsh (1981) and Bandis *et al.* (1983) suggested that the joint normal stiffness is proportional to the applied normal stress (Equation 7). Based on the observations from the Forsmark lab testing, the stress dependent normal stiffness model for the Äspö HRL site can be developed (Equation 8).

$$\frac{d\delta_n}{d\sigma_n} \left( = \frac{1}{k_n} \right) \propto \frac{1}{\sigma_n} \quad (7)$$

$$k_n = 2.44 \times 10^5 \sigma_n \quad (8)$$

Here  $\delta_n$  is the normal displacement of the joint,  $k_n$  is the joint normal stiffness and  $\sigma_n$  is the normal stress acting on the joint surface.

The dilation angles extracted from the Forsmark testing data showed that this parameter decreases significantly as the applied normal stress increases. Barton and Choubey (1977) derived an empirical relationship between the dilation angle of joints and the normal stress applied on the joint surface (Equation 9). Figure 16 shows a logarithmic curve fitted to three different dilation angles from the Forsmark data. The corresponding relationship between the dilation angle and the applied normal stress for this fitted curve is given in Equation 10.

$$\phi_d = JRC \times \log(JCS/\sigma_n) \quad (9)$$

$$\phi_d = 7.09 \log(58.12/\sigma_n) \quad (10)$$

where  $\phi_d$  is the joint dilation angle,  $JRC$  is the joint roughness coefficient,  $JCS$  is the joint compressive strength and  $\sigma_n$  is the normal stress applied on the joint surface.

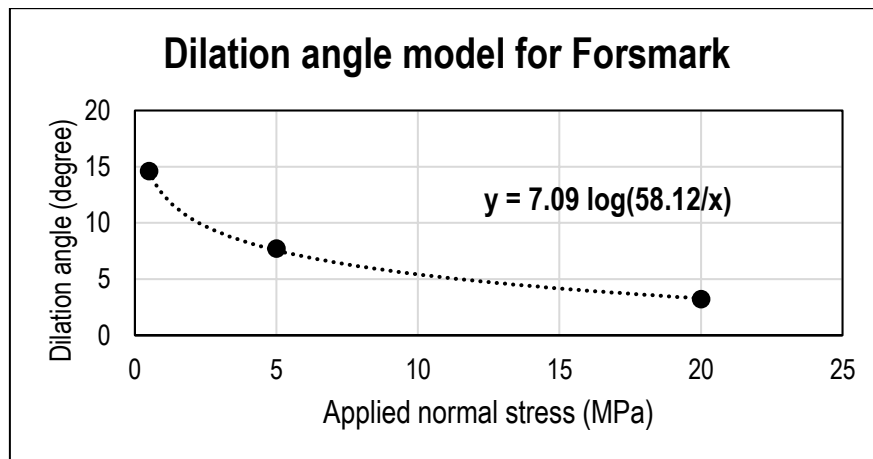


Figure 16. The dilation angles for three different applied normal stresses derived from Forsmark test data and the corresponding fitted logarithmic trend line

The newly established functions for these two properties can be applied to the model inputs to capture their normal stress-dependency. Applying these to the Class 1 and 2 fractures (Figure 15), the resulting apertures after stress re-distribution, deformation and mechanical equilibrium can be determined. Figure 17 shows the distributions of the fracture transmissivities calculated from the model apertures using the 3DEC cubic law relationship. These are compared to the transmissivity data measured from the injection tests performed by SKB at the Äspö HRL (Ericsson *et al.*, 2015). Figure 17a and Figure 17b indicate that the joint normal stiffness and dilation angle input values significantly affect the evolution of the fracture transmissivities through the normal opening and shear dilation, respectively, that develop in the model. Applying the stress-dependent joint normal stiffness and dilation angle relationships (determined above) to the model input values, it can be seen that they produce a better fit to the SKB measured transmissivity distributions with depth than those obtained assuming constant input values (Figure 17c).

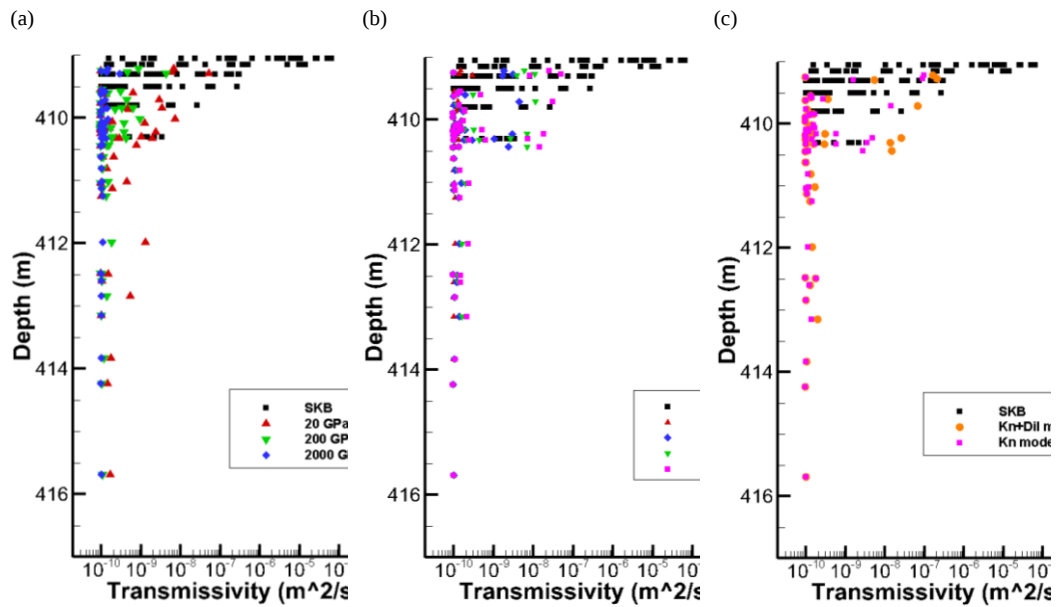


Figure 17. Distributions of the transmissivity values simulated using 3DEC compared to those measured from the Äspö HRL injection experiments. Comparisons include those for: (a) different joint normal stiffness values, (b) different dilation angles, and (c) applying either constant joint normal stiffness values or those calculated using the normal-stress dependent joint normal stiffness (Kn) and dilation angle (Dil) functions derived.

#### 4.2.5. Boundary conditions

Unlike the 2D model in WP 1, the WP 2 modelling incorporated depth-dependent boundary conditions that were applied to the 3D models. The direction of the maximum horizontal stress is parallel to the tunnel axis (x). The minimum horizontal stress, which is of the same magnitude as the vertical stress, is perpendicular to the tunnel axis (Equations 11 to 14). The tunnel surface was assumed to be a free mechanical and hydraulic boundary.

$$\sigma_x = 12 + 0.0295z \text{ (MPa)} \quad (11)$$

$$\sigma_y = 0.0295z \text{ (MPa)} \quad (12)$$

$$\sigma_z = 0.0295z \text{ (MPa)} \quad (13)$$

$$P_p = 0.0008z \text{ (MPa)} \quad (14)$$

where,  $\sigma_x, \sigma_y, \sigma_z$  are the far field stress in x, y, z directions,  $P_p$  is the pore pressure and z is a depth. The TAS04 test tunnel is at 410 m depth and the model is extracted from the depth of 380 m to 430 m.

#### 4.2.6. Interference tests

WP 2 aims to simulate three interference tests performed in the TAS04 tunnel. Each test included one injection drillhole and two or more observation drillholes used to monitor the pressure response during the injections. To simulate the three interference tests, eight drillholes would be required in the model (Figure 18). In Activity 2.1 and Activity 2.2, the final pressure responses under the constant pressure conditions were extracted after the model reached steady state. In Activity 2.3, the transient pressure responses were modelled. Although the pressure curves from the in-situ tests tend to be unstable and continuous, the boundary conditions applied to simulate the injection pressure in the models were simplified to assume that the injection pressure curves were constant and stepwise.

Because the fluid flow through the rock volume was restricted to fracture flow (a limitation of 3DEC as noted previously), the representations of the drillholes were effectively reduced to points on the fractures where the drillholes intersected the fracture. Fluid injection and monitoring of the pressure response was performed solely at these intersection points. The effect of the drillhole presence on the stress and pore pressure distributions was ignored due to the negligible size of the drillholes.

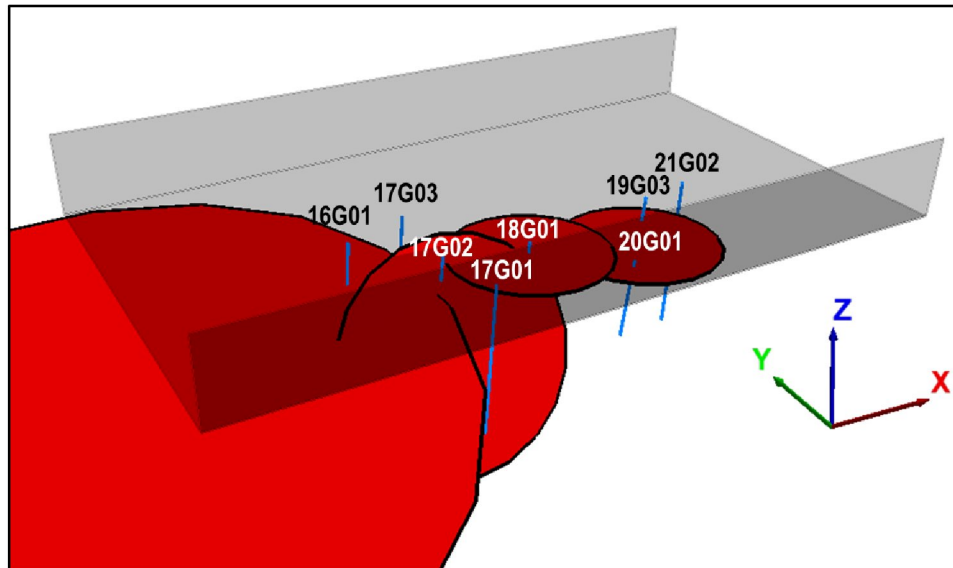


Figure 18. Geometry of the eight drillholes simulated relative to the Class 1 fractures

## 5. Technical University of Liberec and Institute of Geonics of the CAS

### 5.1. Modelling Method Selected

The Technical University of Liberec and Institute of Geonics of the CAS (TUL-IGN) selected the Finite Element Method (FEM) and commercial software package COMSOL Multiphysics® (Versions 5.2-5.4) to carry out their modelling under WP 2. The “Subsurface flow” module, and specifically the built-in interface for fracture flow (COMSOL 2017), was used for the simulations carried out for Activities 2.1 and 2.2.

The COMSOL formulation uses Biot’s poroelasticity (1962), combining solutions for Darcy flow for a saturated porous medium (Equation 15) with linear elasticity, to model the 3D matrix. Within the 3D matrix, fracture flow is modelled by solving for pressure changes along the 2D interfaces representing the fracture network. These are coupled to the surrounding 3D matrix and solved using a 2D approximation for the deformation of a plane (Equation 16).

$$-\nabla \cdot \left( \frac{\kappa}{\mu} \nabla p \right) = 0 \quad (15)$$

$$\begin{bmatrix} \sigma_{xx} \\ \sigma_{yy} \\ \sigma_{xy} \end{bmatrix} = \frac{E}{(1+\nu)(1-2\nu)} \cdot \begin{bmatrix} 1-\nu & \nu & 0 \\ \nu & 1-\nu & 0 \\ 0 & 0 & 1-2\nu \end{bmatrix} \cdot \begin{bmatrix} \varepsilon_{xx} \\ \varepsilon_{yy} \\ \varepsilon_{xy} \end{bmatrix} - \begin{bmatrix} \alpha_B p & 0 & 0 \\ 0 & \alpha_B p & 0 \\ 0 & 0 & \alpha_B p \end{bmatrix} \quad (16)$$

Here  $\kappa$  is the permeability of the material,  $\mu$  is the dynamic viscosity of the liquid,  $p$  is the fluid pressure,  $\sigma_{ij}$  and  $\varepsilon_{ij}$  are the stress and strain tensor components, respectively,  $\nu$  is the Poisson’s ratio,  $E$  is the Young’s modulus, and  $\alpha_B$  is the Biot’s coefficient.

Fracture flow through the 3D matrix considers tangential derivations (Equation 17) to define the flow along lines representing the fractures:

$$-\nabla_T \cdot \left( \frac{\kappa_f}{\mu} \nabla_T p \right) = 0, \quad (17)$$

where  $\kappa_f$  indicates the permeability of the fracture and  $\nabla_T$  is the gradient operator limited to the tangential direction towards the fracture. The problems are defined as time-dependent tasks and solved considering the following governing equations to generalize the description given for the 2D tasks.

$$\nabla \cdot \sigma = F_v \quad (18)$$

$$\sigma = C: (\varepsilon - \varepsilon_0) - \alpha_B p I \quad (19)$$

$$\varepsilon = \frac{1}{2} [(\nabla u)^T + \nabla u] \quad (20)$$

$$\rho S \frac{\partial p}{\partial t} + \nabla \cdot (\rho u) = Q_m - \rho \alpha_B \frac{\partial e_{vol}}{\partial t} \quad (21)$$

$$u = -\frac{\kappa}{\mu} \nabla p \quad (22)$$

$$S = \varepsilon_p \chi_f + \frac{(\alpha_B - \varepsilon_p)(1 - \alpha_B)}{K}, \quad (23)$$

Here  $\sigma$  is the stress tensor,  $F_v$  is the volumetric force,  $C$  is the coefficient of elasticity tensor,  $\varepsilon$  is the strain tensor,  $\varepsilon_0$  is the initial value of the strain tensor,  $u$  is the stress vector,  $\rho$  is the density of the liquid,  $S$  the coefficient of storability,  $Q_m$  is a member expressing the source,  $t$  is time,  $\chi_f$  is the compressibility of the liquid,  $\varepsilon_p$  is porosity,  $K$  is hydraulic conductivity and  $\varepsilon_{vol}$  is the volumetric strain.

## 5.2. Model Implementation

A 3D model geometry and FEM mesh incorporating the TAS04 tunnel and several of the key fractures surrounding the tunnel were constructed for Activity 2.1. Preparation of the 3D mesh required considerable effort, and some operations had to be performed outside the COMSOL environment. The tunnel geometry data, provided as an \*.STL file, was first modified using the Meshmixer tool to simplify the topology data describing the inner surface of the tunnel. GMSH was then used to calculate and mesh the intersections of the individual fractures (this can also be done in COMSOL but difficulties with the mesh generation were encountered).

The external boundaries of the mesh were built to form a rock block 40 m wide, 40 m long and 50 m high. The 3D mesh consisting of 162,000 four-sided elements (average element quality = 0.69) was then shaped to incorporate the excavated tunnel within this block. During the initial phase, two tunnel geometries were generated: one involving a simplified smooth surface created by generating a standard tunnel profile of approximately the same dimensions as the TAS04 and extruding it for the required tunnel length (Figure 19, left); and one with the detailed irregular tunnel surface, generated using the \*.STL geometry file provided (Figure 19, right). The fractures located below the surface of the tunnel (Figure 5) were represented as 2D planes (Figure 19) using the orientations shown in Table 5. Within COMSOL, the same “Fracture Flow” module was used to calculate the fracture flow as was used for the 2D exercise in Activity 1.3.3. Mechanical changes (e.g., changes in fracture aperture) due to flow were not considered for the fractures.

Drillholes were added to the 3D model during the phase of Activity 2.1. The injection drillholes (K04017G02, K04018G01, K04020G01) were represented in the 3D mesh using cuboid-shaped cavities. These were positioned using heights and locations corresponding to the drillhole injection intervals (as specified in Section 3.2.2). The observation drillholes were represented by lines along which the model results could be displayed. For a more detailed description of the injection tests, see Section 1.1.

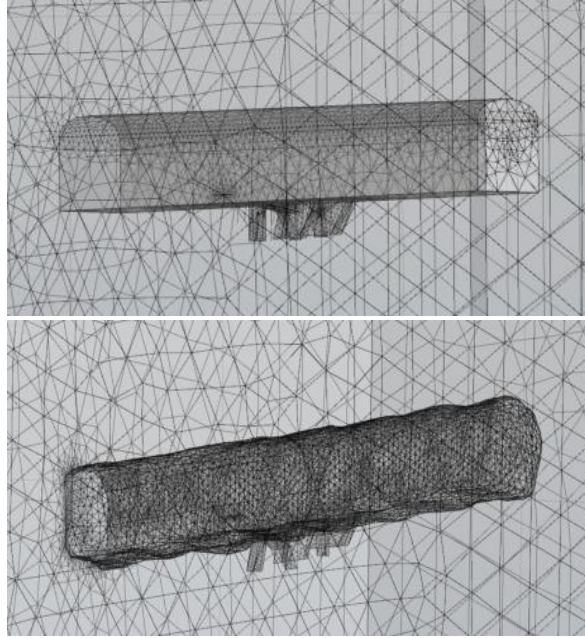


Figure 19. Detail of the updated alternatives of the 3D meshes generated, for models with a regular smooth surface using a representative tunnel profile (left) and with an irregular surface using the TAS04 tunnel shape file provided (right).

### 5.2.1. Rock and fracture input properties

For the initial calculations in Activity 2.1, the input properties used for the rock matrix were taken from those specified in the description of the SKB experiment. These were the same as those used for the 2D models in WP 1 and are given in Table 6.

The input properties for the fractures were also based on those provided in the Activity description of the 2D task. Added to these was the hydraulic conductivity of the fractures, which was calculated using a cubic law relationship according to the opening of the fractures described in Table 5.

### 5.2.2. Boundary conditions

The following hydraulic and mechanical boundary conditions were applied to the 3D model mesh (according to those defined in Section 3.2.3). The hydraulic boundaries were set as:

- Outer boundary of the model: pressure 5 MPa
- Inner boundary of the model: pressure 0 MPa

The mechanical boundary conditions were set, assuming a uniform initial stress distribution, as (when looking into the tunnel from the open end):

- Upper outer boundary of the model: vertical stress = 12 MPa at a depth of 385 m.
- Right outer boundary of the model: horizontal stress = 12 MPa
- Front outer boundary of the model: horizontal stress = 24 MPa
- Outer boundaries of the model: zero normal displacement
- Inner boundaries of the tunnel: stress = 0 MPa, displacement = free.



### 5.2.3. Model initialisation

A steady-state model using the regular smooth tunnel geometry was solved first to obtain the initial pore pressure and stress field distribution in the model. This served as the initial condition for the time-dependent injection tests. The behavior of the steady-state model was based on the input assumptions and experience gained from the 2D models developed in the earlier phase of the study. From the simulations, it was also possible to determine the total modelled inflow rates into the tunnel stemming from (fracture and matrix flow), which was  $5.2959 \cdot 10^{-6} \text{ m}^3 \cdot \text{s}^{-1}$ .

### 5.2.4. Representation of injection holes

Figure 20 shows the distribution of the individual injection drillholes together with the positions of the observation drillholes and the nearby fractures. It is interesting to note that K04020G01 does not intersect any of the fractures, which would result in a low-pressure response in the corresponding observation drillholes. In contrast, drillholes K04017G02 and K04018G01 are intersected by a common fracture, indicating the possibility for communication and a higher-pressure response.

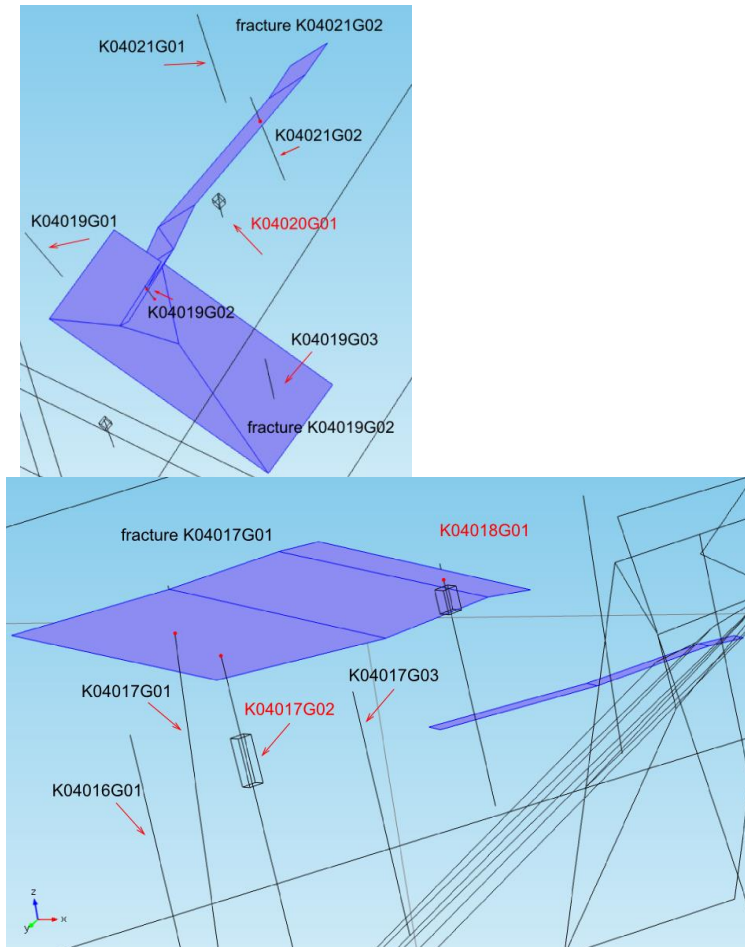


Figure 20. Position of the injection and observation drillholes together with the positions of the surrounding fractures.

### 5.2.5. Updates for Activity 2.2

Several changes were made to the model based on the results of Activity 2.1 and to incorporate new data provided for Activity 2.2. This included changes made to the 3D geometry and mesh. First, the overall dimensions of the model were increased to 60 m wide, 60 m long, and 50 m high. Two new sub-horizontal fractures were added below the tunnel floor based on the DFN data (Figure 21 left) and a simple EDZ (twice the size of the initial tunnel) was added to surround the tunnel (Figure 21 right). These two additions were made to ensure better connectivity between the existing fractures and to improve the responses to the injection tests in the observation drillholes.

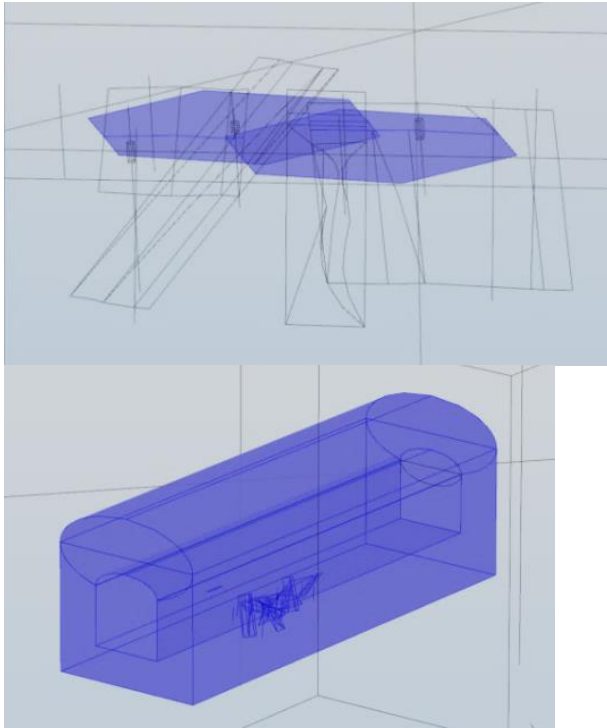


Figure 21. Additions to the 3D model, including two new sub-horizontal fractures below the tunnel floor (left) and an EDZ added to surround the tunnel (right).

### 5.2.6. Sensitivity study

Using the newly defined geometry, a sensitivity analysis was performed to test the influence of the hydraulic conductivity of each fracture together with other related assumptions. The starting material properties corresponded to those given for WP1, except for the hydraulic conductivity of the rock which, on the basis of the test model, was reduced to  $5 \cdot 10^{-12} \text{ m} \cdot \text{s}^{-1}$ .

The base case was started by using the initial hydraulic conductivity values for each fracture represented in the model. These are listed in the column labelled “0” in Table 12. The EDZ was not considered for the base case. Each additional column represents an alternative model where the hydraulic conductivity of one fracture was changed. This involved a 10x increase for each case, except for fracture K04021G01 where a 100x increase was applied. Each column header indicates the fracture number that was changed. Except for the “0” base case, all other alternatives included the presence of the EDZ around the tunnel. Alternatives “hor1” and “hor2” refer to models where the hydraulic conductivity of the sub-horizontal fractures was changed. In the alternative

“rock”, the hydraulic conductivity of the rock matrix was modified, and in the alternative “EDZ2”, the hydraulic conductivity of the EDZ was modified.

**Table 12.** Alternatives tested in the sensitivity study. Each column represents a different sensitivity case. The base case using the starting hydraulic conductivities for each fracture is labelled “0” in the column header. The hydraulic conductivity of each fracture being tested (columns from left to right) was increased by 10x, except for fracture K04021G01, which was increased 100x. The base case did not consider the presence of the EDZ, but all other alternatives included the EDZ. “hor1” and “hor2” denote the sub-horizontal fractures. The hydraulic conductivity values highlighted by a background color indicate the value changed for each sensitivity test.

Hydraulic conductivity (m·s <sup>-1</sup> )	0	EDZ	1701	1702	1902	2101	2301	hor1	hor2	Rock	EDZ <sub>2</sub>
1701	7.4E-02	7.4E-02	7.4E-01	7.4E-02	7.4E-02	7.4E-02	7.4E-02	7.4E-02	7.4E-02	7.4E-02	7.4E-02
1702	3.3E-02	3.3E-02	3.3E-02	3.3E-01	3.3E-02	3.3E-02	3.3E-02	3.3E-02	3.3E-02	3.3E-02	3.3E-02
1902	8.2E-03	8.2E-03	8.2E-03	8.2E-03	8.2E-01	8.2E-03	8.2E-03	8.2E-03	8.2E-03	8.2E-03	8.2E-03
2101	5.1E-02	5.1E-02	5.1E-02	5.1E-02	5.1E-02	5.1E-01	5.1E-02	5.1E-02	5.1E-02	5.1E-02	5.1E-02
2301	2.0E-01	2.0E-01	2.0E-01	2.0E-01	2.0E-01	2.0E-01	2.0E+00	2.0E-01	2.0E-01	2.0E-01	2.0E-01
hor1	2.0E-01	2.0E-01	2.0E-01	2.0E-01	2.0E-01	2.0E-01	2.0E-01	2.0E+00	2.0E-01	2.0E-01	2.0E-01
hor2	2.0E-01	2.0E-01	2.0E-01	2.0E-01	2.0E-01	2.0E-01	2.0E-01	2.0E-01	2.0E+00	2.0E-01	2.0E-01
k_rock	5.0E-12	5.0E-12	5.0E-12	5.0E-12	5.0E-12	5.0E-12	5.0E-12	5.0E-12	5.0E-12	5.0E-13	5.0E-12
k_edz	bez EDZ	5.0E-11	5.0E-11	5.0E-11	5.0E-11	5.0E-11	5.0E-11	5.0E-11	5.0E-11	5.0E-11	5.0E-10

## 6. Geomecon GmbH (GMC)

### 6.1. Modelling Method Selected

Activities 2.1, 2.2, and 2.3 within WP 2 of Task G in DECOVALEX-2019 were modelled numerically using the Finite Element Method (FEM) and the software package COMSOL Multiphysics® (Versions 5.3-5.4). FEM is a widely established numerical method for solving problems in engineering and mathematical physics. These problems are generally described by partial differential equations, which are derived from conservation laws of physics such as conservation of mass, energy or momentum. To solve the problem, FEM subdivides the problem domain into smaller, simpler finite elements. The simple equations that model these finite elements are then assembled into a larger system of equations modelling the entire problem domain. FEM then uses variational methods from the calculus of variations to approximate a solution by minimizing an associated error function. The approximation is achieved by discretizing the partial differential equations which can then be solved using numerical methods.

The FEM numerical approach and COMSOL software used are well established for a range of different working applications and FEM is a widely used numerical approach. As any numerical method, FEM is only an approximation of the real situation. Model building and model assumptions cannot precisely reflect in-situ conditions. Furthermore, convergence studies with increasing mesh refinement need to be performed to evaluate the error between different mesh sizes. The chosen software package contains a set of verified and tested partial differential equations for poroelasticity, which allows to evaluate the simulation results of such problems with confidence. Moreover, the interface for setting up the model (geometry, material properties, boundary conditions, mesh, solver) is easy to use and thereby prevents users to make errors, e.g. selecting wrong boundaries in particular with the fracture networks, or using wrong units.

### 6.2. Model implementation

The following sections explain the model geometry, boundary conditions, material parameters, model size, and mesh discretization. The chosen numerical approach is directly compared with the envisaged boundary conditions and model setup given in the corresponding definition of the activities.

Due to problems in implementing the different fracture sets into COMSOL Multiphysics®, two approaches were tested. The first approach was to introduce as many of the mapped fractures as possible to model fluid flow along these fractures. The second approach tried to model fluid flow in the rock volumes showing yield, thus accounting for the presence of stress-induced fractures (EDZ) without explicitly modelling them. For the sake of comparison to the other modelling teams, the latter approach is not described here. A separate publication is in preparation.

In the following, the construction of the model will be described with respect to the activities that provided progressively more information. Since the provided data sets were not obligatory, not all data sets were fully integrated in COMSOL Multiphysics. In particular, the reflector and the DFN data sets were only included after significant reduction and manipulation using other programs external to COMSOL Multiphysics®.

### 6.2.1. Tunnel geometry and boundary conditions

The number of points forming the surface of the TAS04 tunnel was reduced and meshed in MeshLab<sup>2</sup>. Even though the point cloud was reduced from 137,525 points to 5285 points the characteristics of the tunnel the widening of the tunnel at the end of each blast round, can still be recognized. Figure 22 shows the reconstructed tunnel surface in COMSOL.

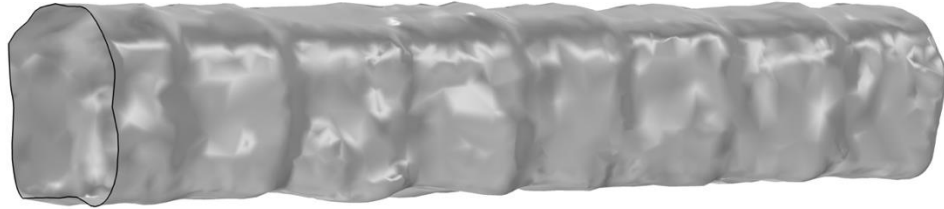


Figure 22. Reconstructed tunnel surface used for FEM model geometry.

The tunnel surface was assigned a fixed pore pressure of 0 MPa (i.e., atmospheric pressure with 1 atmosphere of suction due to a relative humidity of less than 1), and was free to deform under the given far-field stress during all Activities. This fixed pore pressure boundary condition was applied as a Dirichlet boundary:

$$p = p_0 \quad (24)$$

where  $p_0$  is the input pore pressure.

### 6.2.2. Open fractures

The open fractures were imported into COMSOL Multiphysics using the \*.STL files provided. The fractures were trimmed at their intersection with the tunnel boundary. Figure 23 shows the imported fractures in green after trimming.

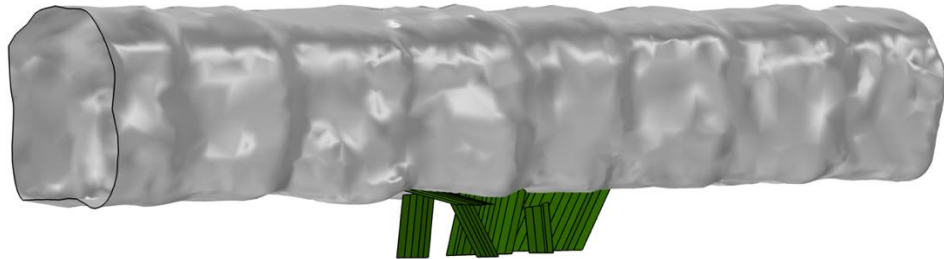


Figure 23. Imported open fractures (green) below tunnel.

The open fractures were assigned a tangential form of Darcy's law (i.e. the flow on the surface between two domains) described as fracture flow in the COMSOL Multiphysics® manual. This approach is similar to the approach taken by SNU. The boundary conditions for the fractures are given by:

$$\nabla_T \cdot (d_f \rho u_f) = d_f Q_m \quad (25)$$

---

<sup>2</sup> <http://www.meshlab.net/>

$$u = -\frac{\kappa}{\mu} \nabla_T p \quad (26)$$

which is a tangential derivative of Darcy Flow with  $d_f$  being the fracture aperture.

For Activity 2.1, each fracture was assigned individual apertures as defined in Table 5. However, the permeability and porosity of these fractures were fixed to 1 D and 0.7%, respectively. No additional dependency on stress or aperture change was included for the fracture flow within this activity.

In Activities 2.2 and 2.3, the fractures were assigned a fracture stiffness of 34 GPa/mm to allow fracture deformations to be accounted for. In these models, for fractures that open in response to a stress or pore pressure change, i.e. the effective normal stress on the fracture was tensile, the calculated aperture was subsequently used to update the permeability assigned to the fracture based on the cubic law relationship.

### 6.2.3. Drillholes

In Activity 2.1, the drillholes were modelled as lines based on the details provided in Image of the tunnel floor and the relevant drillholes taken from the Appendix 2 from Ericsson et al. (2015).

**Table 2.** This was then revised to implement them as cylinders for Activities 2.2 and 2.3 (see Figure 24). For this purpose, the two points were manually inserted together with a third randomly placed point. The three points were used to construct a cross section of the drillhole, which was then axi-symmetrically rotated around the drillhole axis to form a cylinder. This cylinder was then trimmed at its intersection with the tunnel floor. The injection holes were further segmented to correspond to the injection intervals, which were then assigned a time-dependent pore pressure function.

In Activities 2.1 and 2.2, a smoothed rectangular function was used to prescribe the 20-minute-long pore pressure pulse as indicated in the activities' descriptions. The smoothed rectangular function increased from 0 to 1 between minutes 2 to 4 and decreased from 1 to 0 between minutes 22 to 24 to model an injection time of 20 min. The rectangular function was then multiplied by the injection pressure for each individual injection drillhole as presented in Table 7. In Activity 2.3, the true injection pressure data was ascribed to the injection intervals of the corresponding drillholes.

The observation drillholes were assigned a no-flow boundary condition in all activities, so that the pore pressure at the observation hole was not overwritten by any other boundary condition to properly reflect the pore pressure changes.

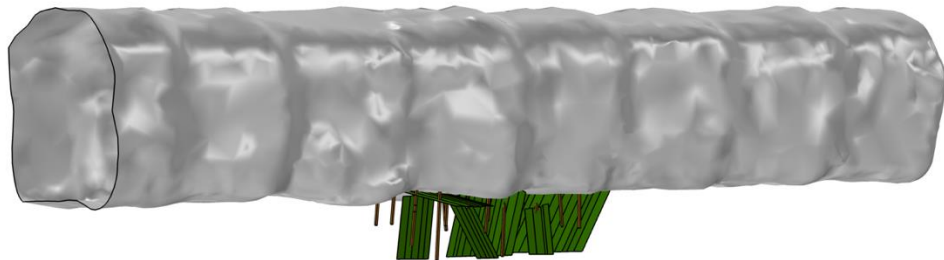


Figure 24. Drillholes modelled as cylinders below the tunnel surface shown in light brown.

#### 6.2.4. Discrete Fracture Network Data

The DFN data could not be implemented in COMSOL Multiphysics.

#### 6.2.5. Reflectors

Additional fracture data was made available for Activity 2.3 in \*.STL format. The fracture data stem from interpreted ground penetrating radar (GPR) measurements, which indicate the presence of fractures parallel to the tunnel floor at shallow depths. The depth that these fractures extend below the tunnel floor is unknown due to the low penetration depth of the GPR measurements. Because of the irregular shape of the fractures, significant problems arose when importing and meshing them as is in COMSOL. Deleting isolated fractures and fractures that are not related to the drillholes significantly reduced the data set. Further manipulations and smoothing procedures of the irregular shaped fractures in external programs like Paraview<sup>3</sup> and MeshMixer resulted in a data set that could be implemented into COMSOL. Figure 25 shows the reworked reflector data that could be loaded into COMSOL Multiphysics after editing.

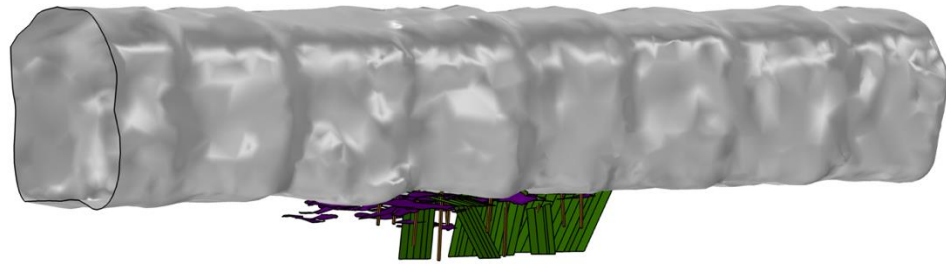


Figure 25. Reduced and manipulated reflector data in purple.

Similar to the open fractures, the reflectors were assigned to model fracture flow within Activity 2.2.

#### 6.2.6. True Injection data

For Activity 2.3, the injection pressure and observation pressures were provided. The injection pressures could be applied along the corresponding intervals of the injection holes via a time-dependent pore pressure boundary condition following the pressure-time record shown in Figure 26.

---

<sup>3</sup> (<https://www.paraview.org/>)

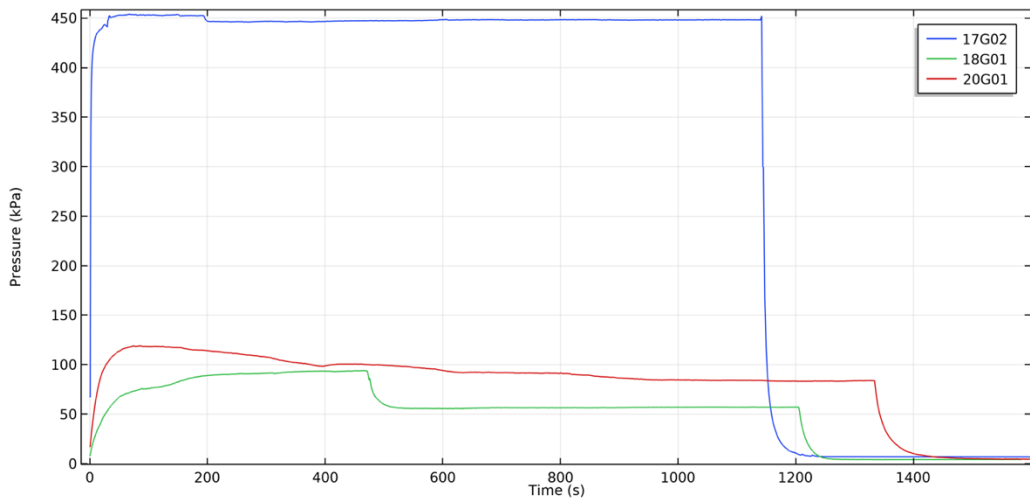


Figure 26. True injection curves from the TAS04 experiment modelled.

### 6.2.7. Inner modelling domain

In order to simplify the meshing procedure and to maintain a high-quality mesh in the region of interest below the tunnel floor where the main fracture flow was occurring, a small inner modelling domain was set up as shown in Figure 27.

The inner modelling domain was modelled as a poroelastic rock mass. The partial differential equations employed for modelling the static part of the activity links the interaction of fluid flow and deformation in a porous medium by means of poroelasticity (Biot 1962). For more information about poroelasticity in COMSOL Multiphysics, the reader is referred to the software manual (COMSOL Multiphysics Manual, Introduction to Subsurface Flow Module, p10).

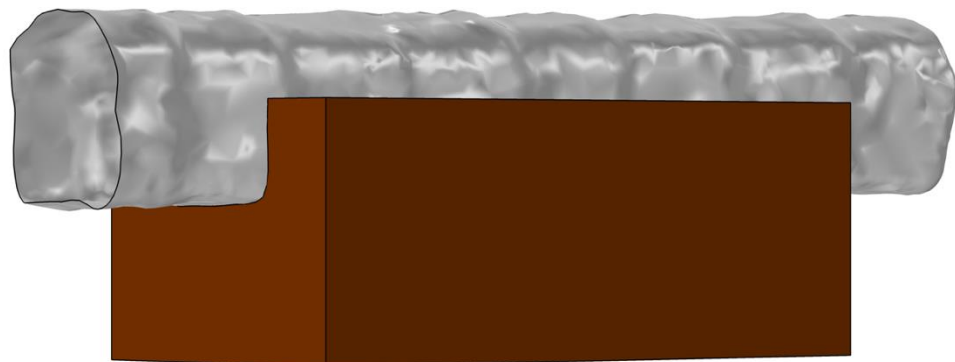


Figure 27. Sub-domain built around drillholes, open fractures and reflectors.

### 6.2.8. Outer modelling domain

The simplified tunnel contour, open fractures, drillholes, and reflectors are embedded into a cuboid of 39 x 25 x 25 m. Approximately, one meter of the tunnel at the tunnel entrance has been removed since problems occurred in the model building process. Due to the low matrix permeability of the rock, the chosen size of the modelling domain is



considered to be large enough to avoid excessive boundary influences. For comparison, the longest drillhole is about 2 m and hence an order of magnitude smaller than the cuboid. Figure 28 shows the outer modelling domain with only a partly visible tunnel surface.

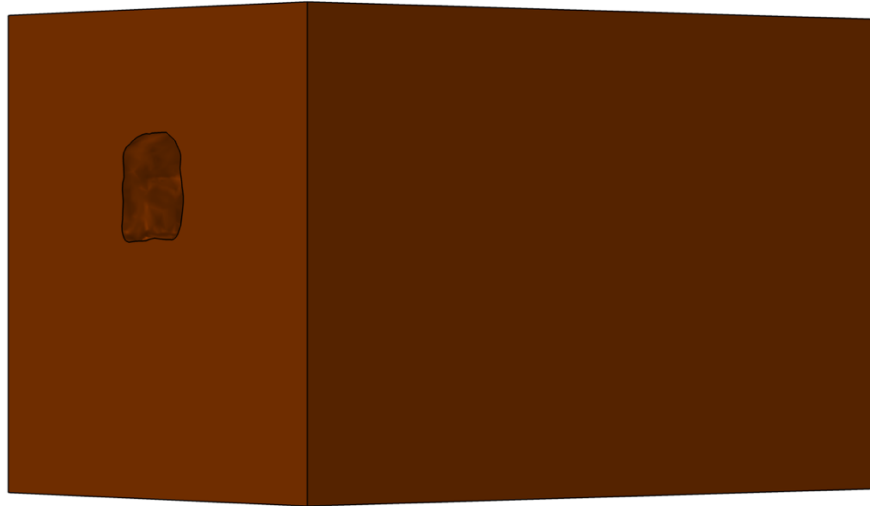


Figure 28. Complete model domain, 25 x 25 x 39 m in size.

The outer modelling domain was assigned to act as a poroelastic material similar to the inner modelling domain. In addition, mechanical boundary conditions to define the initial stress condition were applied as suggested in the Activity definition.

This involved assigning a gradual stress state in WP 2.2 and 2.3 of

- Upper outer boundary of the model: vertical stress = 11.72 MPa at a depth of 397.5 m.
- Right outer boundary of the model: horizontal stress = 29.5 MPa/km
- Front outer boundary of the model: horizontal stress = 29.5 MPa/km + 12 MPa
- Outer boundaries of the model: zero normal displacement
- Inner boundaries of the tunnel: stress = 0 MPa, displacement = free.

COMSOL Multiphysics® allows the user to define Neumann boundary conditions with pressures directed normal to the boundary as input:

$$S \cdot n = F_A, \quad F_A = -p \cdot n \quad (27)$$

where  $n$  is the vector normal to the boundary,  $S$  is the stress and  $p$  is the normal directed input pressure.

All external boundaries were modelled as roller boundaries (first order symmetry boundaries), which allow only face parallel displacements and suppresses displacements in the normal direction. This is achieved by setting the displacement in the normal direction for each element on the boundary to zero:

$$n \cdot u = 0 \quad (28)$$

where  $n$  is the vector normal to the boundary and  $u$  is the displacement vector.

In Activity 2.1, it was suggested applying a fixed pore pressure of 5 MPa and 0 MPa to the outer and inner boundaries, respectively. We did not apply the outer 5 MPa boundary

conditions. Instead we fixed the pore pressure to 0 MPa on the inner and outer boundary. By doing so, it is possible to relate any change in pore pressure to the interference tests without subtracting the initial pore pressure conditions, which is different from drillhole to drillhole (due to different depths, orientations or other circumstances).

### 6.2.9. Material properties

The input properties used for water and rock were unaltered from the properties defined in the activities (Table 4 and Table 6). Only the properties for the fractures (Table 13) were altered in the different activities.

**Table 13.** Properties of the fractures.

Property	Activity 2.1	Activity 2.2	Activity 2.3	Unit
Permeability	1000	Cubic law	Cubic law	mD
Porosity	0.7	0.7	Stress-dependent	%
Aperture	0.2-0.5*	Stress-dependent	Stress-dependent	mm
Fracture stiffness	-	-	34*	MPa/mm
Fracture data	Open fractures	Open fractures	Open fractures, reflectors	

\* According to Activity Definition 2.1

### 6.2.10. Mesh discretisation

Initial runs of the model showed that the pressures at the injection drillholes were higher than the prescribed value. The mesh was subsequently refined along the injection drillhole until the prescribed pressure matched the observed pressure within approximately 5%. The model was meshed with an increasing mesh fineness towards the tunnel as well as increased mesh fineness along the fractures and drillholes. In the vicinity of the tunnel, the resulting mesh size was between 0.05 and 0.5 m. This then increased to 5 m at the outside boundary of the model. The final mesh used consisted of 1,078,339 tetrahedral elements with an average mesh quality of 0.66. The fractures and the tunnel surface consisted of 18,507 triangular elements with an average quality of 0.85.

Figure 29 shows the mesh for the entire model domain. Figure 30 shows a close-up of the mesh quality for the tunnel surface and fractures.

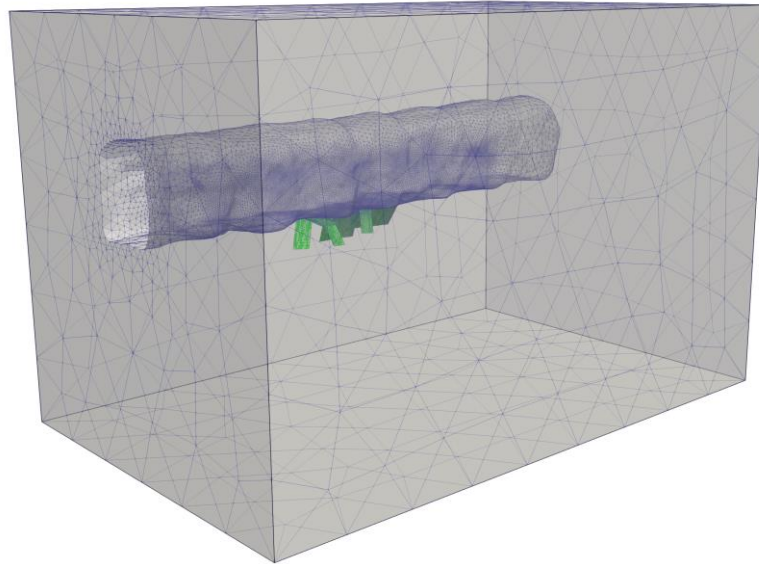


Figure 29. Discretisation of the model geometry (except drillholes) showing a finer mesh in the area where the open fractures (green) are located.

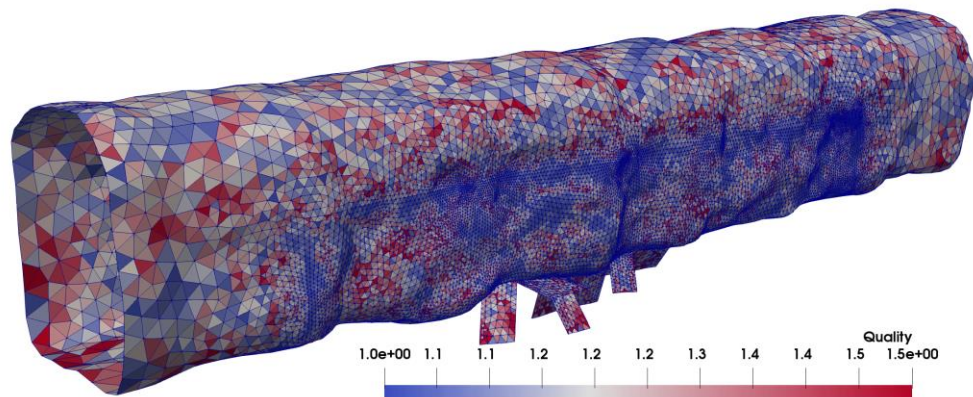


Figure 30. Edge ratio of the tunnel surface and fracture discretisation showing that the ratio of the longest to the shortest triangle edge is between 1 and 1.5 indicating uniformly shaped triangles.

### 6.2.11. Solver settings and computing

The solution was obtained by two serially connected solution steps consisting of a static and a subsequent time-dependent fluid flow solution. Both steps used a fully coupled direct solver with linear and quadratic shape functions for the fluid flow and solid mechanical parts. The static step was used to calculate the initial stress and pore pressure state to be used for the time dependent step corresponding to the interference tests. The calculation time for the stationary step was about 8 min while the calculation time increased to 36 h 45 min for the time-dependent step.

The solution is obtained if the relative error between each calculation step is less than  $1e-3$ . The time dependent study covered a total of 60 min with calculation steps each 30 s using a constant Newton solver to address the non-linear convergence. If the criteria for the relative error is not met, the solution is not obtained (i.e., the solution does not converge). The simulations were conducted on a MacPro Late 2014 with 6 cores @ 3.50GHz (Intel® Xeon(R) CPU E5-1650 v2) and 64 GB RAM.

## 7. Results

The following sections describe the modelling outcome in terms of the redistributed stress field around the tunnel, the static and dynamic inflow into the tunnel, as well as the pressure responses during the different activities. Each section contains a short discussion where the different modelling team results are compared against each other. However, due to the different approaches taken by the modelling teams, the results are quite varied and difficult to compare directly.

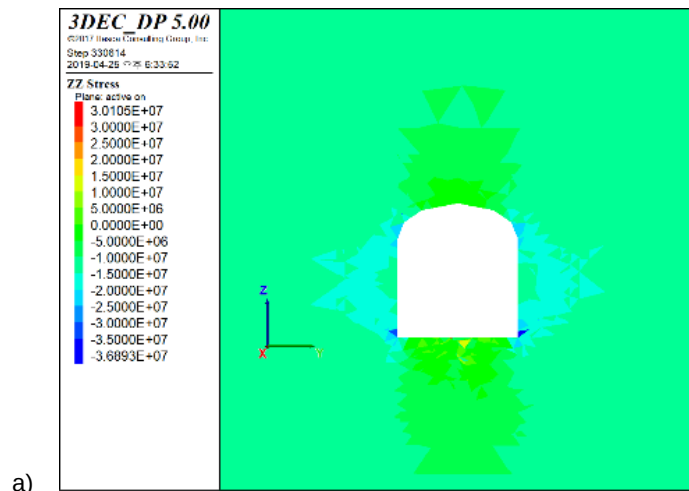
### 7.1. Tunnel stresses (Activity 2.1)

This activity called for visualization of a cross section normal to the tunnel axis to be provided showing the vertical, maximum horizontal (y-axis) and minimum horizontal (x-axis) stresses computed. Specific reference coordinates for preparing the figures were provided to allow for direct comparison of the mesh discretization (level of detail) and results between the modelling teams in order to discuss any differences. The tunnel axis was defined as a line starting from coordinates (X = 2420.3, Y = 7361.92) to coordinates (X = 2441.11, Y = 7336.76). For reference, the images should be similar to Figure 6-15 in Ericsson et al. (2015). The images normal to the coordinate axis should pass through coordinates (X = 2430, Y = 7352).

Appendix A summarizes the sensitivity investigation performed by TUL-IGN on the influence of the tunnel surface resolution and discretization on the modelled vertical stress and pore pressure field. This was outside the scope of Task G but provides useful insights for upcoming simulations in WP 3.

#### 7.1.1. SNU

Stress re-distribution induced by the tunnel opening appears around the tunnel perimeter (Figure 31). In each figure, compressive stress concentrations are clearly visible at the corners of the tunnel floor and generally in the tunnel floor, while highest stress relaxation is generally seen in the tunnel walls. This is in agreement with what would be expected given the initial stress field defined in the model setup. This high stress anisotropy also results in increased shear stresses acting on the fractures in the tunnel floor, especially those that are inclined, inducing shear slip as indicated by the localized stress changes seen around specific fractures.



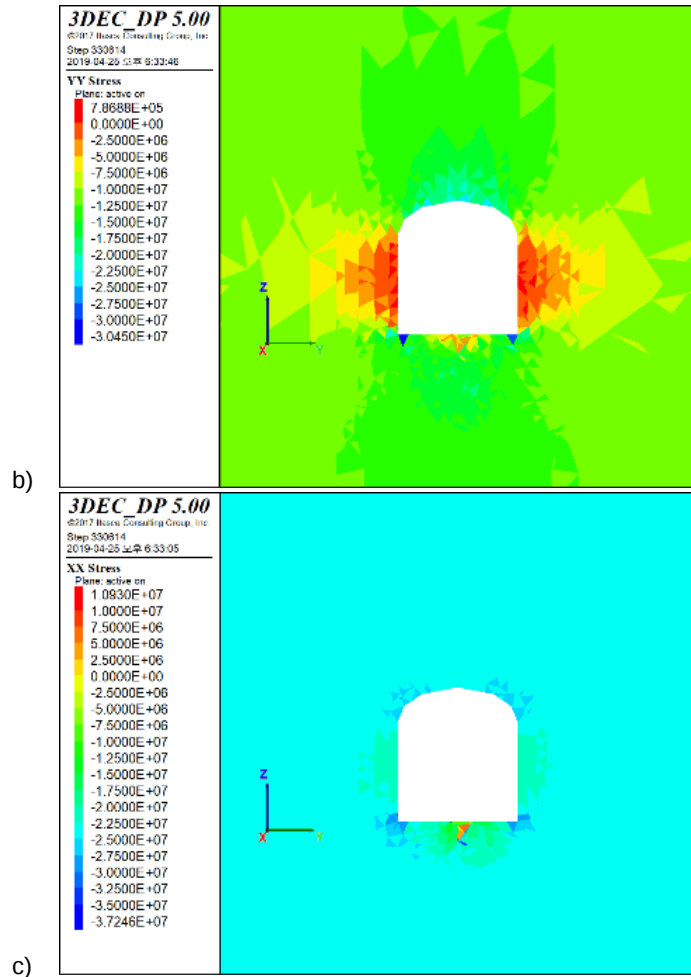


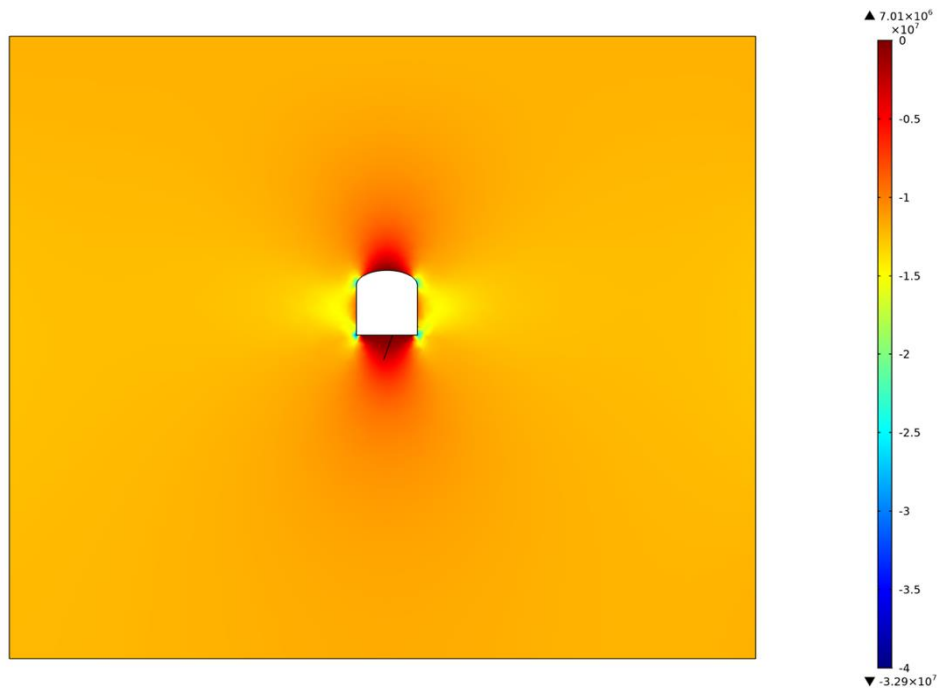
Figure 31. Cross section normal to the tunnel axis showing the modelled stresses for WP 2.1, plotting: a) vertical stresses (z direction), b) minimum horizontal stress normal to the tunnel axis (y direction), and c) maximum horizontal stresses parallel to the tunnel axis (x direction). Note that the stresses are in units of Pa and compression is negative.

### 7.1.2. TUL-IGN

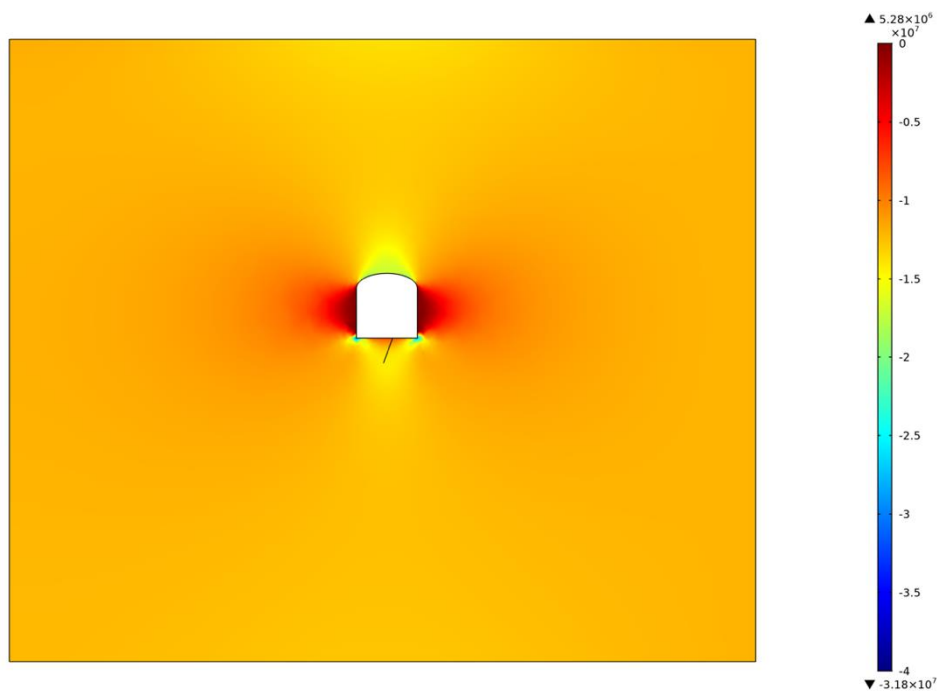
The results provided by TUL-IGN included the modelled vertical and horizontal stress distribution for their simplified tunnel geometry case, as shown in Figure 32. However, a separate study performed by TUL-IGN (see Appendix A) indicates that the simplified surface might produce stresses that differ from the irregular tunnel geometry in the range of a few kPa. TUL-IGN considers these to be insignificant and below the uncertainty of the data, and hence, decided to proceed using the simplified tunnel surface within WP 2.

The results shown in Figure 32 show a reduction in vertical stresses (i.e., relaxation) in the tunnel walls, roof and floor close to and below zero stress relative to the initial stress boundary conditions. In contrast, the corners of the horse-shoe shaped TAS04 tunnel show concentrations (compression) in vertical stress.

a)



b)



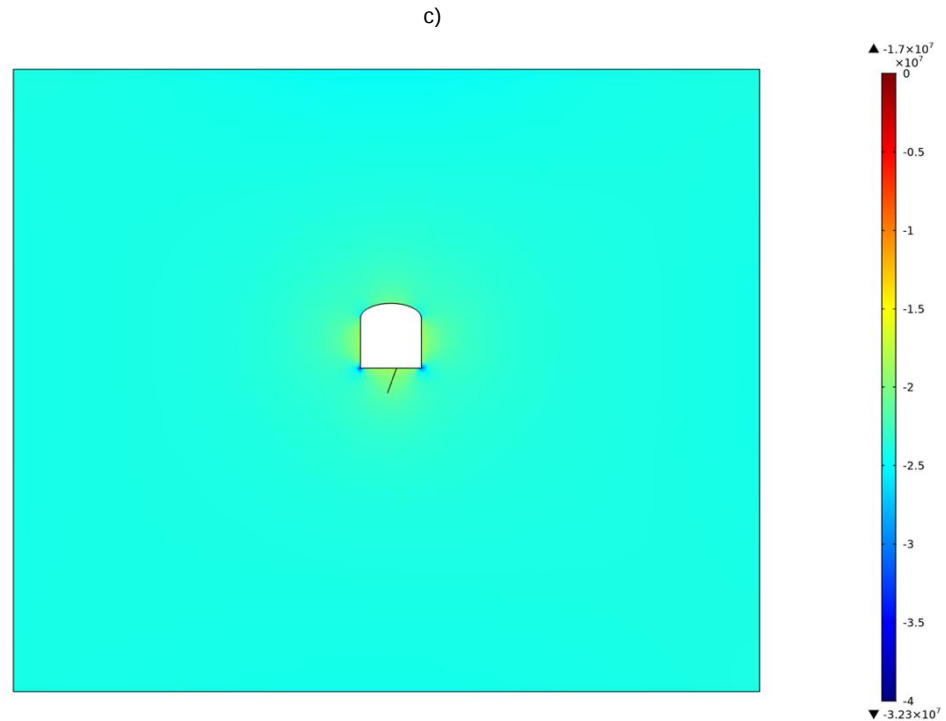


Figure 32. (continued from previous page) Cross section normal to the tunnel axis showing the modelled stresses for WP 2.1, plotting: a) vertical stresses (z direction), b) minimum horizontal stresses parallel to the tunnel axis (x direction), and c) maximum horizontal stresses normal to the tunnel axis (y direction). Note that the stresses are in units of Pa and compression is negative.

### 7.1.3. GMC

Figure 34 presents the stress field normal to the tunnel axis as modelled by GMC. The stress field around the tunnel is highly anisotropic.

The vertical stress (Figure 34a) shows that the top and bottom of the tunnel are subjected to tensile stresses while the flanks of the tunnels are subjected to compressional stresses. So, particularly horizontal fractures located below the tunnel floor might be opened due to very low or even positive (i.e. dilative) normal stresses.

The maximum and minimum horizontal stresses around the tunnel periphery nicely depict localized stress alterations that arise due to the irregular nature of the tunnel surface caused by the blasting rounds. The minimum horizontal stress normal to the tunnel axis shows high stress concentrations in the corners of the tunnel and stress relaxation in the tunnel floor and walls. The tunnel walls show tensile stresses while the tunnel floor remains in compression as shown in Figure 34b.

Interestingly, the maximum horizontal stress parallel to the tunnel axis shows areas where the rock mass experiences stress relaxation, and it is noted that this includes the tunnel floor where the interference tests have been conducted. However, these are in the order of a few MPa of stress reduction and these areas do not undergo tension.

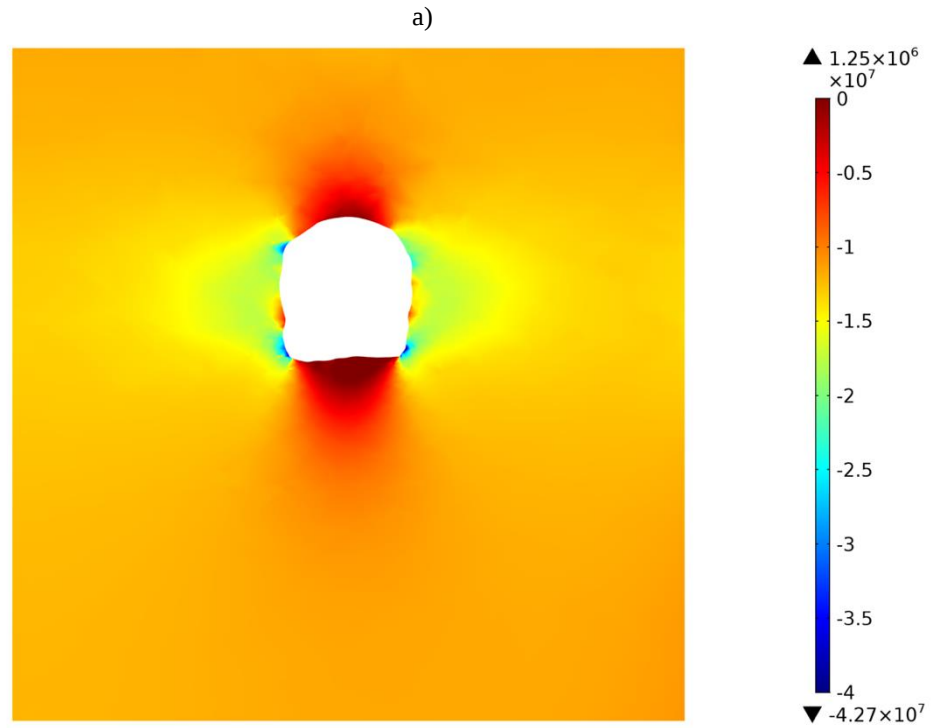


Figure 33 (continued on next page). Cross section normal to the tunnel axis showing the modelled stresses for WP 2.1, plotting: a) vertical stresses (z direction), b) horizontal stresses perpendicular to the tunnel axis (x direction), and c) horizontal stresses parallel to the tunnel axis (y direction). Note that the stresses are in units of Pa, and compression is negative.



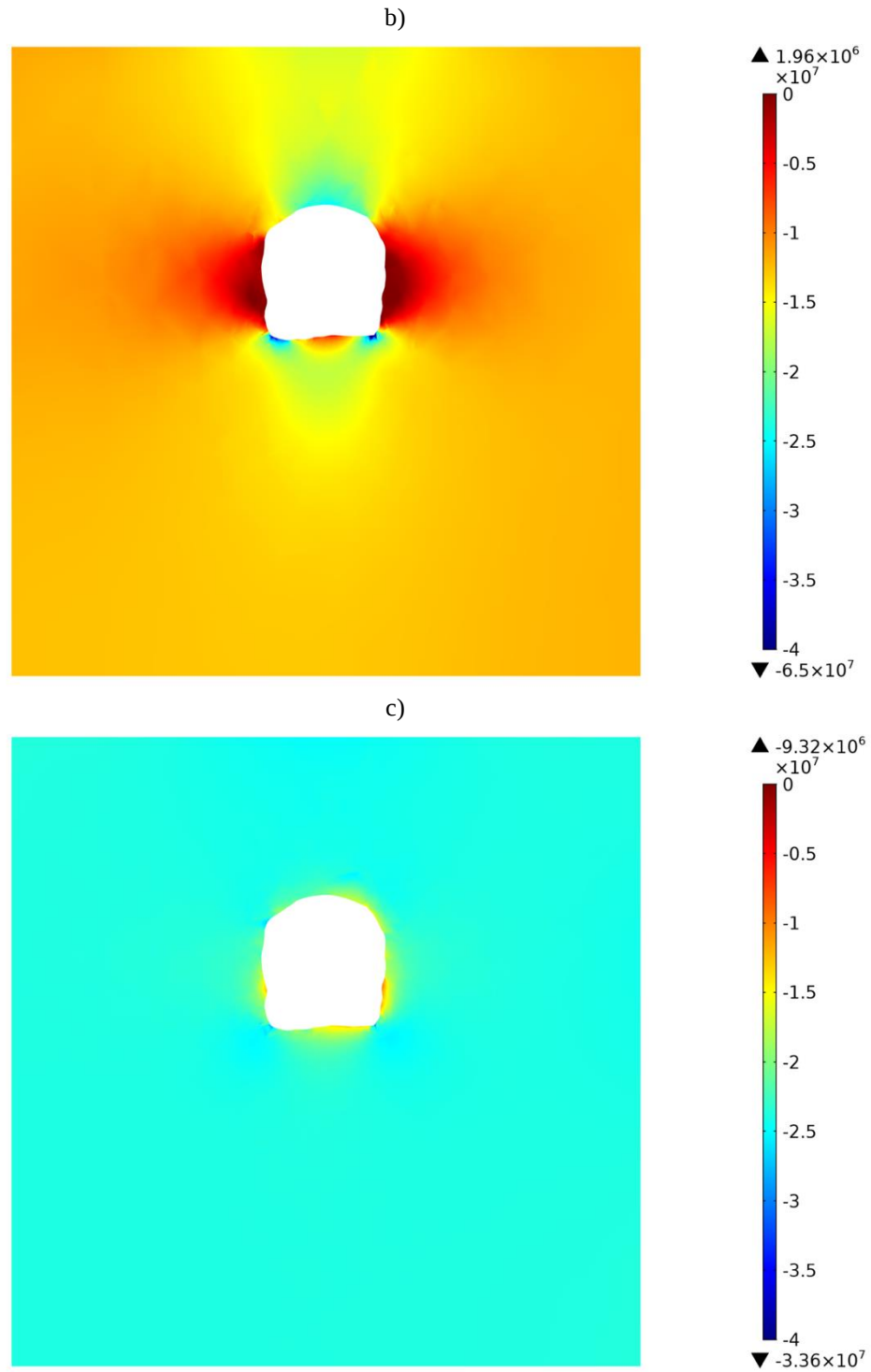


Figure 34 (continued from previous page). Cross section normal to the tunnel axis showing the modelled stresses for WP 2.1, plotting: a) vertical stresses (z direction), b) minimum horizontal stresses perpendicular to the tunnel axis (x direction), and c) maximum horizontal stresses parallel to the tunnel axis (y direction). Note that the stresses are in units of Pa and compression is negative.

#### 7.1.4. Discussion

In the following the different stress fields obtained by the modelling teams are compared among each other and against values that can be expected in order to gain confidence in the modelling results.

The results for the vertical stresses show similar patterns although with different stress magnitudes for the three modelling teams. We observe high stress concentrations in the order of 30 to 60 MPa (compression) in the corners of the tunnel and stress relaxation in the tunnel roof and floor of up to -1 to -6 MPa (dilation). The latter indicates that shallow horizontal fractures beneath the tunnel floor, where the interference test have been performed, are exposed to negative stresses opening up the fractures. The negative stresses are localized in an area approx. 1 m below the tunnel floor.

The minimum horizontal stresses vary in the range of 30 to 65 MPa (compression) in the corner of the tunnel and -0.8 to -5 MPa (dilation) in the tunnel flanks. Vertical fractures oriented parallel to the tunnel axis and below the tunnel floor are exposed to normal stresses in the order of 10 MPa, potentially closing these fractures. Similarly, the maximum horizontal stress closes steeply dipping fractures oriented normal to the tunnel axis below the tunnel floor with a normal stress of 10 to 20 MPa.

In general, the maximum horizontal stress parallel to the tunnel axis shows the fewest variations independent of the modelling approaches. This is correct since this stress is least influenced by the tunnel. All modelling results show the applied maximum horizontal stress of approx. 24 MPa at some distance to the tunnel. The largest variations in the stress field are shown by the minimum horizontal and vertical stress. This is also in line with the principle of stress concentrations around a tunnel. Furthermore, at some distance to the tunnel, the applied minimum horizontal and vertical stress of approx. 12 MPa can be seen in the results of the modelling teams. Furthermore, the stresses seem to be altered by the presence of fractures for the 3DEC results while the results of the COMSOL Multiphysics simulations do not show stress alterations. The different stress magnitudes and stress localizations also show the discrepancy in the level of detail used to realize the tunnel surface geometry (i.e., detailed rough walls versus simplified smooth walls). This results in local differences in the calculated stress around the tunnel and, hence, potentially influences the conductivity of the fractures in case a stress-dependent aperture and cubic-law permeabilities are considered. Figure 35 shows the differences in the vertical, minimum horizontal, and maximum horizontal stress obtained for a monitoring line below the tunnel floor for the generalized and irregular tunnel surface at 410 m depth based on a comparison on the influence of the tunnel shape by TUL. The figure shows that especially the vertical stress, which also has the greatest impact on the permeability of shallow horizontal fractures, might vary only slightly. Please note that at this depth below the tunnel floor all stresses are already compressive except a spike in vertical stress at the beginning of the tunnel, which corresponds to a boundary of the modelling domain.

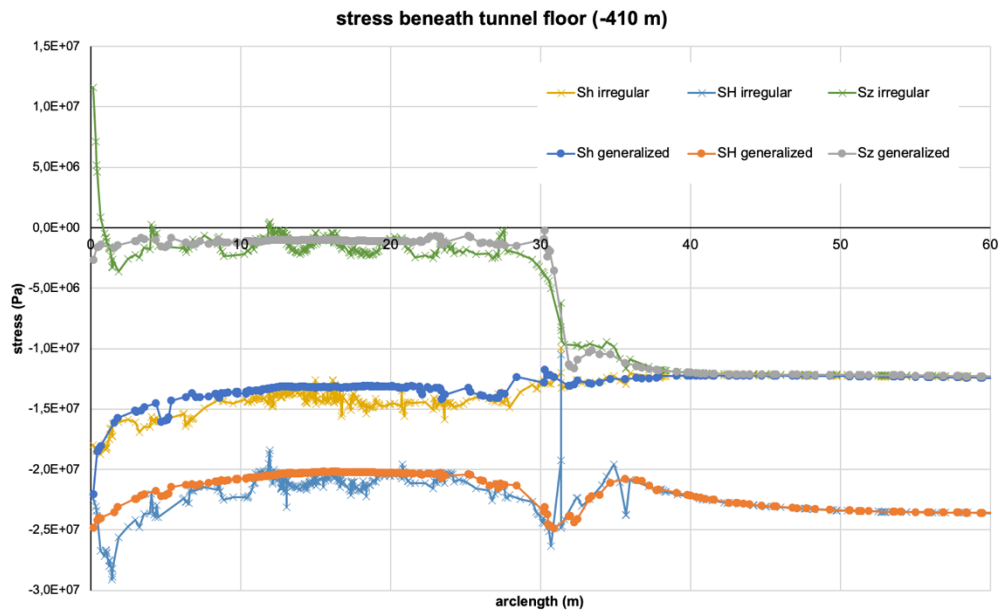


Figure 35. Vertical (Sz), minimum horizontal (Sh) and maximum horizontal (SH) stress along a monitoring line at 410 m depth parallel to the tunnel axis for the irregular and generalized tunnel surface.

Furthermore, different levels of discretization might influence the results. Discretizing sharp corners of the tunnel or irregularities of the tunnel wall with a fine mesh yield very high stress concentrations that would lead to failure of the rock at these positions. However, since the interference test has been performed mostly in the central part of the tunnel floor, these stress concentrations do not influence the stress field on the fractures that control the fluid flow.

The large differences between the horizontal stress magnitudes in the x- and y- directions and low confinement in the tunnel floor might furthermore enable slip to occur on the fractures as highlighted by SNU, which might additionally cause the sub-vertical fractures in the tunnel floor to open by shear dilation.

## 7.2. Inflow into tunnel prior to any injection test (Activity 2.1)

The following results should indicate whether the numerical codes yield comparable inflow rates into the tunnel, as well as provide a basis for general comparison as to how each code models fluid flow. The static inflow into the tunnel was an output requested for Activity 2.1 to provide insights into how much the open fracture network contributes to the tunnel inflow before any interference tests.

### 7.2.1. SNU

The static inflow into the tunnel through the fracture intersecting the tunnel floor can be extracted from the model before performing the injection tests. The total inflow into the tunnel was  $2.72 \cdot 10^{-10} \text{ m}^3 \cdot \text{s}^{-1}$ .

### 7.2.2. TUL-IGN

From the simulations performed, the total inflow into the tunnel was  $5.30 \cdot 10^{-6} \text{ m}^3 \cdot \text{s}^{-1}$ . When normalized to the total tunnel surface area ( $625.4 \text{ m}^2$  for the TUL-IGN tunnel geometry) the corresponding flux is  $8.4680 \cdot 10^{-9} \text{ m} \cdot \text{s}^{-1}$ .

### 7.2.3. GMC

Different outer pore pressure boundary conditions were tested to calculate the corresponding tunnel inflows. For the case of a hydrostatic pore pressure boundary condition (i.e.  $9.81 \text{ MPa/km}$ , or  $4 \text{ MPa}$  at the TAS04 tunnel depth), the inflow into the tunnel without the drillholes was  $3.29 \cdot 10^{-6} \text{ m}^3 \cdot \text{s}^{-1}$ . For the case of a  $5 \text{ MPa}$  pore pressure boundary condition, the inflow increased to  $4.14 \cdot 10^{-6} \text{ m}^3 \cdot \text{s}^{-1}$ . When normalizing these inflows to the total tunnel surface area of the tunnel ( $587.5 \text{ m}^2$  for the GMC tunnel geometry), the flux values are  $5.6 \cdot 10^{-9} \text{ m} \cdot \text{s}^{-1}$  and  $7.1 \cdot 10^{-9} \text{ m} \cdot \text{s}^{-1}$ , respectively.

### 7.2.4. Discussion

The TUL-IGN and GMC models produced very similar inflow magnitudes, even though they differed in how the fracture flow was modelled, i.e., stress-dependent fracture permeability (GMC) or not (TUL-IGN). The similarity in results suggest a lack of sensitivity with respect to the significance of accounting for stress-dependent fracture permeability, at least with respect to the fracture properties and boundary conditions assumed in Activity 2.1 to model the inflow into the tunnel.

The main difference between the 3DEC simulations performed by SNU and the COMSOL Multiphysics simulations performed by GMC and TUL-IGN are that the fluid flow is controlled by fracture flow and fracture and matrix flow, respectively. This is why the 3DEC result is smaller in comparison to the COMSOL Multiphysics results.

## 7.3. Inflow into the tunnel during injection test (Activity 2.3)

During the TAS04 interference tests, a significant amount of water was observed leaking into the tunnel via fractures and accumulating in ponds, providing another means to compare and validate the different codes used and simulations performed by the modelling teams. Since the amount of fluids entering the tunnel during the injection test could not precisely be measured, the inflow was estimated and given in l/min for the whole interference test (see Ericsson et al. 2015). This measure can be assumed as an average inflow during the injection test. Hence, the definition of Activity 2.3 requested the modelling teams to provide a measurement of the tunnel inflow in response to simulations of the interference tests.

### 7.3.1. SNU

For Activity 2.3, the modified fracture model was modelled by SNU as having a uniform initial aperture but allowed for stress-dependent fracture stiffness and aperture (permeability) properties applied to the Class 1 fractures for simulating the interference tests. The total inflow into the tunnel at steady state in response to the three different injection pressures is summarized in Table 14.

### 7.3.2. TUL-IGN

Not reported.

### 7.3.3. GMC

GMC's results for Activity 2.3 are presented in Table 14. These correspond to the cumulative tunnel inflows modelled in response to the simulated injection tests for the case of a hydrostatic pore pressure (9.81 MPa/km) boundary condition.

### 7.3.4. Discussion

Table 14 summarizes the inflows into the tunnel during the time-dependent Activity 2.3, both measured during the TAS04 experiments and those modelled by SNU and GMC. In general, the modelled inflow values are three to four orders of magnitude lower than the TAS04 in-situ observations. It can also be noted that whereas the observed tunnel inflows were seen to increase with increasing injection pressures (over three tests), the model results from both SNU and GMC showed the reverse. The general expectation would be that higher injection pressures would produce higher inflows as observed during the interference tests. This indicates that the tunnel inflow response in the observation drillholes is not being correctly modelled and/or missing other key fluid flow pathways and considerations. Fluid inflows do not seem to be drawing symmetrically from the volume around the injection drillhole, as would be expected if the source of inflow was through the rock matrix. Instead, inflows occur where fractures intersect the drillholes or tunnel floor, and accordingly, fluid flow through the low permeability rock matrix can be ignored. Furthermore, the additional water pressure during injection might wash out or widen fractures as pointed out by Ericsson et al. (2015). This might be another indicator that the not all fractures have been monitored and implemented in the numerical models.

The low tunnel inflows being modelled might also indicate that the prescribed pore pressure being used to simulate the injections involve lower volumes than those used during the in-situ experiments. This, in turn, means that the permeability/transmissivity properties of the fractures are too low or that fluid pathways exist that are not accounted for in the numerical models.

**Table 14.** Observed and modelled leakage into the tunnel floor for the three different interference tests.

Injection drillhole	Injection pressure (kPa)	Tunnel inflow (l/min)			
		In-situ observation	SNU	TUL	GMC
K04017G02	442	0.5	0.00097	-	0.0021
K04018G01	92	0.3	0.0017	-	0.0021
K04020G01	80	0.1	0.00013	-	0.0063

## 7.4. Pressure Responses (Activity 2.1)

This section describes the pressure responses obtained by the different modelling teams within Activity 2.1. In comparison to the other activities, the definition of Activity 2.1 recommended the usage of the open fracture data set and a 20-minute-long, constant fluid injection phase.

### 7.4.1. SNU

To simulate the injection tests, constant pressure conditions were applied at the intersection points between the injection drillholes and each fracture. The injected fluid then diffused through the fracture network, which consisted of six open fractures with permeabilities depending on the deformed apertures. After the pressure response in each of the monitoring drillholes returned to steady state, the final pressure responses were extracted. Table 15 shows the test conditions and the pressure responses for both the TAS04 in-situ tests and those produced from the 3DEC numerical simulations. The pressure responses from the model were seen to vary in terms of how close both the magnitude and trend of the results were to those from the in-situ tests in the TAS04 tunnel. In several cases these were of the same order, whereas others were two to three orders of magnitude different.

**Table 15.** Pressure responses monitored during three interference tests in WP 2.1 models, and the corresponding model results.

Injection drillhole	Injection pressure (kPa)	Observation drillhole	Pressure response (kPa)	
			In-situ test	Simulation
K04017G02	442	K04016G01	1.4	2.4
		K04017G01	0.3	324.1
		K04017G03	3	1.6
		K04018G01	0.4	25.6
K04018G01	92	K04017G01	88	9.0
		K04017G03	4	2.3
K04020G01	80	K04019G03	4	0.6
		K04021G02	21	0.9

### 7.4.2. TUL-IGN

Activity 2.1 closely followed on from the previous simulations, starting from the same base model. The first phase of modelling the injection tests was performed on the simplified smooth-wall tunnel geometry. These involved time-dependent simulations, where fluid (water) was injected under a defined constant pressure into one of the three injection drillholes for 20 minutes. The results were obtained after steady-state conditions were reached in the model, for the following combination of injection and monitoring drillholes:

Injection drillhole: **K04017G02** (injection interval depth 0.4 – 0.6 m, injection pressure: 442 kPa),

Observation drillholes: K04016G01, K04017G01, K04017G03, K04018G01,

Injection drillhole: **K04018G01** (injection interval depth 0.1 – 0.2 m, injected pressure 92 kPa),

Observation drillholes: K04017G01, K04017G02,

Injection drillhole: **K04020G01** (injection interval depth 0.2 – 0.4 m, injection pressure: 80 kPa),

Observation drillholes: K04019G03, K04021G02.

The boundary conditions used in the simulations are based on those reported in Activity 2.1. In addition, for each injection scenario, the corresponding injection water pressure was applied to the inner surface of the corresponding injection drillhole, with zero pressure boundary conditions being applied to the surface of the other two injection drillholes. Each injection test was designed as a separate model with and without fractures. The responses to the injection tests are summarized in Table 16, from which two conclusions are initially drawn. First, the results of the injection tests were not seen

to be significantly influenced by the presence of fractures. The injection response to drillhole K04017G02 showed some slight differences, but these were within 10 to 25%. Second, it is clear from the results in Table 16 that the modelled injection response to drillholes K04018G01 and K04020G01 is minimal and on the order of tenths of 1 kPa (for both model alternatives with and without fractures).

**Table 16.** Pilot version of injection tests for geometry from chapter 3.2.

Injection drillhole	Injection Pressure (kPa)	Observation drillhole	Pressure response (kPa)		
			In-situ test	With fractures	Without fractures
K04017G02	442	K04016G01	1.4	4.07	4.40
		K04017G01	0.3	7.19	8.87
		K04017G03	3	3.72	4.61
		K04018G01	0.4	3.90	5.01
K04018G01	92	K04017G01	88	0.13	0.33
		K04017G03	4	0.14	0.27
K04020G01	80	K04019G03	4	0.18	0.18
		K04021G02	21	0.15	0.15

### 7.4.3. GMC

Different boundary conditions were tested within Activity 2.1: a) no flow boundary on tunnel surface and model with embedded fractures, b) ambient pore pressure boundary on tunnel surface and model with embedded fractures, and c) ambient pore pressure boundary on tunnel surface and model without embedded fractures. The results presented here focus on the case with an ambient (zero) pore pressure boundary condition assigned to the tunnel surface, as well as to the outer model boundaries, and with the mapped fractures represented in the tunnel floor. Table 17 summarizes the results.

During the simulations, it was observed that the maximum pressure applied to each drillhole during the injection phase exceeded the applied pressure in the interference tests by approximately 4%. However, this pressure difference is not expected to cause any significant changes in the pressure response recorded in the modelled observation drillholes. In general, a poor fit was observed between the modelled and measured interference tests as shown in Table 17, although the pressure response values were on the same order of magnitude in several cases.

**Table 17.** Pressure responses monitored during three interference tests in WP 2.1 models.

Injection drillhole	Injection Pressure (kPa)	Observation drillhole	Pressure response (kPa)	
			In-situ test	Simulation
K04017G02	442	K04016G01	1.4	6.30
		K04017G01	0.3	10.20
		K04017G03	3	5.06
		K04018G01	0.4	1.91
K04018G01	92	K04017G01	88	0.32
		K04017G03	4	0.28
K04020G01	80	K04019G03	4	0.23
		K04021G02	21	0.273

#### 7.4.4. Discussion

The numerically derived pressure responses from each modelling team are displayed in Figure 36 alongside the measured pressure responses from the TAS04 experiment. The reader should keep in mind that this figure does not differentiate between the different interference tests. The intent is to provide a quick comparison between what was modelled versus what was measured in the observation drillholes.

For the first interference test, where the injection was performed in K04017G02, a good fit was obtained for observation holes K04016G01 and K04017G03. GMC tends to produce higher pressure responses probably due to the matrix permeability being too high. The applied fracture flow permeability seems to be in the correct magnitude range. SNU derived higher pressure responses in K04017G01 and K04018G01, probably due to the direct connection of the injection drillhole with the two observation holes via the fractures explicitly modelled. Please note that the SNU result for K04017G01 is cut off at 100 kPa for better comparison. On the contrary, K04016G01 and K04017G03 show pressure responses in the range measured, indicating that there is no direct connection via fractures between the two observation holes and the injection hole. SNU transformed the open fractures from the rectangular shapes provided to ellipsoidal form and thereby slightly altered the connectivity of the fractures. Even though an ellipsoid of the same length as a rectangle involves less surface area and therefore less likelihood of enhancing connectivity, these ellipsoids were oriented such that a connection is established between neighboring fractures. The TUL-IGN results produced a higher-pressure response for their model case where fractures were implemented in the model. It is noted that the first interference test involved injection pressures of up to 442 kPa, yet very low pressures were recorded in the observation drillholes. This raises questions regarding the connectivity of the fractures relative to the drillholes involved with the first test.

For the second interference test, where the injection was performed in K04018G01, the injection pressure of 92 kPa was directly transmitted to observation hole K04017G01. However, only a low-pressure response was measured in K04017G03, even though the three drillholes are connected via the same open fracture located close to the tunnel surface. The modelling teams were not able to reproduce this hydraulic behavior, probably due to differences between the connectivity of the fracture network in the models compared to the in-situ case, or other simplifying assumptions regarding the permeability characteristics of the fractures. For example, the adoption of the cubic law for fracture flow assumes that the fracture is uniformly open, thus neglecting the channeling effects and tortuosity that normally exist along the fracture. TUL-IGN and GMC observed pressure responses that were too low, which contrasts with SNU who obtained results with a higher-pressure response. However, the direct pressure transfer across the fracture network from the injection drillholes could not be modelled. Additional efforts have been made by GMC (not presented within this report) to back-calculate the permeability distribution for the modelled fractures.

For the third interference test, where injection was performed in K04020G01 with 80 kPa, a similar pressure response as for the second interference test was observed. Firstly, the modelled pressure responses were less than the measured pressure responses. Secondly, none of the modelling teams was able to model the trend of a high-pressure response in K04021G02 and a lower pressure response in K04019G03. This is probably due to the likelihood that the injection hole is connected to the other two observation holes by a fracture or fractures not included in the open fracture data set provided.



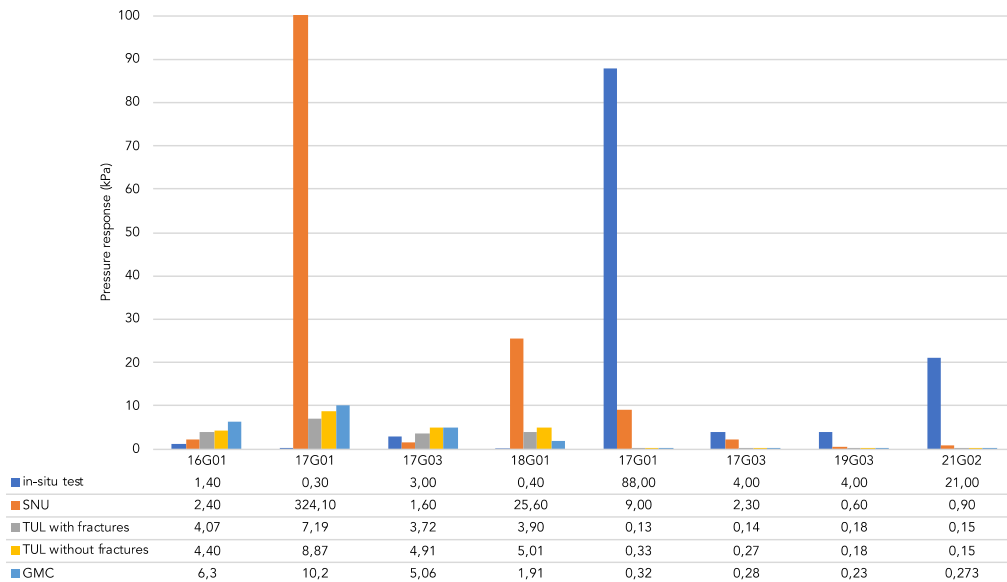


Figure 36. Measured and modelled pressure response for Activity 2.1 in direct comparison for each observation drillhole. Please note that the y-scale has been cut off at 100 kPa for better comparison. The exact values are provided in the included table.

## 7.5. Pressure responses (Activity 2.2)

This section describes the pressure responses obtained by the different modelling teams within Activity 2.2. In comparison to the other activities, the definition of Activity 2.2 recommended the use of the open fracture data similar to Activity 2.1, but also the DFN data sets, the reflector data, and inclusion of stress and pore pressure gradients as boundary conditions. The injection was to be modelled as a 20 minute long, constant pressure phase.

### 7.5.1. SNU

In WP 2.2, the addition of the Class 1 fractures from the DFN dataset to the 3DEC model significantly changed the connectivity between the injection and observation drillholes. The final pressure responses extracted from the modified model appear in Table 18. The model simulating the injection test in K04020G01 wasn't able to solve properly (i.e., the model did not converge) and the results are not reported here. Otherwise, the results indicate that the addition of the fractures from the DFN dataset result in a significant increase in the modelled pressure response, compared to the models from WP 2.1 which only considered the six mapped open fractures.

**Table 18.** Pressure responses monitored during three interference tests in WP 2.2 models.

Injection drillhole	Injection Pressure (kPa)	Observation drillhole	Pressure response (kPa)	
			In-situ test	Simulation
K04017G02	442	K04016G01	1.4	276
		K04017G01	0.3	436
		K04017G03	3	276
		K04018G01	0.4	259
K04018G01	92	K04017G01	88	83.1
		K04017G03	4	22.8
K04020G01	80	K04019G03	4	-
		K04021G02	21	-

### 7.5.2. TUL-IGN

The results of the sensitivity study performed in relation to the described model alternatives are summarized in Table 19. All three injection tests for each alternative, together with the responses in the observation drillholes and the measured values are included. When comparing the results with the base case alternative, or with the measured data, we can make several conclusions:

- The response to the injection to drillhole K04017G02 changed only when the permeability of the EDZ was changed (but, at the same time, the results were not affected by injection into drillholes K04018G01 and K04020G01);
- A tenfold increase in the hydraulic conductivity of fractures K04017G02 and K04023G01 did not significantly influence the modelled pressure response in any of the observation drillholes;
- The addition of sub-horizontal fractures positively influenced the observed results. Pressure response to injection into drillholes K04018G01 and K04020G01 were more sensitive to changes in the properties assumed for the fractures, but only in the test cases that included the sub-horizontal fractures;
- The test models failed to produce a different response between the individual observation drillholes; similar values were observed. For example, injection into drillhole K04018G01 produced different pressure responses for the different alternatives tested. However, in each case, the pressures observed in drillholes K04017G01 and K04017G02 were generally the same.

**Table 19.** Sensitivity of modelled pressure responses to the injection tests for varied hydraulic conductivity values of individual fractures (based on Table 12). Those numbers shaded with an orange background indicate where changes occur in the modelled response.

Injection drillhole	Injection pressure (kPa)	Observation drillhole	Measured response	EDZ	1701	1702	1902	2101	2301	hor1	hor2	rock	EDZ2
K04017G02	442	K04016G01	<b>1.4</b>	1.35	1.35	1.35	1.35	1.35	1.35	1.35	1.35	1.35	5.26
		K04017G01	<b>0.3</b>	3.48	3.48	3.48	3.48	3.48	3.48	3.48	3.48	3.48	8.38
		K04017G03	<b>3</b>	1.25	1.25	1.25	1.25	1.25	1.25	1.25	1.25	1.25	3.33
		K04018G01	<b>0.4</b>	1.38	1.38	1.38	1.38	1.38	1.38	1.38	1.38	1.38	3.98
K04018G01	92	K04017G01	<b>88</b>	65.70	30.58	65.70	55.65	56.12	65.70	87.67	64.13	65.70	65.69
		K04017G02	<b>4</b>	67.59	39.90	67.59	55.54	57.35	67.59	87.91	65.91	67.59	67.59
K04020G01	80	K04019G03	<b>4</b>	55.33	55.09	55.33	39.93	25.16	55.33	51.60	76.29	55.33	55.33
		K04021G02	<b>21</b>	54.14	54.03	54.14	46.89	15.87	54.14	52.40	76.23	54.14	54.14

A similar sensitivity study was carried out assuming the same material input properties as used for the basic alternative “EDZ”, but where one fracture at a time was closed to fluid flow. The injection responses for this set of models is given in Table 20, from which the following conclusions can be drawn:

- According to the previous results, the addition of the sub-horizontal fractures improved the connectivity and pressure response to injection into drillholes K04018G01 and K04020G01. However, when they were closed to fluid flow (see alternatives “hor1” and “hor2” in Table 20), there was an almost complete loss in pressure response in the observation drillholes (marked red in Table 20); and
- In the other cases, the removal/closure of each individual fracture led to only minor changes in the pressure response to injection. As in the previous cases, these responses correlated across the different observation drillholes.

**Table 20.** Sensitivity of modelled pressure responses to the injection tests to the closing of individual fractures to fluid flow. Orange shading highlights a complete loss in the pressure response in case the two horizontal fractures are closed.

Injection drillhole	Injection pressure (kPa)	Observation drillhole	Meas. response (kPa)	EDZ	Closed fracture						
					1701	1702	1902	2101	2301	hor1	hor2
K04017G02	442	K04016G01	<b>1.4</b>	1.35	1.31	1.31	1.31	1.31	1.31	1.52	1.31
		K04017G01	<b>0.3</b>	3.48	3.49	3.45	3.45	3.45	3.45	3.72	3.45
		K04017G03	<b>3</b>	1.25	1.24	1.34	1.24	1.24	1.24	1.61	1.24
		K04018G01	<b>0.4</b>	1.38	1.41	1.43	1.41	1.41	1.41	1.62	1.43
K04018G01	92	K04017G01	<b>88</b>	65.70	76.17	65.67	66.16	76.21	65.67	0.01	69.12
		K04017G02	<b>4</b>	67.59	76.20	67.57	68.16	78.57	67.57	0.01	71.28
K04020G01	80	K04019G03	<b>4</b>	55.33	55.34	55.28	55.85	77.72	55.28	60.29	0.05
		K04021G02	<b>21</b>	54.14	53.91	53.88	54.14	78.78	53.88	56.18	0.09

The three alternatives from the sensitivity analyses that produced the best fit to the injection test data are given in Table 21, together with the corresponding hydraulic conductivities of the individual fractures in these models. For alternative “var1”, the hydraulic conductivity of fracture K04021G01 was changed to  $0.031 \text{ m}\cdot\text{s}^{-1}$  and the hydraulic conductivity of sub-horizontal fracture No.1 was changed to  $10 \text{ m}\cdot\text{s}^{-1}$ . The same changes were made for alternative “var2”, but in addition, the hydraulic conductivity of the EDZ was reduced by half. Alternative “var3” included the same changes as “var1”, but the hydraulic conductivity of the rock matrix and that of the EDZ zone was increased by a factor of 10. However, the results for these alternatives, individually, only provided agreement with at most three of the eight observed pressure responses (Table 23, cells shaded green). The other responses were not properly captured by the alternative.

Further effort was placed into trying to improve the match between results by considering anisotropy for the fractures and EDZ. For this, TUL-IGN performed a hydraulic conductivity parametric sweep for each fracture and the EDZ equivalent continuum. These were seen to have a negligible effect except for one of the horizontal fractures (hor\_2) and the EDZ. A best fit result was chosen for each of the three injection tests, resulting in three sets of best-fit parameters (marked green in Table 22). Results for each of the three injection tests are shown in Table 23. We can see that the model fit to the measured pressure values does not generally improve, but there are some exceptions. Overall, no parameter set amongst these three provided a better total fit to the data than the others.

**Table 21.** Model alternatives from the sensitivity analyses that showed the best agreement with the measured data (orange shaded values indicate changes in fracture hydraulic conductivity; blue shaded values indicate changes in the hydraulic conductivity of the rock matrix and EDZ).

Model area	Hydraulic conductivity ( $m \cdot s^{-1}$ )		
	var_1	var_2	var_3
1701	7.4E-02	7.4E-02	7.4E-02
1702	3.3E-02	3.3E-02	3.3E-02
1902	8.2E-03	8.2E-03	8.2E-03
2101	3.1E-01	3.1E-01	3.1E-01
2301	2.0E-01	2.0E-01	2.0E-01
hor1	1.0E+01	1.0E+01	1.0E+01
hor2	2.0E-01	2.0E-01	2.0E-01
k_rock	5.0E-12	5.0E-12	
k_edz	5.0E-11	2.5E-11	5.0E-10

**Table 22.** Optimal hydraulic conductivity parameter sets marked in green obtained from the parametric sweep. Hydraulic conductivity in units of m/s.

Hydraulic conductivity/permeability	initial values	hole 20	hole 18	hole 17
K04017G01	7.4E-02	7.4E-02	7.4E-02	7.4E-02
K04017G02	3.3E-02	3.3E-02	3.3E-02	3.3E-02
K04019G02	8.2E-03	8.2E-03	8.2E-03	8.2E-03
K04021G01	3.1E-01	5.1E-02	5.1E-02	5.1E-02
K04023G01-03	2.0E-01	2E-01	2E-01	2E-01
hor_1	1.0E+01	2E-01	2E-01	2E-01
hor_2	2.0E-01			
hor_2_x		0.002	0.002	0.2
hor_2_y		0.002	0.02	0.2
hor_2_z		2.0E-01	2.0E-01	2E-01
k_rock [ $m^2$ ]	5.0E-19	5.0E-19	5.0E-19	5E-19
k_edz [ $m^2$ ]	5.0E-18			
k_edz_x [ $m^2$ ]		5E-18	5.E-20	5E-18
k_edz_y [ $m^2$ ]		5E-19	5E-18	5E-18
k_edz_z [ $m^2$ ]		5E-18	5E-18	5E-18

**Table 23.** Modelled pressure responses to the three interference tests for WP 2.2 showing the best fit cases to the measured values (shaded green).

Injection drillhole	Injection Pressure (kPa)	Observation drillhole	Pressure response (kPa)				
			In-situ test	Anisotropy	Parametric		
					Var_1	Var_2	Var_3
K04017G02	442	K04016G01	1.4	5.36	1.3	0.2	5.2
		K04017G01	0.3	5.57	3.4	1.0	8.5
		K04017G03	3	2.19	1.2	0.2	3.3
		K04018G01	0.4	2.27	1.4	0.2	4.0
K04018G01	92	K04017G01	88	46.55	89.4	89.4	89.4
		K04017G03	4	7.64	89.4	89.4	89.4
K04020G01	80	K04019G03	4	4.68	26	26	26
		K04021G02	21	17.44	21.1	21.1	21.1

### 7.5.3. GMC

Within Activity 2.2, open and closed DFN fractures were tested together with the consideration of stress-dependent permeability applied to fractures derived from the reflector data and mapped open fractures. For the sake of simplicity, only the stress dependent permeability results are presented. Figure 37 to Figure 39 show the pressure responses for the case of open fractures as described in Section 4. The main difference between the previous results for Activity 2.1 and those shown here for Activity 2.2 is the differing geometry of the drillholes (i.e. a change from representing the drillholes as lines to cylinders). The results are provided in Table 24.

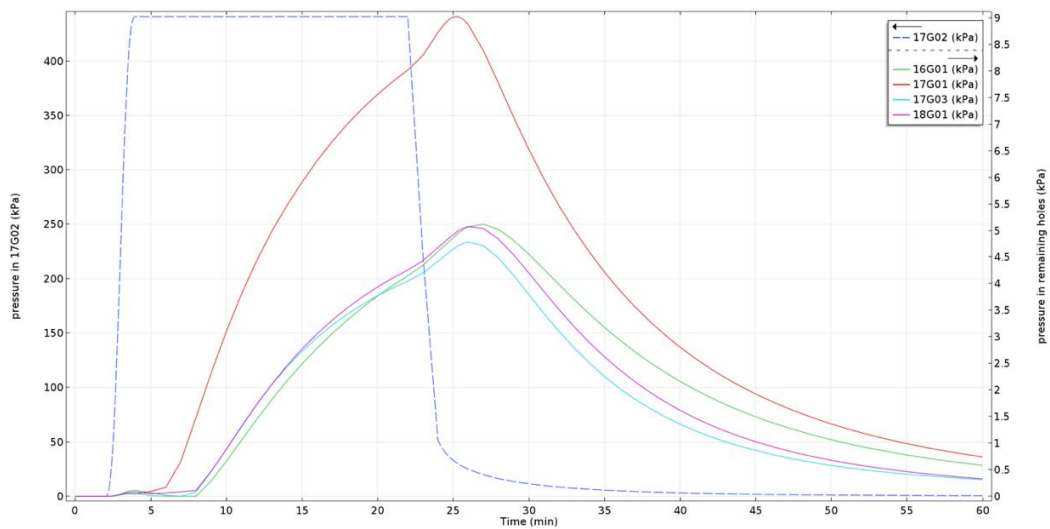


Figure 37. Modelled pore pressure response (solid lines) compared to the injection pressure (dashed line) for the interference test conducted in 17G02.

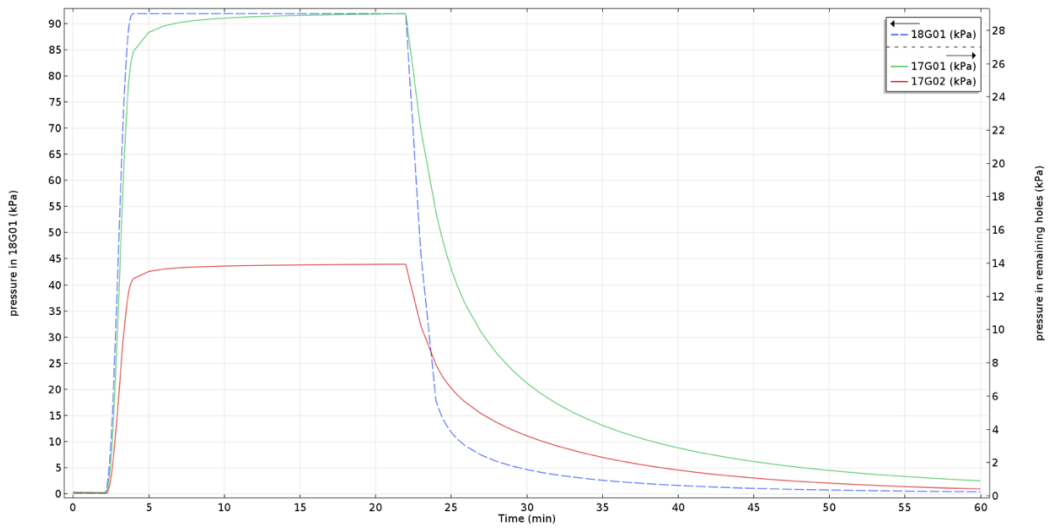


Figure 38. Modelled pore pressure response (solid lines) compared to the injection pressure (dashed line) for the interference test conducted in 18G01.

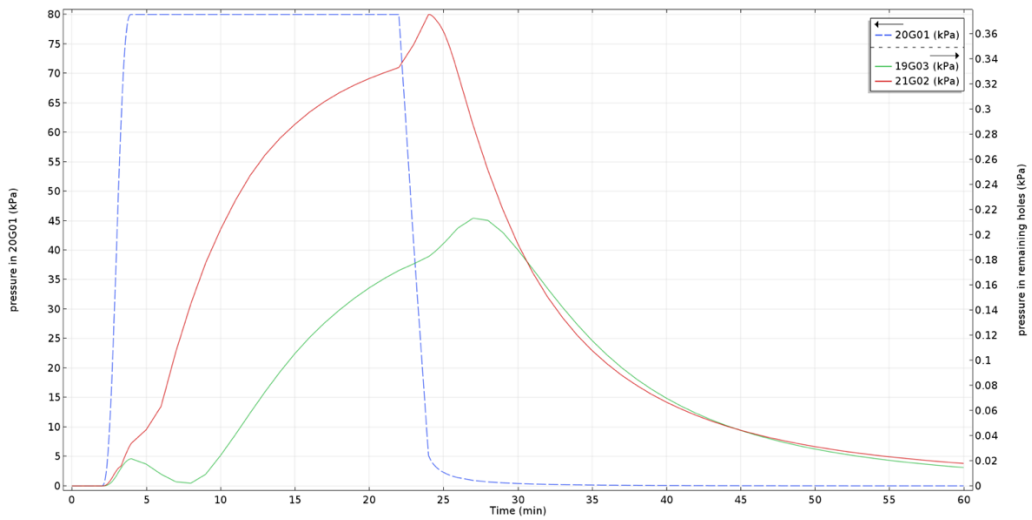


Figure 39. Modelled pore pressure response (solid lines) compared to the injection pressure (dashed line) for the interference test conducted in 20G01.

**Table 24.** Pressure responses monitored during three interference tests in WP 2.2 models.

Injection drillhole	Injection Pressure (kPa)	Observation drillhole	Pressure response (kPa)	
			In-situ test	Simulation
K04017G02	442	K04016G01	1.4	5.10
		K04017G01	0.3	9.0
		K04017G03	3	4.5
		K04018G01	0.4	5
K04018G01	92	K04017G01	88	29
		K04017G03	4	14
K04020G01	80	K04019G03	4	0.21
		K04021G02	21	0.37

### 7.5.4. Discussion

A comparison of the modelled pressure responses from each modelling team is provided in Figure 40 alongside the measured pressure responses from the TAS04 experiment.

The SNU results show a poor fit to the in-situ tests except for the pressure response in K04017G01 when K04018G01 is the injector. All pressure response values are notably greater than those obtained for Activity 2.1 due to the addition of the fractures represented in the DFN data. This is the result of more direct connectivity between the injection and observation drillholes, resulting in fracture flow that is too high.

While the parametric study from TUL-IGN shows very good agreement for individual pressure responses (six out of eight), it shows significant errors for the two remaining interference tests. The parametric study of fracture, EDZ and rock matrix hydraulic conductivities, also produced individual responses with reasonably good fits to the interference tests (4 out of 8).

The GMC results for Activity 2.2 seem to fit slightly better compared to the results obtained for Activity 2.1. However, there is still considerable misfit to the in-situ data especially in cases where an interference test caused high- and low-pressure responses in different drillholes.

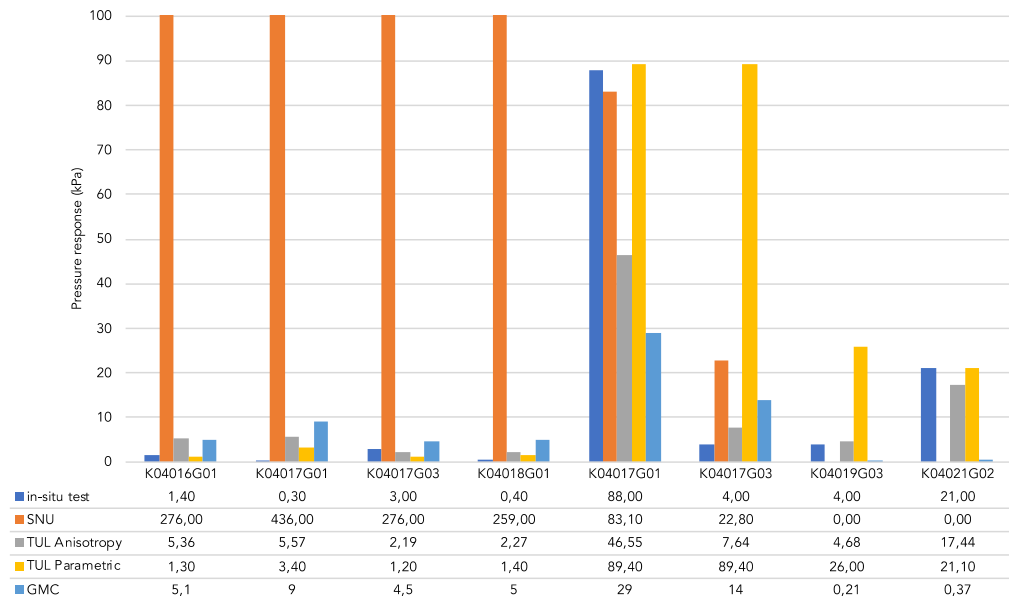


Figure 40. Measured and modelled pressure response for Activity 2.2 in direct comparison for each observation drillhole. Please note that the y-scale has been cut off at 100 kPa for better comparison. The exact values are provided in the included table.

### 7.6. Pressure responses (Activity 2.3)

This section describes the pressure responses obtained by the different modelling teams for Activity 2.3. In comparison to the other activities, the definition of Activity 2.3 recommended the use of the reworked reflector data and the true fluid-injection data.



### 7.6.1. SNU

For WP2.3, the modified fracture model with the uniform initial aperture and the stress dependent properties were applied to the Class 1 fractures for the 3DEC modelling of the interference tests. The transient pressure response relative to the fluid injection history was monitored for the corresponding injection and observation drillholes (Figure 41, Figure 42, and Figure 43). The trends of the pressure response to the simulated injections were seen to provide a better fit to the in-situ measured response than the previous results. Moreover, the model results for the injection tests performed in the K04018G01 and K04020G01 drillholes closely reproduced the in-situ test result values. The transient simulations were also able to show the same immediate pressure response under the change of injection pressures as observed in the in-situ tests.

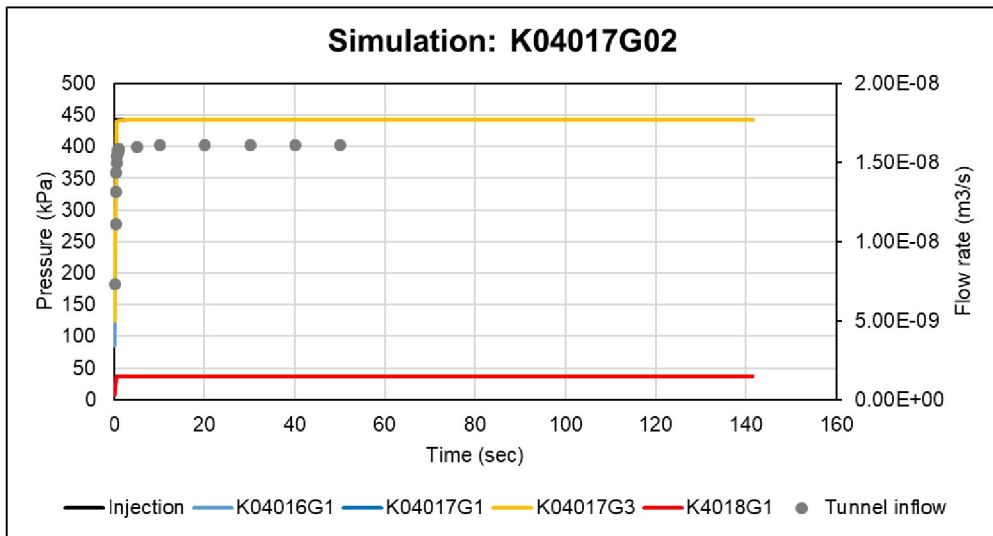


Figure 41. Modelled transient pressure response and simulated injection flow rate (black) for the K04017G02 injection test.

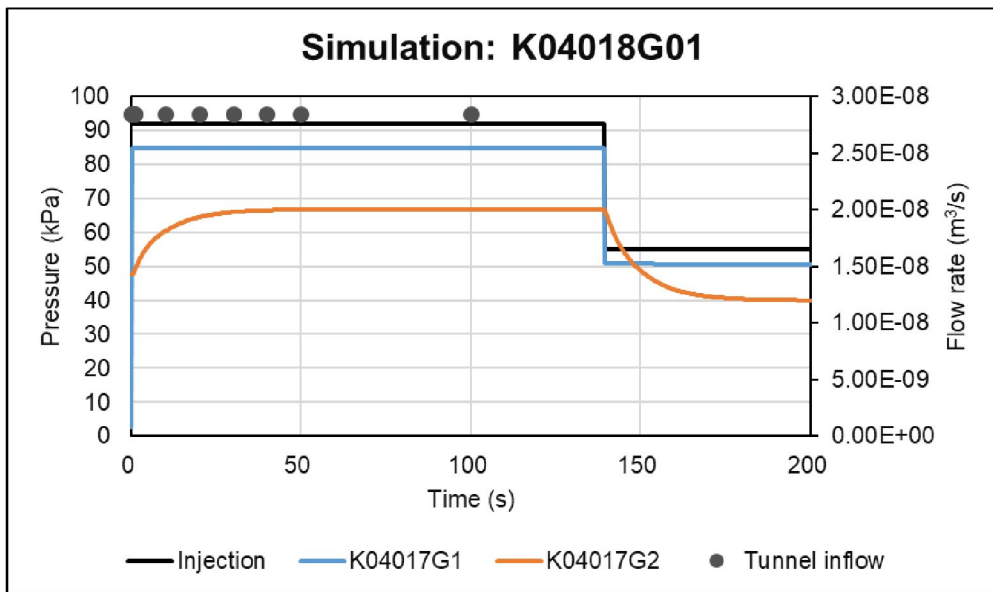


Figure 42. Modelled transient pressure response and simulated injection flow rate for the K04018G01 injection test.

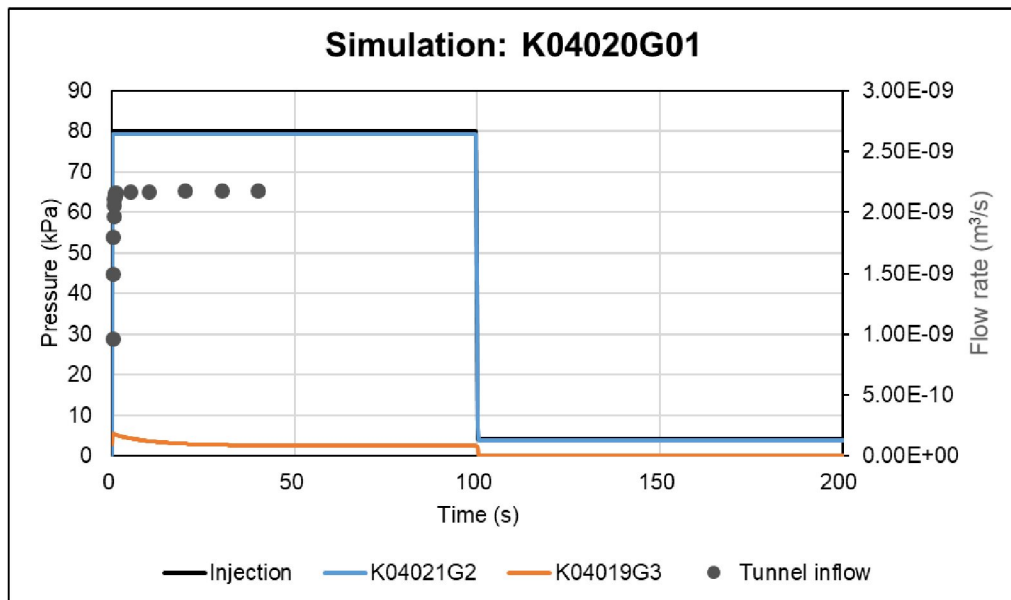


Figure 43. Modelled transient pressure response and simulated injection flow rate for the K04020G01 injection test.

### 7.6.2. TUL-IGN

The goal of this activity was to enhance the best fit model from Activity 2.2 by including the time-dependent injection pressures from the injection holes and the pore pressure responses in the observation holes. For this, the model with parameter set “var\_1” (see Table 21) was selected as the previous best fit model, noting though that it was not able to perfectly fit the measured data. The results after incorporating the time-dependent injection pressure are shown in Figure 44, Figure 45, and Figure 46. These show a similar degree of fit to the measured data as obtained for the static simulations except for the results simulating the K04017G02 injection test. For this case, the simulated responses are significantly delayed compared to the measured ones even though their magnitudes are similar. This might indicate that the connectivity is too low and that the addition of more fractures and their behaviour in the model might be required to improve the fit. Furthermore, channeling might be influencing the fracture flow.

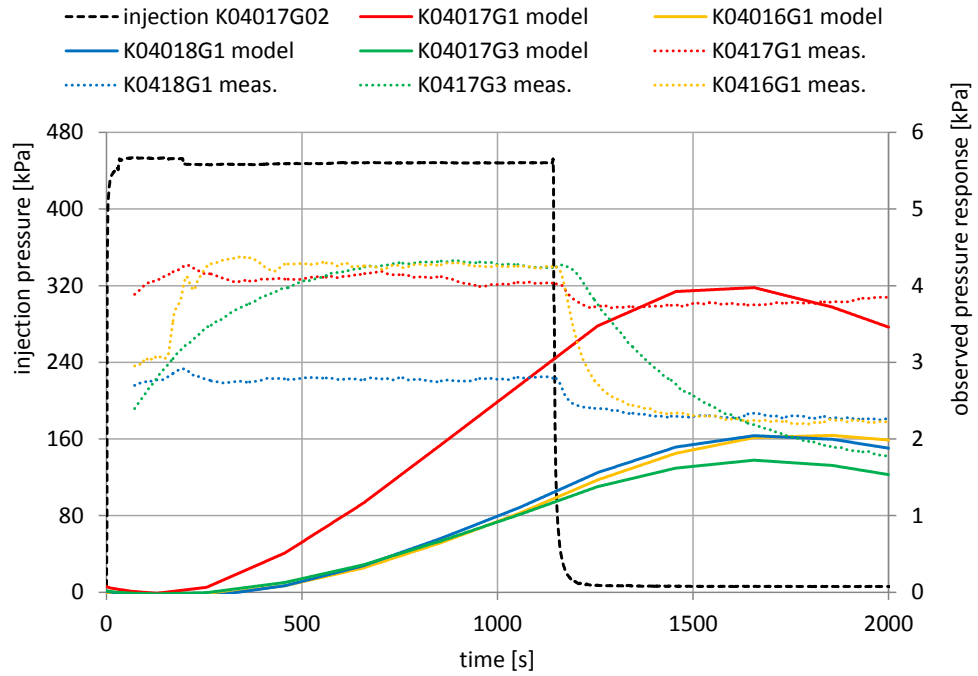


Figure 44. Measured (dotted) and simulated (solid) responses to time-dependent injection pressures (dashed) in drillhole K04017G02.

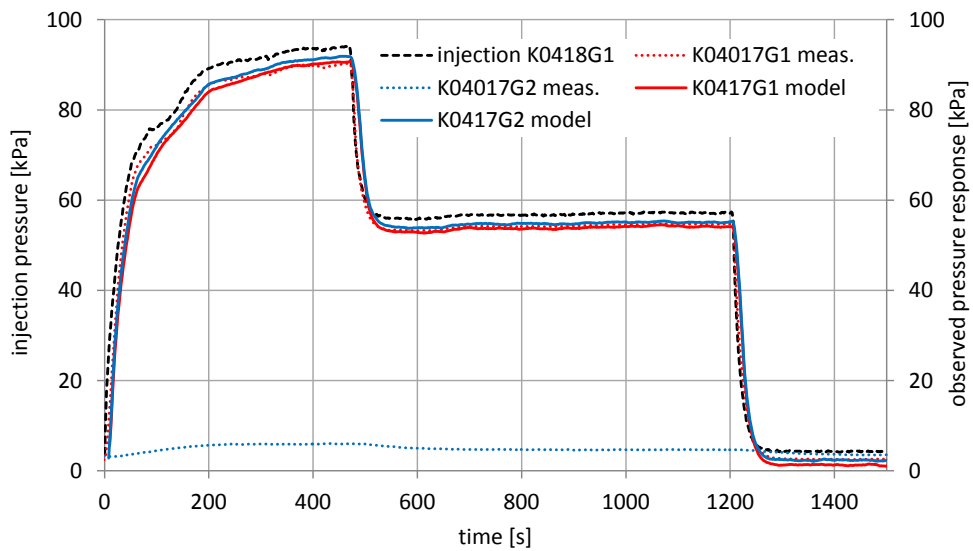


Figure 45. Measured (dotted) and simulated (solid) responses to time-dependent injection pressures (dashed) in drillhole K04018G01.

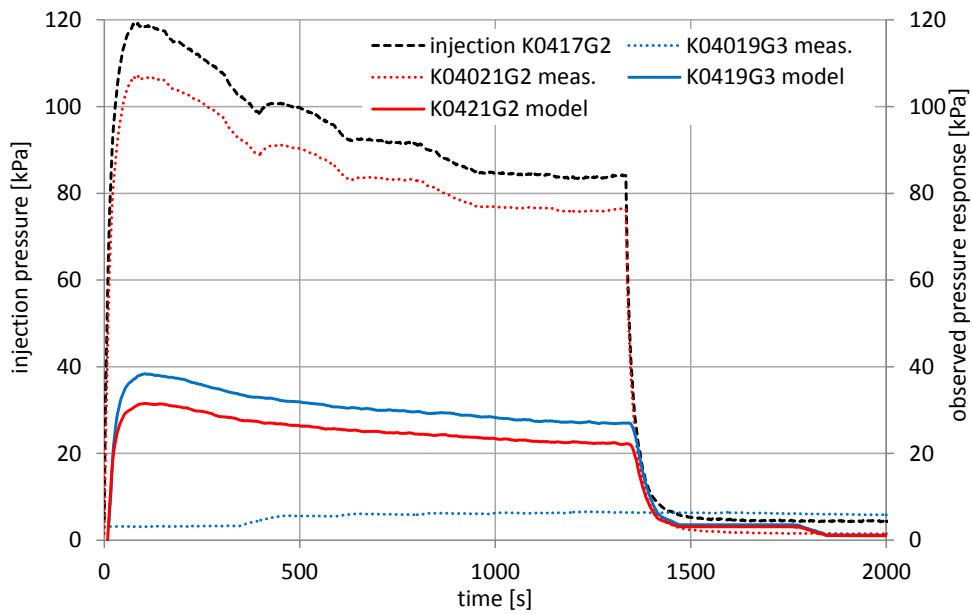


Figure 46. Measured (dotted) and simulated (solid) responses to time-dependent injection pressures (dashed) in drillhole K04020G01.

### 7.6.3. GMC

Figure 47, Figure 48, and Figure 49 show the model results for Activity 2.3 when adding transient pore-pressure responses for the three interference tests.

For the interference test where K04017G02 was the injector, the modelled pressure responses were too high in observation drillholes K04016G01 and K04017G03; the remaining two drillholes showed pressure responses in the correct magnitude range.

For the interference test where K04018G01 was the injector, the modelled pressure responses were also too high for one of the two observation drillholes. The high- and low-pressure plateaus generated for the injection pressure were also not reflected in the modelled pressure responses. Additionally, a significant delay in the pressure response was also observed for this case.

For the interference test where K04020G01 was the injector, we observed an almost identical pressure response in K04021G02 with regard to its temporal development. For the response observed in K04019G03, the magnitude was too low but otherwise showed a good fit to the temporal trend of the simulated injection pressure.

Overall, the degree of fit obtained between the in-situ and modelled pressure responses for Activity 2.3 decreased from the previous activity.

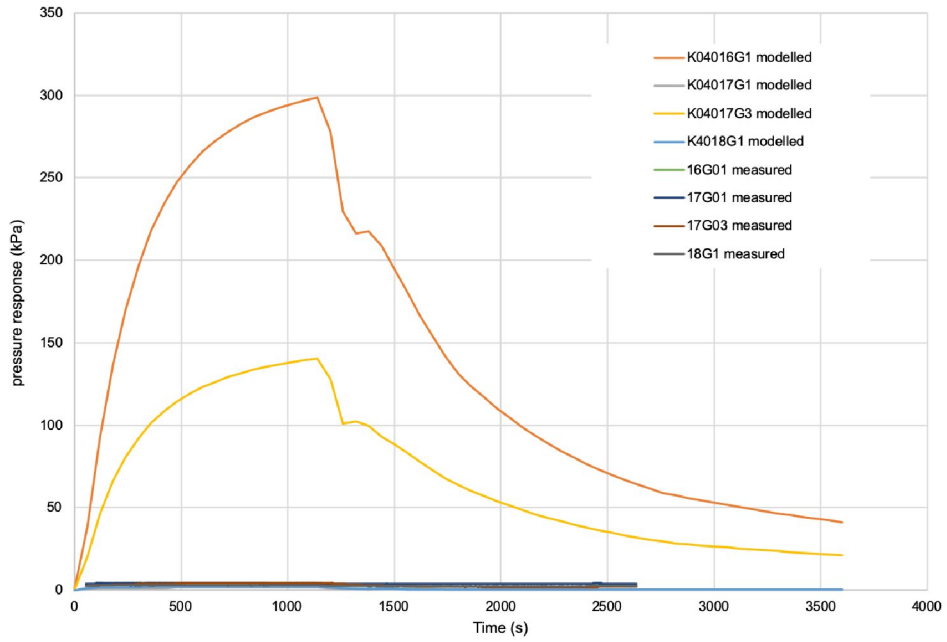


Figure 47. Modelled pressure response curves for the interference test where K04017G02 was the injector, for Activity 2.3.

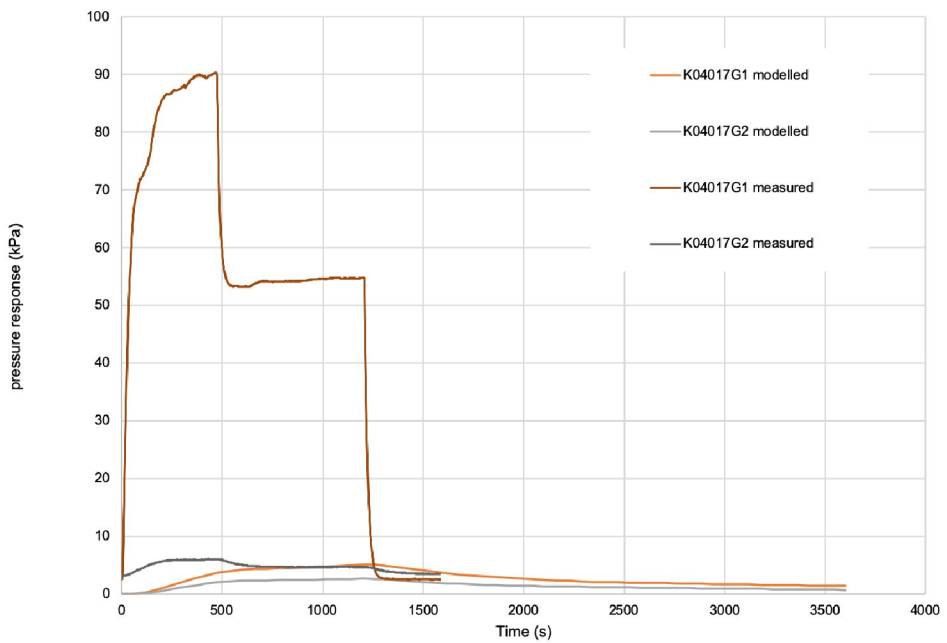


Figure 48. Modelled pressure response curves for the interference test where K04018G01 was the injector, for Activity 2.3.

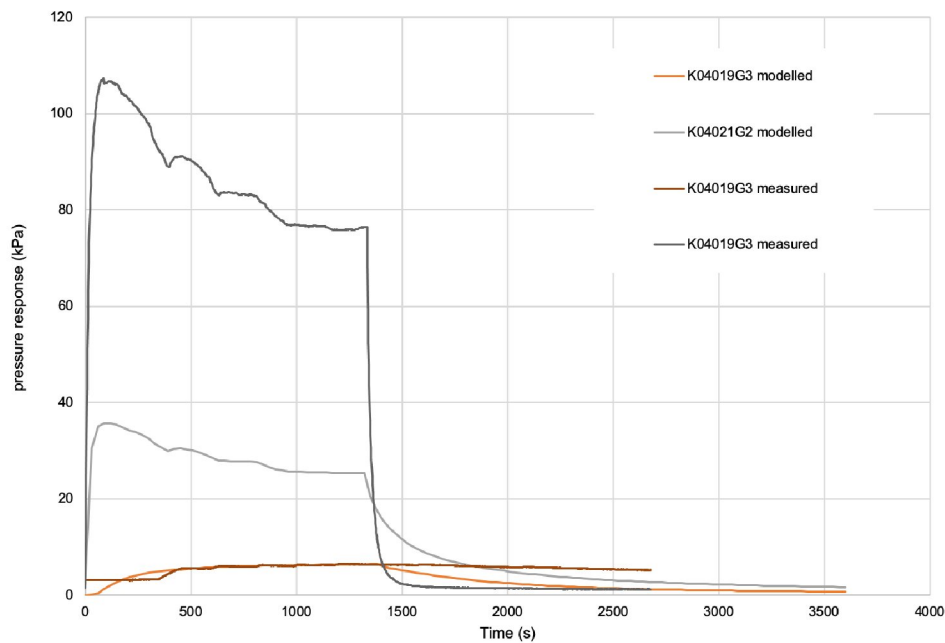


Figure 49. Modelled pressure response curves for the interference tests where K04020G01 was the injector, for Activity 2.3.

#### 7.6.4. Discussion

Activity 2.3 contains the most complete data set provided within Work Package 2 for which all available data was provided for consideration to the modelling teams. However, this added complexity came at a cost.

The teams using COMSOL Multiphysics struggled with implementing the new fracture data sets provided. Especially the implementation of the reflector data and the DFNs derived from the conditional stochastic fracture simulations were almost impossible to use. Shallow intersection angles and highly irregular-shaped fractures caused problems in the construction of the model geometry and the subsequent discretization of the FEM mesh. Hence, TUL-IGN implemented an EDZ by assigning a constant volume around the tunnel with a higher permeability. GMC also tried to replace EDZ fractures by modelling yielded volumes and assigning higher permeabilities to them (not presented here). Only by reducing the amount of fractures and applying smoothing procedures could a few of the provided fractures be implemented (with significant effort).

The SNU team using 3DEC also only used a limited number of fractures in their simulations to avoid the heavy computing times that would be required. Therefore, even though realistic data sets were provided to the modelling teams, they were not fully utilized.

Figure 50 provides an overview of the modelled pressure responses obtained by each modelling team compared to the values measured in-situ. Generally, TUL-IGZ seems to be successful in modelling the interference test in K04017G01 as the pressure responses in K04016G01, K04017G01, K04017G03, and K04018G01 show a good fit to the in-situ measurements. Furthermore, the pressure responses in K04017G01 and K04021G01 are also within an acceptable margin. In total, 6 of 8 pressure responses were modelled reasonably well by TUL.

SNU shows only a good match for 2 out of 8 pressure responses, namely those in K04017G01 and K04019G03 for interference tests K04017G02 and K04020G01, respectively. The approach taken by GMC also provides only 2 out of 8 positive pressure responses.

Clearly, the implementation of the time-dependent injection curves improved the results of TUL-IGZ in comparison to the previous activities. For SNU and GMC, Activity 2.3 did not significantly increase the fit achieved between the modelled and measured pressure responses.

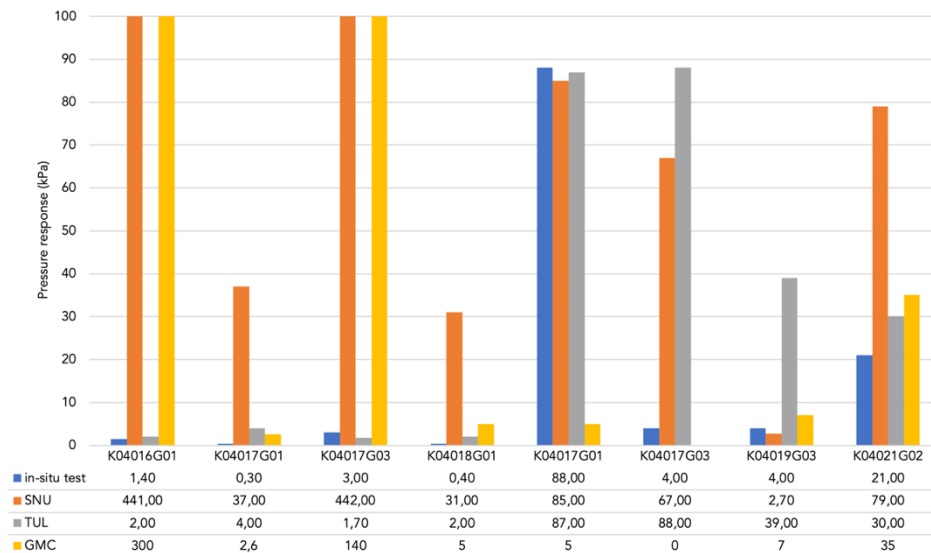


Figure 50. Measured and modelled maximum pressure responses for Activity 2.3 in direct comparison for each observation drillhole. Please note that the y-scale has been cut off at 100 kPa for better comparison. The exact values are provided in the included table below the graph.

## 7.7. General Discussion

Two different numerical codes and several different geomechanical models have been tried to predict the interference test and the flow between the drillholes in the TAS04 tunnel. Among the different numerical models are stress and aperture dependent fracture permeabilities, parametric sweeps to obtain best fit hydraulic parameters, isotropic and anisotropic excavation damage zones and many more which are beyond the scope of this report.

Independent of the chosen numerical approach, the overall hydraulic performance of the rock is controlled by the fractures that have been modelled with stress-dependent or constant hydraulic properties. The stress field on the fractures is controlled by the applied far-field stress, the chosen geometry of the tunnel, and the discretization. Depending on these parameters local variances in the stress acting on the fractures might be present and in turn have a significant effect on the apertures or hydraulic properties. These parameters need to be compared in order to understand the differences in the modelling results that have arisen within Work Package 2.

The stress field has been modelled by each research team with constant boundary stresses, meaning that the vertical stress does not increase with depth. Despite the fact that the stress field might be not entirely correct, it is comparable across the modelling teams with only small stress changes. The ascribed vertical stress and minimum

horizontal stress varies between 11.2 MPa and 12 MPa. Similarly, the maximum horizontal stress varies by 0.8 MPa between the modelling teams, from 23.2 to 24 MPa. The difference of 0.8 MPa in the applied stress field is well within the error of the given in-situ stress field estimates presented in Section 3.2.3.

Despite the applied constant stress field on the outer boundaries, the tunnel alters the stress field within the modelling domain as indicated by the figures in Section 7.1. Depending on the generalized or irregular tunnel surface and the linear elastic modelling approaches, high stress concentrations occur on corners or irregularities (lookouts). In fact, the highest stress concentration, which is at the same time also related to high differential stresses, occurs in the corners of the generalized tunnel surface. However, the differences in the concentrated stresses between the generalized and irregular tunnel surface are relatively small, very localized and independent of the stress direction. It is interesting to note that the vertical stress directly below the tunnel floor is positive, i.e. tensile, potentially opening horizontal fractures in a very shallow region of approx. 5 to 20 cm below the tunnel floor. This observation is consistent for all modelling teams. Hence, the difference in the modelled pressure responses cannot only be related to the differences in the applied stress field. It is more questionable in just how far the uncertainty in the in-situ stress field influences the performed interference tests. For instance, minor changes in the vertical stress would have a significant effect on the normal stress of tunnel-floor-parallel fractures and the permeability of these fractures.

The largest discrepancy in the different model set-ups of the modelling teams is observed in the discretization, which can have a significant impact on the modelling results. Coarse discretization might reduce stress concentrations and cut off theoretically infinite stress values at very sharp corners, which would in reality also not exist due to failure of the rock. Only finely discretized geometries yield results comparable to analytical solutions of stress concentrations for such sharp corners. The differences can be observed when comparing the horizontal stresses obtained by TUL-IGN and SNU for the regular tunnel surface. The range of the minimum horizontal stress varies between -0.78 MPa to -30 MPa for SNU and 5.3 MPa to -32 MPa for TUL-IGN, with the latter having the finer discretization. The reason for different levels of discretization are manifold but are mostly related to computational cost (the finer the mesh, the longer the calculations) and the discretization process itself.

Within work package 2, it was recognized that COMSOL Multiphysics was not always able to discretize the domain as desired by the modeler. The geometry had to be simplified in order to arrive at a discretized model. On the other hand, SNU observed that 3DEC would require extremely long computation times in case of a fine discretization. This makes it complicated to achieve a consistent discretization applicable for all modelling teams, resulting in comparable stress concentrations at sharp corners. The stress field therefore varies on a very local scale between the models and might cause higher closure rates of fractures where a stress-dependent permeability approach is implemented. Table 25 summarises the findings of the causes and consequences that have contributed to the differences in the modelling results.



Table 25. Causes and consequence for the modelling results.

Cause (decision)	Stress field definition (gradient or constant)	Geometry (regular or irregular)	Mesh (fine or coarse)
	⇓	⇓	⇓
Reason for decision	Modelers choice or numerical software limitations	Implementation of exact geometry difficult to impossible	Computational resources and discretisation limitations
		⇓	
Consequences	Compressional or tensional stresses around the tunnel wall	Changing properties, such as fracture apertures	Varying stresses leading to low or high fracture permeabilities

Unfortunately, none were successful in modelling the interference tests completely. Especially if an interference test caused high- and low-pressure responses in different, neighboring drillholes, the numerical models were unable to predict the pressure differences. This is particularly troublesome because it indicates that not all drillholes are connected to the interference test or that fracture flow towards one observation hole is blocked while it was open to another drillhole. An example for this behavior was the interference test where K04018G01 was the injector. In two neighboring drillholes K04017G01 and K04017G02, pressure responses with significant spread were observed despite both being connected by one fracture to the injection hole. This is probably related to channeling effects along the fractures since stress- and aperture-dependent models failed to predict this pressure response. Attempts to include channeling on the fractures have been not tested, further underlining the possibility of channeling along the fractures below the TAS04 tunnel.

With increasing complexity of the underground model, i.e. from activity to activity, the modelled pressure responses increased as indicated by Figure 51, Figure 52, and Figure 53. While in Activity 2.1 most pressures were recorded below 10 kPa, the majority of pressures in Activity 2.2 and 2.3 were above 10 kPa. In Activity 2.3 no pressure was recorded below 1 kPa. This is strongly related to the greater number of fractures implemented, providing a higher connectivity between the drillholes. However, higher pressure responses do not necessarily increase the fit to the in-situ experiments. The coefficient of determination, i.e. that high pressures during the in-situ experiments should cause high modelled pressure, derived for each activity and modelling team has a clear peak in Activity 2.2. In the theoretical best case in which the modelled pressure matches the in-situ pressure (neglecting irreducible errors from the measurements or other uncertainty and variability), all points in Figure 51, Figure 52, and Figure 53 should fall on a diagonal line starting at the origin with an coefficient of determination of  $R^2=1$ .

The closest results to this have been observed in Activity 2.2 with  $R^2=0.66$  and  $R^2=0.98$  by GMC and TUL, respectively. Activity 2.1 and Activity 2.3 have much lower coefficients of determination.

### Activity 2.1

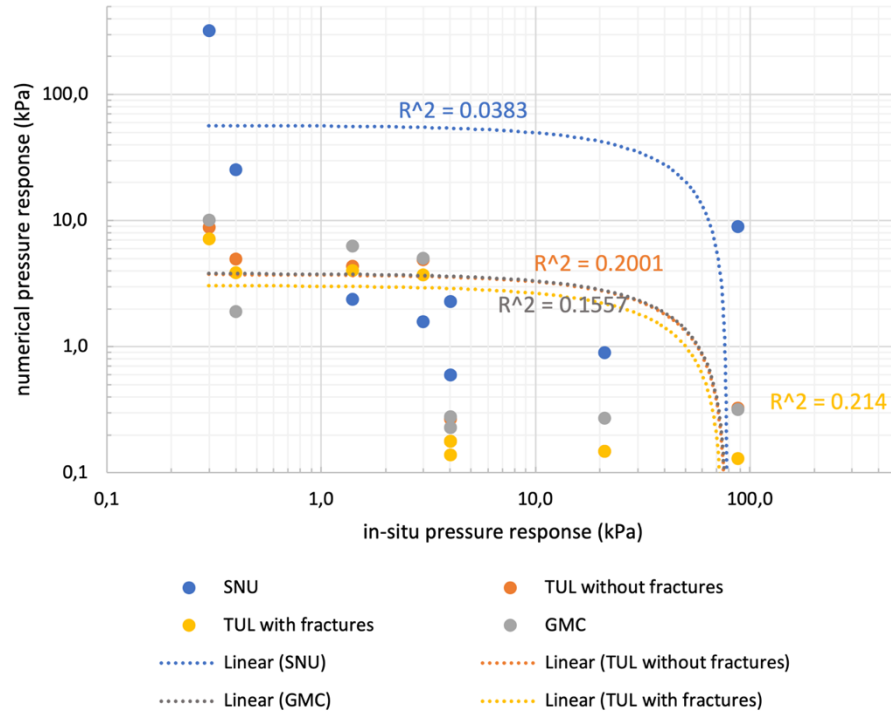


Figure 51. Numerically modelled maximum pore pressure vs. maximum in-situ pore pressure from different interference tests obtained in Activity 2.1.

### Activity 2.2

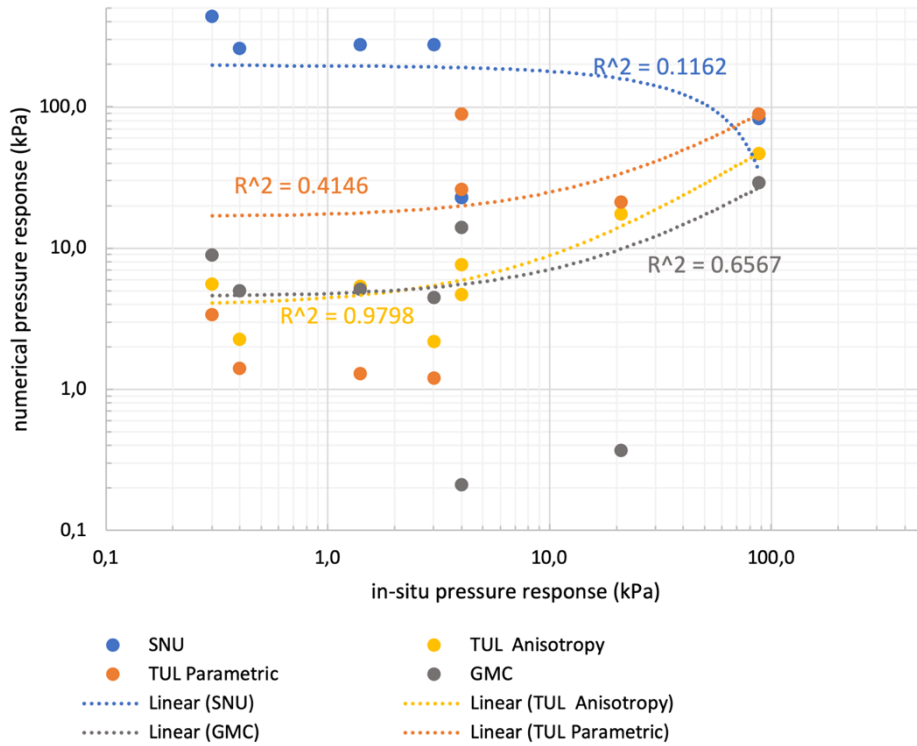


Figure 52. Numerically modelled maximum pore pressure vs. maximum in-situ pore pressure from different interference tests obtained in Activity 2.2.

### Activity 2.3

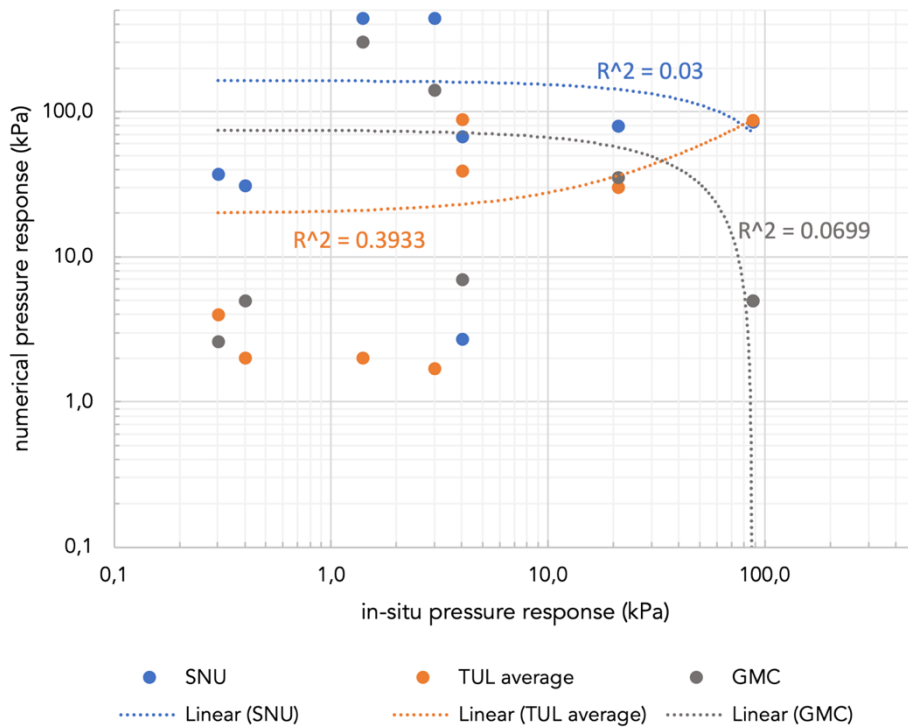


Figure 53. Numerically modelled maximum pore pressure vs. maximum in-situ pore pressure from different interference tests obtained in Activity 2.3.

The modelling results were expected to deliver the following results:

- Validation of suitability of the numerical models for simulation of the evolution of the rock in the vicinity of tunnels and holes.
- Analysis of representativeness and relevance of the conditions during construction and operations for the evolution of the repository after closure.
- Analysis of significance of the changes after closure with respect to the initial values and accuracy of the measuring methods.

It can be summarized that the codes were not able to predict all the in-situ pressure responses, particularly those with significant pressure differences in the observation holes. Therefore, the numerical models are not suitable for modelling the evolution of the rock in the immediate vicinity of tunnels and holes due to the fact that a) not all provided data could be implemented, b) the provided data might be incomplete with reference to channels along the fractures, and c) the differences between the regular and irregular tunnel geometry induce stresses that differ from the in-situ stresses. Interestingly, the numerical codes did quite well represent the inflow into the tunnel.

## **7.8. Outlook**

A third work package has been defined to simulate the changes in transmissivity induced by thermal loading during the thermal phase of the repository and ice loading due to glaciation.

In how far the upcoming results from the WP3, which deals with the post closure processes like thermal phase, glaciation, and earthquake, will yield reliable results is quite questionable. However, the results from WP3 might indicate relative changes, e.g. whether the transmissivity in the EDZ is going to increase or decrease during the post closure process. In this aspect they will bring about valuable insights, which will enhance the prediction of the evolution of the repository after closure.

## 8. Acknowledgements

DECOVALEX is an international research project comprising participants from industry, government and academia, focusing on development of understanding, models and codes in complex coupled problems in sub-surface geological and engineering applications; DECOVALEX-2019 is the current phase of the project. The authors appreciate and thank the DECOVALEX-2019 Funding Organizations Andra, BGR/UFZ, CNSC, US DOE, ENSI, JAEA, IRSN, KAERI, NWMO, RWM, SÚRAO, SSM and Taipower for their financial and technical support of the work described in this report. The statements made in the report are, however, solely those of the authors and do not necessarily reflect those of the Funding Organizations.

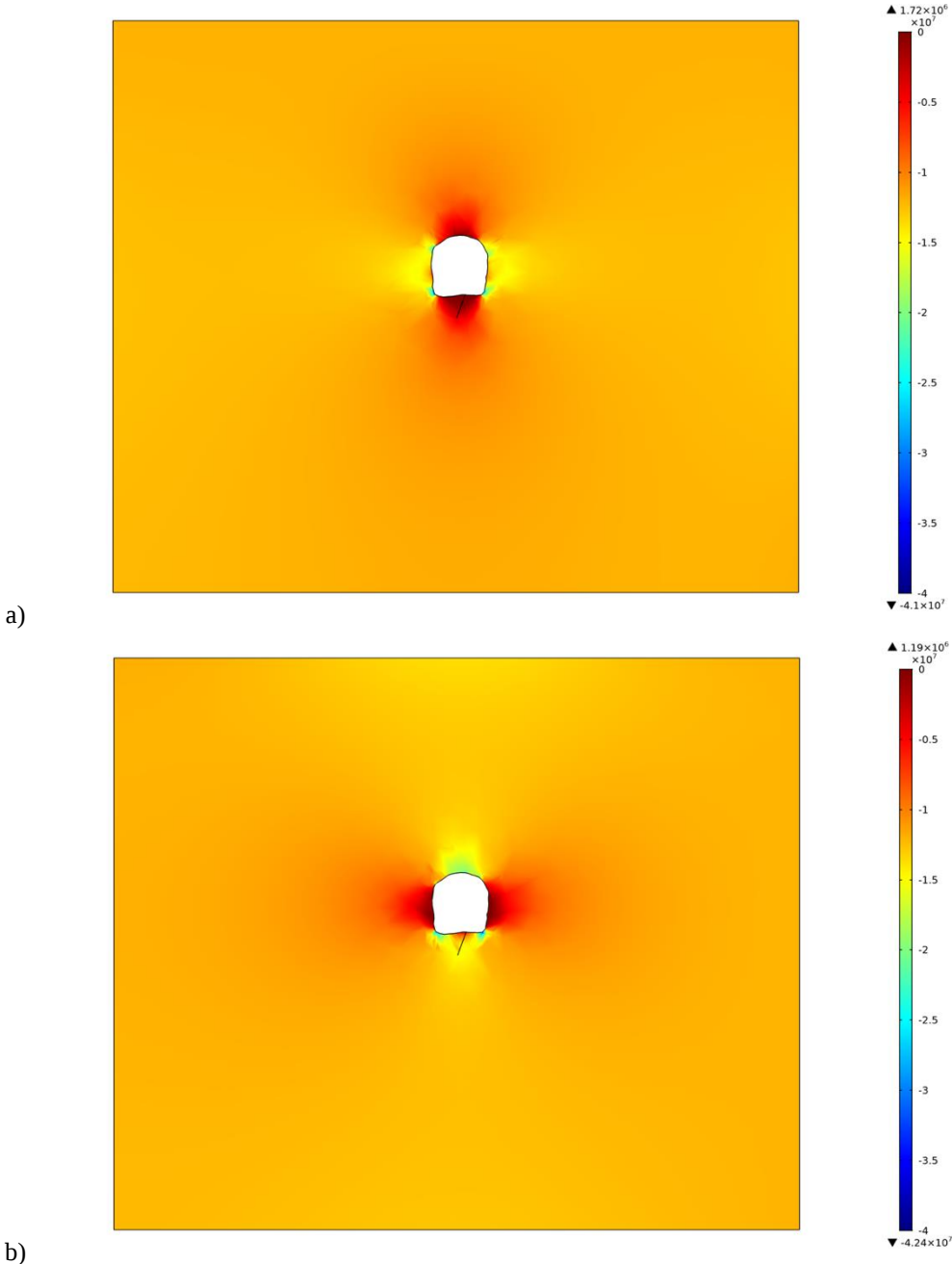
## 9. Literature

- Backers T., Blaheta R., Geier J., Hancilova I., Hasal M., Kwon S., Lanaro F., Meier T., Min K.-B., Pettersson C.-H., Riha J. (2018). Reliability, Feasibility and Significance of Measurements of Conductivity and Transmissivity of the Rock Mass for the Understanding of the Evolution of a Repository of Radioactive Waste. SSM Report SSM2016-1671.
- Bandis, S.C., Lumsden, A.C., Barton, N.R., 1983. Fundamentals of Rock Joint Deformation. *International Journal of Rock Mechanics and Mining Sciences & Geomechanics Abstracts*, Vol. 20(6), p. 246-268.
- Barton, N., Choubey, V., 1977. The Shear Strength of Rock Joints in Theory and Practice. *Rock Mechanics* Vol. 10, p. 1-54.
- Biot M.A. (1962): Mechanics of Deformation and Acoustic Propagation in Porous Media, *J. Appl. Phys.*, vol. 33, pp. 1482–1498.
- Christiansson, R., Janson, T., 2003. A test of different stress measurement methods in two orthogonal bore holes in Äspö Hard Rock Laboratory (HRL), Sweden. *International Journal of Rock Mechanics and Mining Sciences* 40(7):1161-1172
- COMSOL Multiphysics® v. 5.0.. COMSOL AB, Stockholm, Sweden. [online]. [cit. 2017-05-25]. [www.comsol.com](http://www.comsol.com)
- DECOVALEX-THMC Task D: Long-Term Permeability/Porosity Changes in the EDZ and Near Field due to THM and THC Processes in Volcanic and Crystalline-Bentonite Systems, Status Report October 2005.
- Ericsson L.-O., Christiansson R., Butronc C., Hansson K., Lehtimäki T. (2014). Characterization of the Excavation Damaged Zone by means of Geological, Geophysical and Hydrogeological Co-interpretation, 8th Asian Rock Mechanics Symposium.
- Ericsson L.-O., Thörn J., Christiansson R., Lehtimäki T., Ittner H., Hansson K., Butronc C., Sigurdsson O., Kinnbom P. (2015). A demonstration project on controlling and verifying the excavation-damaged zone – Experience from the Äspö Hard Rock Laboratory, SKB TR-14-30, Swedish Nuclear Fuel and Waste Management Co (SKB).
- Glamheden, R., Fredriksson, A., Röshoff, K., Karlsson, J., Hakami, H., Christiansson, R., 2007. Rock Mechanics Forsmark: Site descriptive modelling Forsmark stage 2.2. SKB Report R-07-31, Swedish Nuclear Fuel and Waste Management Co., Stockholm, Sweden.
- Ittner H., Bouvin A. (2015). Undersökning av sprängsprickor från mekaniserad laddning med bulkemulsion i bergtunnel (in Swedish with English summary), BeFo Report 144, Stiftelsen Bergteknisk forskning (Rock Engineering Research Foundation), Sweden.
- Ittner H., Bouvin A., Fogdeby M., Karlzen R. (2015). Investigation of blast induced fractures from string emulsion in tunnel, *Bergmekanikdag 2015*, Stockholm, Sweden.
- Ittner H., Lehtimäki T., Christiansson R. (2014). Design and control of the EDZ for a deep repository in crystalline rock. *Rock Engineering and Rock Mechanics: Structures in and on Rock Masses – Alejano, Perucho, Olalla & Jiménez (Eds)*. 2014 Taylor & Francis Group, London, 978-1-138-00149-7.

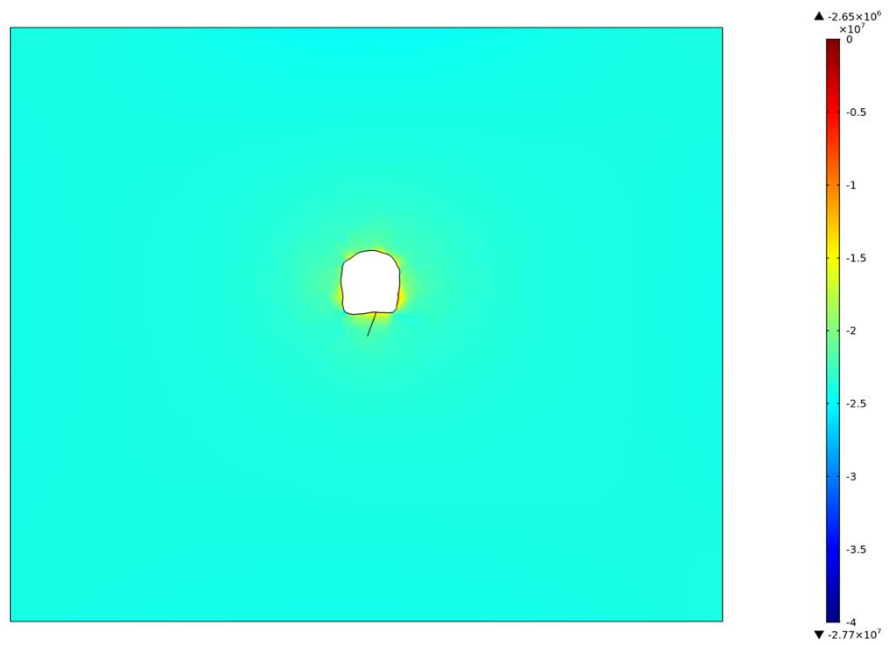
- Liu Q., Wu Y., Liu B. (2011). Discrete element analysis of effect of stress on equivalent permeability of fractured rockmass, *Yanshilixue Yu Gongcheng Xuebao/Chinese Journal of Rock Mechanics and Engineering*, 30(1), 176-183.
- Mas Ivars, D., Veiga Rios, M., Shiu, W., Johansson, F., Fredriksson, A., 2014. Long term stability of rock caverns BMA and BLA of SFR, Forsmark. SKB Report R-13-53, Swedish Nuclear Fuel and Waste Management Co., Stockholm, Sweden.
- Min K.-B., Rutqvist J., Tsang C.-F., Jing L. (2004). Stress-dependent permeability of fractured rock masses: a numerical study, *Int J Rock Mech & Min Sci*, Vol. 41(7), p. 1191-1210.
- Öhman J., Niemi A., Tsang C.-F. (2005). Probabilistic estimation of fracture transmissivity from Wellbore hydraulic data accounting for depth-dependent anisotropic rock stress, *Int J Rock Mech & Min Sci*, Vol. 42(5-6), p. 793-804, ISSN 1365-1609.
- Rutqvist J., Barr D., Birkholzer J.T., Fujisaki K., Kolditz O., Liu Q.-S., Fujita T., Wang W., Zhang C.-Y. (2009a). A comparative simulation study of coupled THM processes and their effect on fractured rock permeability around nuclear waste repositories, Special Issue: The DECOVALEX-THMC Project (Safety assessment of nuclear waste repositories), *Journal of Environmental Geology*, Vol. 57(6), p. 1347-1360.
- Rutqvist J., Börgesson L., Chijimatsu M., Hernelind J., Jing L., Kobayashi A., Nguyen S. (2009b). Modeling of damage, permeability changes and pressure responses during excavation of the TSX tunnel in granitic rock at URL, Canada, Special Issue: The DECOVALEX-THMC Project (Safety assessment of nuclear waste repositories), *Journal of Environmental Geology*, Vol. 57(6), p. 1263-1274.
- Rutqvist, J., Stephansson, O., 2003. The role of hydromechanical coupling in fractured rock engineering. *Hydrogeology Journal*, Vol. 11, p. 7-40.
- SKB (2010). Framework programme for detailed characterisation in connection with the construction and operation of a final repository for spent nuclear fuel, Swedish Nuclear Fuel and Waste Management Co (SKB).
- Walsh, J.B., 1981. Effect of Pore Pressure and Confining Pressure on Fracture Permeability. *International Journal of Rock Mechanics and Mining Sciences & Geomechanics Abstracts*, Vol 18, p. 429-435.
- Wang W., Rutqvist J., Görke U.-J., Birkholzer J.T., Kolditz O. (2011). Non-isothermal flow in low permeable porous media: a comparison of Richards' and two-phase flow approaches, *Environmental Earth Sciences*, Vol. 62(6), p. 1197-1207, DOI:10.1007/s12665-010-0608-1.
- Witherspoon, P.A., Wang, J.S.Y., Iwai, K., Gale, J.E., 1980. Validity of Cubic Law for Fluid Flow in a Deformable Rock Fracture. Vol. 16(6), p. 1016-1024.

# 10. Appendix 1 – Influence of tunnel surface

A comparison of the effect of the tunnel surface on the simulation results was also made by TUL-IGN using a generalized and the irregular tunnel surface (see Figure 19). The geometry of the tunnel with an irregular surface uses approximately 3,000 points to describe it, and the computational network includes approximately 158,000 four-sided elements with an average element quality of 0.55. For comparison, the horseshoe-shaped, generalized tunnel has approximately 162,000 four-sided elements with an average element quality of 0.69. Comparisons were made between the vertical and horizontal stresses in the steady-state simulations with the generalized and irregular tunnel surface (compare Figure 32 and Figure 54, respectively).







c)

Figure 54. (continued from previous page) Cross section normal to the tunnel axis showing the modelled stresses for WP 2.1, plotting: a) vertical stresses (z direction), b) minimum horizontal stresses normal to the tunnel axis (x direction), and c) maximum horizontal stresses parallel to the tunnel axis (y direction). Note that the stresses are in units of Pa and are compression-negative.

# 11. Appendix 2 - Literature Review of Measurement Methods for Understanding the Status and Evolution of a Repository for Nuclear Reactive Waste

Dr. Brendan Fisher<sup>1</sup>, Prof. Erik Eberhardt<sup>1,2</sup>

<sup>1</sup> Fisher Rock Engineering, USA

<sup>2</sup> Geological Engineering, University of British Columbia, Vancouver, Canada

## 11.1. Introduction

The measurement of geomechanical and hydrogeological parameters critical for determining deposition-tunnel and -hole acceptability during the operation of a repository must have sufficient accuracy, resolution and reliability to meet any safety-related performance indicators required to establish that the design premises of the repository are being met. This is reflected in SKB R-17-16, which states that measurement systems incorporated into the design, operation and closure of a repository should be devised to provide a holistic overview of the system for the purpose of confirming design premises, and ensuring appropriate safety. Key parameters to measure include: water inflows into boreholes and excavations, fracture transmissivity, equivalent rock permeability, rock stresses, excavation-induced displacements, fracture orientation and persistence (including detection behind the excavation walls), depth of construction and stress-induced excavation damage (termed CDZ and EDZ, respectively), rock temperatures, and any changes to these parameters over the evolution of the repository. Specific questions related to these parameters and their potential impact on the repository design premises and performance are described in earlier reviews (Eberhardt & Diederichs 2012, 2014).

Initial measurements start with surface-based site investigations for those parameters where borehole measurements are applicable, such as in situ rock stress. It is recognized that borehole drilling might be limited within the repository footprint and performed in representative rock volumes outside the footprint in order to limit the potential of the boreholes serving as permeability pathways. These site investigations will continue and progress through construction and operation, allowing more direct measurements to be made at depth at the repository level, thus enabling measurement of changes in response to the excavation process. At all stages, numerical modelling should be an integral part of the investigation activities; typically focusing on identifying those parts of the system where stress-induced rock mass damage and/or groundwater inflows may be a concern. Those activities necessary for continuation of stepwise underground construction and deemed necessary to decrease uncertainties related to long-term safety after closure take precedent. During construction, the geological and hydrogeological models are updated based on observations of the rock geomechanical, hydrogeological and thermal properties. Rock stress measurements will play an important role in designing the deposition-tunnels and -holes, especially their orientation for the selected repository depth (which might also be determined from the in situ stress measurement campaign). At defined intervals, the integrated site description model should be updated to include all geoscientific disciplines (SKB R-17-16).

More specifically, SKB R-10-08 states that the purposes of detailed investigations are to:

- provide evidence for adaptation of the repository to the site-specific conditions to meet the design conditions, including with regard to long-term safety;

- provide evidence for engineering decisions on, for example, grouting and reinforcement measures; and
- update site models, which in turn should be the basis for long-term safety assessments.

According to SKB R-04-13, monitoring during the stepwise implementation of the repository is executed for several reasons, but mainly to:

- describe the primary baseline conditions of the repository site;
- develop and demonstrate understanding of the repository site and the behaviour of engineered barriers;
- assist in the decision-making process; and
- show compliance with international and national guidelines and regulations.

Specific rationales for monitoring are to:

- obtain knowledge of undisturbed conditions in nature and their seasonal variations (baseline) in order to identify and evaluate the impact of activities related to the deep repository during different phases;
- obtain a better understanding of the function of the deep repository system to support the safety account and to test models and assumptions;
- monitor the environmental impact of the deep repository (not covered in this report);
- provide evidence that the working environment is safe with regard to radiological and non-radiological effects; and
- show that requirements on radioactive waste verification (safeguards) are fulfilled.

Ongoing monitoring provides input for updating geological and hydrogeological models that will continuously be updated during the construction and operational phases. Subsequent phases benefit from forecasts predicated on advanced numerical modelling and in accordance with the principles of the *observation method of design*. Forecasts are compared with documented outcomes after tunnel and depositional hole excavation, to assess whether acceptable conditions are present allowing uncertainties to efficiently be addressed.

Measurement methods typically employed include “routine” measurements such as face mapping and probe drilling (ahead of the excavation advance) following best practice guidelines. Other investigation techniques to probe into the rock mass, such as geophysical surveys (non-invasive) and borehole viewers (invasive), may be incorporated but require significant processing and interpretation and therefore are subject to verification during the early stages of construction using other techniques to ground-truth the interpretations.

## 11.2. Measurement Accessibility

### 11.2.1. Direct Measurements

Tunnel mapping, together with the survey results from boreholes, is the primary activity for the routine updating of geologic and hydrogeologic models at a detailed scale. These include the following:

**Pilot holes** are key to many detailed investigation techniques. They are typically 200 to 300 m long (or longer for shaft locations) and may be utilized in the ramp and staging

areas depending on the uncertainties associated within those areas (SKB R-10-08). These exploration holes provide a means for carrying out a number of *in situ* measurements including borehole imaging, downhole hydraulic testing, and stress measurements, etc. The number of probe holes, their location and types of testing carried out, for example overcoring versus hydraulic fracturing for stress measurement, may be limited depending on any risk posed to the potential for permeability pathways being created. Preferably, such holes would be aligned ahead of a future excavation, although it needs to be recognized that deeper boreholes often deviate from their intended trajectory.

**Probe Holes** are shorter than pilot holes and are drilled to correspond with blast cycles during tunnel excavation. They can serve in a similar manner as pilot holes to provide information on local rock and hydraulic conditions several blast rounds in advance. Probe holes are the basis for establishing the need and sizing of any pre-support or pre-injection grouting required to improve the tunnel wall stability and permeability conditions (SKB R-10-08).

**Tunnel Mapping** is an integral part of each tunnel advance or deposition hole excavation, providing a direct and non-invasive means to determine and document the geology (lithology, fractures, etc.), geomechanical conditions (rock quality), and water inflows and quality (temperature, hydrogeochemistry, etc.). Tunnel mapping is performed routinely and continuously in all rock excavations (SKB R-10-08).

### 11.2.2. Indirect Measurements

Other methods, such as **geophysics**, are non-invasive and measure properties which can be used to indirectly infer geotechnical/hydrogeological properties of interest. These types of measurements include active sensing techniques such as ground penetrating radar (GPR) and seismic refraction, as well as passive techniques such as acoustic emission/microseismicity to detect brittle fracturing activity. Geophysical methods require the integration of systematic geospatial data collection, modelling and inversion techniques to infer changes in geological, geomechanical and hydrogeological properties.

## 11.3. Rock Stresses

Measuring the orientation and magnitude of rock stresses is important for understanding excavation stability, EDZ, and for optimal alignment of deposition-tunnels and -holes. At the same time, as important as *in situ* stress is as a boundary condition for repository design, the testing methods are considered to be amongst the most difficult and unreliable measurements there are in rock engineering. The issue is that the measurements are intended to characterize the far-field *in situ* stress conditions, but they are highly susceptible to localized measurement effects that are hard to identify and therefore to account or correct for.

### 11.3.1. Detection and Measurement Methods

Methods for measuring *in situ* rock stresses include:

- Overcoring (incl. CSIRO hollow inclusion cell, USBM probe)
- Undercoring
- Hydraulic fracturing

- Hydraulic tests on pre-existing fractures (HTPF)

In situ rock stresses can also be back analysed from other stress indicators:

- Convergence measurements
- Core diskings
- Evaluation of nonlinear strains and acoustic emissions (e.g. Kaiser effect) in laboratory samples
- Measuring borehole breakout frequency and orientations
- Microseismic/seismic activity

Given the susceptibility of in situ stress measurements to errors and misleading results, it is important that values be interpreted with an understanding of both the regional and local geology (especially the presence of faults) and tectonics. This includes making use of existing stress data such as that in the World Stress Map database ( ), which includes roughly 500 entries from sites in Sweden, Finland and Norway.

### 11.3.2. State of Practice and Other Considerations

Overcoring coupled with tunnel convergence measurements are generally considered to be more reliable for establishing the full in situ stress field (three principal stress magnitudes and orientations) relative to being less invasive than other common techniques such as hydraulic fracturing. Other recent developments include:

- The LVDT-cell method, which was developed as an alternative stress measurement to overcome problems encountered with traditional overcoring techniques (Hakala et al. 2016). This involves overcoring measurements made within a meter of an excavation and therefore require that a significant EDZ is not encountered.
- The SLITS method, which is performed by drilling a short borehole before a deposition hole is fully drilled. A heater is installed in the hole and heats the hole for a given period (typically a few weeks). The heat provides an additional load, which leads to spalling and verification of the orientation of the principal stresses (Hakami 2011).

## 11.4. Natural Fractures

Repository design and construction needs to reliably detect conductive natural fractures that intersect or are adjacent to deposition-tunnels and holes that may impact long-term safety through high water inflows that may lead to piping and erosion of the buffer material as well as serving as permeability pathways. Similarly, large natural fractures intersecting deposition hole positions may further impact the long-term safety by introducing detrimental shear movements in excess of those that storage canisters are designed to withstand as a consequence of an earthquake event. Natural fracture detection with respect to the latter (i.e., identifying those fractures long enough to accommodate significant slip displacement) is outlined within the Extended Full Perimeter Criterion (EFPC) developed by SKB to select acceptable deposition holes at a sufficient distance from fractures large enough to constitute a (seismic) hazard (SKB TR-10-21).

#### 11.4.1. Detection and Measurement Methods

Detection begins during feasibility studies with focus on mapping regional/site-scale deformation zones. Steeply-dipping zones may be identified based largely on low magnetic lineaments in airborne magnetic data (SKB TR-11-01). Further refinement (e.g. orientation, thickness and location at the repository depth) is gained through surface-based geotechnical boreholes (SKB R-07-45). Deformation zones that are gently dipping (<45 degrees) have been detected using surface seismic reflection data integrated with borehole data (SKB R-07-45).

On a smaller scale, large natural fractures are generally detected through a combination of geotechnical boreholes and surface mapping carried out during excavation. Photogrammetry and laser scanning techniques (LiDAR) offer a means to obtain high resolution point clouds of the excavation surface that can be used for identifying and extracting orientation information of large natural fractures that intersect the excavation. During construction and operation, further measurement of these features may be obtained by:

- The use of high-resolution seismic networks for passively monitoring the location of microseismic events detecting slip events along adversely stressed fractures and deformation zones thus identifying these fractures. These systems are useful for updating the structural geologic model (SKB R-17-16).
- Employing active geophysical survey methods (radar and seismic). These require significant processing and interpretation efforts, and are subject to orientation biases.
- Where drilling gives rise to pressure responses between boreholes, hydraulic interference tests and cross-hole geophysical measurements (mainly electrical) can be used to define hydraulic and physical conditions which in turn may be used to identify significant water-bearing structures.
- Geotechnical drilling from the excavation (pilot holes), in combination with core logging (of oriented core) and/or borehole mapping by televiewer to identify fractures and measure their orientations.

#### 11.4.2. State of Practice and Other Considerations

In a review of feature detection and confirmation methodologies, Karasaki et al. (2007) examined the experiences from several underground laboratories and repository programme sites around the world: Yucca Mountain (USA), Tono and Horonobe (Japan), AECL-URL (Canada), Äspö (Sweden), and Olkiluoto (Finland). The description of the different experiences at these sites suggests that a combination of geophysical techniques is needed and that reliability is a key challenge. Seismic reflection surveys were favoured to detect major fractures. Ground Penetrating Radar (GPR) was cited for locating low dipping fractures. Borehole and cross-hole seismic and radar were cited for detecting the location, continuity and geometry of fractures and features between and away from the boreholes.

In a similar review by Eberhardt & Diederichs (2014), they cite investigations performed at Posiva using radar and seismic methods to identify large discriminating fractures (Sireni 2011; Heikkinen & Kantia 2011). These suggested that the detectability of large natural fractures using seismic reflection was poor, and that GPR was limited to 7 to 12 m penetration depth but that fractures could go undetected if they were not suitably oriented relative to the GPR sensing direction or if the fractures were dry or tightly closed.

At the deposition-tunnel and -hole scale, it would appear that mapping of tunnel exposures and borehole imaging and logging are among the best practices, and are required where geophysical techniques are used to confirm any interpreted results.

#### 11.4.3. Feasibility and Reliability

With respect to their applicability, reliability and confidence, researchers are reticent to claim that geophysical techniques are discriminatory enough for confident identification of large-scale structural features. For example, studies at the Grimsel Laboratory in Switzerland concluded that GPR techniques are “adequate” for mapping water filled fractures in crystalline rock sub-parallel to the measurement surface (Carbonell et al., 2006); but dry fractures are significantly less visible as the contrast in the dielectric property between the fractures and the rock matrix decreases. Similar sensitivities to water-filled versus dry fractures also apply to seismic reflection. Certainty in knowing whether fractures are water filled or dry *a priori* may be determinable based on the local hydrogeology. However, this may become less certain for sparsely connected fracture networks, or where local draining of fractures occurs during construction. Likewise, the presence of saline water in fractures limits the effectiveness of radar due to the significant attenuation caused by the high electrical conductivity of saline water (Day-Lewis et al., 2004). As noted in R-11-14, this increased attenuation serves to reduce the penetrating power of radar, making radar measurements less reliable for zones at greater distances from the tunnel where saturated by saline groundwater.

Thus, radar and seismic reflection methods may be capable of detecting water filled discriminating fractures, however the question becomes one of fracture/fluid characteristics and whether an unacceptable number of discriminating fractures will go undetected due to one of the limiting factors discussed above. Where a large natural fracture is identified through tunnel mapping and radar/seismic reflection is used to determine its length, the results are still questioned whether the full length of the fracture can be reliably resolved, or again, due to the limitations of these techniques, whether only part of the fracture length might be detected misrepresenting its total length.

Projecting ahead to the coming decades, it is certain that computing power and inversion algorithms for processing geophysical data will continue to improve. However, this will still not counter limitations related to the fact that the measurements being made only indirectly identify the presence of a large natural fractures; verification would still be required to establish confidence. Issues of measurement noise, attenuation and subjectivity in the interpretation of geophysical results will likely continue. Instead, the necessary advances in the reliability of seismic and radar methods in the years to come, and robustness of the data interpretations, will likely not come from improved data processing (an area where much research and development is currently being focused by practitioners) but from the deployment of more sensing sources and receivers. Denser data sets are required. Cross-hole tomography between two boreholes only images a 2-D plane. What is needed is to utilize the full 3-D geometry of the repository with its different tunnels and deposition holes providing different sensing directions relative to the different orientations and spatial characteristics of any large natural fractures present.

### 11.5. Rock Damage, Fracturing and CDZ/EDZ

The terms CDZ (Construction Damage Zone) and EDZ (Excavation Damaged Zone) have been used to distinguish between damage to the rock around a tunnel or deposition hole caused by blasting and the redistribution of stresses, respectively. Within the latter,

spalling is an important mechanism as is the disturbance and dilation of existing natural fractures. The primary purpose for identifying and mapping the extent of rock damage around deposition holes is to assist in the determination of any developed and hydraulically connected CDZ/EDZ. Typical regulatory requirements regarding the CDZ/EDZ are strictest in the deposition tunnels, especially in the tunnel floor. This emphasizes the importance of distinguishing between CDZ and EDZ as they develop with different orientations relative to the tunnel excavation; stress-induced fractures within the EDZ will preferentially develop parallel to the excavation floor or walls (depending on the orientation of the principal stress field; whereas blast-induced fractures in the CDZ are generally radial relative to the tunnel boundary. Thus, each may introduce different degrees of connectivity and changes to the rock permeability with respect to how they intersect with each other as well as any natural fractures present (Eberhardt & Diederichs 2014).

### 11.5.1. Detection and Measurement Methods

Experiences in trying to measure the depth and transmissivity of the combined CDZ and EDZ include:

- Resistivity surveys using surfaced coupled current electrodes (Kruschwitz & Taramanci 2004; Lesparre et al. 2013).
- Ground penetrating radar (GPR) surveys in combination with tunnel mapping (Silvast & Wiljanen 2008, Heikkinen et al. 2010).
- High-frequency seismic and radar reflection and refraction surveys (Mustonen et al. 2010).
- Dye injection and trace mapping, such as that performed at the Äspö laboratory using wire-sawed slots cut into the tunnel walls (Ittner and Bouvin 2015).
- Cross-hole injection testing measuring pressures and flow across a series of short parallel boreholes, such as that carried out using packers to isolate specific zones beneath a tunnel floor at the Äspö laboratory. Geostatistical interpolation was then completed to analyse the transmissivity of the rock mass in the tunnel floor (Ericsson et al. 2015).
- Televiwer investigations or ultrasonic measurements of drill core to provide depth of damage data and other complementary information.

### 11.5.2. State of Practice and Other Considerations

High frequency GPR holds promise as a routine operational tool for tunnel-scale CDZ/EDZ depth determination and spatial distribution assessment. Resistive rock is optimal for GPR analysis because of its' relatively low attenuation. With this methods fractures can be detected to a depth of about 1 m (Ericsson et al., 2015). In their study, Ericsson et al. (2015) combined GPR with hydraulic testing of short holes drilled into the tunnel floor and obtained encouraging results for determining the extent of CDZ/EDZ and the transmissivity of different zones.

However, GPR has significant limitations for detection of more distal fractures. Resistivity surveying can be combined to detect EDZ depth with some confidence although the results may be unreliable if the water content within the EDZ varies. There are challenges with effective and repeatable data collection due to coupling issues. Seismic refraction can detect EDZ but is not an operationally practical tool. Seismic reflection cannot detect the damaged/undamaged rock transition.



In certain lithologies, specifically clay shales, electrical methods have been shown to be successful in detecting EDZ/CDZ in both air filled and water filled meso-fractures (Kruschwitz & Yaramanci 2004, Suzuki et al. 2004, Lesparre et al. 2013). These methods do not “see” individual fractures but rather a cumulative change in electrical properties due to the increased density of micro/meso fractures.

### 11.5.3. Feasibility and Reliability

If water is present within the fractures, then GPR and direct resistivity surveying have a greater chance of successfully delimiting the CDZ/EDZ. Coupling is an issue for resistivity although this is a practical issue than can be resolved with experimentation. While resistivity is a very promising tool in this regard, resistivity surveying at this scale does require a significant preparation logistics and may not serve well as a routine operational tool.

GPR is the most practical tool to date as systems have been developed based on similar applications such as masonry quality control, pavement analysis, etc. The difficulties lie in rigorous processing and filtering to obtain accurate data. Heikkinen et al. (2010) provide updated information on the potential of GPR for CDZ/EDZ detection. There are many physical issues and challenges with resistivity and GPR in detecting fractures of different sizes in dry and wet crystalline rocks. This includes the reduction of penetration range when water is present or when conductive mineralogy is present. There is also an issue of limiting resolution with lower penetrative frequencies. The frequency surveying used for tunnel wall CDZ/EDZ detection does show promise for detection of damage where the depth is limited to less than one or two metres in these conditions.

Seismic refraction is an effective tool for detecting the transition from damaged to undamaged rock based on density increase, but is logistically challenging as an operational tool. This method again depends on a cumulative change in density and acoustic velocity such that refraction can occur at the boundary of the damaged zone. Cabrera et al. (1999) showed promising but inconclusive success in defining CDZ/EDZ with useful reliability. This mixed success is likely due to the gradual nature of CDZ/EDZ dissipation and the lack of a sharp refraction boundary between damaged and undamaged rock.

The results of the work at Äspö laboratory are encouraging and suggest a new technique for this verification work (i.e. combining non-invasive GPR with invasive hydraulic testing in short boreholes in the deposition hole floor). However, calibration and refinement of the resolution and accuracy of this method is cited as requiring on-going development.

## 11.6. Excavation Displacements

### 11.6.1. Detection and Measurement Methods

Measurement of excavation-induced displacements include techniques that are invasive and non-invasive, with a key differentiating factor being the measurement of the distribution of displacements with depth into the rock mass versus those that only give the cumulative displacement at surface.

To measure the depth of displacements around a tunnel excavation, multi-point borehole extensometers (MPBX) are the most common and reliable tool used. These are usually

comprised of up to 8 measurement points along a borehole with a measurement range of between 25 to 100mm and a sensitivity of between 0.01 and 0.1mm. Automatic measurements are used to monitor the changing distances between each fixed point as a function of time. These can be employed in the walls, floor and roof of an excavation to monitor any changes in displacement caused by the advance of a tunnel excavation or excavation of an adjacent tunnel.

Non-invasive displacement monitoring includes the use of convergence monitoring. Convergence measurements are made between two or more fixed points around the excavation perimeter, with repeat measurements used to determine rates of convergence, changes in rate and total convergence values. Instruments are simple, inexpensive and robust (and therefore reliable), with accuracies of 0.1 mm over a 10 m span. Manual measurements involve using tape extensometers. Automatic measurements involve the use of tunnel profile monitoring systems, which are comprised of a series of linked rods fixed to the tunnel wall to monitor displacement; each rod has a high accuracy displacement meter and a tilt meter which record changes in tilt and displacement. Advanced systems include ShapeAccelArray (SAA), which use MEMS accelerometers housed within rigid segments to measure 3-D tilt (Abdoun & Bennett 2008), and Smart Rods, which use fiber-optics to measure displacements and deformations across fixed positions around the circumference of the tunnel (Metje et al. 2006).

However, the most recent advances in excavation displacement monitoring involve the use of remote sensing techniques like Terrestrial Laser Scanning (TLS), also known as LiDAR, in combination with change detection software. TLS systems can acquire the 3D coordinates of millions of points at very high resolutions and speed using laser ranging LiDAR. Change detection algorithms are then used to align and compare point clouds captured at different time intervals to calculate and display the relative deformations that occurred between consecutive tunnel scans. The limitation of using TLS, especially in stronger crystalline rock where excavation-induced displacements might be quite small is that the detection accuracies reported are often around 1-2 mm (e.g., Sanpei & Mizoguchi 2018).

New developments in the horizon include the use of high-accuracy and high resolution radar monitoring technology adapted for use in underground tunnelling. Early systems can fit in narrow spaces typical of underground operations and have ranges of up to 200 m, providing a spatial resolution of centimetres with sub-millimetre accuracy and updated displacement information every 30 seconds (GroundProbe 2017, IDS GeoRadar 2017).

Lastly, at a large scale, rock mass deformations related to tunnel/shaft excavation have also been measured using a high-resolution seismic network (Berglund and Lindborg, 2018).

## **11.7. Temperature**

The thermal properties of the bedrock represent a key design input in determining the spacing between repository deposition holes to ensure that maximum peak temperatures do not exceed the design thresholds for the clay buffer or levels that might result in significant rock spalling. The presence and spatial distribution of subordinate rock types with lower thermal conductive properties is of concern with respect to satisfying the maximum temperatures to be allowed between holes and in the buffer.

### 11.7.1. Detection and Measurement Methods

Ensuring that the thermal properties are determined correctly currently entails combining geological mapping with measurement techniques:

- Routine and continuous mapping in all underground openings.
- Mapping of rock lithologies by rock core logging and borehole photogrammetry.
- Measuring the thermal properties of rock in the laboratory.

In addition, review of the scientific literature related to geophysical methods that provide direct determination of bedrock type or thermal conductivity measurements of bedrock on a scale equivalent to that of a deposition-tunnel or -hole are limited. Determination of thermal conductive properties of bedrock on a scale similar to that of a canister are generally limited to empirical relationships developed based on lab and/or in-situ measured properties such as density from gamma-gamma logging (Sundberg et al. 2009) and P-wave velocity (Khandelwal 2012; Ozkahraman et al. 2004). To date, other nuclear waste disposal facility projects have primarily utilized lab testing of cored rock samples to evaluate the thermal conductive properties of the host rock (Karasaki et al. 2007).

Kukkonen et al. (2007) reported on the development of a borehole logging device for determining rock thermal properties. Although the device was observed to be technically functional, a number of problems were encountered, especially when borehole water inflows were encountered, that required further development and improvement before the equipment could be recommended for use.

### 11.7.2. State of Practice and Other Considerations

Currently, borehole and tunnel mapping of encountered/exposed rock types is the primary means of characterizing subordinate rock types and providing information for routine updating of detailed-scale geological and thermal property models. In the future, yet-to-be developed in-situ thermal conductivity testing within the deposition tunnels and holes may be available. As of the issue date of SKB R-11-14, SKB were awaiting recommendations from a working group under the International Society of Rock Mechanics (ISRM) tasked with devising a methodology for determination of thermal properties. Guidelines have since been released specific to laboratory based measurements (Popov et al. 2016).

### 11.7.3. Feasibility and Reliability

Boreholes (pilot and probe) with investigation and tunnel mapping are currently the primary evaluation methods being used at Posiva in Finland (Paulamäki et al. 2011). Considering this represents the state of practice, this would be considered the most applicable and currently reliable method for evaluating subordinate rock types. However, the following items are recommended for consideration.

- 1) Site characterisation programmes should include additional consideration of reported studies for empirical estimation of thermal conductivity of encountered bedrock based on density and P-wave velocities obtained by geophysical borehole logging methods and/or lab testing.
- 2) Kriging techniques should be investigated to estimate the rock thermal properties using the properties mapped along the floor of the deposition

tunnel and, when available, along pilot holes for the deposition holes, assuming there is a correlation between thermal properties in adjacent positions in the rock.

- 3) Future research and development by SKB, Posiva and the ISRM of an in-situ test methodology for evaluating the thermal properties of bedrock (on a relevant measurement scale of 3 to 5 meters) should be closely monitored and supported.

## **11.8. Water Inflows, Fracture Transmissivity and Rock Permeability**

The detection of critical, conductive fractures intersecting deposition hole positions is critical for ensuring the long-term safety of a nuclear waste repository. Conductive fractures pose the risk of allowing high water inflows into a deposition hole that may lead to piping and erosion of the clay buffer material thus threatening its long-term integrity. Application of the Extended Full Perimeter Criterion (EFPC) is one of the planned strategies for protection against buffer erosion and canister corrosion failures. It is likely that a subset of critical fractures identified by the EFPC are also hydraulically active, display previous shear displacements, or have large apertures to help make identification during mapping easier if only a small trace of the fracture is exposed (SKB TR-10-21).

Therefore, a framework program for detailed characterization is required to identify the potential for water inflows into deposition holes.

### **11.8.1. Detection and Measurement Methods**

Hydraulic properties are first estimated during feasibility studies from surface-based drilling and instrumentation. Large-scale pumping tests may be employed during these early investigations to establish regional subsurface permeability. Small-scale laboratory testing of intact rock cores sampled from the borehole drilling is also possible (ASTM 2016).

During construction and operation, there are several methods to measure water inflow, fracture transmissivity and rock permeability:

- Using pilot holes to document water-bearing fractures, measure inflows and sample groundwater for chemical analysis.
- Measuring overall water inflows into specific deposition tunnels and different parts of the repository through weirs and by measuring the pumped-out volume of groundwater.
- Using hydraulic interference tests in combination with geophysical surveys (mainly electrical resistivity) to define cross-hole hydraulic responses to injection pressures relative to mapped fracture locations to detect and characterize important water-bearing and/or conductive fractures.
- Pilot boreholes can be packed-off and instrumented to measure pressure responses when new holes are drilled.

The section on “Natural Fractures” discusses additional methods of EFPC detection which apply to large-scale fractures with high transmissivity.

### 11.8.2. State of Practice and Other Considerations

Many high flow fractures intersecting a deposition hole will likely be screened out by the application of the EFPC. This is based on the frequently observed correlation between fracture size and transmissivity such that the application of the EFPC would significantly reduce the number of high Darcy flux deposition holes (SKB TR-11-01).

### 11.8.3. Feasibility and Reliability

Although a subset of fractures identified by the EFPC would likely be hydraulically active, direct measurement of deposition-tunnel and -hole inflows is required to verify conformance with the relevant Design Premises. Any monitoring and assessment of deposition tunnel/hole inflows need to also consider the potential for changing flow conditions. Performance assurance measures should be developed to ensure that deposition holes initially assessed as being acceptable do not afterwards experience high inflows due to a change in the connectivity of the fractures intersecting the deposition hole, for example through the development of a high permeability EDZ/spalling zone in the deposition tunnel floor that serves as a conduit.

Since the goal of identification of highly permeable fractures is to maintain the integrity of the buffer material, it would appear that invasive methods including drilling within deposition hole walls would be the least favourable method of identifying large-scale structural features. Tunnel mapping and drilling of pilot and probe holes are considered non-invasive because of the subsequent excavations along the drilled hole. Geophysical studies for the identification and characterization of fractures is questionable. See the previous discussions for the section on “Natural Fractures”.

Eberhardt & Diederichs (2012) also raised concerns regarding how Design Premises based on allowable transmissivities or hydraulic conductivities associated with the CDZ/EDZ will be measured and verified. Direct measurement would be difficult without invasive/undesirable techniques given that the enhanced permeability will be aligned parallel to the boundaries of the deposition-tunnels and -holes. SKB R-11-14 makes reference to seismic and radar reflection as a possibility, however this would require reliable correlations to be established between hydraulic conductivity and seismic/radar output. As stated in SR-Site, a method to inspect EDZ as well as a demonstration of the reliability of the method is still needed (SKB TR-11-01). This need is emphasized in the feedback to the Design Premise on controlling EDZ (SKB TR-11-01), stating that transmissivities above the threshold value will start to affect risk.

## 11.9. References

- Abdoun, T. & Bennett, V., 2008. A new wireless MEMS-based system for real time-deformation monitoring. *Geotechnical News* 26(1): 36–40.
- ASTM International, 2016. Test Standard D5084-16a Standard test method for measurement of hydraulic conductivity of saturated porous materials using a flexible wall permeameter.
- Backblom, C. & Almen, K-E., 2004. Monitoring during the stepwise implementation of the Swedish deep repository for spent fuel. SKB R-04-13.
- Cabrera, J., Volant, P., Baker, C., Pettitt, W.S. & Young, R.P., 1999. Structural and geophysical investigations in the EDZ (Excavation Disturbed Zone) in indurated argillaceous media: The tunnel and the galleries of the IPSN Tournemire site, France. In

*Proceedings 37th US Rock Mechanics Symposium, Vail*. A.A. Balkema, vol. 2, pp. 957-964.

Carbonell, R, Perez-Estaun, A, Missana, T., Suso, J., Carretero, G., Bueno, J., Martinez, L, Buil, B., Garralon, A., Gomez, P. & Hernan, P., 2006. Geology and geophysics of new boreholes at the FEBEX site. *2<sup>nd</sup> Annual Workshop Proceedings 6<sup>th</sup> EC FP-FUNMIG IP, Stockholm*, pp. 307-314.

Day-Lewis, F.D, Lane, J.W. & Gorelick, S.M., 2004. Combined interpretation of radar, hydraulic, and tracer data from a fractured-rock aquifer near Mirror Lake, New Hampshire, USA. *Hydrogeology Journal* 14: 1-14.

Eberhardt, E. & Diederichs, M., 2012. Review of Engineering Geology and Rock Engineering aspects of the construction of a KBS-3 repository at the Forsmark site – Initial Review Phase. Technical Note, Swedish Radiation Safety Authority, Report: 2012:39.

Eberhardt, E. & Diederichs, M., 2014. Review of the Geological Mapping and Geophysical Measurement Techniques for the Determination of Critical Properties Around Deposition Holes – Main Review Phase. Technical Note, Swedish Radiation Safety Authority, Report: 2014:07.

Ericsson, J. T., Christiansson, T, L, Hansson, G., Burton, C., Sigurdsson, O. & Kinnbom, P., 2015. A demonstration project on controlling and verifying the excavation-damaged zone. Experience from Äspö Hard Rock Laboratory. SKB R-14-30.

GroundProbe, 2017. Introducing GML-Underground. GroundProbe Newsletter, October 2017.

Hakala, M., Siren, T., Ström, J., Valli, J., Hakala, V., Heine, J., Sireni, S., Kemppainen, K. & Savunen, J., 2016. In Situ Stress Measurements in ONKALO with LVDT – Cell. Posiva Report 2016-20.

Hakami, E., 2011. Rock stress orientation measurements using induced thermal spalling in slim boreholes. SKB R-11-12.

Heidbach, O., Rajabi, M., Reiter, K., Ziegler, M. & WSM Team, 2016. World Stress Map Database Release 2016. GFZ Data Services, doi:10.5880/WSM.2016.001.

Heikkinen, E. & Kantia, P., 2011. Suitability of ground penetrating radar for locating large fractures.

Heikkinen, E., Kantia, P., Lehtimäki, T., Silvast, M. & Wiljanen, B., 2010. EDZ assessments in various geological environments using GPR method. Posiva Oy, Olkiluoto, Finland, Working Report 2010-04.

IDS GeoRadar, 2017. HYDRA-U: Underground Safety Monitoring of Ground Fall Hazards. Product Brochure.

Ittner, H. & Bouvin, A., 2015. Undersökning av sprängsprickor från mekaniserad laddning med

bulkemulsion i bergtunnel. BeFo Report 144, Stiftelsen Bergteknisk forskning (Rock Engineering

Research Foundation), Sweden.

Karasaki, K., Apps, J., Doughty, C., Gwatney, H., Tiemi-Onishi, C., Trautz, R. & Tsang, C-F., 2007. Feature detection, characterization and confirmation methodology. Final

- Report, NUMO-LBNL Collaborative Research Project, Lawrence Berkeley National Laboratory. U.S. Department of Energy Contract DE-AC02-05CH11231.
- Kruschwitz, S. & Taramanci, U., 2004. Detection and characterization of the disturbed rock zone in claystone with the complex resistivity method. *Journal of Applied Geophysics* 57: 63-79.
- Lesparre, N., Gibert, D., Nicollin, F., Nussbaum, C. & Adler, A., 2013. Monitoring the excavation damaged zone by three-dimensional reconstruction of electrical resistivity. *Geophysics Journal International* 195(2): 972-984.
- Metje, N., Chapman, D.N., Rogers, C.D.F., Henderson, P. & Beth, M., 2006. Smart rod tunnel monitoring system. *Geotechnical News* 24(4): 46–49.
- Munier, R., 2010. Full perimeter intersection criteria Definitions and implementations in SR-Site. SRK TR-10-21.
- Mustonen, S., Norokallio, J., Mellanen, S., Lehtimäki, T. & Heikkinen, E., 2010. EDZ09 project and related EDZ studies in ONKALO 2008–2010. Posiva Oy, Eurajoki, Finland, Working Report 2010-27.
- Paulamäki, S., Paananen, M., Kuivamäki, A. & Wikström, L., 2011. Geological and geophysical investigations in the selection and characterization of the disposal site for high-level nuclear waste in Finland. *Geological Survey of Finland, Special Paper 4*: 131-144
- Karasaki, K., Apps, J., Doughty, C., Gwatney, H., Tiemi-Onishi, C., Trautz, R. & Tsang, C-F., 2007. Feature detection, characterization and confirmation methodology. Final Report, NUMO-LBNL Collaborative Research Project, Lawrence Berkeley National Laboratory. U.S. Department of Energy Contract DE-AC02-05CH11231.
- Kruschwitz, S. & Taramanci, U., 2004. Detection and characterization of the disturbed rock zone in claystone with the complex resistivity method. *Journal of Applied Geophysics* 57: 63-79.
- Kukkonen, I., Suppala, I., Korpisalo, A. & Koskinen, T., 2007. Drill hole logging device TER076 for determination of rock thermal properties. Posiva Oy, Olkiluoto, Finland, Working Report 2007-01.
- Paulamäki, S., Paananen, M., Kuivamäki, A. & Wikström, L., 2011. Geological and geophysical investigations in the selection and characterization of the disposal site for high-level nuclear waste in Finland. *Geological Survey of Finland, Special Paper 4*: 131-144.
- Popov, Y., Beardsmore, G., Clauser, C. & Roy, S., 2016. ISRM suggested methods for determining thermal properties of rocks from laboratory tests at atmospheric pressure. *Rock Mechanics and Rock Engineering* 49(10): 4179–4207.
- Sanpei, T. & Mizoguchi, T., 2018. Fundamental study for real-time detection of sudden displacement by high-speed laser scanner. *Journal of Structural Integrity and Maintenance* 3(4): 227-232
- Silvast, M. & Wiljanen, B., 2008. ONKALO EDZ-measurements using Ground Penetrating Radar (GPR) method. Posiva Oy, Eurajoki, Finland, Working Report 2008-58.

Sireni, S., 2011. Applicability of reflection seismic measurements in detailed  
2011-24.

Stephens, M.B., Fox, A., La Pointe, P., Simeonov, A., Isaksson, H., Hermanson, J. & Öhman, J., 2007. Geology Forsmark. Site descriptive modeling Forsmark stage 2.2. SKB R-07-45.

Sundberg, J., Back, P-E., Ericsson, L.O. & Wrafter, J., 2009. Estimation of thermal conductivity and its spatial variability in igneous rocks from in situ density logging. *International Journal of Rock Mechanics & Mining Sciences* 46: 1023-1028.

Suzuki, K., Nakata, E., Minami, M., Hibino, E., Tani, T., Sakakibara, J. & Yamada, N., 2004. Estimation of the zone of excavation disturbance around tunnels using resistivity and acoustic tomography. *Exploration Geophysics* 35: 62-69.

Svensk Kärnbränslehantering AB, 2008. Ramprogram för detaljundersökningar vid uppförande och drift av slutförvar för använt kärnbränsle. SKB R-10-08.

Svensk Kärnbränslehantering AB, 2010. Full perimeter intersection criteria: Definitions and implementations in SR-Site. SKB TR-10-21.

Svensk Kärnbränslehantering AB, 2011. Long-term safety for the final repository for spent nuclear fuel at Forsmark. Main report of the SR-Site project. SRK TR-11-01.

Svensk Kärnbränslehantering AB, 2012. Framework programme for detailed characterisation and inconnection with construction and operation of a final repository for spent nuclear fuel. SKB R-11-14.

Svensk Kärnbränslehantering AB, 2018. Detailed site investigation programme for the construction and operation of the Repository for spent nuclear fuel. SKB R-17-16.



## 12. Appendix 3 - WP 1: Reliability, Feasibility and Significance of Measurements of Conductivity and Transmissivity of the Rock Mass for the Understanding of the Evolution of a Repository of Radioactive Waste

Appendix B is based on an interim report and is included here for reference because it describes WP1. The general aim of WP 1 is to set-up simple, two-dimensional models of the TAS04 cross section with an isotropic and fractured representation of the rock mass in order to compare and benchmark the employed codes at an early stage of the project and to pinpoint upcoming challenges when considering more complex tunnel geometries, fracture networks, and material laws. Therefore, WP 1 has been split up into three activities. This section explains the aim of each activity and the used data and model definitions.

### 12.1. Aim of Activities

#### 12.1.1. Activity 1.1.1: Simulation of Isotropic Material

The purpose of the Activity 1.1.1 is to achieve an understanding of the results of the different simulations approaches when simulating isotropic materials. By direct comparison of results of simulations of similar models, the codes are verified against each other. From these analyses, also an understanding about the accuracy of simulation results is achieved. A second aim is to establish a common understanding of how to extract the numerically derived properties and convert them into measures comparable to the field data. To be able to accurately derive results for comparison to field or lab data, the result interpretation must be challenged and well understood.

The results were presented during the DECOVALEX-2019 (D-2019) Taiwan workshop on 29<sup>th</sup>/30<sup>th</sup> of November 2016.

#### 12.1.2. Activity 1.1.2: Definition of DFN for Rock Mass Simulation

Activity 1.1.2 is to define the fractures for Activity 1.1.3. This has been completed and delivered to the modelling groups via the internal file-sharing system along with the necessary data on 7<sup>th</sup> of February 2017. The work has been conducted by Joel Geier from Clearwater Hardrock Consulting.

#### 12.1.3. Activity 1.1.3: Simulation of Fractured Rock Mass

The purpose of this activity is to achieve an understanding of the results of the different simulations approaches when simulating fracture networks. By direct comparison of the results of simulations of similar models, the codes are verified against each other. From these analyses, an understanding about the accuracy of simulation results is also achieved. A second aim is to establish a common understanding of how to extract the numerically derived properties of fractured rock mass and convert them into measures comparable to the field data. To be able to accurately derive results for comparison to

field or laboratory data, the result interpretation must be challenged and well understood. The results were presented during the Stockholm workshop on 26<sup>th</sup> to 28<sup>th</sup> of April 2017.

## Acknowledgments

SKB performed the interference test in the TAS04 tunnel and is gratefully acknowledged for the quality of the data and providing the information for modelling the interference tests. The authors thank the Funding Organizations for their financial and technical support of the DECOVALEX project work described in this report. Seoul National University and geomecon GmbH received funding from SSM; Technical University of Liberec received funding from SURAO. The statements made in this report are solely those of the authors and do not necessarily reflect those of the Funding Organization(s). Also, no responsibility is assumed by the authors for any damage to property or persons as a result of operation or use of this publication and/or the information contained herein.

The report presents the results of work in progress that have not necessarily been subject to a comprehensive review. They are intended to provide rapid dissemination of current information.

## 12.2. Introduction

### 12.2.1. Purpose of this study

In the review of SKB's application for the construction, possession and operation of a final repository for spent nuclear fuel in Forsmark, Sweden (SKB, 2011), questions have been raised by SSM regarding the feasibility, relevance and reliability of in-situ measurements of hydraulic conductivity of the rock mass and transmissivity of the fractures at the time of closure of the repository (SSM Report 2018:07). Such measurements constitute the basis for the calculations of the evolution of the repository and for the analysis of the consequences of possible radionuclide releases a long time after closure. The questions are general and include how the measurements are affected during the operation of a final repository, and how representative they are for the time after the closure of the repository, after which measurements are not planned to be carried out according to the principle of "passive barriers" after closure in the Swedish Regulations.

### 12.2.2. The KBS-3 Method

The application for a final repository for spent nuclear fuel and associated radioactive waste in the form of structural materials in fuel elements at Forsmark was delivered to SSM on March 16th, 2011 (SKB, 2011). As a starting point for the reference layout of the repository, SKB has chosen the KBS-3 Method, a method for geological disposal, developed by SKB and Posiva through the Swedish nuclear industry's research, development and demonstration program in accordance with the Nuclear Activity Act. The KBS-3 Method also forms the basis of the encapsulation technology intended for use in encapsulation facility (Clink) to be located in another municipality.

The KBS-3 Method involves emplacing fuel elements into a load-bearing insert of cast iron. Each insert will be encapsulated in a copper canister, which acts as a corrosion-resistant layer preventing radionuclides from leaking out. After encapsulation, the canisters will be deposited approximately 470 m down in the bedrock at the chosen site

in Forsmark. In so-called deposition tunnels at repository depth, vertical deposition holes are drilled in which the canisters are emplaced. The canisters will be embedded in compacted bentonite clay that swells as it is resaturated with groundwater. The swollen bentonite clay will ensure that mass transport to and from the canisters can only be done via slow diffusion and that no significant microbial activity occurs in the bentonite; both of which will significantly retard any corrosion processes. Additional safety functions of the bentonite are to (from TR-11-01)

- limit advective transport,
- damp rock shear movements,
- resist transformations (requirement on temperature),
- prevent canister sinking,
- limit pressure on canister and rock.

After emplacement of bentonite and canisters, the repository tunnels are backfilled with bentonite clay. At the beginning of each tunnel, a sealing system of concrete plugs and various filters will be emplaced. The sealed repository should, without human intervention, contain spent nuclear fuel for a very long time (i.e. hundreds of thousands of years), which is the time required for the fuel to entail no greater risk from ionizing radiation than the natural uranium ore once used to produce the fuel. At the same time, the repository will retard the release of radionuclides that could potentially leak out for as long as possible, such that the human and environmental protection requirements in the Swedish Regulations can still be met.

The Swedish Regulations prescribe that a Safety Report should show how a nuclear facility is designed, constructed and operated in such way as to protect human health and the environment against radiological accidents (SSMFS 2008:1). Further provisions on safety reporting for nuclear waste disposal and nuclear waste can be found in the Swedish Regulations (SSMFS 2008:21 and 2008:37). It is apparent from the provisions in the Regulations that the safety report should reflect the facility as it was built, analyzed and verified as well as show how the requirements for its design, function, organization, operations and closure are met.

SKB has applied the provisions in the Regulations and demonstrated the safety of the repository for spent nuclear fuel. These provisions have in turn resulted in a series of requirements on all the technical and natural components (i.e. barriers) in the repository. The requirements applying to the rock mass in the near field of the excavations of a repository designed according to the KBS-3 method are summarized in Figure 55.

Based on the analyses in the Safety Report, SKB sets requirements (SKB 2009a and 2009b) limiting:

- The effective hydraulic transmissivity of the rock along the walls of the deposition positions (i.e. deposition holes),
- The hydraulic transmissivity of the natural fractures intercepting the deposition positions,
- The effective hydraulic transmissivity of the rock along the floor of the deposition tunnels,
- The water inflow into the deposition tunnels during operation and,
- The hydraulic conductivity of the rock mass around the tunnel of the access ramp to the repository.

### 12.2.3. The technical issues treated in this project

Through the project, SSM wants to assess the possibility of measuring a range of parameters during the construction and operation of the repository. These parameters include: the hydraulic permeability of rock; rock stress changes due to construction; deformations around an underground space where excavation damage zone (EDZ) or other cracking has occurred due to construction (e.g. drill-and-blasting); natural rock stresses (e.g. in-situ) and/or artificial heating from spent nuclear fuel. Insights into the differences between the rock mass state during operation and after closure of a final repository can be also obtained by means of the modelling results.

The development of EDZ around deposition tunnels and deposition holes has been a target of attention in the development of radioactive waste disposal concepts in crystalline rocks. The reason for aiming at understanding the formation of an EDZ is not primarily related to rock stability issues. More important for the long-term safety of the repository is the characteristics of the EDZ that changes the hydraulic properties of the rock mass in the vicinity of the excavations. Due to these changes, there is a potential for an increase in fluid-conductive pathways around the disposal canister and buffer. These induced pathways may act as transport channels for radionuclides away from the repository. As the EDZ may enhance the hydraulic conductivity between the excavations and the fractures in the rock mass, this could also impact on the radionuclide transport from the spent fuel locations to the biosphere, and on the resaturation timescales for the bentonite buffer.

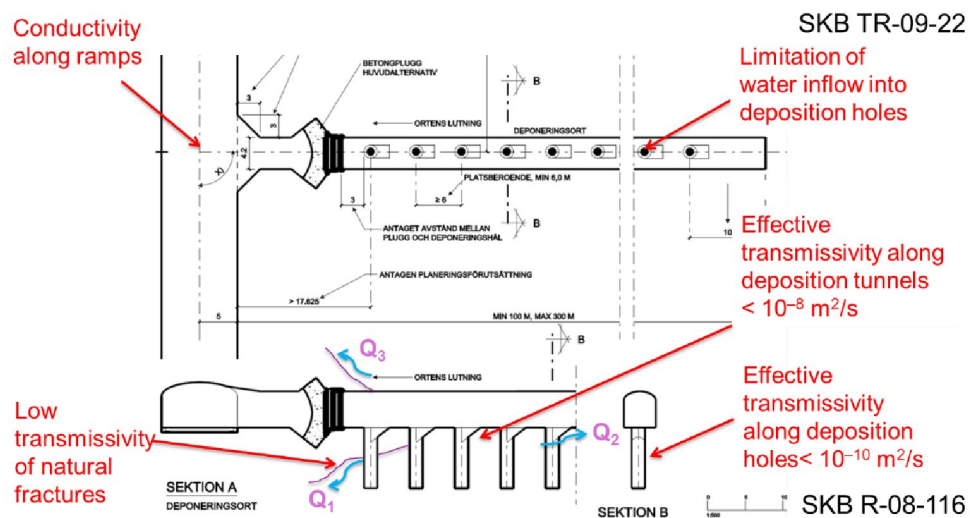


Figure 55. Summary of the requirements on the rock mass and rock fractures around an excavation for a KBS-3 repository of spent nuclear fuel presented in SKB's application for the Forsmark Site (SKB, 2011).

The formation of the EDZ and the associated change of rock mass hydraulic conductivity has been a continuous matter of research, not exclusive of, but prominently in former DECOVALEX tasks (Liu et al., 2011; Wang et al., 2011; Rutqvist et al., 2009a; Rutqvist et al., 2009b; Min et al., 2004; Min et al., 2009; Öhman et al., 2005; and many more). Within these studies, many aspects have been covered and among them the changes of boundary conditions affecting the formation and evolution of the EDZ have been analysed. However, the impact EDZ development have on a repository for radioactive waste, and in particular for spent nuclear fuel, on the have not been fully analysed and understood. Furthermore, it is unclear how to monitor and measure rock mass

conductivity and fracture transmissivity during the construction and operational phases in order to obtain a description of the initial conditions of a repository facility to be used for further analysis of its performance after closure. Other parameters, such as hydrogeological conditions and rock stresses are also important parameters for understanding the evolution of EDZ and have potential effects on the repository performance.

#### 12.2.4. Approach in this Project

In this research project, it is proposed to simulate the evolution of transmissivity throughout the lifetime of a repository for radioactive waste, and in particular a repository of spent nuclear fuel, in sparsely fractured and competent rock mass of crystalline type. For the simulations, the project takes advantage of the in-situ measurement of connectivity of the EDZ measured in relation to the experiment at the TAS 04 tunnel that the Swedish Nuclear Fuel and Waste Management Co. (SKB) has performed at Äspö, Sweden (Ericsson et al., 2014; Ittner et al., 2014). This set-up offered the opportunity to use very detailed field data from the construction phase, including characterization of the rock mass and the EDZ and also hydraulic interference tests under the floor of the tunnel. The field data constitutes a robust description of the initial state of a repository after excavation in the perspective of the uncertainties that arise several millennia after the emplacement of the spent fuel, backfilling and sealing (i.e. closure of the repository).

Over the course of the simulations, not only shall the change in hydraulic conductivity be studied and the best approaches to simulate the change be identified, but also strategies shall be developed about how to monitor significant parameters characterizing the conductivity change before closure of the repository. This is important to decide upon the fulfilment of the requirement on the excavation and hydraulic conductivity of its near field. The history of events simulated in the calculations shall include the construction phase of a repository with the excavation and its associated EDZ, the backfilling and sealing, the thermal phase, the following temperate phase and the glacial phase. Based on the numerical results, guidelines about what a control program and a monitoring system for a repository should include and be able to measure should be proposed and delivered to SSM. Furthermore, instructions about how their implementation can be done in practice should be obtained at the end of the research project. These guidelines and instructions should also consider the evolution of measuring techniques, data handling and scientific progresses that are expected to occur during the long operational life of a repository facility, stretching to up to a century.

The proposed research project will require benchmarking of the simulations against measured field data to validate the initial transmissivity of the rock mass, develop integrated concepts to be able to simulate the conditions of the EDZ and its evolution around the excavations, and related fracture transmissivity changes, and identify possible measurement concepts that reflect the lessons learned from the simulations.

In conclusion, this research project shall aim at answering the following questions:

- How experiences from construction and operation of a repository can be used to predict the response of the rock mass to future loading and pressure conditions
- How do the different steps of the evolution of the boundary conditions throughout the lifespan of a repository (i.e. before and after closure) affect the hydraulic conductivity and transmissivity?

- What will be meaningful measurements to assess the initial state of the repository and with what accuracy and precision will these measurements be provided?
- Will it be possible to design a monitoring system that provides measurement results that are meaningful to describe the performance of a repository after closure?

### 12.2.5. Expected outcome of this Project

The Project is expected to deliver the following results:

- Validation of suitability of the numerical models for simulation of the evolution of the rock in the vicinity of tunnels and holes.
- Analysis of representativeness and relevance of the conditions during construction and operations for the evolution of the repository after closure.
- Analysis of significance of the changes after closure with respect to the initial values and accuracy of the measuring methods.
- Indication of importance of sampling position for representative measurements. An opinion on the scope of systematic or selective measurements during construction and operation of the repository facility should be provided.
- Strategies to estimate and monitor the transmissivity and its change in the surrounding rock mass close to deposition excavations.
- Validation of feasibility of the measuring methods with respect to number of measurements, features to be measured and significance of the measurements for the long-term safety.

## 12.3. Definition of Work Package 1

We follow the geomechanical stress sign convention in which compression is positive. This includes both compressive stress and compressive strain. Dilation on the other hand is considered negative, again including stress and strain. Positive stresses and strains oriented normal to a surface are always compressive and inward directed, while negative stresses and strains are dilative and outward directed.

Displacements and flow vector components are defined to be positive if the direction coincides with the coordinate system and negative if they act in the negative coordinate direction. As the origin of the coordinate system is in the center of the tunnel, changes in the sign for displacement and fluid flow may occur. For example, an outward directed displacement of the tunnel wall might be positive for negative x-values and negative for positive x values.

Changes in pore pressure are considered positive in case of overpressure and negative in case of reduced pressure.

The coordinate system in the center of the model is used as a reference coordinate system for which results of interests can be created. For example, the heave of the tunnel floor is given as a diagram with the ordinate ranging from -2.1 m to 2.1 m and the abscissa showing the movement of the tunnel wall with respect to the initial tunnel wall coordinate at -1.8 m (see Figure 56).

### 12.3.1. Simulation of Isotropic Material

The following section describes the definition of the Activity 1.1.1.

#### 12.3.1.1. Geometry

The geometry of the excavation is based on the S-Tunnel, where the TAS experiment was performed. The tunnel has a horseshoe shape and is excavated according to KBS-3 reference design in TR-10-16 (pp. 2, Fig. 2-1). The S-Tunnel has a height of 4.8 m and a width of 4.2 m, totaling a cross sectional area of 19 m<sup>2</sup>. The form can be approximated in the model by a geometry composed of a rectangle with its center at (0, 0), a height of 3.6 m and a width of 4.2 m plus an ellipse with its center at (0, 1.8), a width of 2.1 m (a-semi axis) and a height of 1.2 m (b-semi axis). The cross-sectional area based on the composed geometry is 19.07 m<sup>2</sup> and has a total perimeter of 16.68 m. The horse-shoe shaped tunnel is located within a square with its center at (0, 0) and a side length of 100 m. Figure 56 shows the total model (Figure 56a) and a magnified area around the tunnel (Figure 56b).

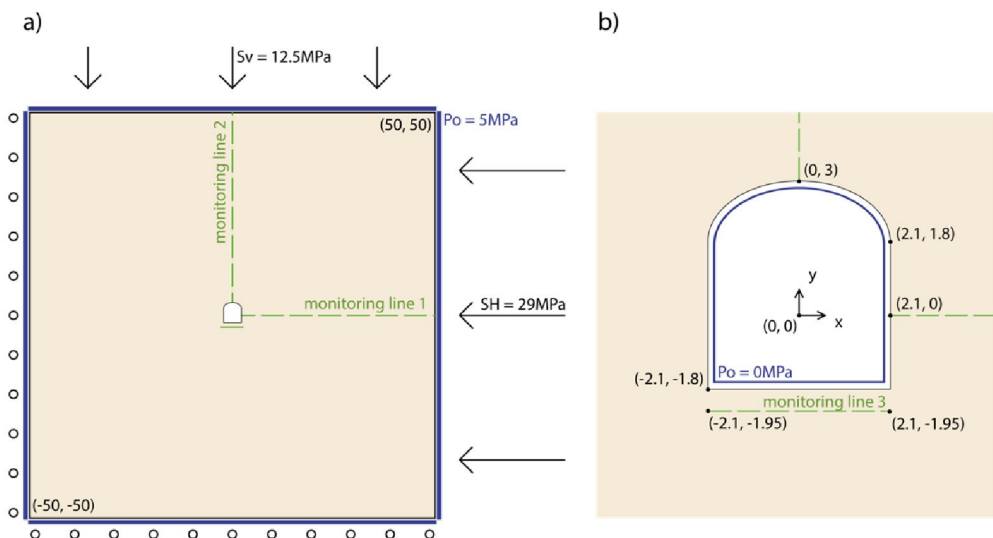


Figure 56. Model overview in cross section (a) and close-up (b).

#### 12.3.1.2. Constitutive Models and Input Parameters

The materials surrounding the tunnel are modelled as poroelastic. The according input parameters for the granite and water are given in Table 26 and Table 27, respectively. The rock mechanical parameters are from SKB (TR-14-30, Table 6-4), the hydraulic parameters from (TR-10-23, Table 4-5, and Figures 4.10/4.11), albeit the hydraulic data is from Forsmark.

**Table 26.** Petrophysical and geomechanical properties of the granite (isotropic and homogeneous parameters).

Rock Properties	Value	Unit
Young's modulus	76	GPa
Poisson's ratio	0.25	1
Dry Density	2.750	g/cm <sup>3</sup>
Porosity	0.01	%
Intrinsic permeability	5E-18	m <sup>2</sup>
Biot Coefficient	1	1

**Table 27.** Input parameters of the fluid.

Water Properties	Value	Unit
Dynamic viscosity	1E-03	Pa s
Compressibility	4.4e-10	Pa <sup>-1</sup>
Density	1000	kg/m <sup>3</sup>

### 12.3.1.3. Boundary Conditions

The domain boundaries are categorized for easier comparison into inner and outer boundaries. The latter comprise two horizontal and two vertical outer boundaries confining the model. The inner boundaries comprise the boundaries related to the tunnel. The tunnel is located at 450 m depth with the major horizontal stress orientated normal to the tunnel axis of 28-30 MPa (29 MPa). The minor and vertical stresses are close to the weight of the overburden with 12-13 MPa (12.5 MPa) (Ericsson et al. 2009). The boundary conditions are shown in Figure 56 and collected in the following list:

Hydraulic Boundary Conditions (HBC):

- outer boundaries: pore pressure boundary of 5 MPa
- inner boundaries: pore pressure boundary of 0 MPa

Mechanical Boundary Conditions (MBC):

- upper outer boundary: normal to boundary directed load of 12.5 MPa
- right outer boundary: normal to boundary directed load of 29 MPa
- lower outer boundary: roller boundary (only boundary parallel displacement allowed)
- left outer boundary: roller boundary (only boundary parallel displacement allowed)
- inner boundaries: boundary load of 0 MPa

### 12.3.1.4. Monitoring Lines

Three monitoring lines are included for comparison of the results of the modelling. Monitoring line 1 starts from the right side of the tunnel at (2.1, 0) and continues to the right outer boundary at (50, 0). Monitoring line 2 is located from the roof of the tunnel at (0,3) to the outer upper boundary (0, 50). Monitoring line 3 is located 15 cm below the tunnel floor from (-2.1, -1.95) to (2.1, -1.95). All monitoring lines are shown as dashed lines in Figure 56.



### 12.3.1.5. Results of Interest

A series of plots is created for intercomparison of the results of the different software packages and results by each modelling group. An example of a plot is given in Figure 57 showing the displacement in the x-direction along the complete tunnel wall. The data was delivered as a Microsoft Excel file in a format illustrated in Figure 58. The plots and data comprise:

- All Monitoring Lines showing the pore pressure in MPa, fluid velocity in the x- and y-direction (mm/h) as well as stresses (MPa) and strains (%) in the x- and y-directions.
- The tunnel wall is used as a scanline starting from the lower left corner in clockwise directions showing the pore pressure (MPa), fluid velocity in x- and y-direction (mm/h) as well as stresses (MPa) and strains (%) in the x- and y-direction.
- The heave of the tunnel floor is given as a diagram with the ordinate ranging from -2.1 to 2.1 and the abscissa showing the pore pressure (MPa), fluid velocity in the y-direction (mm/h) as well as stresses (MPa) and strains (%) in the y-direction with respect to the initial tunnel wall coordinate (-1.8).

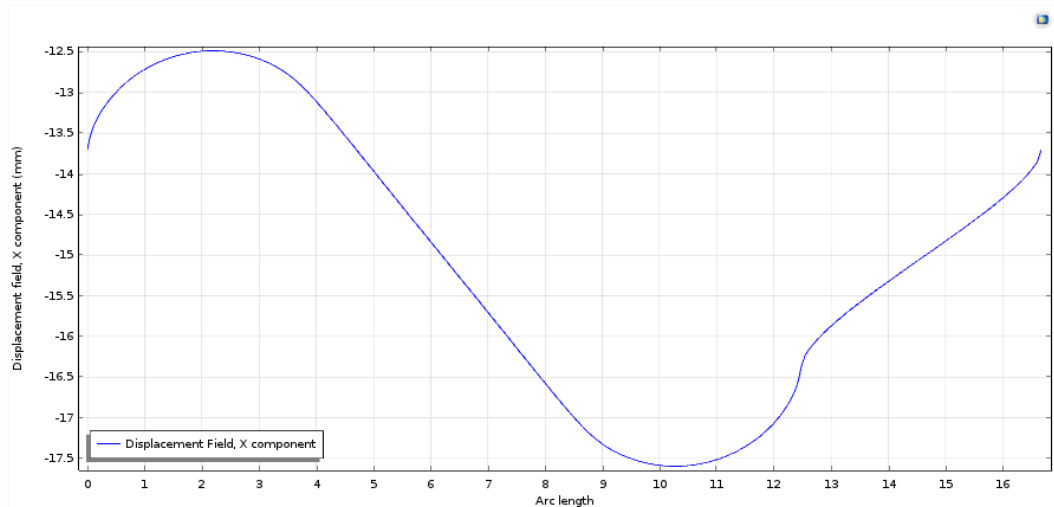


Figure 57. Example of the displacement in x direction along the tunnel wall starting at the lower left corner of the tunnel.

	A	B	C	D	E	F	G	H	I
1	Modelling Group:		geomecon						
2	WP:		1A						
3	Arc Length	Pressure	Fluid velocity in x	Fluid velocity in y	stress in x	stress in y	strain in x	strain in y	
4	m	MPa	mm/h	mm/h	MPa	MPa	%	%	
5	0								
6	0,1								
7	0,2								
8	0,3								
9	0,4								
10	0,5								
11	0,6								
12	0,7								
13	0,8								
14	0,9								
15	1								
16	...								
17									
18									
19									
20									

◀ ▶
Monitoring Line 1
Monitoring Line 2
Monitoring Line 3
Tunnel wall
Tunnel floor
+

Figure 58. Output format of the requested data.

### 12.3.2. Simulation of Fractured Rock Mass

The following section describes the definition of the Activity 1.1.3. The geometry and boundary conditions are similar to Activity 1.1.1. In addition, a discrete fracture network (DFN) had to be implemented in the models.

#### 12.3.2.1. Discrete Fracture Network

For ease of comparison with the subsequent work packages WP2 and WP3, an initial discrete fracture network (DFN) model for Activity 1.1.3 has been chosen based on the DFN statistical model that was developed for the rock in the Äspö Hard Rock Laboratory in the vicinity of the TAS04 experimental drift by the Äspö Task Force (Dershowitz et al., 2003; 2005). This model is used at this stage only for producing a 2D cross-section model based on a single 3D realization of the DFN statistical model. Figure 59 shows the DFN and the tunnel geometry.

The DFN was chosen such that very small acute angles are avoided, which might pose problems for gridding in finite-element models by using discrete distributions. Even though the chosen fracture network is not percolating, fluctuations in the pore pressure and stresses are assumed and stationary solutions are calculated. The fracture network was distributed in digital form in ASCII format.

Further information on the creation of the fracture network and the derived fracture flow parameters are given in the Appendix. One (realization t1DdP\_1\_NESW2dg) of the presented DFNs is used in this work package. The according fracture properties are given in table 28. **Fel! Hittar inte referenskälla..** Input parameters of the discrete fracture network.

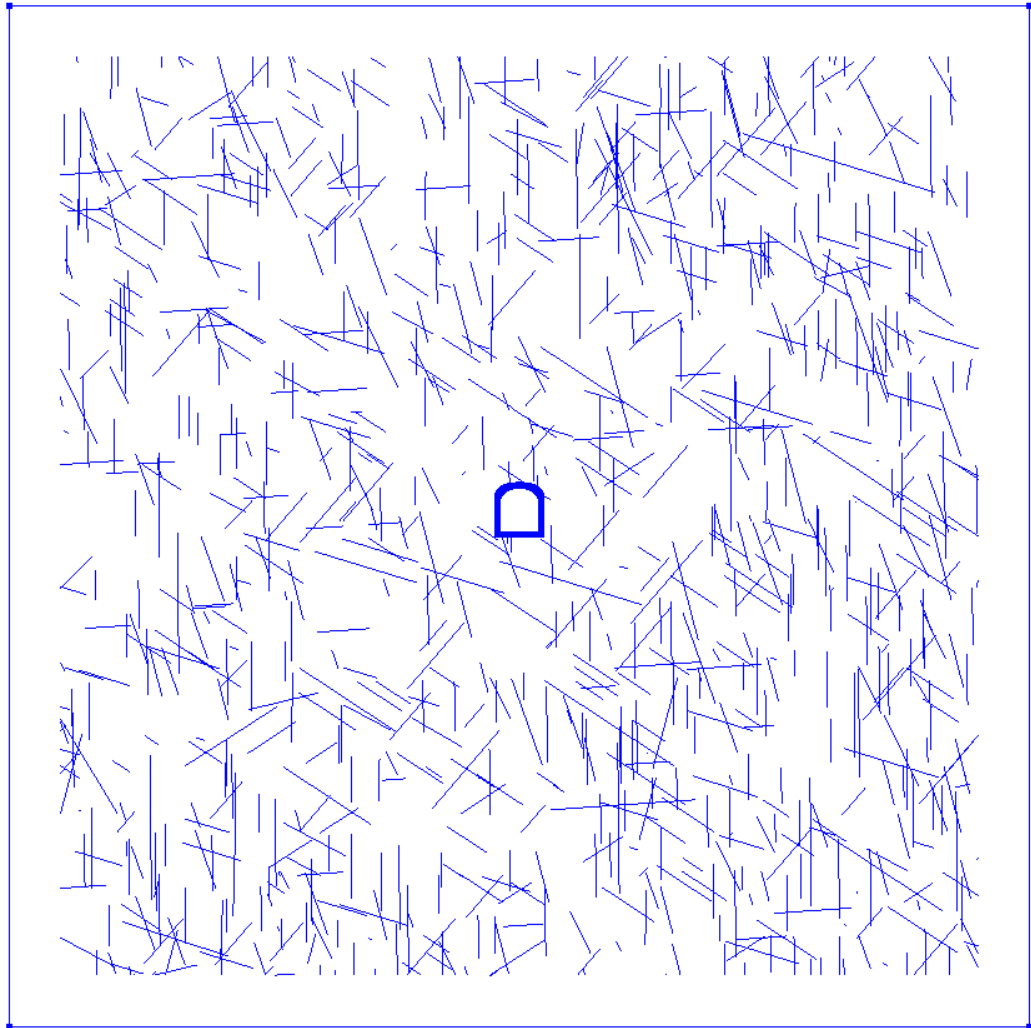


Figure 59. Fracture network t1DdP\_1\_NESW2dg.

### 12.3.2.2. Deterministic Fracture Network

A deterministic network of long fractures is added to increase the connectivity and achieve percolation to the effective boundaries at  $x, y = \pm 45$  m (see Figure 60). The according input parameters are given in **Table 28**.

**Table 28.** Input parameters of the deterministic fracture network.

Fracture Properties	Value	Unit
Permeability	2.8e-10	m <sup>2</sup>
Aperture	3e-5	m
Porosity	1	1
Storativity	3e-8	1
Transmissivity	5e-8	m <sup>2</sup> /s

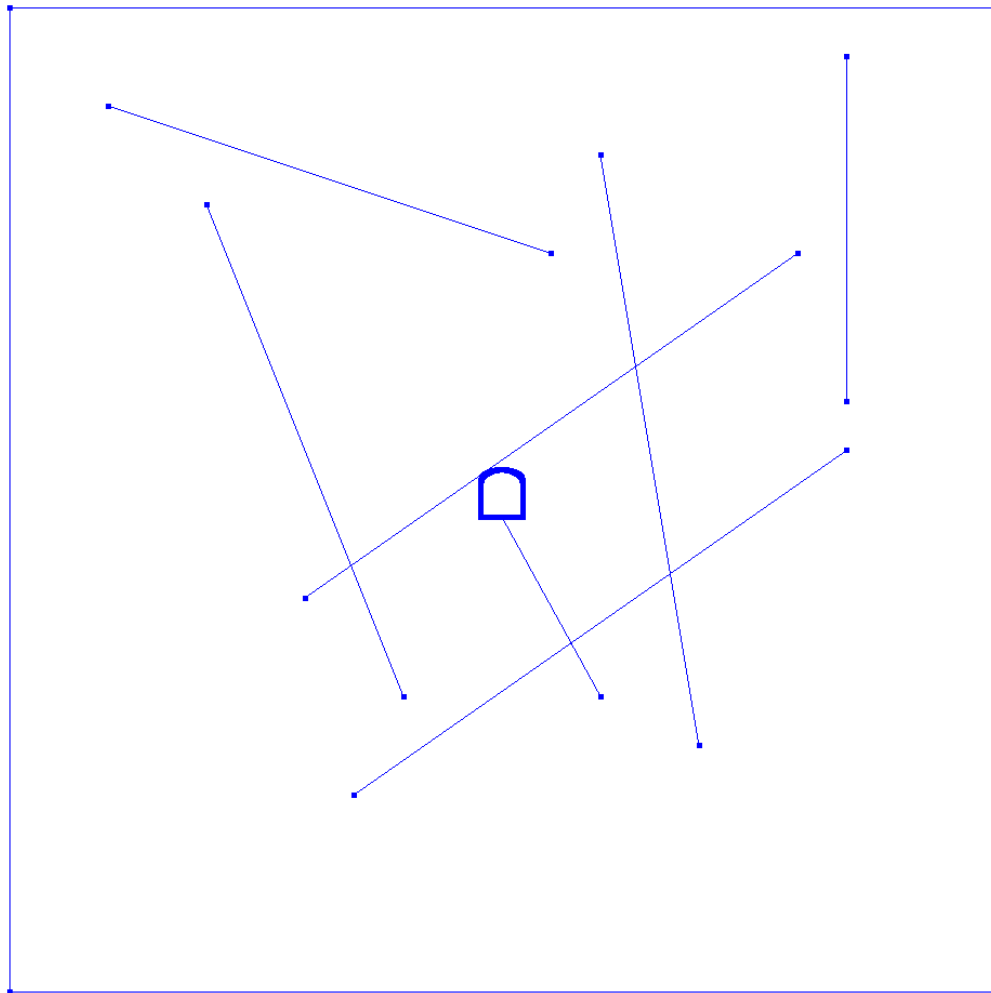


Figure 60. Deterministic fracture network.

### 12.3.2.3. Constitutive Models and Input Parameters

The material surrounding the tunnel was modelled as being poroelastic. The according input parameters for the fractured granite and water are given in **Table 26**, **Table 27**, **Table 28**, and **Table 29**, respectively. The rock mechanics parameters are from Ericsson et al. (2015, Table 6-4), the hydraulic parameters from (Hökmark et al., 2010, Table 4-5, and Figures 4.10/4.11) and the hydraulic data is from Forsmark.

#### 12.3.2.4. Validation Simulations

The simulations were performed as defined previously but in two variants: firstly, by simulating only the discrete fracture network (small fractures), and secondly, by simulating the discrete plus the deterministic fracture network (small and large fractures). The two fracture networks were distributed as two separate files (\*.prn) in ASCII format. The file named DFN.prn contained the information about the discrete fracture network while DTM.prn contained the information about the discrete fracture network. The fractures are separated by a semicolon “;” and each line consists of one coordinate pair (x, y) of one fracture. Hence, two lines encapsulated between two semicolons span a straight line, i.e. the fracture. Data are in the following format:

```
x1 y1
x2 y2
;
x3 y3
x4 y4
;
...
```

where (xi, yi) are the coordinates of the *i*th point.

### 12.4. Results

#### 12.4.1. Team geomecon (GMC) - roxol

Both activities (1.1.1 and 1.1.3) within work package 1 of Task G in DECOVALEX-2019 have been modeled with a software package based on the eXtended Finite Element Method (xFEM). In the following description, the software package roxol build 3965 is used. The simulations were conducted on a MacPro Late 2014 with 6 cores @ 3.50GHz (Intel® Xeon(R) CPU E5-1650 v2) and 32 GB RAM. The models have been built according to the Activity definition.

##### 12.4.1.1. Numerical Approach

The mechanical and hydraulic behavior of rock mass is governed by the fracture network. Fractures host the deformation and govern fluid flow. Therefore, it is a logical move to introduce a software that can simulate the evolution of the fracture network. roxol is developed to achieve this task. The software is built on the xFEM which is a numerical technique based on the generalized finite element method and the partition of unity method (PUM). It extends the classical finite element method (FEM) approach by enriching the solution space for solutions to differential equations with discontinuous functions ([https://en.wikipedia.org/wiki/Extended\\_finite\\_element\\_method](https://en.wikipedia.org/wiki/Extended_finite_element_method), 08.08.2017).

##### 12.4.1.2. Model Implementation including Discussion

The partial differential equations employed for modeling the activities in work package 1 links the interaction of fluid flow and deformation in a porous medium by means of

poroelasticity. The poroelastic coupling means that the pore fluid pressure affects the deformation in the porous medium. An influence of the deformation of the porous solid on the pore pressure is not achieved since we are considering stationary problems where the deformation of the solid due to pressure changes has ceased and is in equilibrium.

The following set of equations describe the hydro-mechanical coupling without considering gravitational effects on the solid or the fluid:

$$q = -\frac{k}{\mu}\nabla(p) \quad (1)$$

$$\sigma = C\varepsilon - \alpha pI \quad (2)$$

where  $q$  is the Darcy velocity (m/s),  $\alpha$  is the Biot coefficient (-),  $k$  is the intrinsic permeability (m<sup>2</sup>),  $\mu$  is the fluid dynamic viscosity,  $\sigma$  is the stress tensor (MPa),  $p$  is the pore pressure (MPa),  $C$  is the stiffness matrix,  $I$  is the identity matrix and  $\varepsilon$  is the strain (-).

Equation 1 is Darcy's law describing the flow of a fluid in the subsurface and equation 2 is the constitutive equation for the deformation of a solid influenced by the poroelastic pore pressure. It can be seen that the hydraulics influence the mechanics by the pore pressure in equation 2 while there is no influence of mechanics on hydraulics since we are dealing with stationary (no time-dependency) partial differential equations.

#### 12.4.1.3. Boundary Conditions

Since Activity 1.1.1 and 1.1.3 use the same boundary conditions, they will be described here for both activities. The fracture flow conditions are only applied in Activity 1.1.3 for the deterministic and discrete fracture networks.

##### Roller Boundaries

The bottom and left boundary are modeled as a roller boundary, which allows only edge parallel displacements and suppresses displacements in the normal direction. This is achieved by setting the displacement in the normal (Dirichlet boundary) direction for each boundary element zero. Figure 61 highlights the chosen boundaries.



Figure 61. Left and bottom boundaries are selected as roller boundaries.

### Load Boundaries

roxol allows to define static Neumann boundary conditions with stresses directed normal to the boundary as input.

$$S \cdot \mathbf{n} = F_A, F_A = -p \cdot \mathbf{n} \quad (3)$$

where  $\mathbf{n}$  is the vector normal to the boundary,  $S$  is the stress and  $p$  is the normal directed input pressure.

The upper and right boundary have been prescribed with a pressure of 12.5 MPa and 25 MPa, respectively. Figure 62 highlights the chosen boundaries.

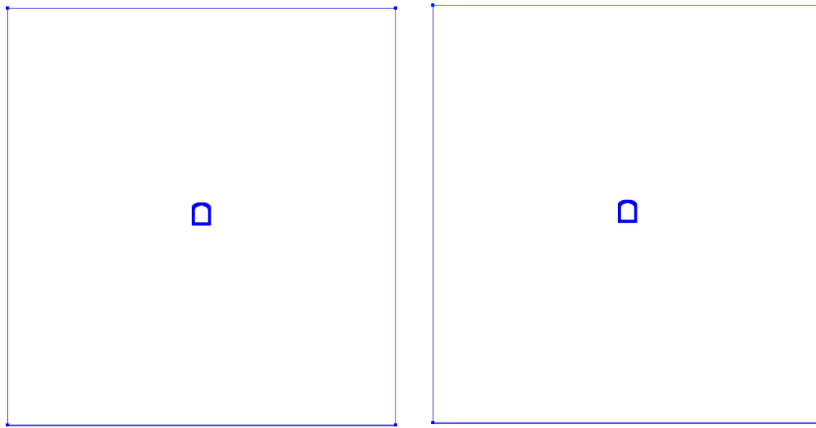


Figure 62. Right (12.5 MPa) and top (25 MPa) boundaries are selected as load boundaries.

### Pore Pressure Boundaries

The outer and inner boundary have been assigned with a fixed pore pressure of 5 MPa and 0 MPa, respectively. Since pressure is the variable to be solved for in the hydraulic sub-model, the pressure can be directly entered through a Dirichlet boundary

$$p = p_0 \quad (4)$$

where  $p_0$  is the input pore pressure.

Figure 63 highlights the chosen boundaries.

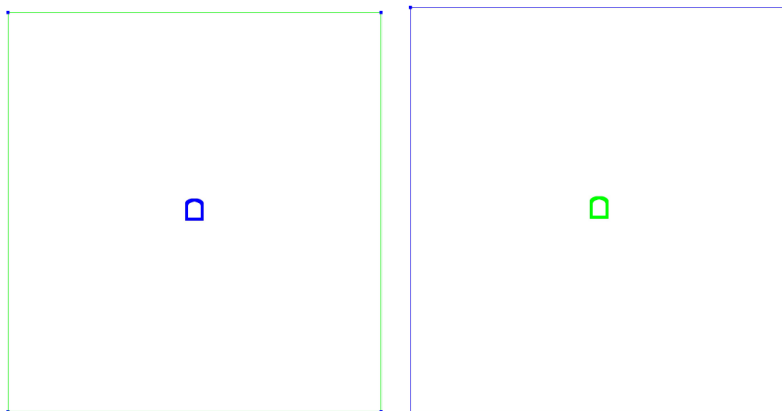


Figure 63. Outer (5 MPa) and inner (0 MPa) boundaries are selected as pore pressure boundaries.

## Fracture Flow

For Activity 1.1.3 a discrete and a deterministic fracture network has been loaded into roxol as shown in Figure 64. Each mesh element intersecting a fracture has been assigned higher fracture permeability and porosity values differing from the remaining domain as described in the work package definition. The fracture aperture is 100 mm since the mesh was generated out of 100 x 100 mm quadrilateral elements (see Discretization).

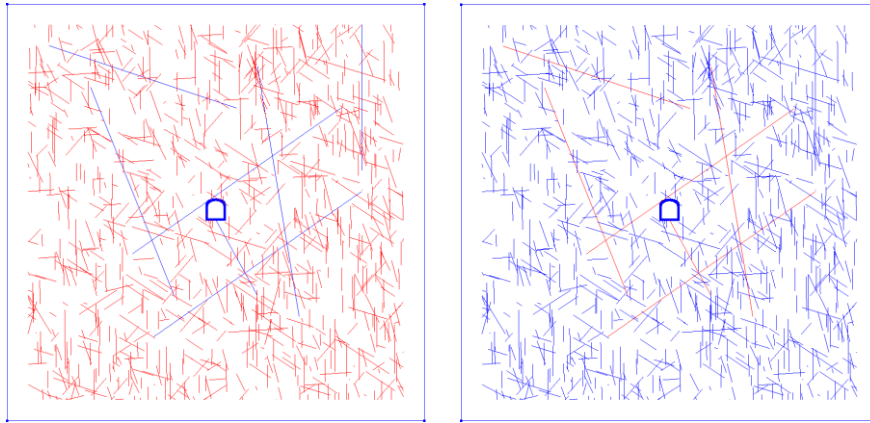


Figure 64. Discrete (left) and deterministic (right) fracture networks.

## Friction on discrete (DFN) and deterministic (DTM) fracture networks

For the DFN and DTM fractures a cohesion of 10 MPa and a friction coefficient of 0.6 have been assigned in order to minimize stress concentrations on the fracture tips and suppress sliding of fracture faces under the applied stress field. The inclusion of friction into the XFEM problem formulation amounts to adding a "friction load vector" term to the variational problem of the linear elasticity formulation, similar to the load vector term.

## Discretization

The models for Activity 1.1.1 and Activity 1.1.3 have been discretized differently due to the implementation of fracture networks in Activity 1.1.3. COMSOL Multiphysics has been used to generate 2d quadrilateral meshes for roxol.

For Activity 1.1.1 a mesh consisting of 226879 quadrilateral elements has been generated with an average element quality of 0.99. The mesh has been refined towards the tunnel as indicated in Figure 65 (left).

For Activity 1.1.3 a mesh consisting of 997244 quadrilateral elements has been generated with an average element quality of 0.99. The mesh has been triangulated in quads containing fractures. The quads are 100 x 100 mm in size.

The mesh qualities are very high and indicate that most of the quads are perfectly shaped (no distortion).



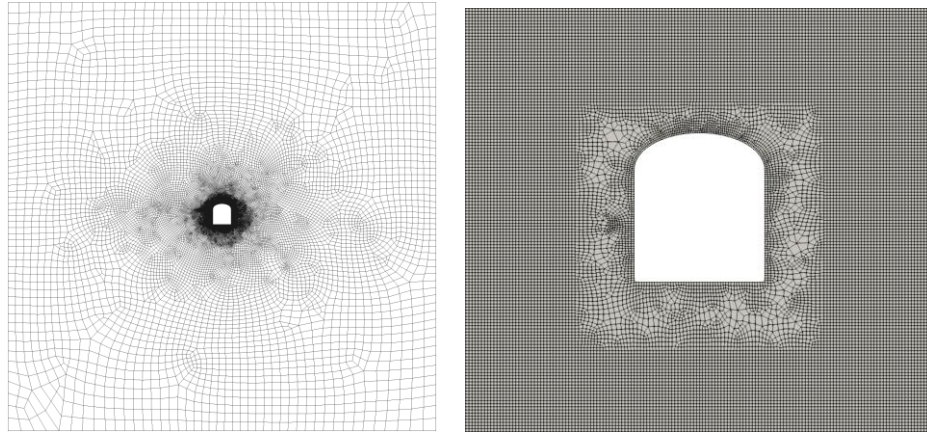


Figure 65. Meshes for Activity 1.1.1 (left) and close up of the mesh for Activity 1.1.3 (right).

### Study Settings

The solution was obtained by a segregated solver with domain composition using a shape function with linear discretization. The calculation time was about 210 s for Activity 1.1.1 and 620 s for Activity 1.1.3. The solution is obtained after 30 iterations.

### Disadvantages

As any numerical method, the FEM is only an approximation of the real situation. Model building and model assumptions cannot precisely reflect in-situ conditions. Furthermore, convergence studies with increasing mesh refinement need to be performed to evaluate the error between different mesh sizes. Furthermore, calculating the flow of a fluid along a fracture without considering the effective normal stress that potentially closes the fracture is not representing in situ conditions. It can furthermore be argued that a Biot coefficient of 1 is too high for the granite. However, these material parameters are beyond the scope of this work package.

### Advantages

The chosen software package contains a set of verified and tested partial differential equations for poroelasticity, which allows to evaluate the simulation results of such problems with confidence. Furthermore, the interface for setting up the model (geometry, material properties, boundary conditions, mesh, solver) is easy to use and thereby prevents users to make errors, e.g. selecting wrong boundaries, in particular with the fracture networks, inputting wrong units.

The basis of the numerical approach (FEM) that the software uses is well established in different working areas and belongs, in fact, to the most widely used numerical approaches.

#### 12.4.1.4. Simulation Results

In the following the numerical results are presented for Activity 1.1.1 (Figure 66 - Figure 70) and Activity 1.1.3 (Figure 71 - Figure 75) as requested by the work package definition for monitoring line 1-3, tunnel wall and tunnel floor.

##### Activity 1.1.1

Steady changes in fluid flow, pore pressure, strain and stresses are observed for the homogeneous poroelastic rock along the monitoring lines. All parameters follow the expected trends and converge towards the applied boundary conditions, e.g., stresses are altered in the vicinity of the tunnel, and pore pressure and fluid flow drop to zero at the tunnel wall.

For the tunnel wall, unsteady changes are observed in the corners of the tunnel, where the stresses are theoretically concentrated to infinity due to the linear elastic material behavior, which would be reduced by yielding of the material in a physical situation.

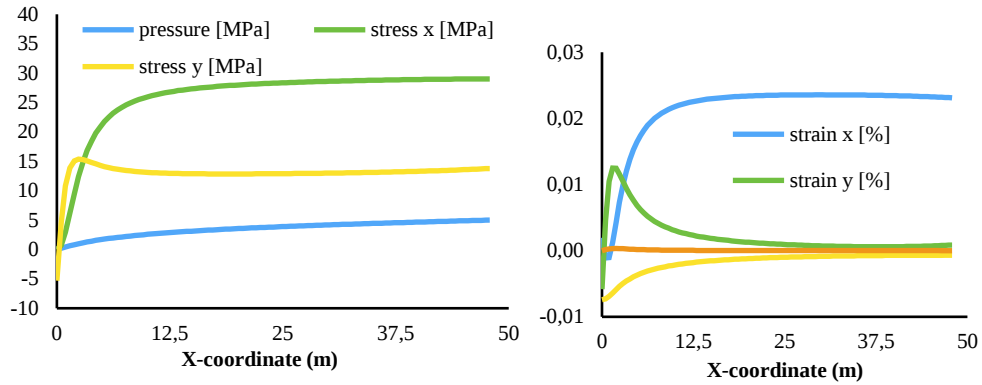


Figure 66. Monitoring Line 1 showing the (left) pore pressure and stresses as well as (right) fluid velocity and strains in x and y direction.

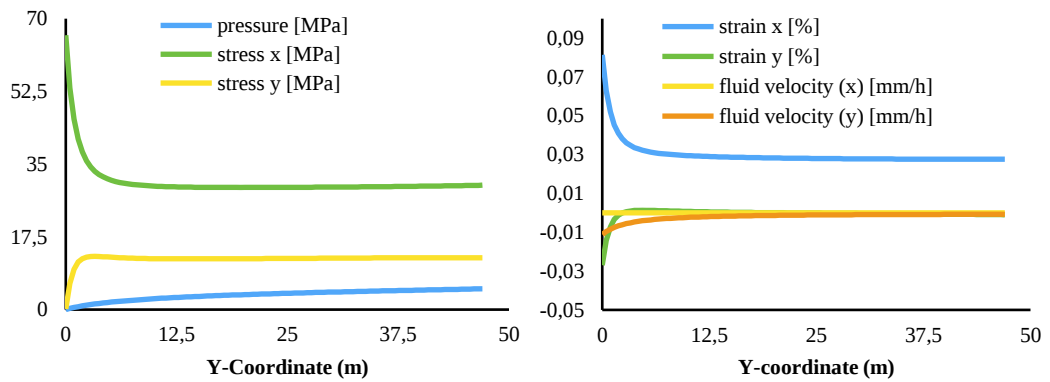


Figure 67. Monitoring Line 2 showing the (left) pore pressure and stresses as well as (right) fluid velocity and strains in x and y direction.

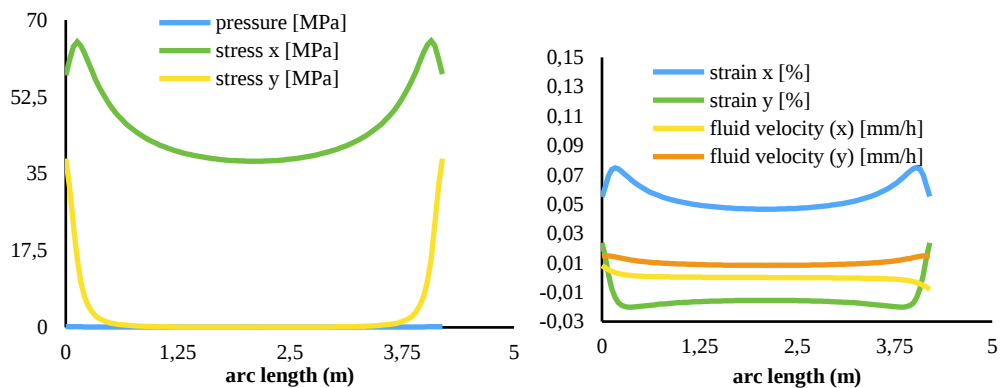


Figure 68. Monitoring Line 3 showing the (left) pore pressure and stresses as well as (right) fluid velocity and strains in x and y direction.

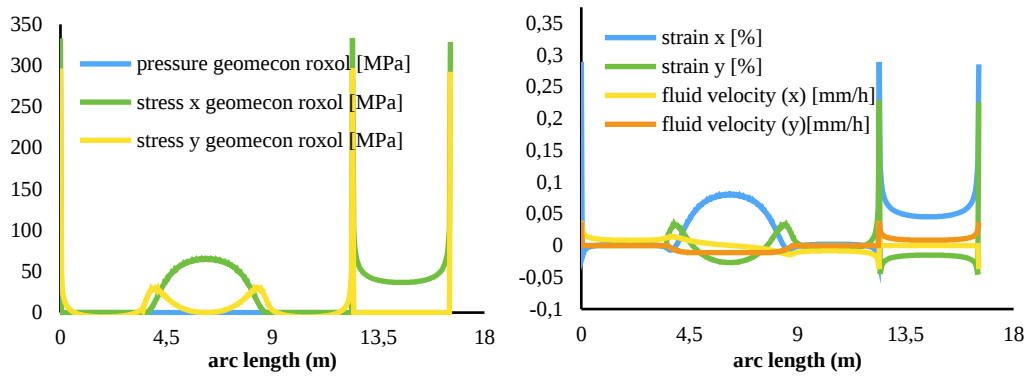


Figure 69. Tunnel wall showing the (left) pore pressure and stresses as well as (b) fluid velocity and strains in x and y direction

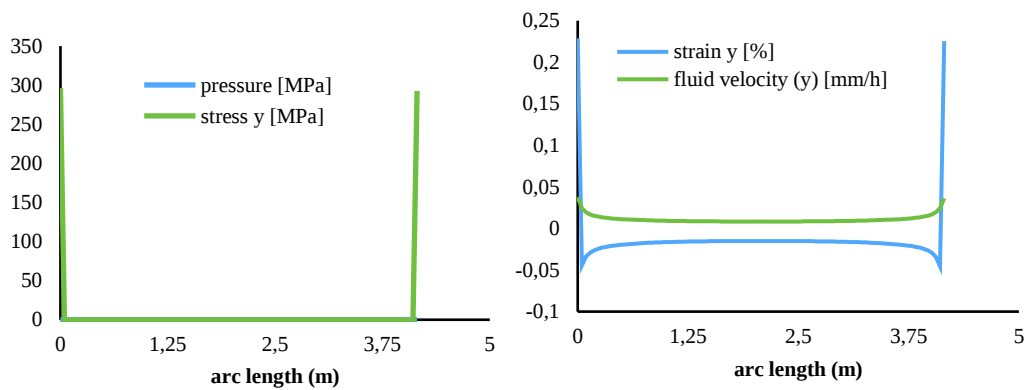


Figure 70. Tunnel floor showing the (left) pore pressure and stresses as well as (right) fluid velocity and strains in y direction.

### Activity 1.1.3

Large fluctuations in all parameters are observed for the highly fractured poroelastic rock along the monitoring lines. However, all parameters yield the applied boundary conditions. Due to the large fluctuations, trends are difficult to resolve.

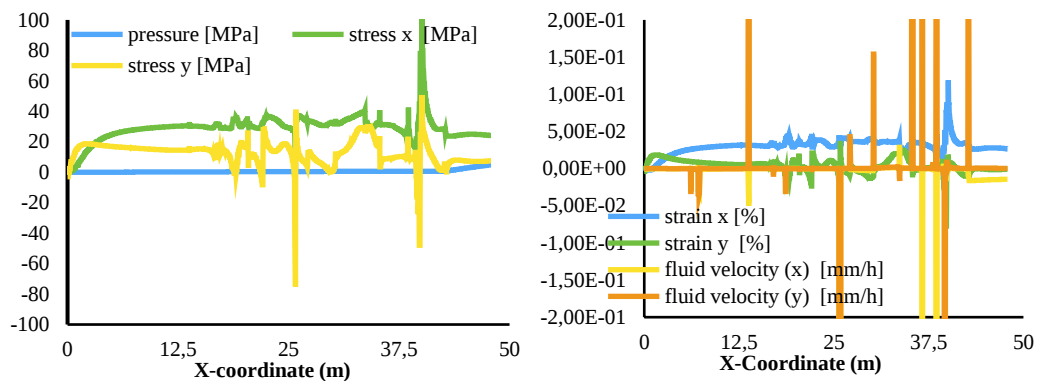


Figure 71. Monitoring Line 1 showing the (left) pore pressure and stresses as well as (right) fluid velocity and strains in x and y direction.

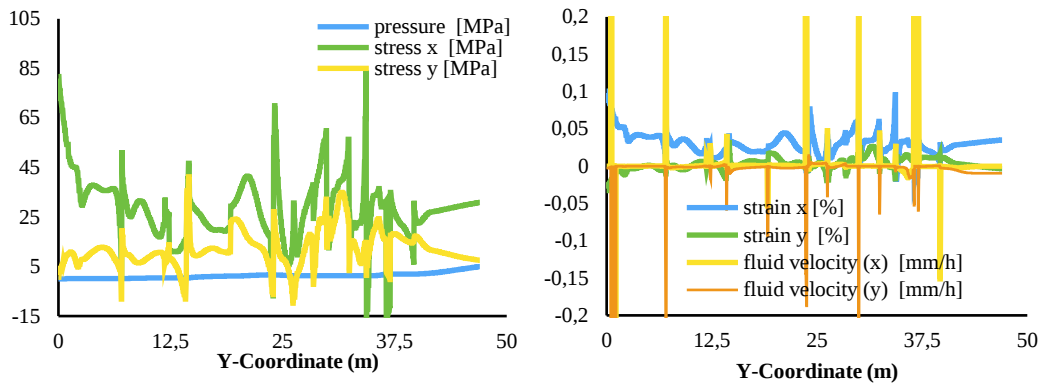


Figure 72. Monitoring Line 2 showing the (left) pore pressure and stresses as well as (right) fluid velocity and strains in x and y direction

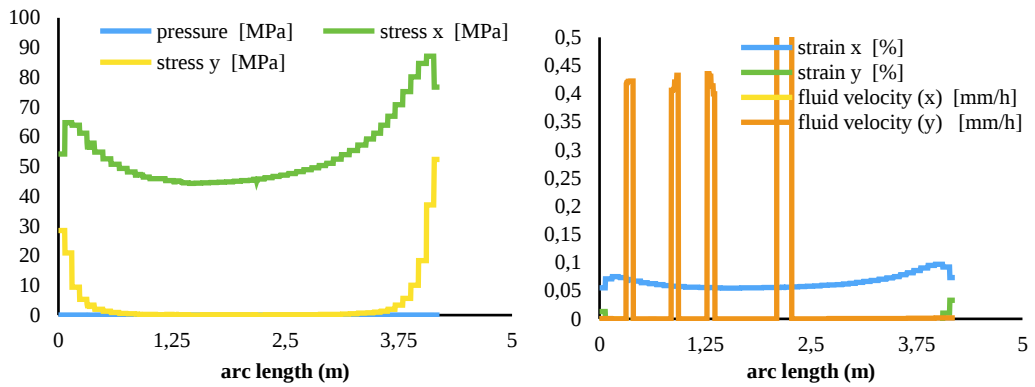


Figure 73. Monitoring Line 3 showing the (left) pore pressure and stresses as well as (right) fluid velocity and strains in x and y direction.

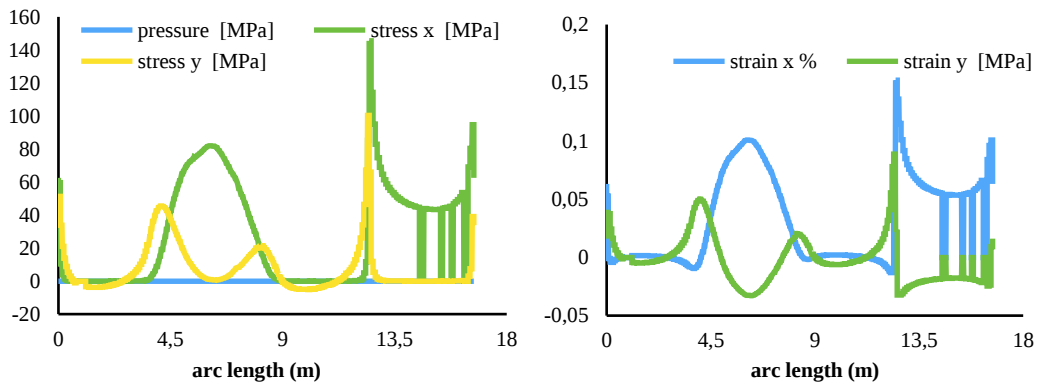


Figure 74. Tunnel wall showing the (left) pore pressure and stresses as well as (b) fluid velocity and strains in x and y direction

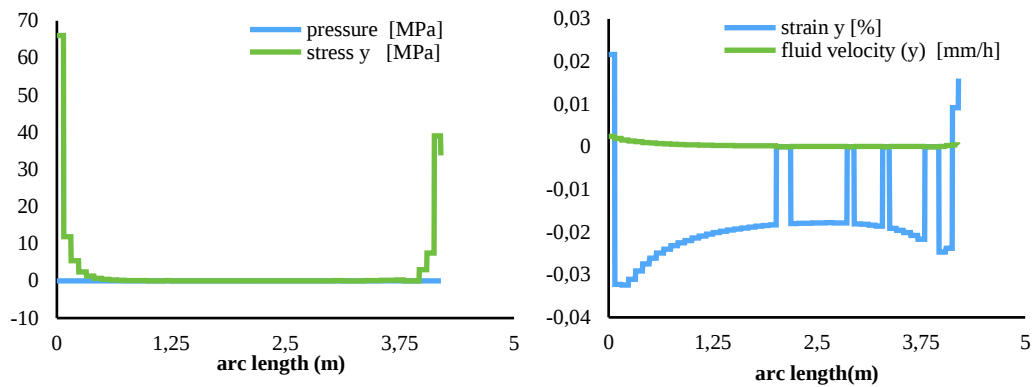


Figure 75. Tunnel floor showing the (left) pore pressure and stresses as well as (b) fluid velocity and strains in x and y direction.

### Discussion of Results

The current fracture flow realization is mesh size dependent and causes unwanted fracture connectivity and percolation if fractures end in close proximity to each other, i.e. in the same mesh cell. Furthermore, the fracture aperture can only be controlled by the fineness of the mesh. Figure 76 shows two intersecting fractures and the cells that belong to the fractures (red) having higher permeability and porosity values in comparison to the remaining rock (blue). Each quadrilateral cell has a width of 100 mm as used in the simulation, which is equivalent to the aperture of the fracture. Apertures in the range of 1 mm would require equivalent quadrilateral meshes and would cause longer calculation times. Due to these reasons, we observe higher pressure drawdown towards the tunnel and a likely unrealistic higher flow rate along fractures.

Furthermore, the fractures were modeled with contact and “low” friction. As a consequence, high strain and stress concentrations still occur at fracture tips. However, this is independent of the fracture and matrix hydraulic flow since both rely on the same partial differential equation which is independent of the deformation of the rock for stationary studies.

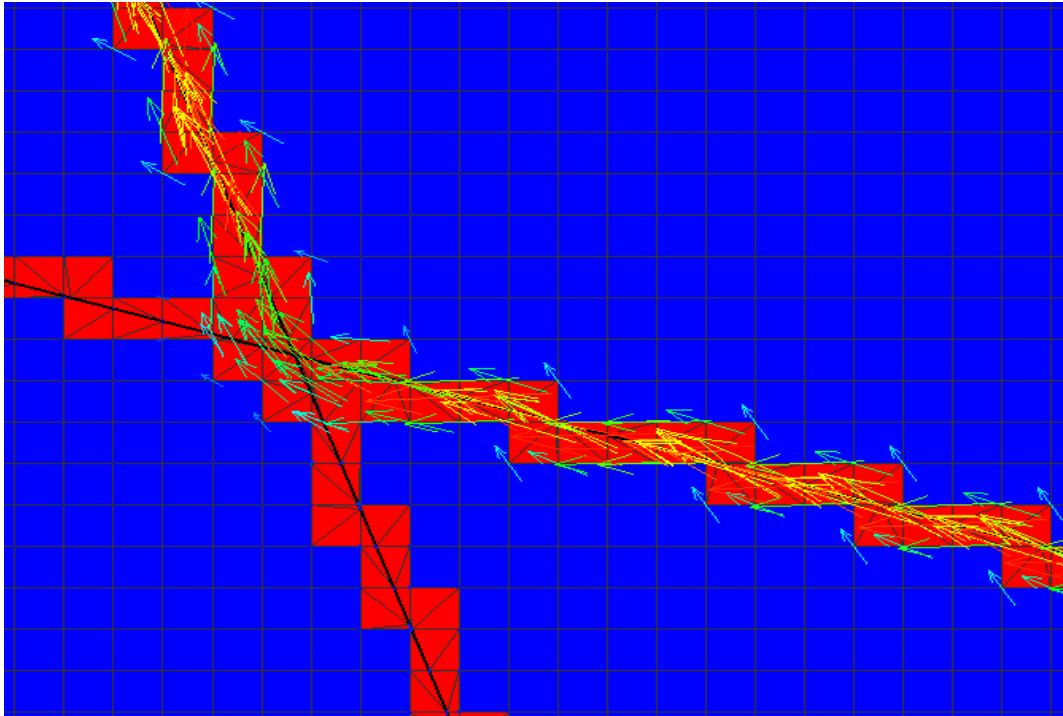


Figure 76. Two intersecting fractures with high fracture permeability (red). Fluid flow indicated by green arrows.

#### 12.4.2. Team geomecon (GMC) - COMSOL Multiphysics

The simulations were conducted using COMSOL Multiphysics (V) on a MacPro Late 2014 with 6 cores @ 3.50GHz (Intel® Xeon(R) CPU E5-1650 v2) and 32 GB RAM. The definition of the two activities were followed.

##### 12.4.2.1. Numerical Approach

The Finite Element Method (FEM) is a widely established numerical method for solving problems in engineering and mathematical physics. These problems are generally described by partial differential equations, which are derived from conservation laws of physics such as conservation of mass, energy or momentum. To solve the problem, it subdivides a large problem into smaller, simpler parts that are called finite elements. The simple equations that model these finite elements are then assembled into a larger system of equations that models the entire problem. FEM then uses variational methods from the calculus of variations to approximate a solution by minimizing an associated error function. The approximation is achieved by discretizing the partial differential equations which can then be solved with numerical methods. The solution calculated by any numerical method can therefore only approximate the real situation.

##### 12.4.2.2. Model Implementation and Discussion

The partial differential equations employed for modeling the activities in work package 1 links the interaction of fluid flow and deformation in a porous medium by means of poroelasticity. The poroelastic coupling means that the pore fluid affects the compressibility of the porous medium, as well as changes in volumetric strains will affect

the mass transport considering time-dependency (COMSOL Multiphysics Manual, Introduction to Subsurface Flow Module, p10).

The following set of equations describe the hydro-mechanical coupling for stationary problems considering gravity.

$$\nabla(\rho_f q) = Q \quad (5)$$

$$q = -\frac{k}{\mu} \nabla(p - \rho g z) \quad (6)$$

$$\sigma = C \varepsilon - \alpha p I \quad (7)$$

$$-\nabla \sigma = (\theta \rho_f + \rho_a) g \quad (8)$$

where  $\rho_f$  fluid density (kg/m<sup>3</sup>),  $Q$  source term (kg/s),  $e_{vol}$  volumetric strain (1),  $k$  permeability (m<sup>2</sup>),  $g$  acceleration due to gravity (m<sup>2</sup>/s),  $z$  height [m],  $\theta$  porosity (1),  $\rho_a$  grain density (kg/m<sup>3</sup>). Equation 6 is Darcy's law describing the flow of a fluid in the subsurface and equation 8 is the Navier equation for a solid under purely gravitational load. The first two equations constitute the hydraulic sub-model and the last two equations constitute the mechanical sub-model. It can be seen that the hydraulics influence the mechanics by the pore pressure in equation 7 while there is no influence of mechanics on hydraulics since we are dealing with stationary (no time-dependency) partial differential equations. For more information about poroelasticity in COMSOL Multiphysics, the reader is referred to the software manual.

### 12.4.2.3. Boundary Conditions

Since Activity 1.1.1 and 1.1.3 use the same boundary conditions, they will be described here for both activities. Fracture flow conditions are only applied in Activity 1.1.3 for the deterministic and discrete fracture networks.

#### Roller Boundaries

The bottom and left boundary are modeled as a roller boundary (Dirichlet boundaries), which allows only edge parallel displacements and suppresses displacements in normal direction. This is achieved by setting the displacement in normal direction for each boundary element zero.

$$\mathbf{n} \cdot \mathbf{u} = 0 \quad (9)$$

where  $\mathbf{n}$  is the vector normal to the boundary and  $\mathbf{u}$  is the displacement vector.

Figure 77 highlights the chosen boundaries.

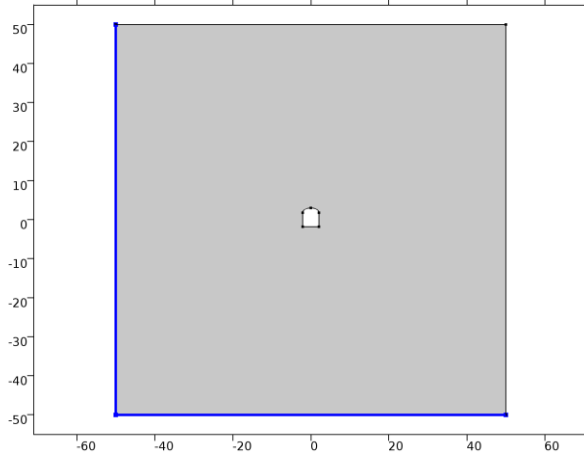


Figure 77. Left and bottom boundaries are selected as roller boundaries.

### Load Boundaries

COMSOL Multiphysics® allows to define Neumann boundary conditions with pressures directed normal to the boundary as input as defined in equation 3.

The upper and right boundary have been prescribed with a pressure of 12.5 MPa and 25 MPa, respectively. Figure 78 highlights the chosen boundaries.

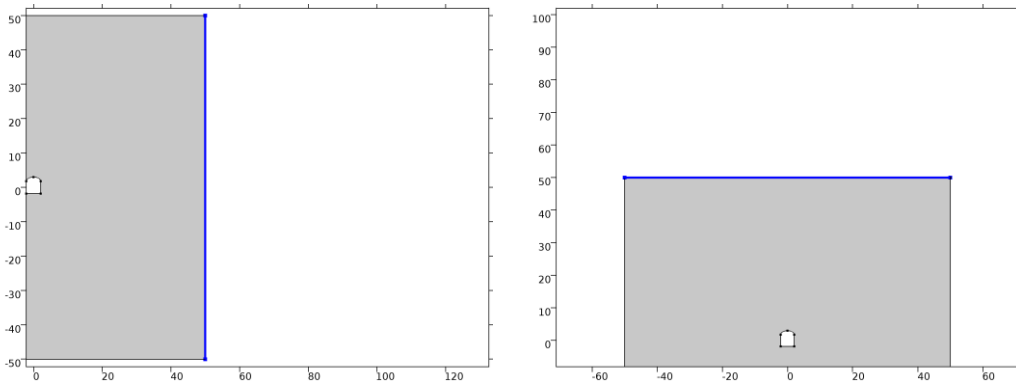


Figure 78. Right (12.5 MPa) and top (25 MPa) boundaries are selected as load boundaries.

### Pore Pressure Boundaries

The outer and inner boundaries have been assigned 5 MPa and 0 MPa, respectively. Since pressure is the variable, which is solved for in the hydraulic sub-model, the pressure can be directly defined by a Dirichlet boundary as described by equation 4. Figure 79 highlights the chosen boundaries.



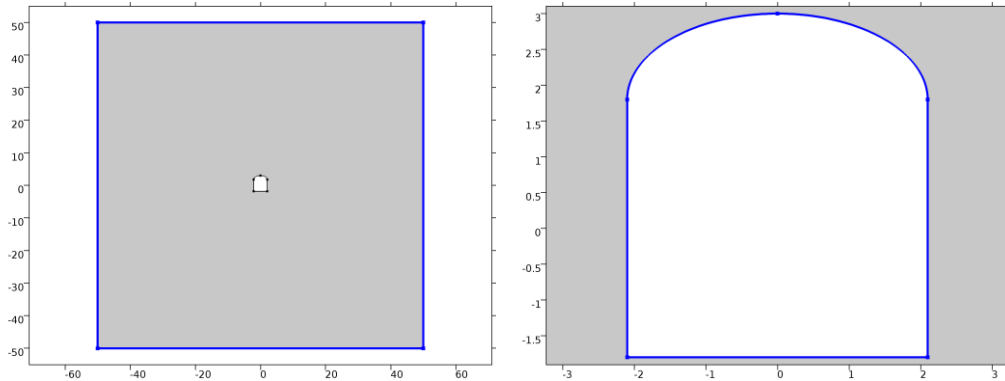


Figure 79. Outer (5 MPa) and inner (0 MPa) boundaries are selected as pore pressure boundaries.

### Fracture Flow

For Activity 1.1.3, a discrete and a deterministic fracture network has been loaded into COMSOL Multiphysics® as shown in Figure 80. Both networks use the same boundary condition given by

$$\nabla_T \cdot (d_f p \mathbf{q}) = d_f Q_m \quad (10)$$

$$\mathbf{q} = -\frac{k}{\mu} \nabla_T p \quad (11)$$

which is a tangential derivative of the Darcy Flow (compare with equation 1) with  $d_f$  and  $e_f$  being the fracture thickness and porosity, respectively.

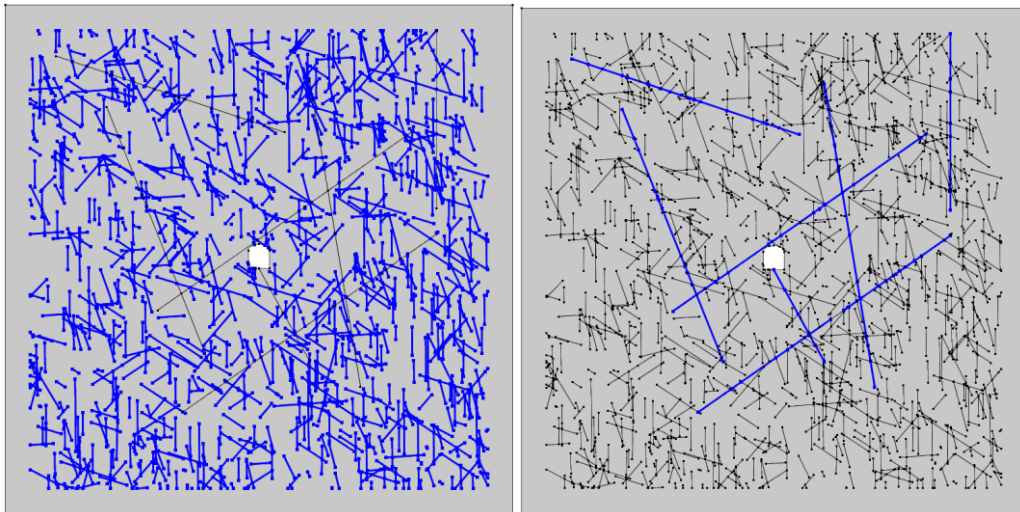


Figure 80. Discrete (left) and deterministic (right) fracture networks.

### Discretization

The models for Activity 1.1.1 and Activity 1.1.3 have been discretized differently due to the implementation of fracture networks in Activity 1.1.3. COMSOL Multiphysics® has an integrated mesh generator, which provides the possibility to produce triangular meshes in 2D among others.

For Activity 1.1.1, a mesh consisting of 30288 triangles has been generated with an average element quality of 0.98. The mesh has been refined towards the tunnel as indicated in Figure 81 (left).

For Activity 1.1.3, a mesh consisting of 246682 triangles has been generated with an average element quality of 0.91. The mesh has been refined towards the tunnel and in places where fracture intersect each other in acute angles as indicated in Figure 81 (right).

The mesh qualities are very high and indicate that most of the triangular elements are perfectly shaped (no distortion).

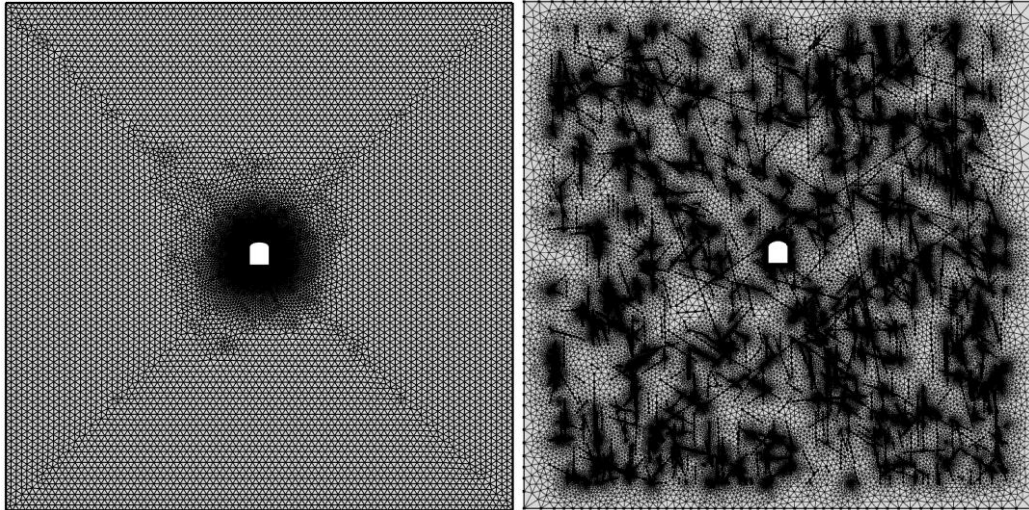


Figure 81. Meshes for Activity 1.1.1 (left) and Activity 1.1.3 (right).

### Study Settings

The solution was obtained by a fully coupled direct solver using serendipity shape function with quadratic discretization. The calculation time was about 5 s for Activity 1.1.1 and 40 s for Activity 1.1.3. The solution is obtained if the relative error between each calculation step is less than  $1e-3$ . In the case that the criterion for the relative error is not met, the solution would not be obtained.

### Disadvantages

As the employed numerical approach is based on the FEM, it can only be an approximation of the real situation as any numerical based approach. Convergence studies with increasing mesh fineness need to be performed to evaluate the error. Furthermore, the derivative of the Darcy flow for a flow of fluid along a fracture without considering the effect of the effective normal stress on the closure and hence flow of the fracture is not representing in situ conditions. It can furthermore be argued that a Biot coefficient of 1 is too high for the granite. However, these material parameters are beyond the scope of this work package.

### Advantages

The chosen software package contains a set of verified and tested partial differential equations for poroelasticity, which allows it to evaluate the simulation results of such problems with confidence. Furthermore, the interface for setting up the model (geometry, material properties, boundary conditions, mesh, solver) is easy to use and thereby prevents users from making errors, e.g. selecting wrong boundaries (in particular with the fracture networks), inputting wrong units.

The numerical approach (FEM) that the software uses is well established in different working areas and belongs, in fact, to the most widely used numerical approaches.

#### 12.4.2.4. Simulation Results

In the following, the numerical results are presented for Activity 1.1.1 (Figure 82 - Figure 91) and Activity 1.1.3 (Figure 92 - Figure 101) as requested by the work package definition for monitoring line 1-3, tunnel wall and tunnel floor.

##### Activity 1.1.1

Steady changes in fluid flow, pore pressure, strain and stresses are observed for the homogeneous poroelastic rock along the monitoring lines. All parameters follow the expected trends and converge towards the applied boundary conditions, e.g. stresses are altered in the vicinity of the tunnel, and pore pressure and fluid flow drop to zero at the tunnel wall.

For the tunnel wall, unsteady changes are observed in the corners of the tunnel, where the stresses are theoretically concentrated to infinity due to the linear elastic material behavior, which would be reduced by yielding of the material.

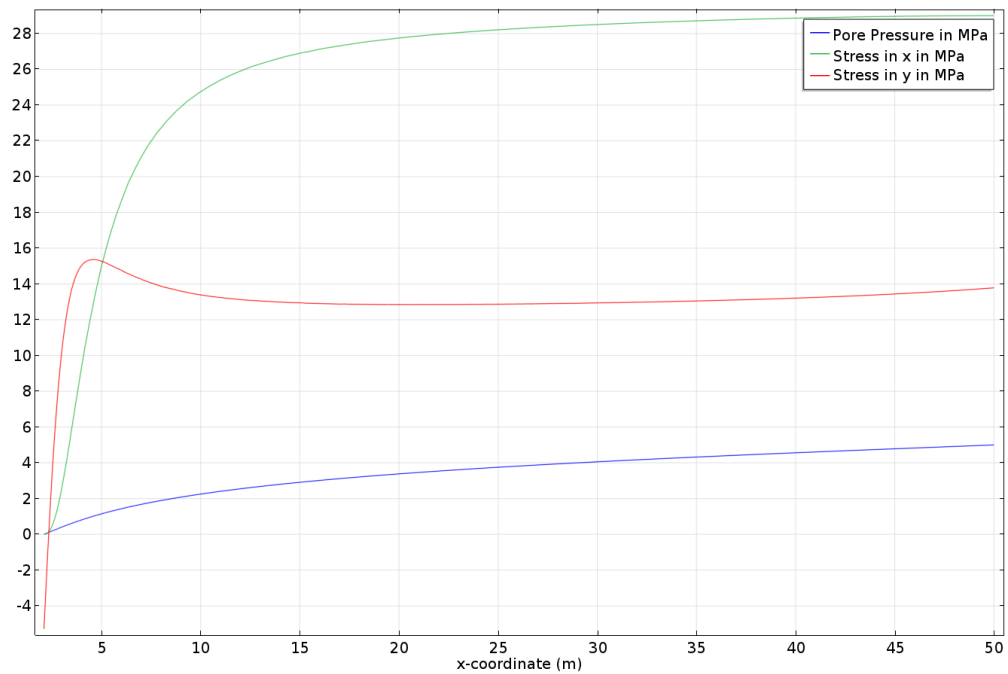


Figure 82. Monitoring Line 1 showing the pore pressure and stresses in x and y direction.

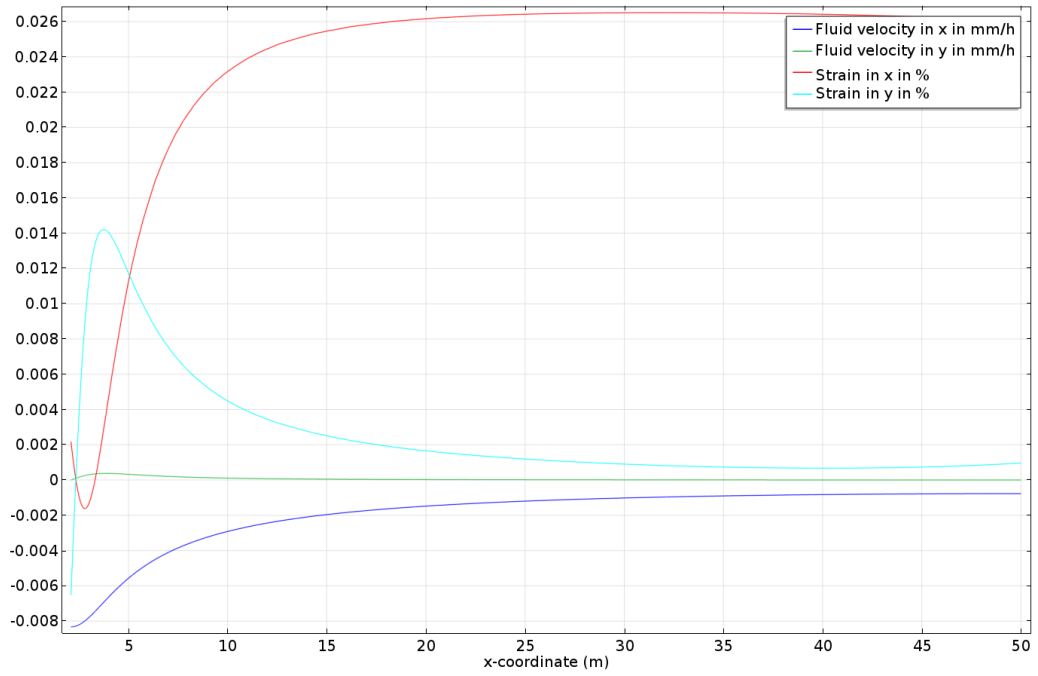


Figure 83. Monitoring Line 1 showing the fluid velocity and strains in x and y direction.

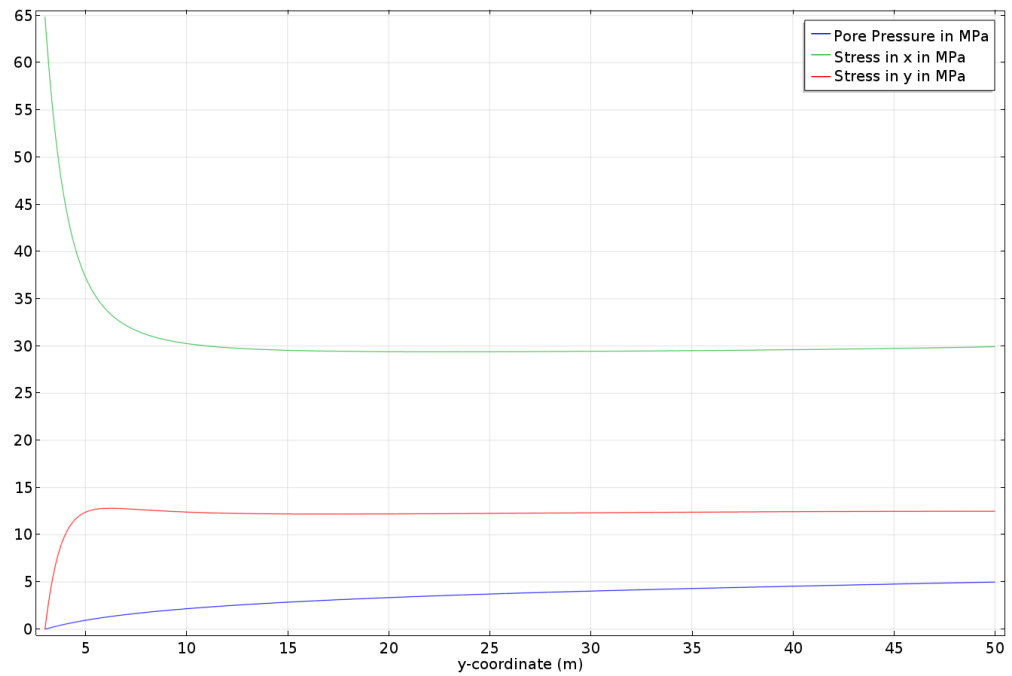


Figure 84. Monitoring Line 2 showing the pore pressure and stresses in x and y direction.

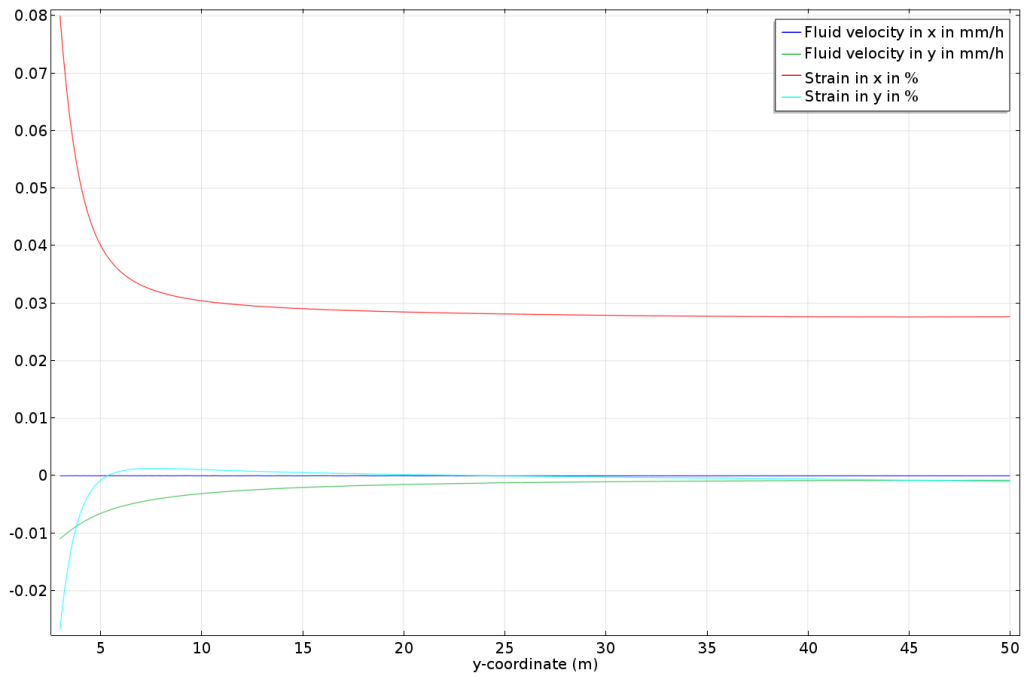


Figure 85. Monitoring Line 2 showing the fluid velocity and strains in x and y direction.

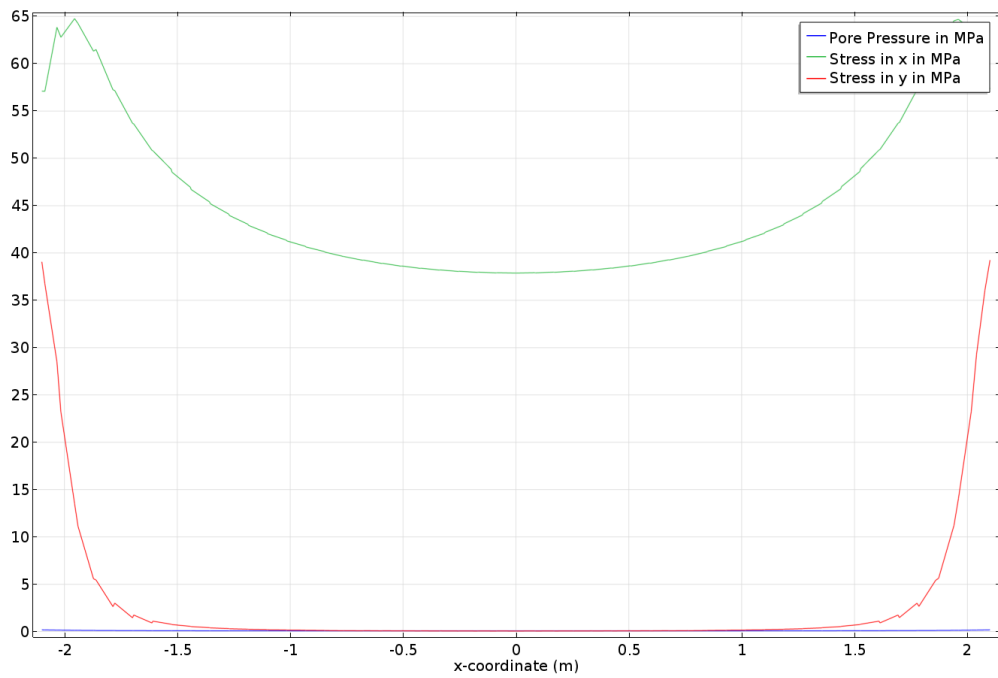


Figure 86. Monitoring Line 3 showing the pore pressure and stresses in x and y direction.

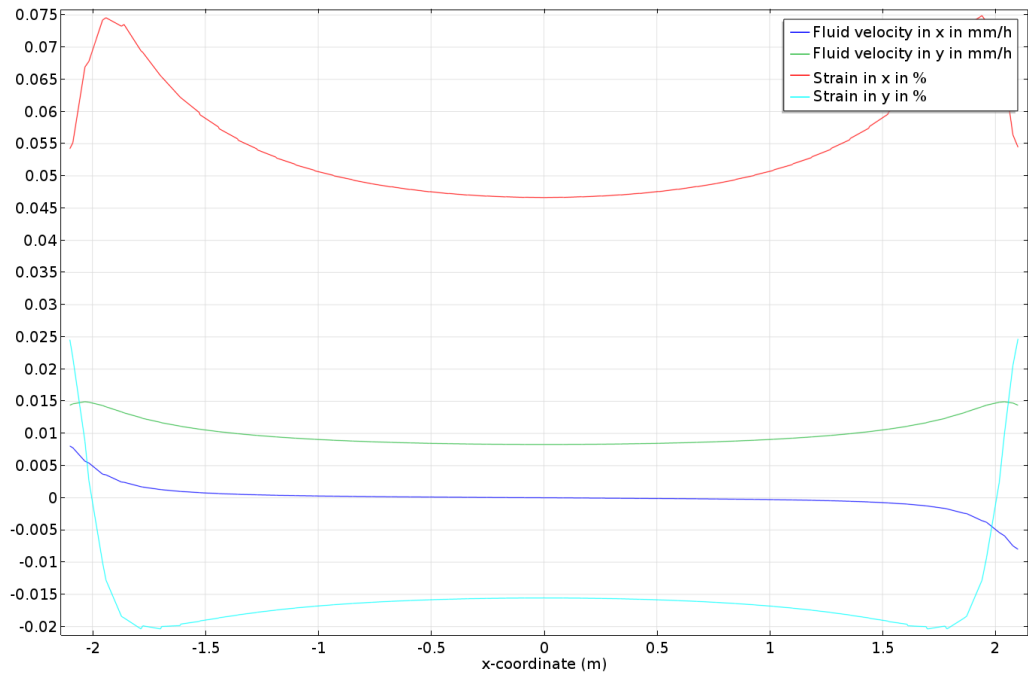


Figure 87. Monitoring Line 3 showing the fluid velocity and strains in x and y direction.

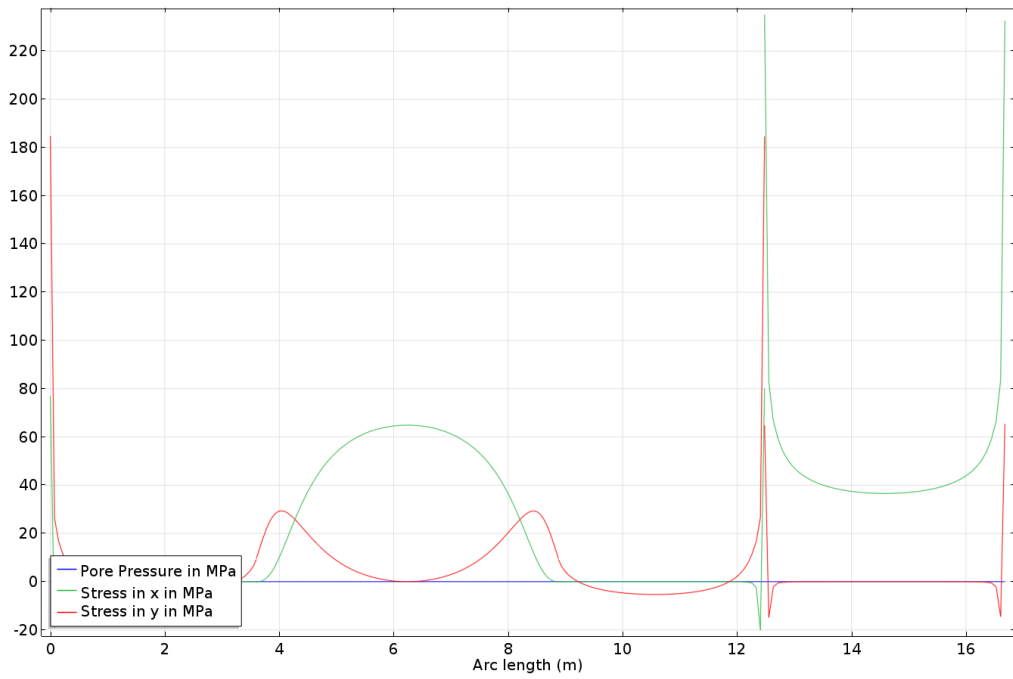


Figure 88. Tunnel wall showing the pore pressure and stresses in x and y direction.

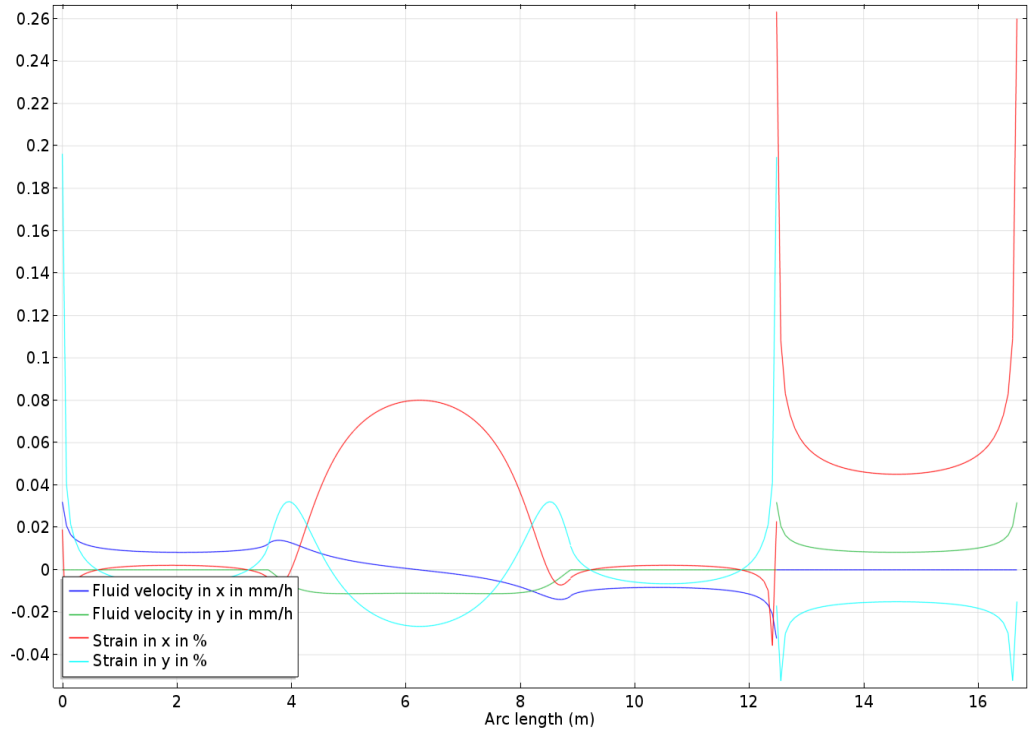


Figure 89. Tunnel wall showing the fluid velocity and strains in x and y direction.

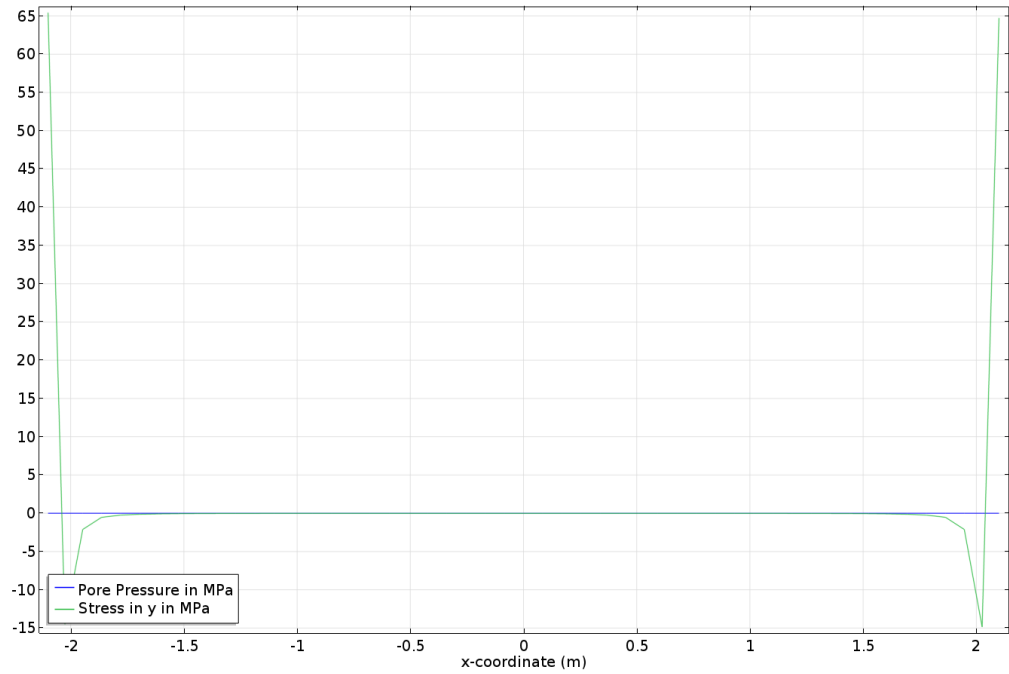


Figure 90. Tunnel floor showing the pore pressure and stresses in y direction.

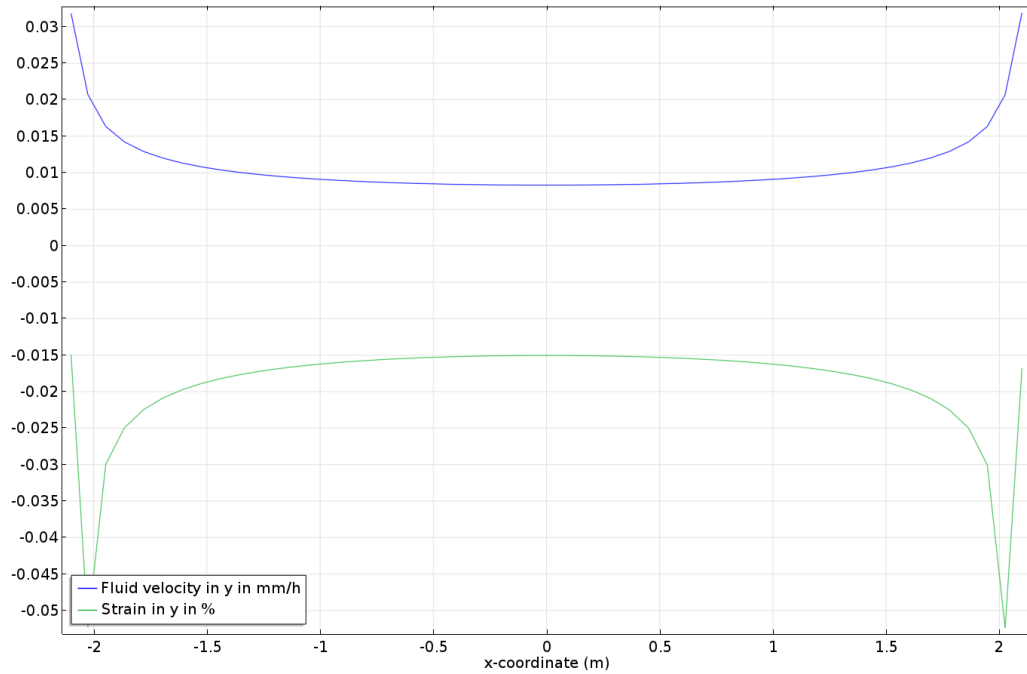


Figure 91. Tunnel floor showing the fluid velocity and strains in y direction.

### Activity 1.1.3

Steady changes in strain and stress are observed for the highly fractured poroelastic rock along the monitoring lines. However, high fluctuations are observed for the fluid flow. All parameters follow the expected trends and converge towards the applied boundary conditions, e.g. stresses are altered in the vicinity of the tunnel, and pore pressure and fluid flow drop to zero at the tunnel wall.

At the tunnel wall, stresses and strains show extreme variations as observed and explained in the Activity 1.1.1. Furthermore, the pore-fluid-related values fluctuate.



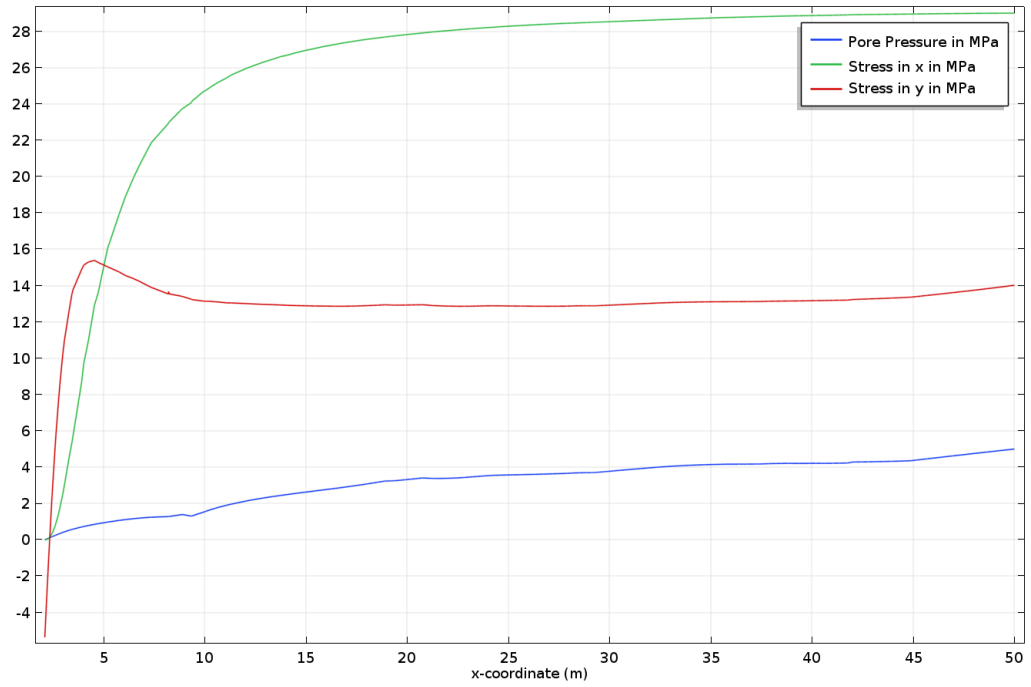


Figure 92. Monitoring Line 1 showing the pore pressure and stresses in x and y direction.

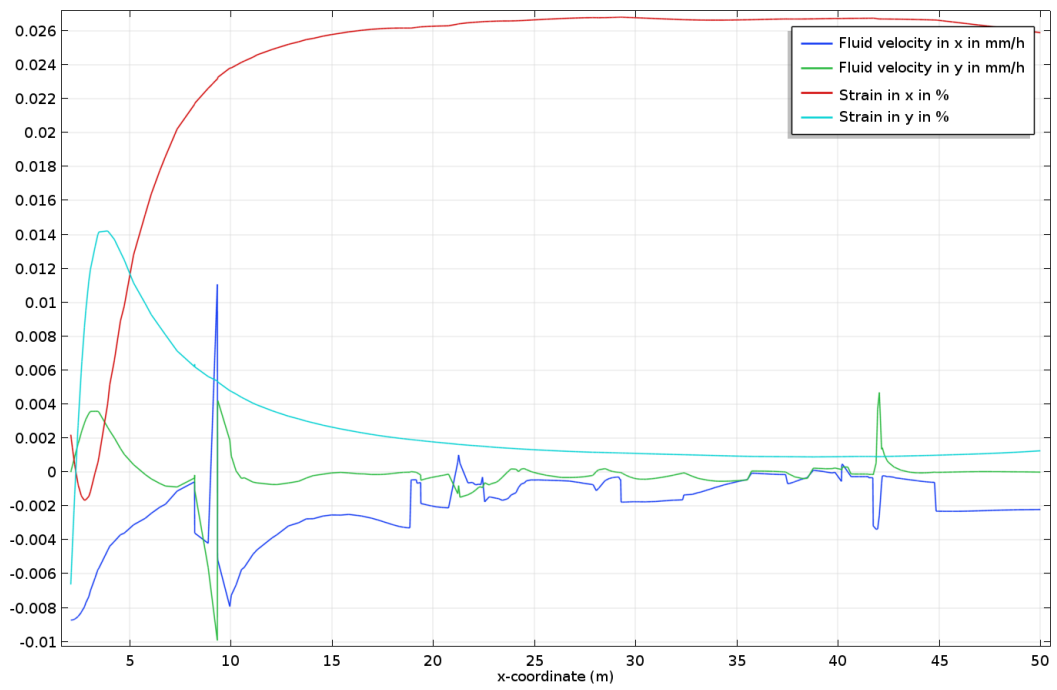


Figure 93. Monitoring Line 1 showing the fluid velocity and strains in x and y direction.

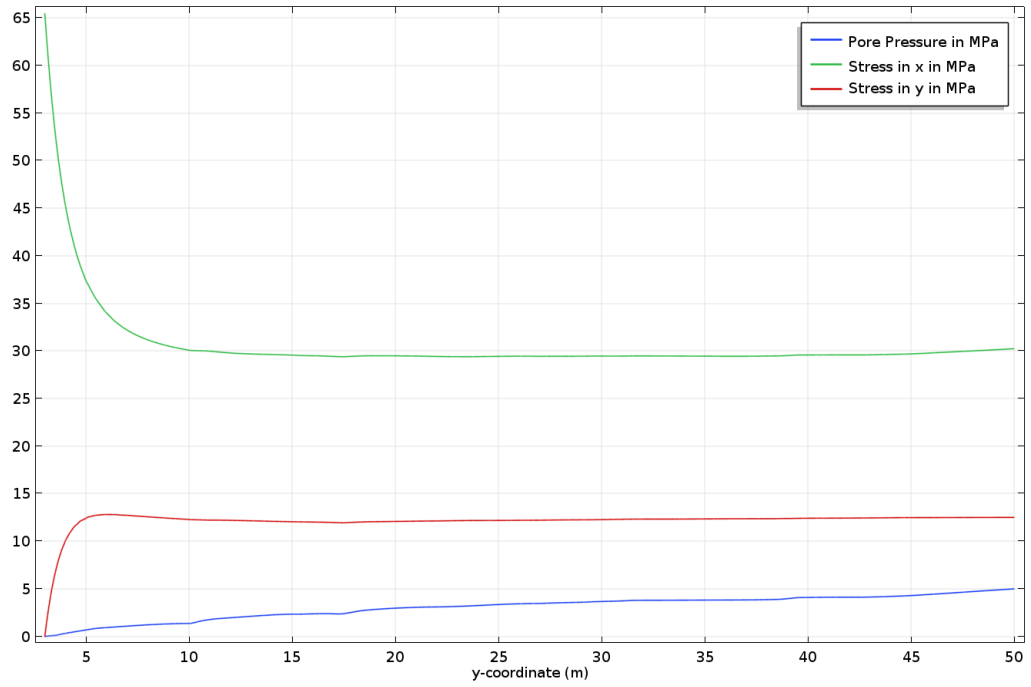


Figure 94. Monitoring Line 2 showing the pore pressure and stresses in x and y direction.

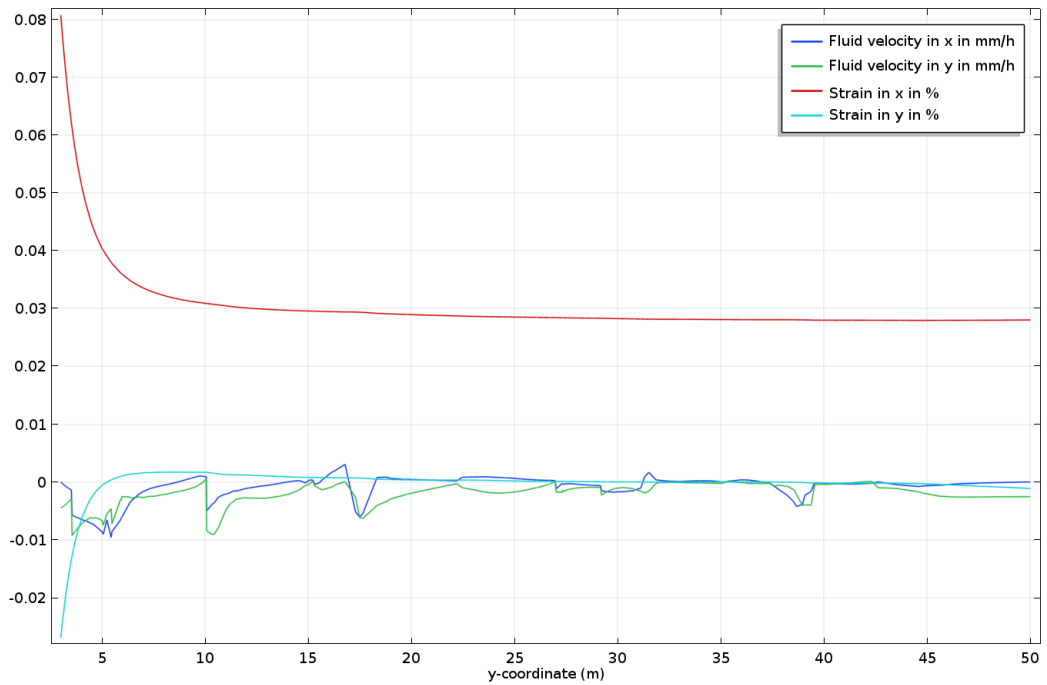


Figure 95. Monitoring Line 2 showing the fluid velocity and strains in x and y direction.

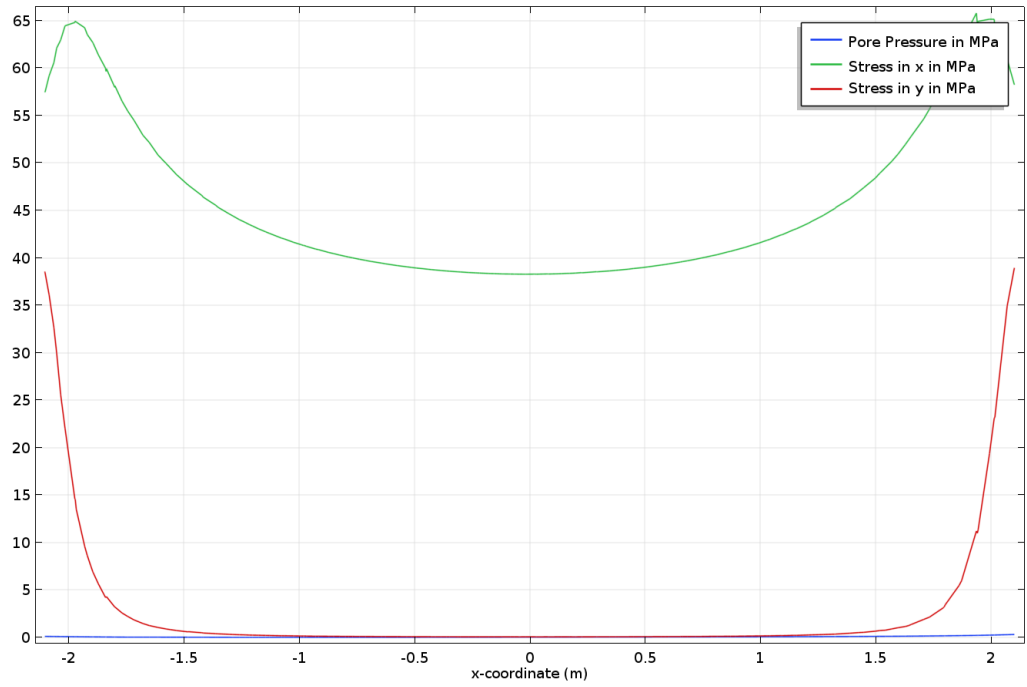


Figure 96. Monitoring Line 3 showing the pore pressure and stresses in x and y direction.

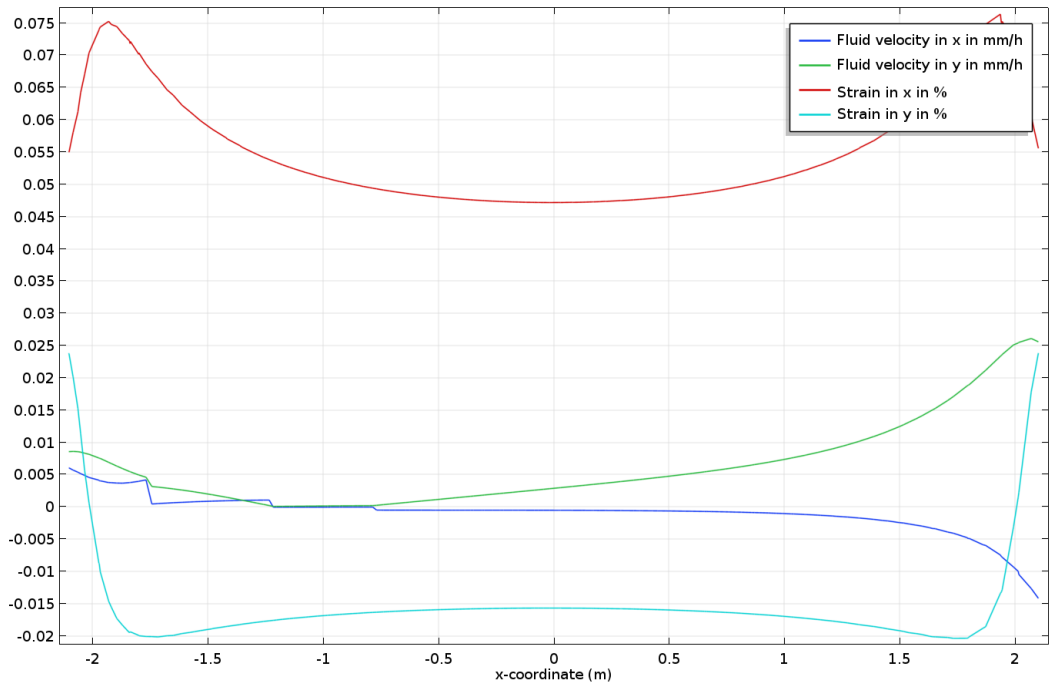


Figure 97. Monitoring Line 3 showing the fluid velocity and strains in x and y direction.

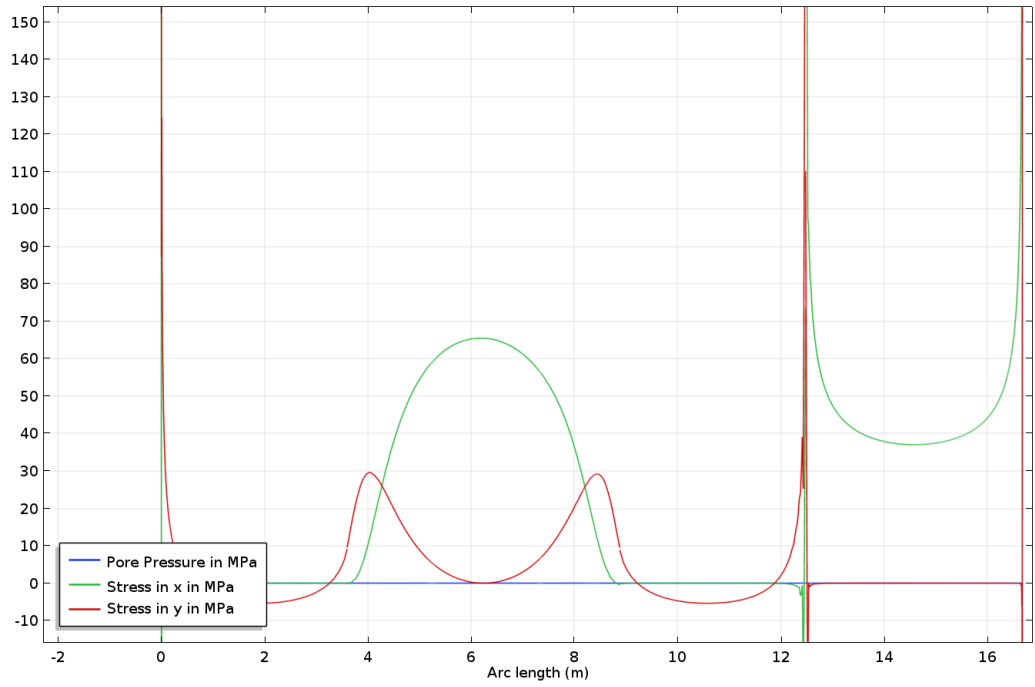


Figure 98. Tunnel wall showing the pore pressure and stresses in x and y direction.

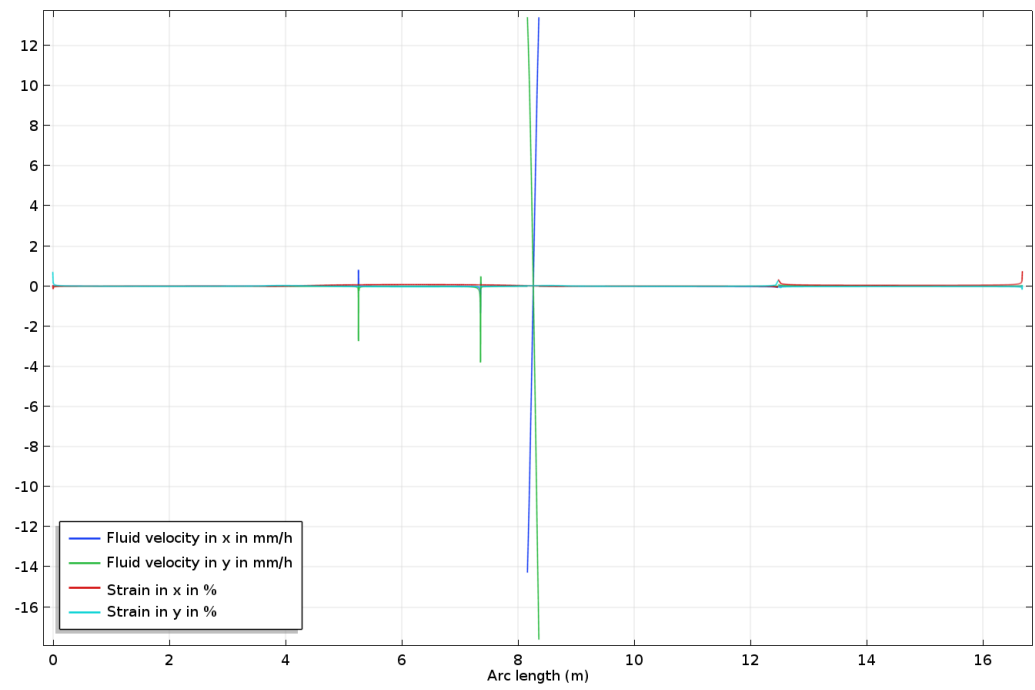


Figure 99. Tunnel wall showing the fluid velocity and strains in x and y direction.

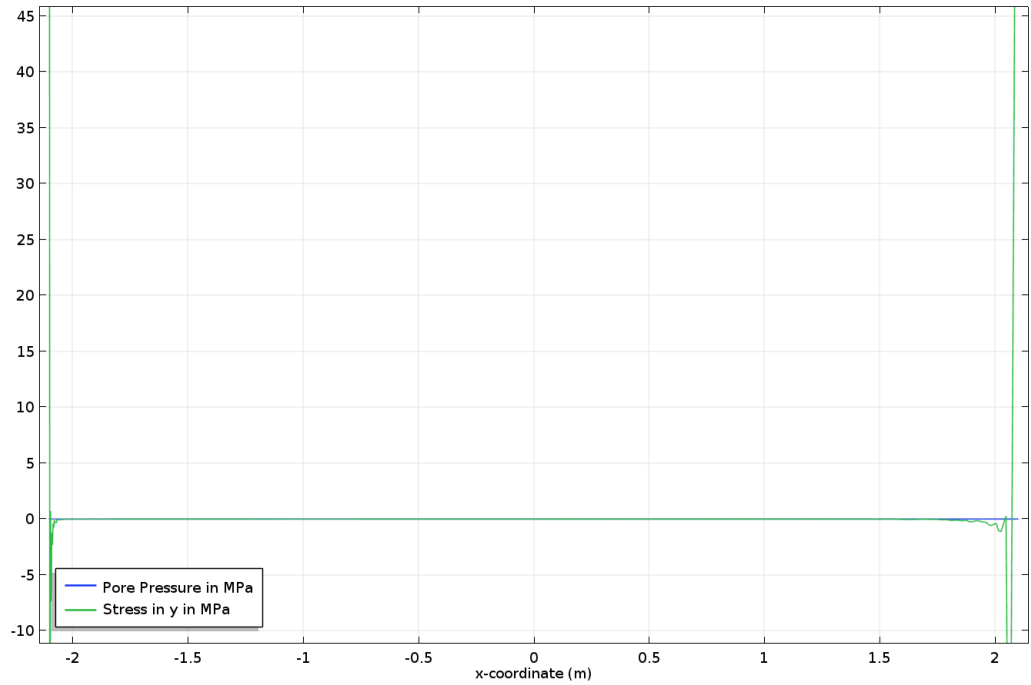


Figure 100. Tunnel floor showing the pore pressure and stresses in y direction.

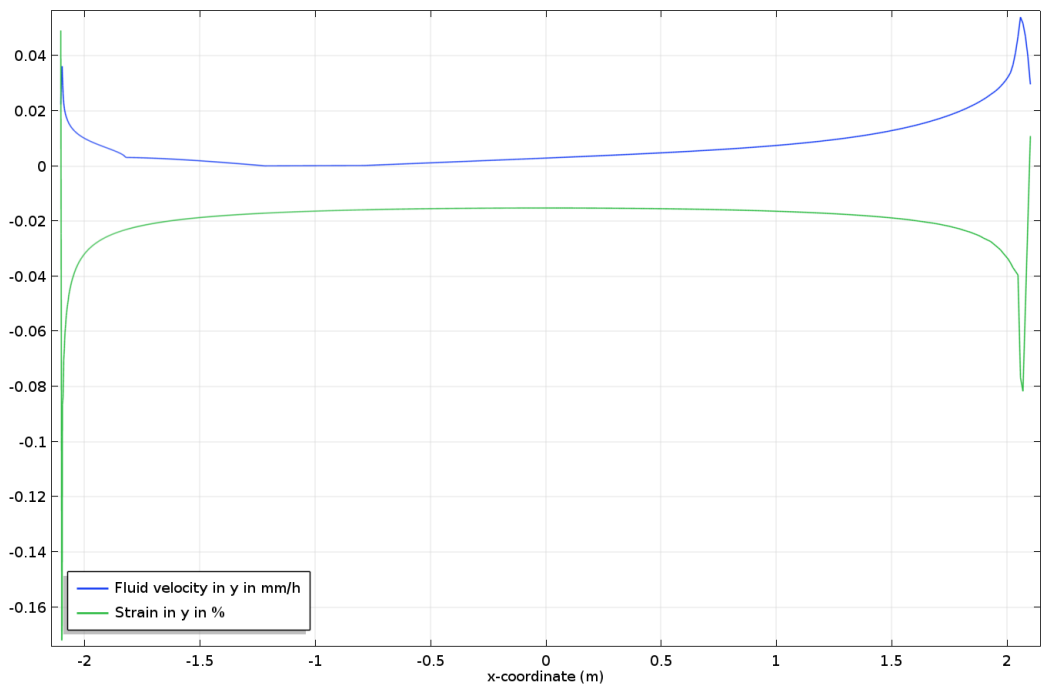


Figure 101. Tunnel floor showing the fluid velocity and strains in y direction.

### Discussion of Results

COMSOL Multiphysics is a well-established numerical software code which was validated and verified against analytical solutions, e.g. for holes in a plate, which is a similar problem to the tunnel geometry defined in the WP 1. The involved coupling of solid deformation and fluid flow through poroelasticity is also well established and has been used to model the stability of faults in porous media (Meier and Backers, 2017) or the deformation of rock (Holzbecher and Oberdorfer, 2014). The solver is set to a very

small tolerance so that the numerical error is negligible in comparison to the magnitude of the evaluated values. The obtained result can be regarded as numerically correct. Unfortunately, no analytical solution exists for these particular problems to validate the numerical results.

### 12.4.3. Team Seoul National University (SNU)

#### 12.4.3.1. Numerical Approach

Team Seoul National University (SNU) adopted the Discrete Element Method (DEM) to describe the mechanical and hydraulic behavior of fractured rock. The core simulating tool was UDEC 5.0 from Itasca Consulting Group Inc. which is two-dimensional DEM simulation tool for jointed and blocky material (see Itasca Consulting Group Inc., 2013). UDEC is specialized to describe the normal and shear deformation of not only rock but also joints based on a prescribed linear or non-linear stress-strain law. Especially, deformation of joint indicates a change of its aperture size which can affect the hydraulic behavior of entire model. Under the hydraulic boundary condition, the updated hydraulic parameters (i.e. flow rate and fluid pressure) by changes in the aperture will disturb the local stress condition around the joint and the deformation of rock and joint will occur again. This cycle is the basic mechanism of the coupled H-M analysis of jointed rock in UDEC.

#### 12.4.3.2. Model Implementation including Discussion

SNU group focused on the fluid flow through the deformed fractures. Other than the suggested fracture properties, we additionally assumed some properties regarding the fracture deformations based on the previous observations in Äspö HRL (Min et al., 2004; Mas Ivars et al., 2014) as shown in **Table 29**.

**Table 29.** Fracture properties regarding deformation.

Properties	Units	Value
Joint normal stiffness	GPa/m	200
Joint shear stiffness	GPa/m	100
Joint cohesion	MPa	0.9
Joint friction angle	deg	36
Dilation angle	deg	3

For fractured granite, the apparent permeability is mainly dominated by the fracture networks of rock mass, due to low permeability of intact rock. Similarly, fractured models in UDEC only allow the fluid flow through fracture networks. However, the suggested model has low connectivity of fractures and permeability of rock could be an important factor for results. To describe the permeability of intact rock, the two orthogonal joint sets were generated (Figure 102). Based on suggested permeability of rock, the aperture size and spacing of joints were calculated and maintained during simulations.

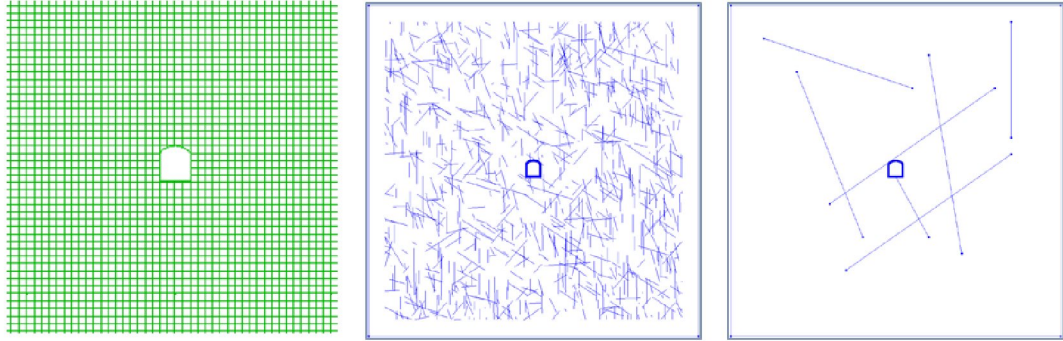


Figure 102. Generated orthogonal joint sets, DFN, DTM fractures.

Suggested DFN and DTM fractures were not directly connected with the outer boundary of model. One purpose of this simulation was determining the effects of fracture behavior on fluid flow and this gap could interfere in fluid flow. Therefore, we decided to reduce the full model size to 90 m x 90 m to make a direct connection between DFN and boundary (see Figure 103).

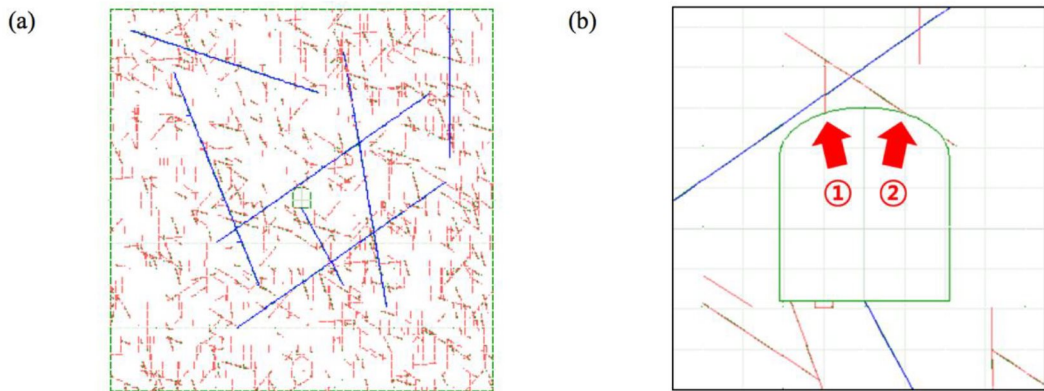


Figure 103. (a) Constructed model with DFN (red line) and DTM fractures (blue line) and (b) magnified image of tunnel wall.

### 12.4.3.3. Simulation Results

After the constructed model reached a steady state, the hydraulic indicators, pore pressure and flow rate, and the mechanical indicators, local stress and strain, were monitored along the suggested monitoring lines.

In every monitoring line, pore pressure showed similar distribution with the results of continuum model which were obtained from Work Package 1.

In case of the flow rate and local stress, there was no significant difference from the results of continuum model along the monitoring line 1. In contrast, the significant drop of flowrate and local stress were observed at the vicinity of tunnel in monitoring line 2, especially in the DFN DTM model. For monitoring line 3, it was not possible to determine meaningful results due to the resolution of the constructed model.

Flow rate and local stresses were monitored along the tunnel wall as shown in Figure 104 and Figure 105. The local stress distribution was slightly disturbed at the roof of tunnel compared to the results of continuum model. The main disturbance occurred in the flow rate distribution of DFN DTM model as shown in Figure 104 and Figure 105. The fluid flow was concentrated on the single fractures located at the roof of tunnel.

#### 12.4.3.4. Discussion of Results

Flow rate along the monitoring line 1 (Figure Figure 104a) showed a continuous decrease that is also exhibited by the flow rate in the continuum model. This model had a direct connection between the outer boundary and discrete fractures, so the flow path that causes the similar tendency of hydraulic parameters (flow rate and pore pressure) with the continuum model was generated from outer to inner boundary.

At a vicinity of tunnel, especially monitoring line 2, local stress conditions were reduced compared to the continuum model. It creates the possibility of fractures shearing due to stress concentration. The decrease of flow rate around the tunnel in monitoring line 2 could also indicate that the fluid flow is deviated through DFN or DFN DTM fractures.

Deviated fluid flow can be observed more clearly from the results on tunnel wall. In Figure 104 (d), DFN DTM model showed high increase of fluid flow at the point number 2. This point corresponds to the fracture number 2 in Figure 103 (b). Dilation of fractures due to shearing entails increases in aperture size and indicates a high flow rate through the sheared fracture. The DTM fracture located at the tunnel roof connected to fracture number 2 interfaced with fractures and created a fluid path through which the fluid flow could be concentrated.

In the case of fracture number 1, the orientation was almost vertical. Therefore, shear stress cannot be applied on this fracture and only normal closure affected the aperture size. Compared with fracture number 2, fluid could not flow through this narrow fracture.

The UDEC simulation obtained hydraulic parameters from fractures. Compiled results indicated the dilation of fractures due to shearing can cause an increase in transmissivity and the fractures in the vicinity of the tunnel may be more vulnerable due to stress concentration. Shearing of fractures is dominated by orientation of fracture.

UDEC, as a DEM simulation tool, successfully reflected the aperture change of fractures which is critical for interpreting the hydromechanical behavior of crystalline rock. Furthermore, DEM allows the application of more complicated mechanisms of fracture behavior, so it can be possible to describe more realistic phenomena that happen in fractured crystalline rock.

On the other hand, the constructed UDEM model contained only several monitoring points at the vicinity of tunnel due to its low resolution. The resolution problem is directly related with the calculation efficiency of the model, algorithm and tool itself. In a further study, we will modify the meshing algorithm to improve the calculation speed and the resolution in the vicinity of the tunnel.



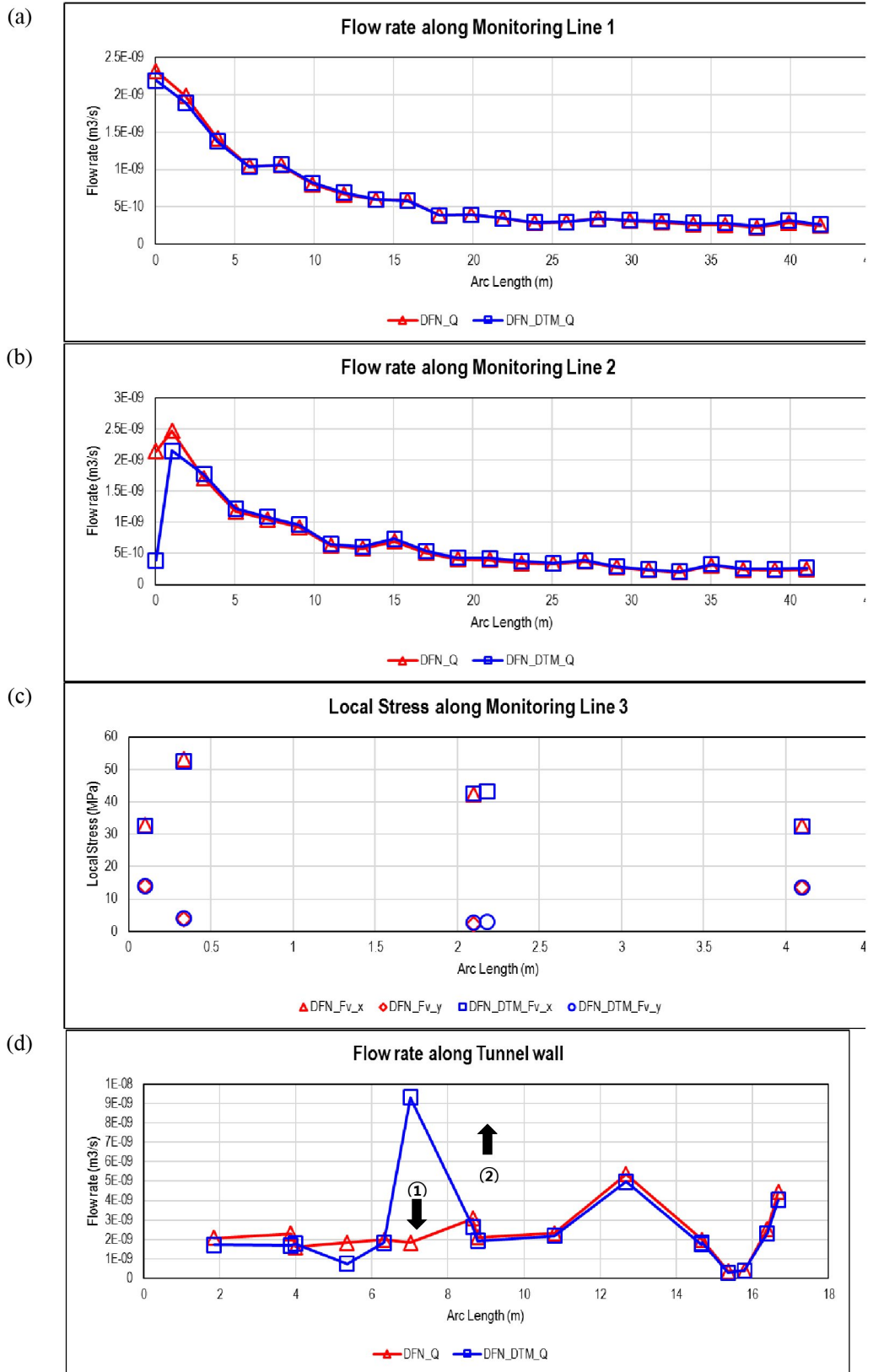


Figure 104. Flow rate distribution along (a) monitoring lines 1, (b) 2, (c) 3 and (d) tunnel wall

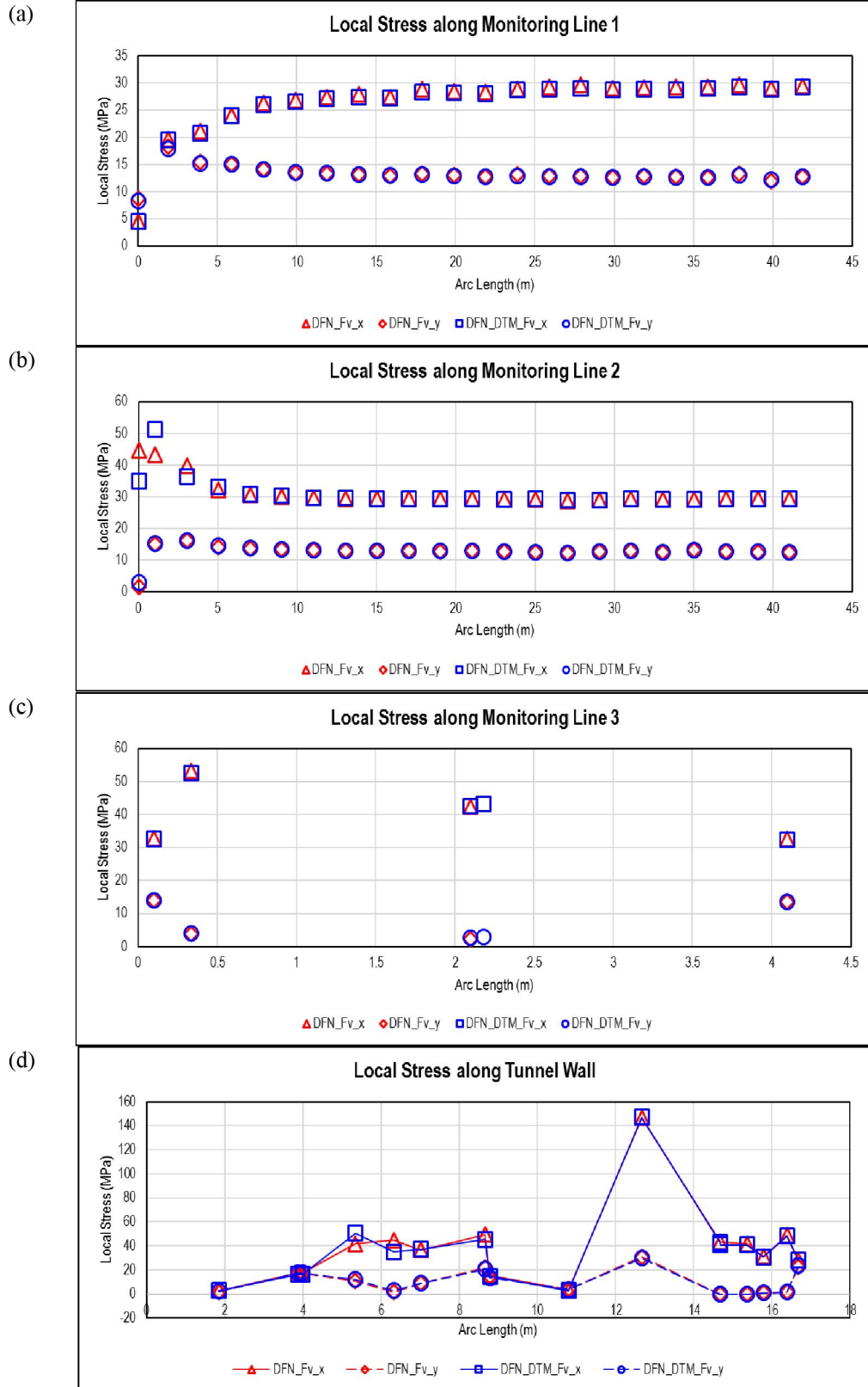


Figure 105. Local stress distribution along (a) monitoring lines 1, (b) 2, (c) 3 and (d).

#### 12.4.4. Team Technical University Liberec (TUL) and UGN

In the Czech Republic, two institutions independently solved this task in parallel. Since both institutions used the same software tool for this phase, the results shown in this section are to be understood as joint but independently verified.

##### 12.4.4.1. Numerical Approach

We used the COMSOL Multiphysics® Subsurface Flow module for our simulations, specifically the built-in interface for computation of poroelasticity (COMSOL Multiphysics, 2017) software (version 5.0.1 at TUL-IGN and version 5.2.0 at UGN). In this interface, the Biot poroelasticity (Biot, 1962) is implemented. It couples Darcy flow in saturated porous media (equation 12) with linear elasticity which is solved as a 2D approximation as a plane strain problem (equation 13).

$$-\nabla \cdot \left( \frac{\kappa}{\mu} \nabla p \right) = 0 \quad (12)$$

$$\begin{bmatrix} \sigma_{xx} \\ \sigma_{yy} \\ \sigma_{xy} \end{bmatrix} = \frac{E}{(1+\nu)(1-2\nu)} \cdot \begin{bmatrix} 1-\nu & \nu & 0 \\ \nu & 1-\nu & 0 \\ 0 & 0 & 1-2\nu \end{bmatrix} \cdot \begin{bmatrix} \varepsilon_{xx} \\ \varepsilon_{yy} \\ \varepsilon_{xy} \end{bmatrix} - \begin{bmatrix} \alpha_B p & 0 & 0 \\ 0 & \alpha_B p & 0 \\ 0 & 0 & \alpha_B p \end{bmatrix}, \quad (13)$$

where  $\kappa$  is a material permeability [ $\text{m}^2$ ],  $\mu$  is a dynamic viscosity of a fluid [ $\text{Pa s}$ ],  $p$  is a fluid pressure [ $\text{Pa}$ ],  $\sigma_{ij}$  are the components of the stress tensor [ $\text{Pa}$ ],  $\varepsilon_{ij}$  are the components of the strain tensor [1],  $\nu$  is the Poisson constant [1],  $E$  is the Young's modulus [ $\text{Pa}$ ] and  $\alpha_B$  is the Biot's coefficient [1].

In the case of the variants with an embedded fracture network, the model additionally uses the so-called 'fracture flow' interface which considers tangential derivations to define the flow along lines that represent fractures using the following equation (14):

$$-\nabla_T \cdot \left( \frac{\kappa_f}{\mu} \nabla_T p \right) = 0, \quad (14)$$

where  $\kappa_f$  is the fracture permeability [ $\text{m}^2$ ] and  $\nabla_T$  is the gradient operator restricted to tangential direction (with respect to the fracture direction).

The coupling of hydraulic and mechanical problems is considered to be unidirectional (this follows the task description): the influence of steady flow in porous medium on stress and strain fields is solved (we deal with stationary models).

##### 12.4.4.2. Model Implementation including Discussion

We prepared three different models.

The first one considers the rock matrix to be homogeneous (Activity 1.1.1). Its geometry, material properties and boundary conditions were given by the task description.

The second and the third models include the discrete fracture network (work package 1\_B). Two variants of fracture network were included. The first fracture model consists of smaller stochastic fractures (from now on noted as the DFN variant). The second fracture model consists of the same stochastic fractures along with seven larger deterministic fractures (from now on noted as DFN+DTM variant). The geometry, material properties and boundary conditions were given by the task description.

#### 12.4.4.3. Simulation Results

In this section, the model results are shown as a comparison of homogeneous rock model with the fracture network models. Besides the required outputs in the form of graphs of the required quantities along the monitoring lines, the chosen quantities are also shown as color maps.

From the pressure field comparison shown in Figure 106, we can see the influence of both fracture network variants (as well as their influence on direction and velocity of water flow in Figure 107). The evenly distributed pressure in the homogeneous rock matrix variant changes only a little in the DFN variant, but in the DFN+DTM variant the changes are more pronounced and the pressure distribution is quite uneven. The pressure field is dominantly influenced by those fractures of which the direction is similar to the flow direction. In contrast, the fractures nearly perpendicular to the flow direction influence the pressure field much less (for example, the two topmost fractures in the model).

Changes in the mechanical quantities are relatively small and do not readily show in the color scale pictures. The only exception is the y component of the displacement vector (shown in Figure 108). The differences are not only in the magnitude but also in the direction. The DFN variant is similar to the homogeneous matrix variant, but the DFN+DTM variant is more distinct. It almost completely shifts downwards (in the bottom part of the model, the displacement is significantly lower than in the top part which can't be seen in Figure 108 due to the arrow normalization). In the homogeneous matrix model, the maximum value of y displacement vector component is 0.000467 m (in  $\uparrow$  direction), in the DFN model 0.000421 m (in  $\downarrow$  direction) and in DFN+DTM model 0.00193 m (in  $\downarrow$  direction). The x component of the displacement vector does not differ much across the model variants and, since it is (due to the boundary conditions) dominant (maximum of 0.03 m in  $\leftarrow$  direction), the differences in the y component do not have significant impact on total displacement.

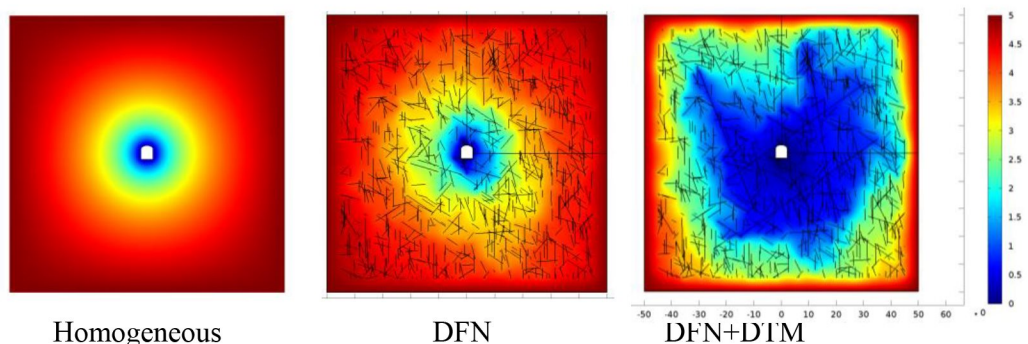


Figure 106. Pressure field (MPa).



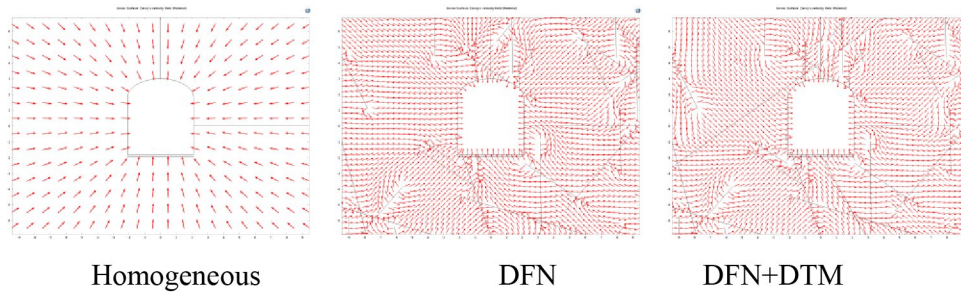


Figure 107. Normalized vector of flow velocity depicted using arrows.

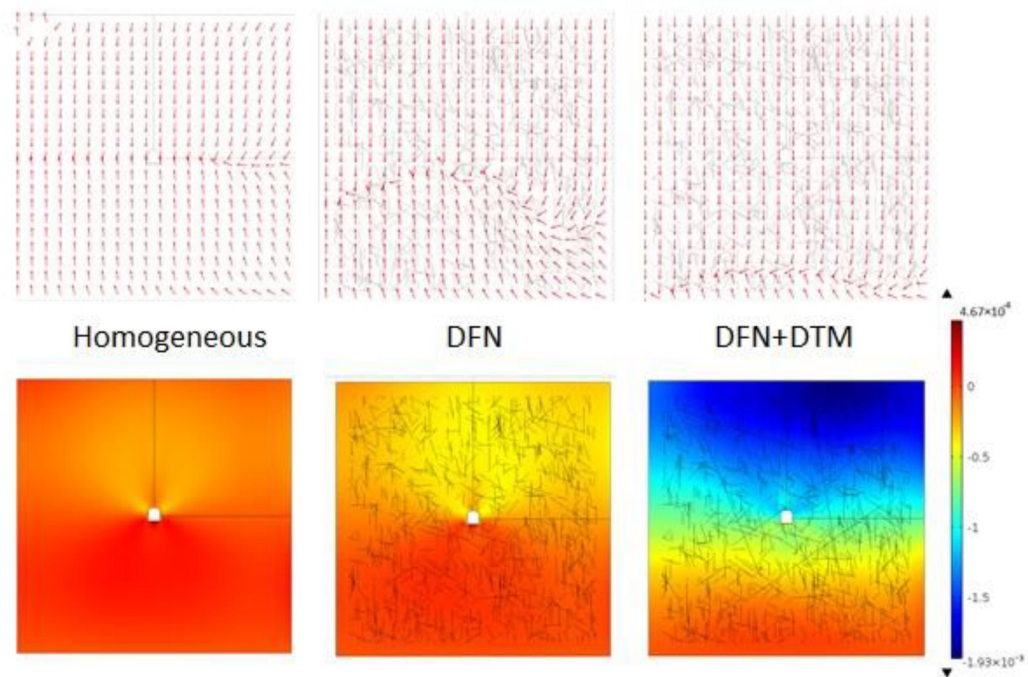


Figure 108. The y component of the displacement vector depicted using arrows and color map (the arrow size is normalized in all cases and in the sake of clarity the x component of the displacement vector is reduced by a factor of 1000).

Figure 109 to Figure 115 show chosen quantities plotted along the monitoring lines (graphs for three individual monitoring lines along with a graph depicting a development along the tunnel boundary where the starting point is situated in the bottom left corner and the progression is in the clockwise direction).

The development of pore pressure is shown in Figure 109. It confirms the differences in pressure field described above. The DFN variant does not differ much from the homogeneous matrix variant along monitoring lines 1 and 2. Along the third line, the differences are more significant. They are caused by higher number of smaller fractures intersecting this line and having similar direction as the water flow. The DFN+DTM variant shows significant differences. Along the third monitoring line, the pressure values at both end-points are considerably lower than for the two remaining variants (this is caused by the overall pressure distribution).

Velocity vector components are shown in Figure 110 and Figure 111, respectively. The values are fluctuating and are (in many cases) discontinuous. The dependence along the third monitoring line is similar for the DFN+DTM model and the homogeneous model. This corresponds to the pressure distribution shown in Figure 115.

The stress tensor (Figure 112 and Figure 113) shows very little differences for both the xx and yy component (the variance from the homogeneous model is little higher for the DFN+DTM variant but it is still tenths of MPa at the highest). Differences in the strain tensor components (Figure 114 and Figure 115) are similar (please note that the axis scales which in some cases skew the difference relevance). The difference between the homogeneous model and the DFN+DTM model is for both components of strain tensor about 2 – 3 mm along the first line, about half of that along the second line, and about  $10^{-4}$  m along the third line.

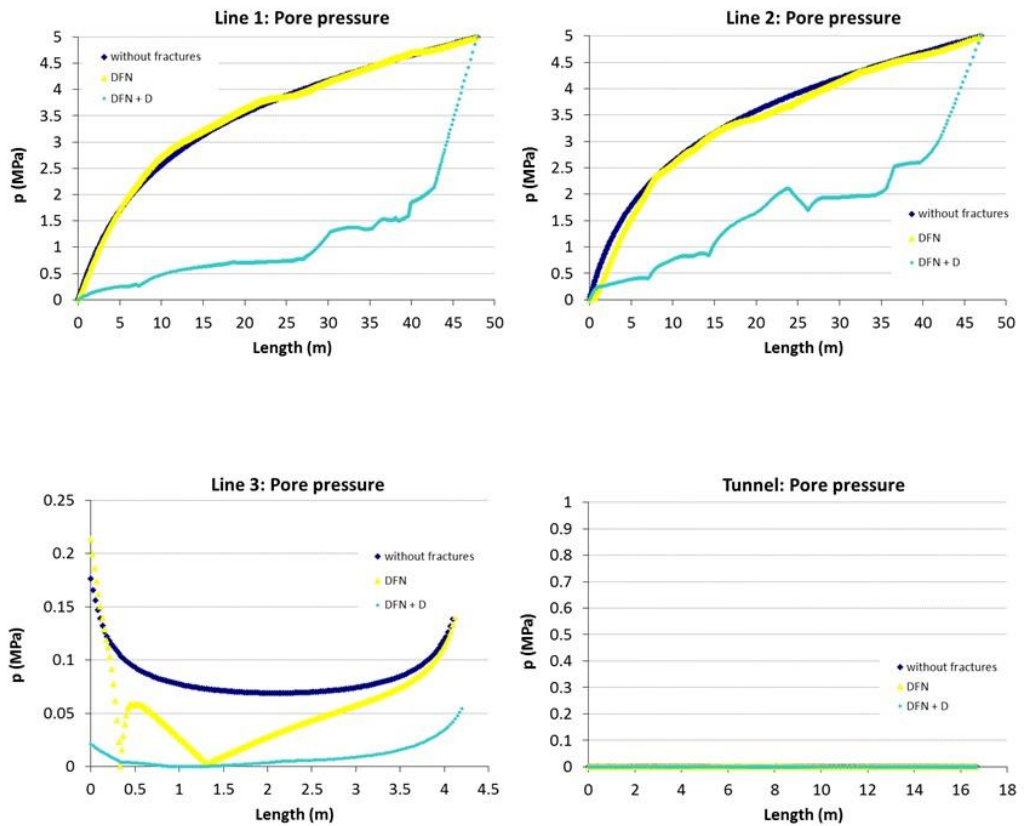


Figure 109. Development of pore pressure over the monitoring lines for all three model variants

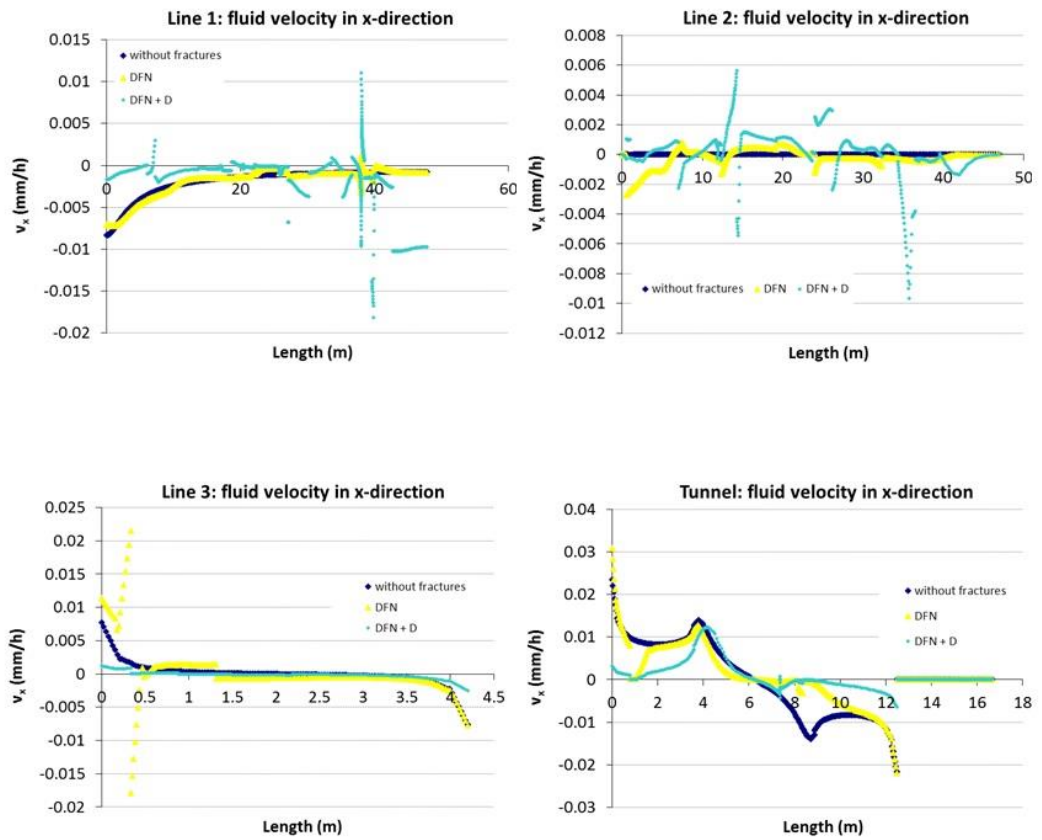


Figure 110. Development of flow velocity vector x component over the monitoring lines for all three model variants.

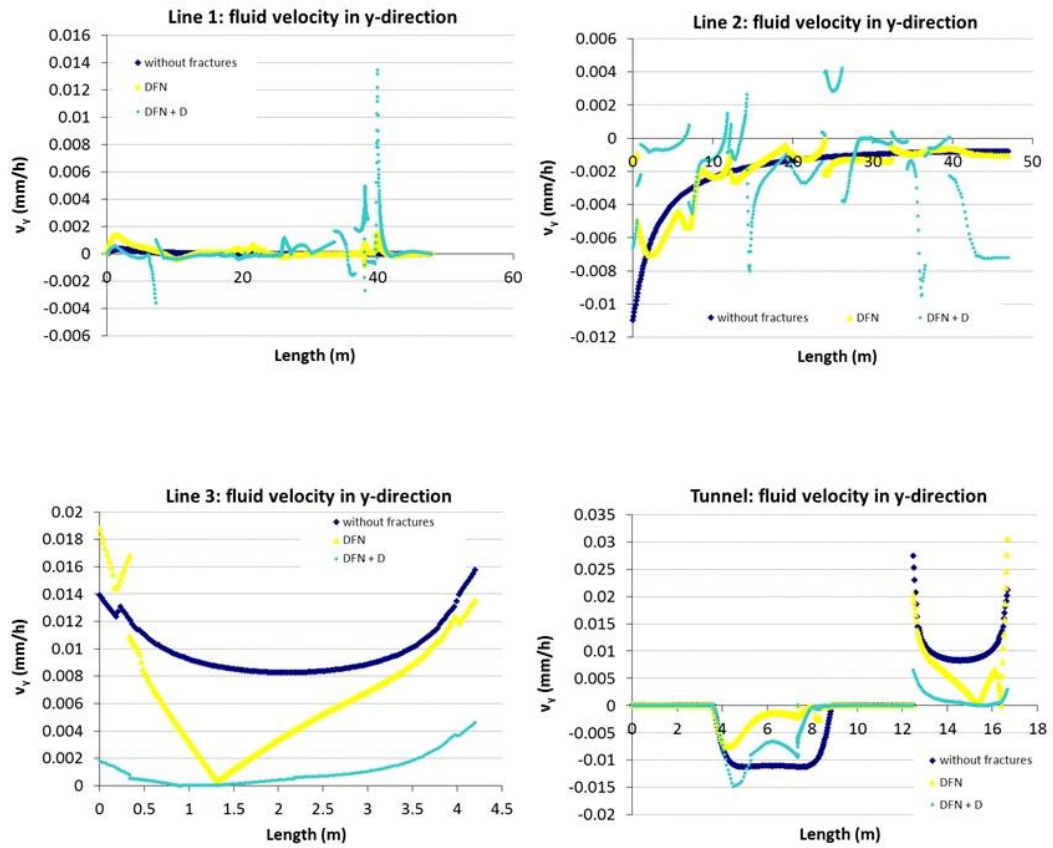


Figure 111. Development of flow velocity vector y component over the monitoring lines for all three model variants.

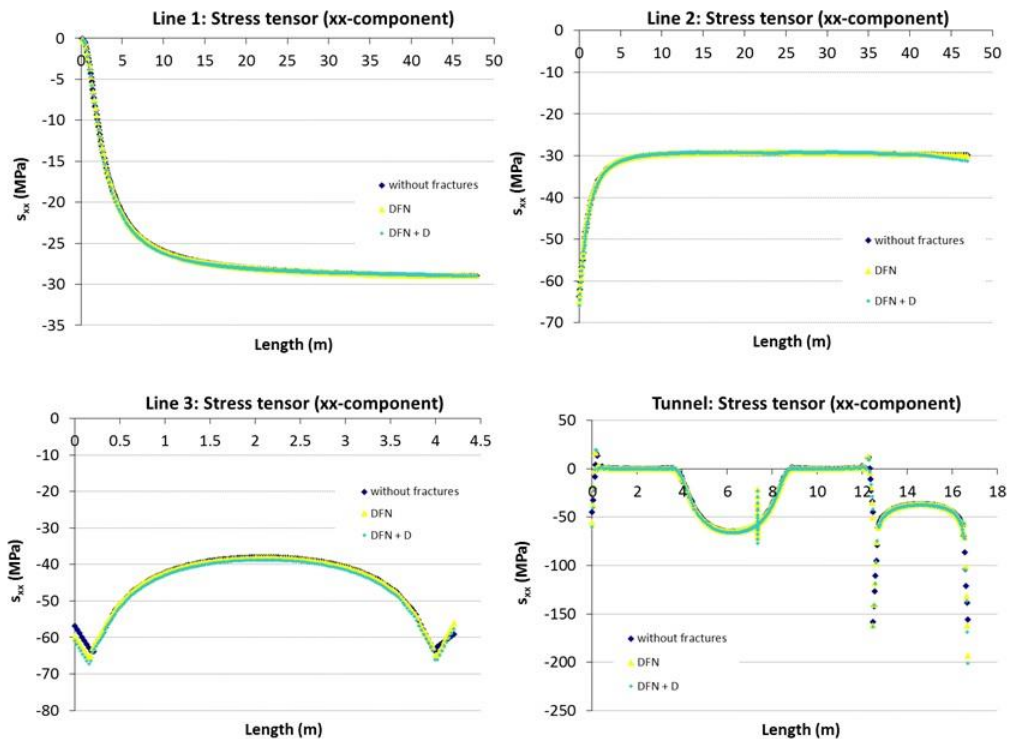


Figure 112. Development of stress tensor xx component over the monitoring lines for all three model variants.



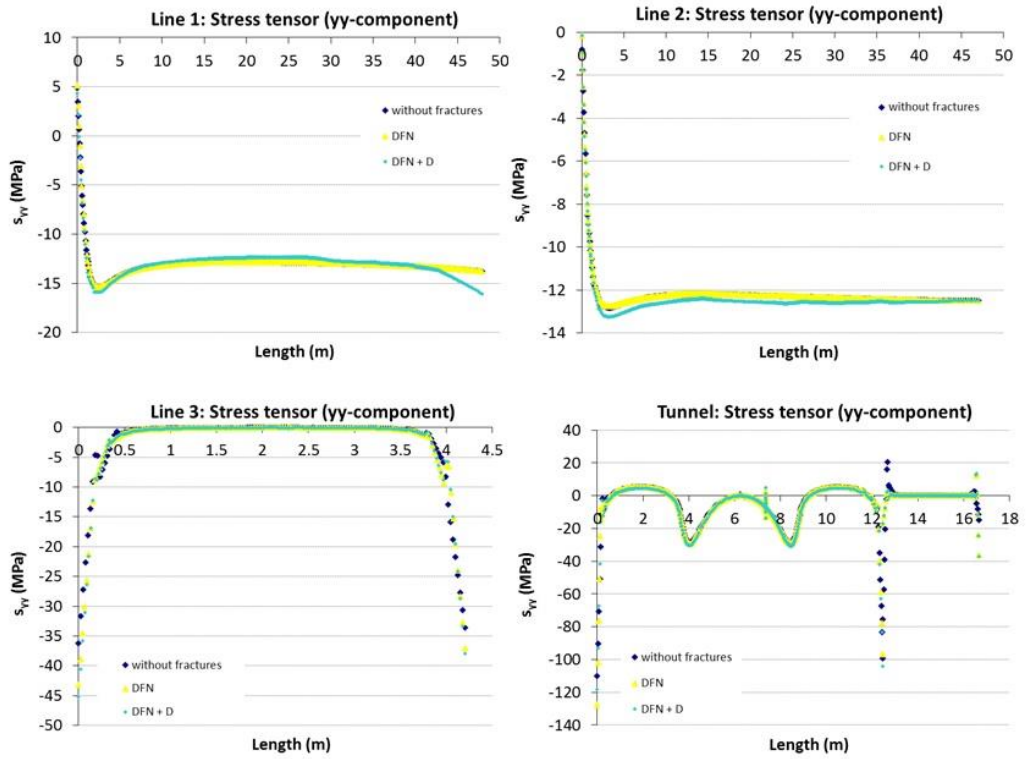


Figure 113. Development of stress tensor yy component over the monitoring lines for all three model variants

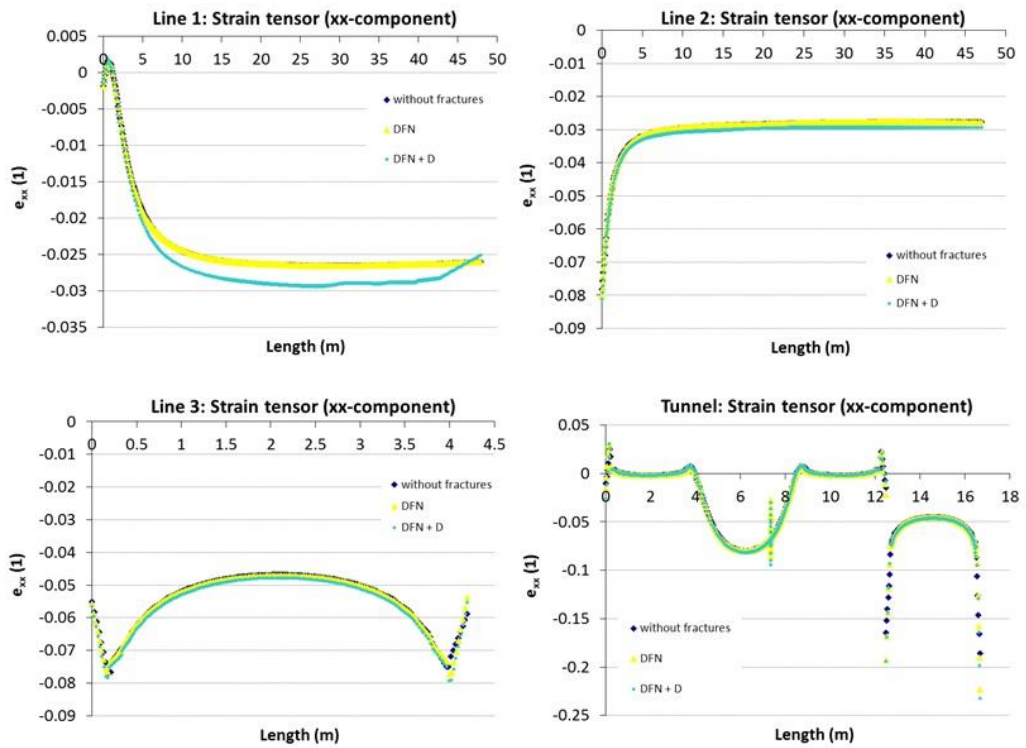


Figure 114. Development of strain tensor xx component over the monitoring lines for all three model variants.

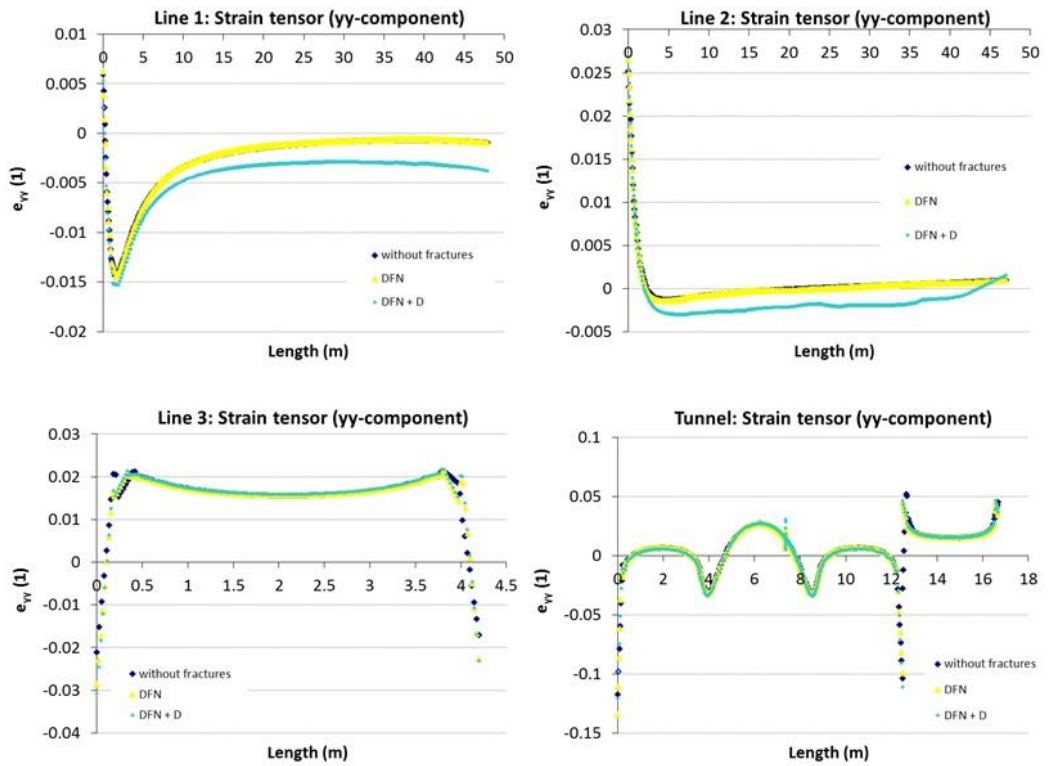


Figure 115. Development of strain tensor yy component over the monitoring lines for all three model variants.

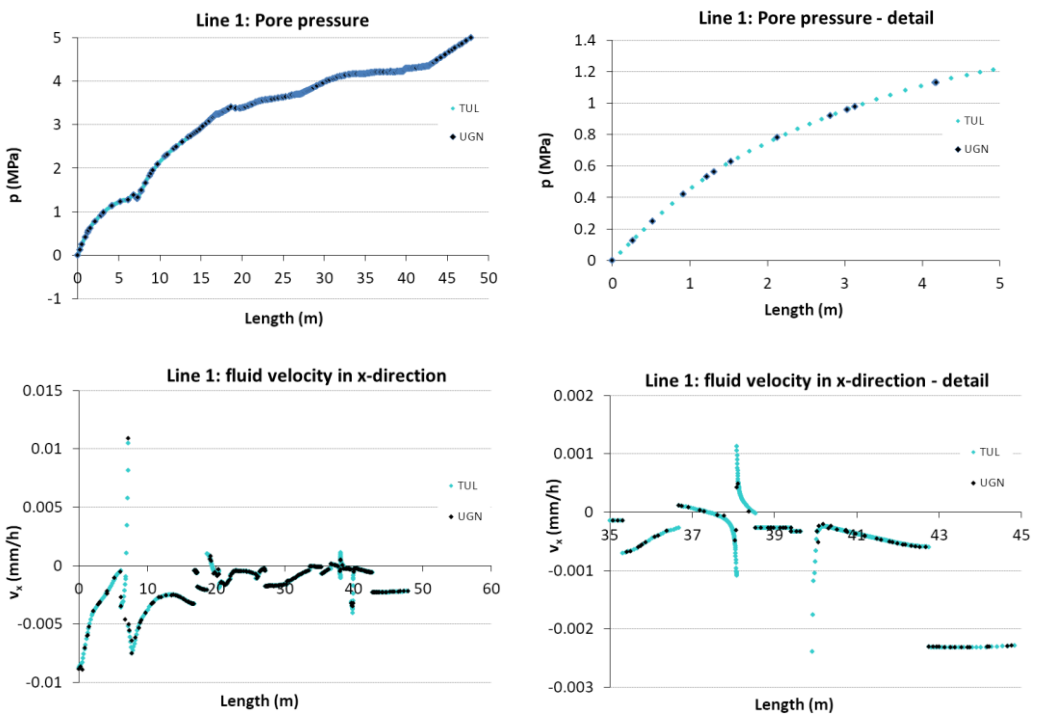


Figure 116. Comparison of the results (TUL-IGN and UGN): pore pressure and fluid velocity in x-direction along the monitoring Line 1.

#### 12.4.4.4. Discussion of Results

The simulation results show that deterministic fractures have more distinct impact on pressure field, flow velocity field and hence on changes in stress and strain. The pressure field and the velocity field are significantly influenced by the fractures. The changes in mechanical quantities (along the monitoring lines, compared to homogeneous matrix model) are of the order of tenths of a MPa for the stress and in units of mm at max for the displacement. Results of both Czech modelling teams were very similar (see Figure 116); slight differences are due to different number of output points.

The main advantage of our approach is the simple definition of the problem (geometry, fractures, input data). Its possible shortcomings are yet to reveal themselves; issues are expected to occur as the problem definition gets more complex.

## 12.5. Summary and Comparison of the Simulation Results

The following sections present a comparison of the simulation results from each modelling team by means of comparative diagrams for Monitoring Line 1 and 2.

### 12.5.1. Activity 1.1.1

Figure 117 to Figure 120 and Figure 121 to Figure 124 show the results of each modelling team for the monitoring line 1 and 2, respectively. An excellent fit can be observed between the TUL-IGN and GMC teams using COMSOL Multiphysics and roxol for all determined values within this Activity. Derived values from SNU deviate from the other modelling teams and show higher strain and stress values, which is possibly related to the reduction of the modelling domain and altered stress concentrations on the tunnel wall, or the resolution. However, it is interesting to note that the reduced domain size - i.e. the fractures are connected to the outer boundary - do not influence the pore pressure or fluid flow significantly. Differences in strain are up to 0.005% and up to ~2 MPa for the stresses.

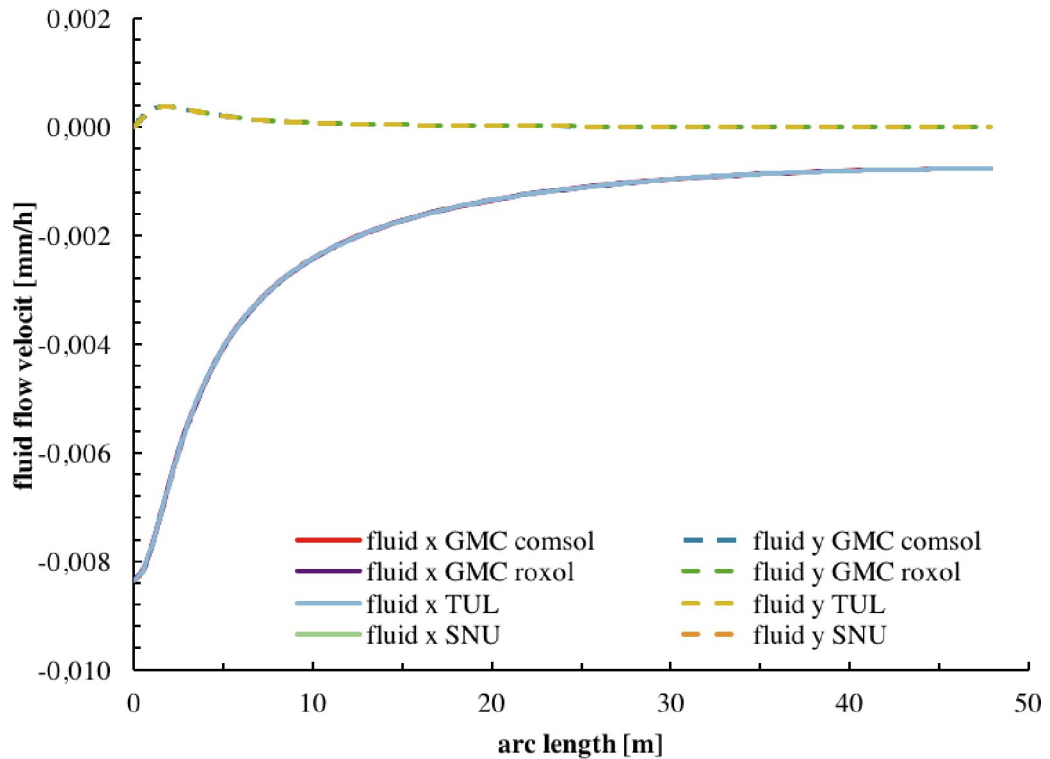


Figure 117. Fluid flow in x and y- direction along Monitoring Line 1 as derived from different modelling teams for Activity 1.1.1.

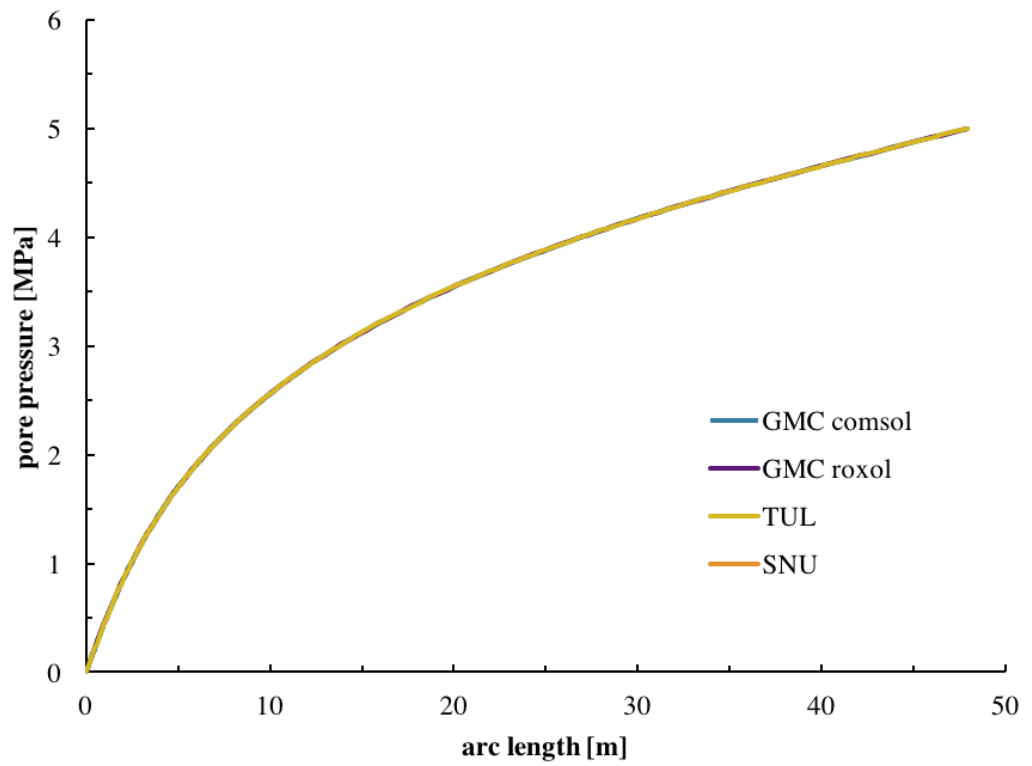


Figure 118. Pore pressure along Monitoring Line 1 as derived from different modelling teams for Activity 1.1.1.

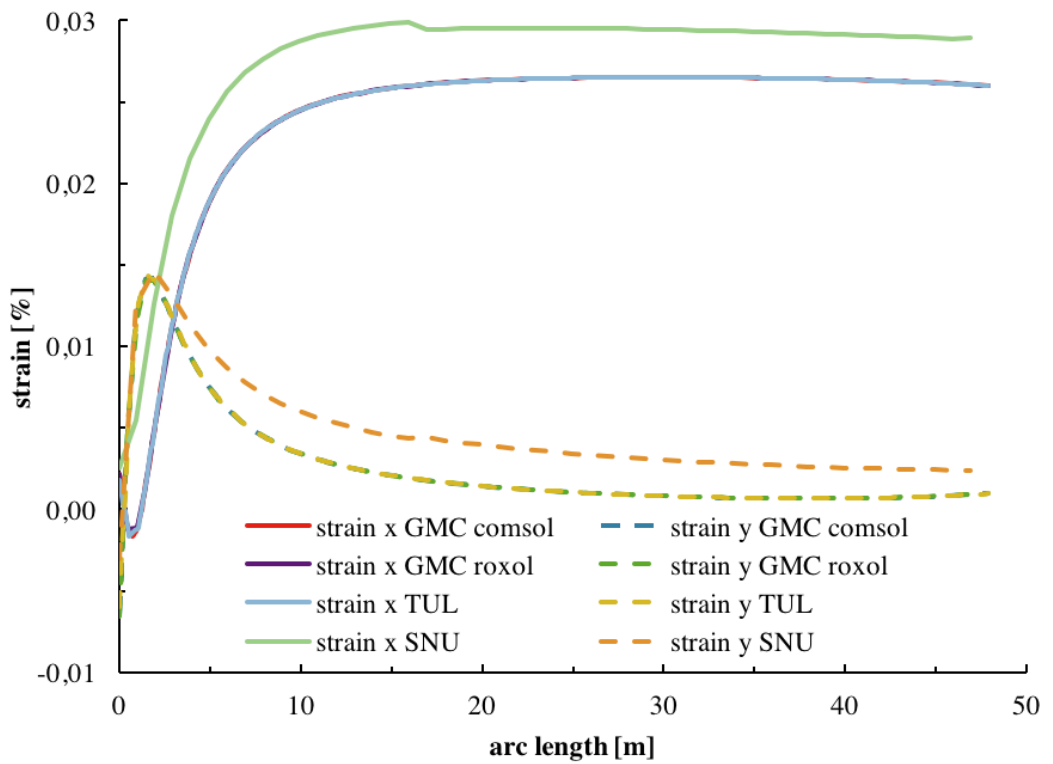


Figure 119. Strain in x- and y-direction along Monitoring Line 1 as derived from different modelling teams for Activity 1.1.1.

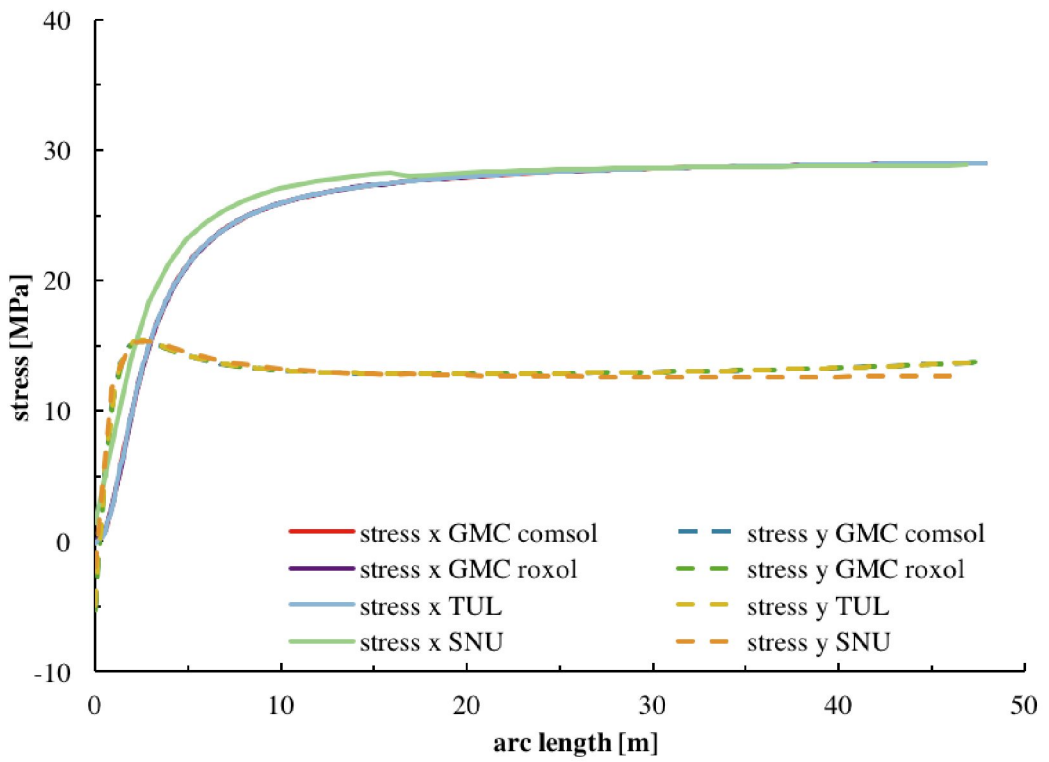


Figure 120. Stress in x- and y-direction along Monitoring Line 1 as derived from different modelling teams for Activity 1.1.1.

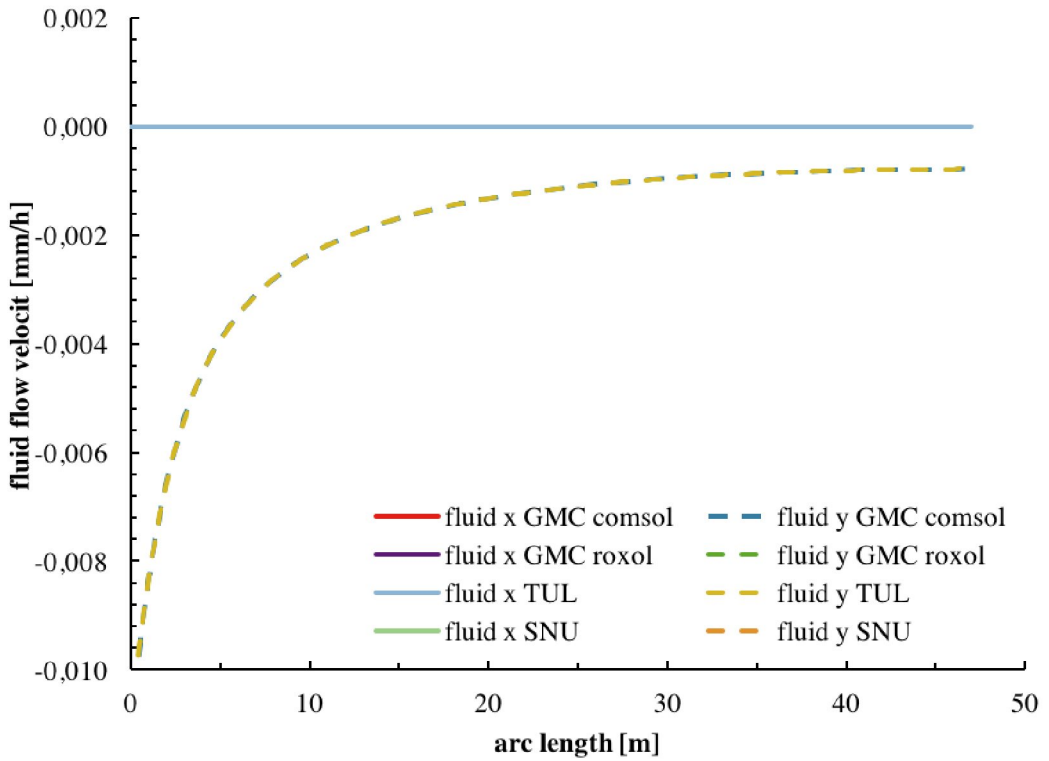


Figure 121. Fluid flow in x- and y-direction along Monitoring Line 2 as derived from different modelling teams for Activity 1.1.1.

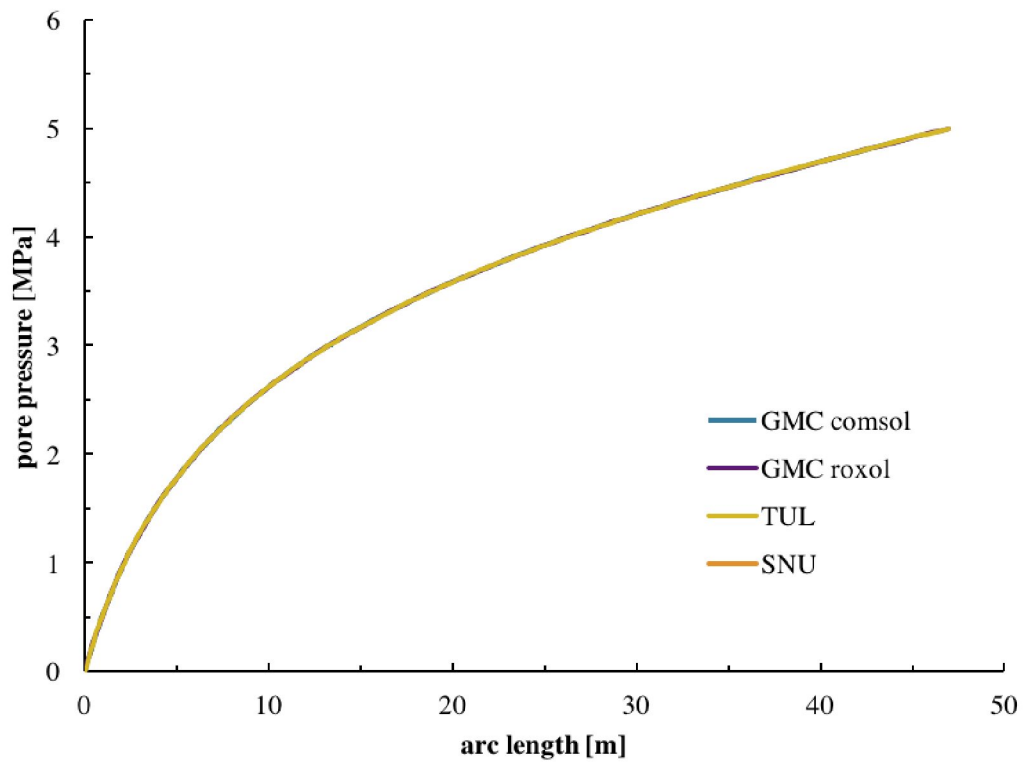


Figure 122. Pore pressure along Monitoring Line 2 as derived from different modelling teams for Activity 1.1.1.

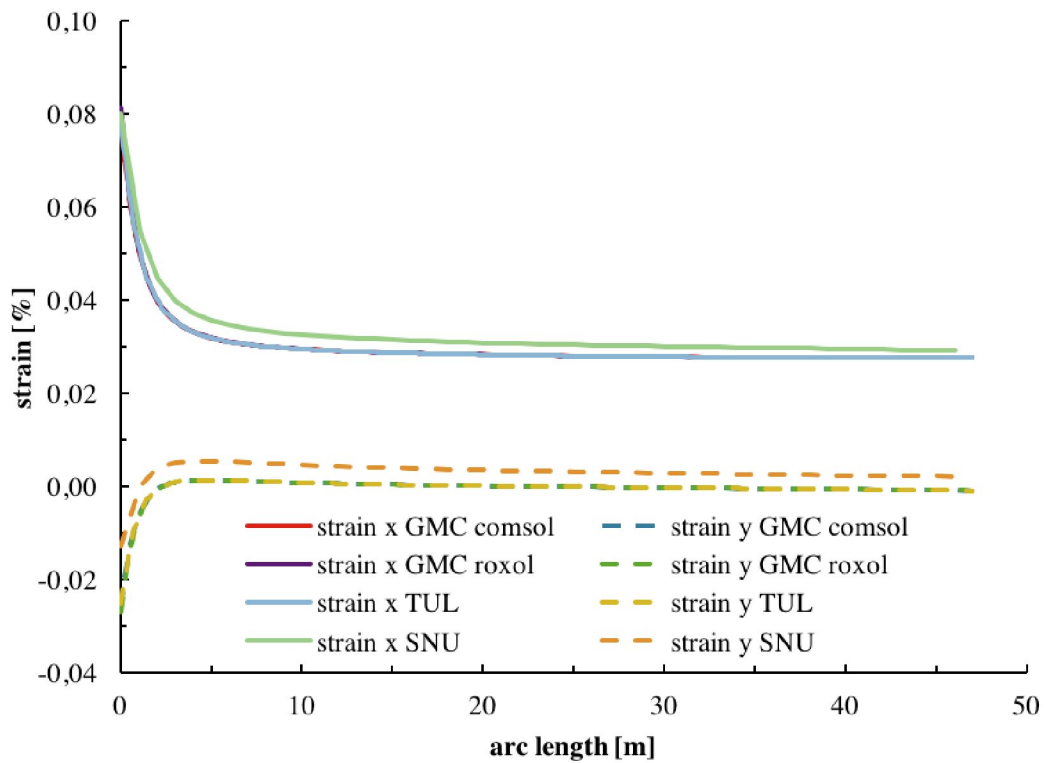


Figure 123. Strain in x- and y-direction along Monitoring Line 2 as derived from different modelling teams for Activity 1.1.1.

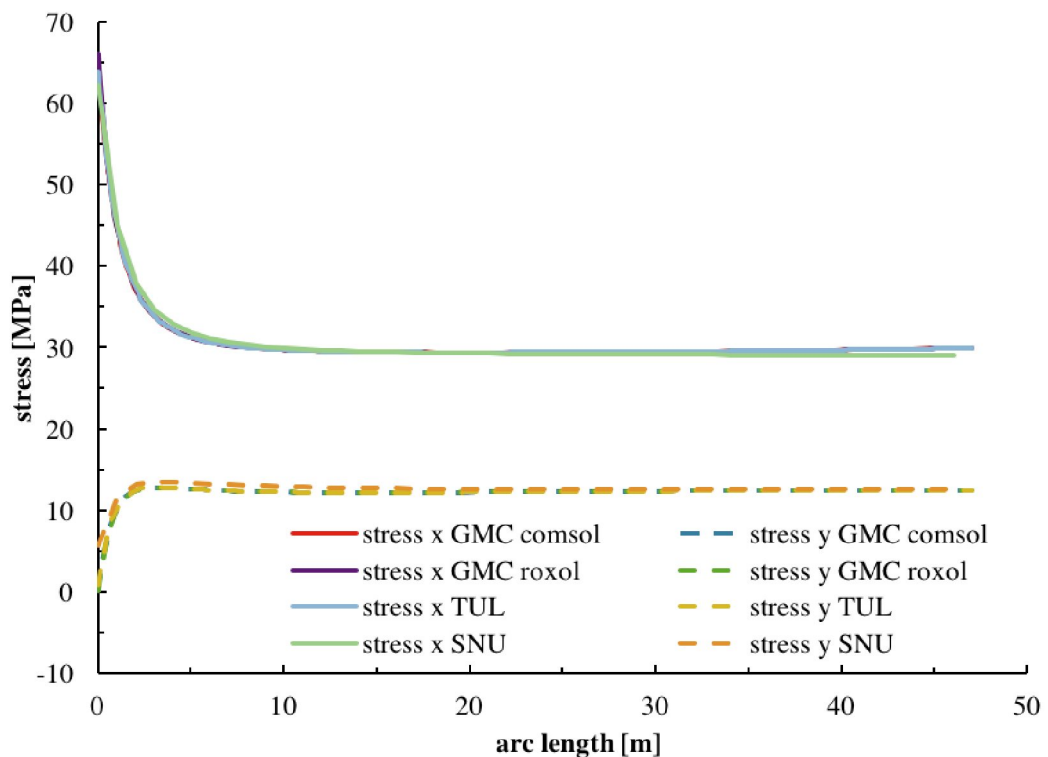


Figure 124. Stress in x- and y-direction along Monitoring Line 2 as derived from different modelling teams for Activity 1.1.1.

### 12.5.2. Activity 1.1.3

In Activity 1.1.3, deterministic (DTM) and discrete (DFN) fracture networks with different fracture properties have been incorporated and added to the homogeneous model. Since each numerical approach handles fracture flow and fracture behavior differently, fluctuations of the results, especially close to fractures, can be expected.

Since no cohesion has been assigned to the fractures during the roxol simulations, the observed fluctuations in stress and strain are maximized. Also, since roxol assigns the fracture permeability to each cell intersected by a fracture, the overall permeability influence of fractures might be overestimated.

In the case where a monitoring line intersects a DTM, jumps in the fluid flow velocity were observed by the teams using COMSOL Multiphysics (see Figure 125). UDEC generally does not show any changes in fluid flow velocity close to DTM, while the roxol results magnify their influence. However, the overall trend is the same for all employed codes.

The pore pressure generally increases with increasing distance from the tunnel wall. Values calculated by COMSOL Multiphysics are generally higher than roxol values but lower than pore pressures determined by UDEC, which seem too high and resemble the pore pressure distribution of the homogeneous rock as observed in Activity 1.1.1.

COMSOL Multiphysics results from the TUL-IGN and GMC teams again show an excellent agreement for the strains due employing the same numerical method and code. roxol, on the other hand, shows high deviations in the vicinity of fracture due to the “cohesion-less” behavior enforcing high deformations along the fracture. The overall trend is, however, in agreement with the COMSOL Multiphysics results. It is interesting



to note that the strain in the x-direction derived by 3DEC is in better agreement with the remaining numerical codes than the strain in the y-direction, independent of the orientation of the monitoring line.

Since strain and stress are closely related, the previous observations can also be made for the stress measurements. roxol shows the highest deviations in the stress values while UDEC is closer to the results of COMSOL Multiphysics.

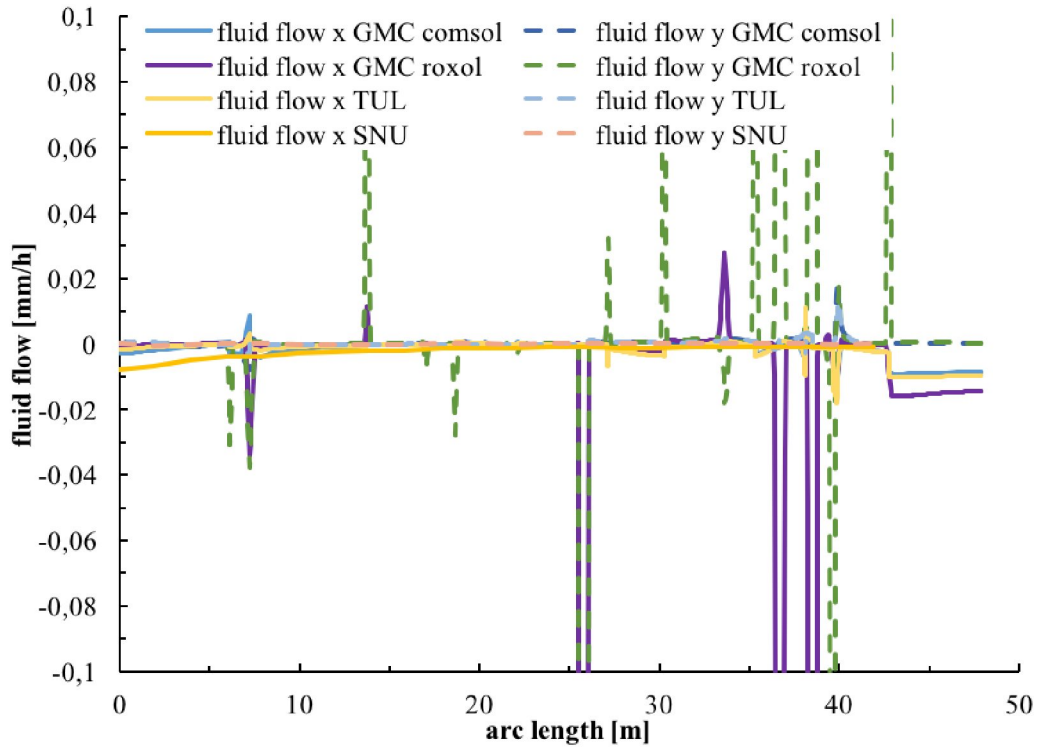


Figure 125. Fluid flow in x- and y-direction along Monitoring Line 1 as derived from different modelling teams.

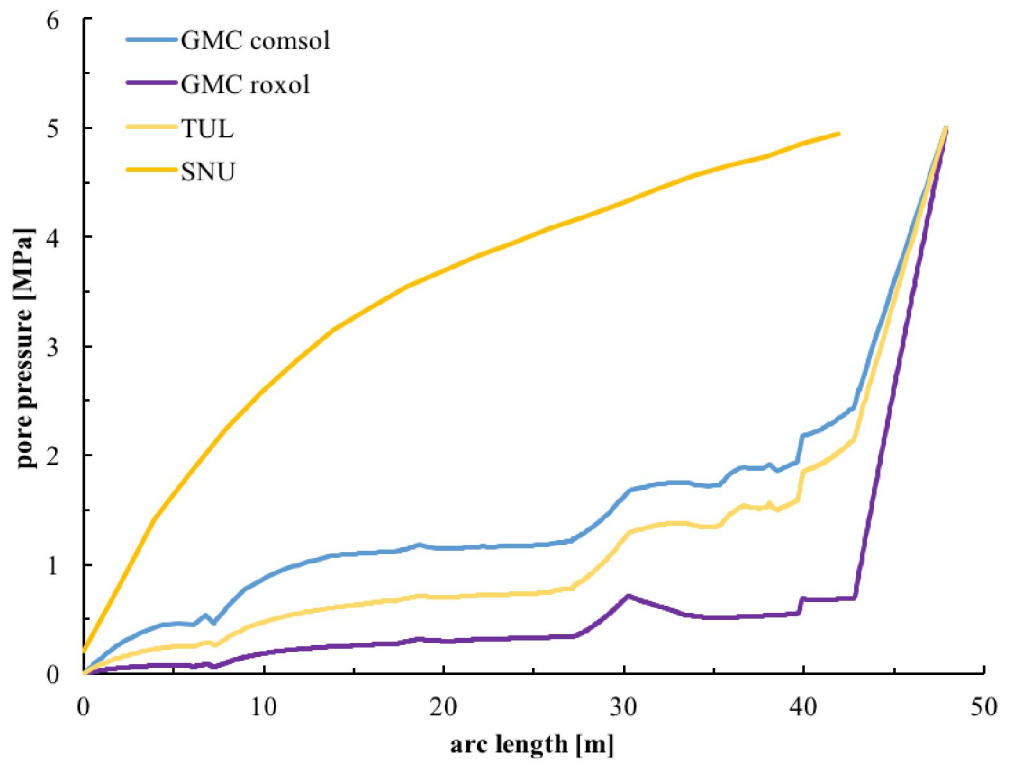


Figure 126. Pore pressure along Monitoring Line 1 as derived from different modelling teams.

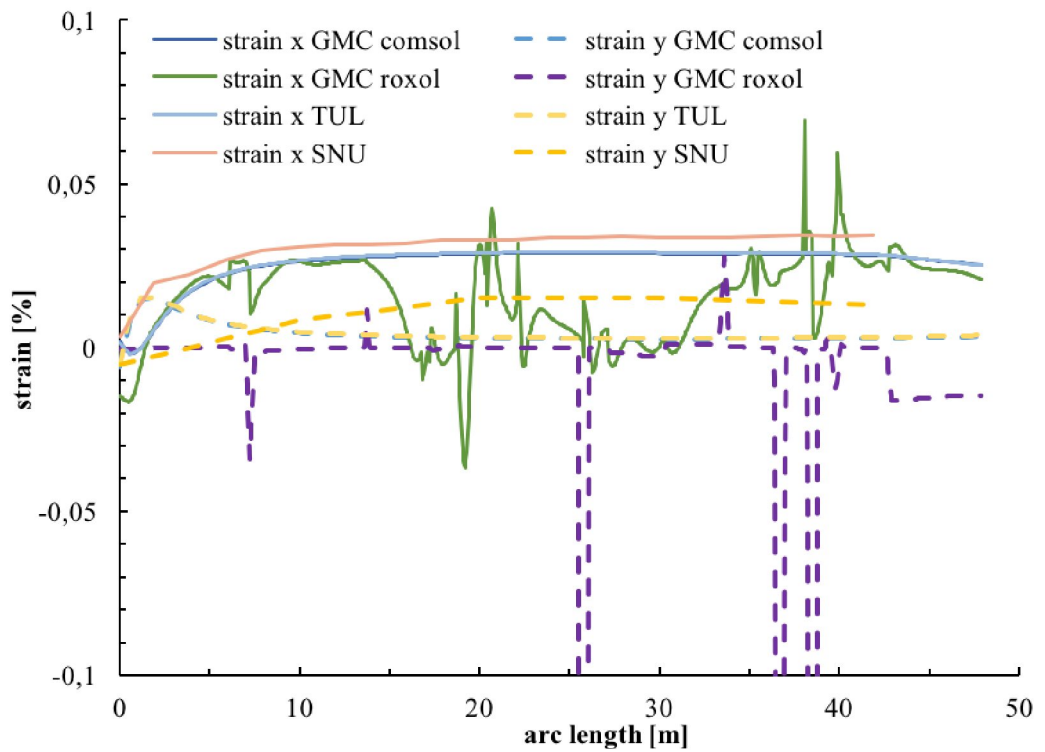


Figure 127. Strain in x- and y-direction along Monitoring Line 1 as derived from different modelling teams.

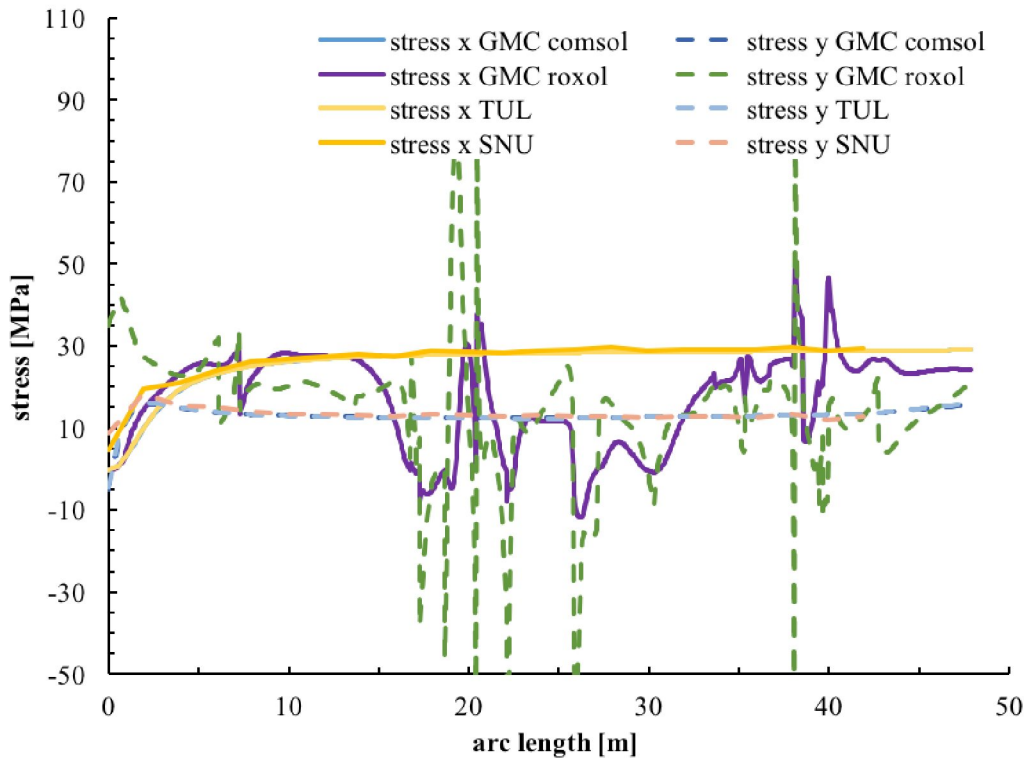


Figure 128. Stress in x- and y-direction along Monitoring Line 1 as derived from different modelling teams.

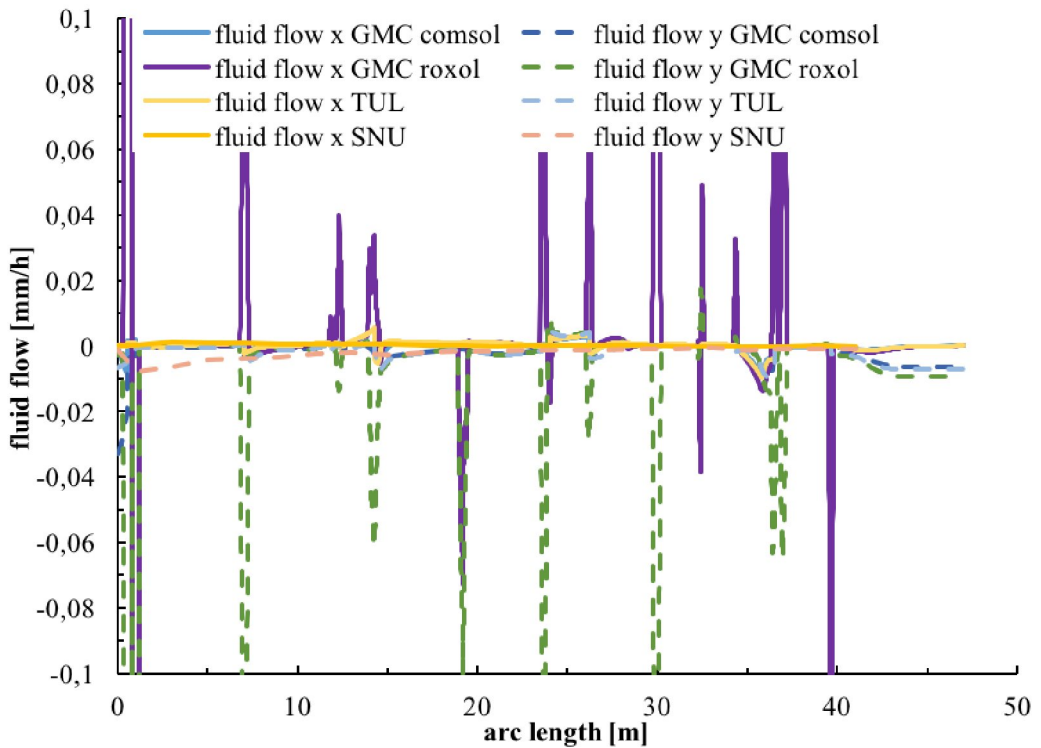


Figure 129. Fluid flow in x- and y-direction along Monitoring Line 2 as derived from different modelling teams.

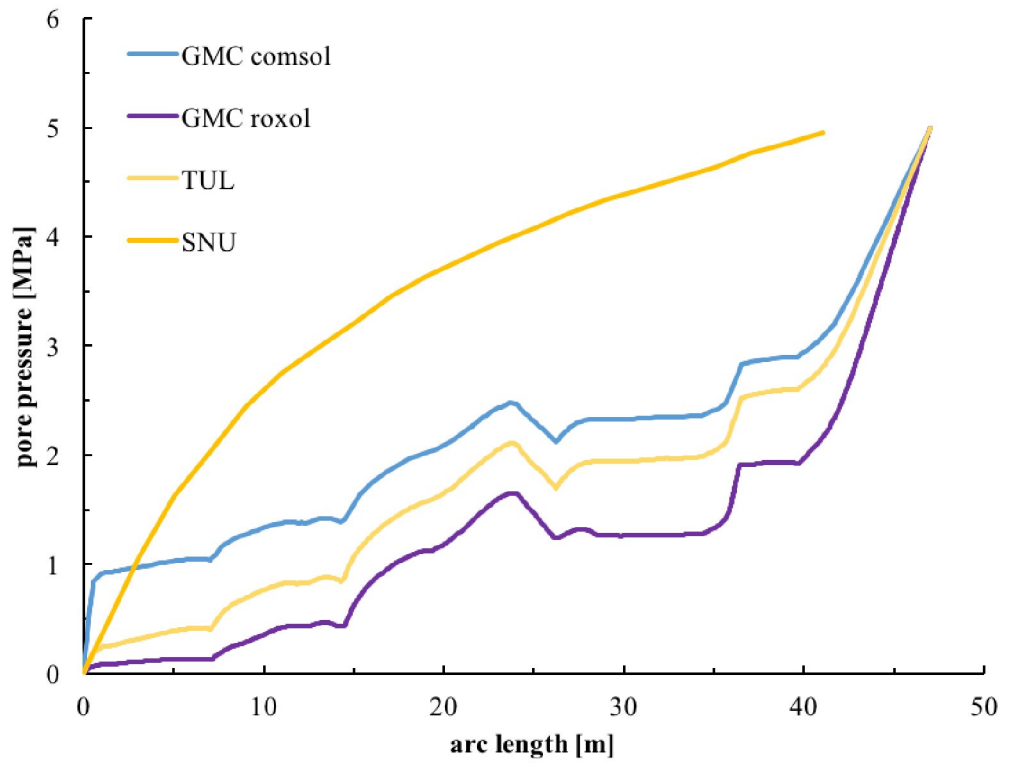


Figure 130. Pore pressure along Monitoring Line 2 as derived from different modelling teams.

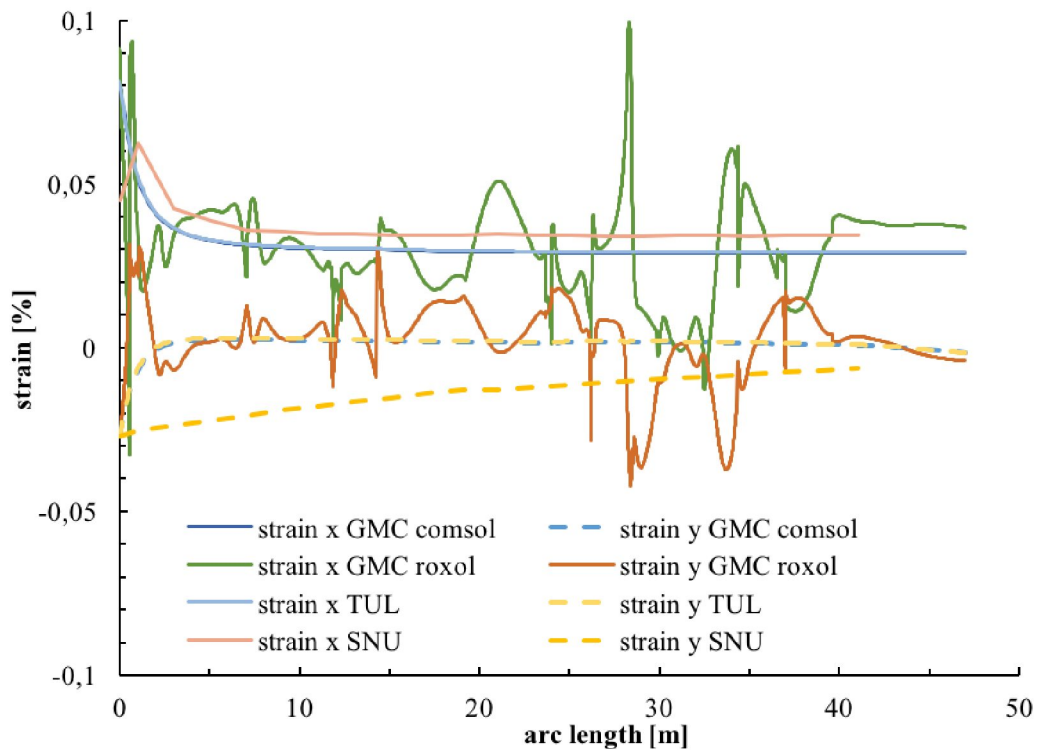


Figure 131. Strain in x- and y-direction along Monitoring Line 2 as derived from different modelling teams.

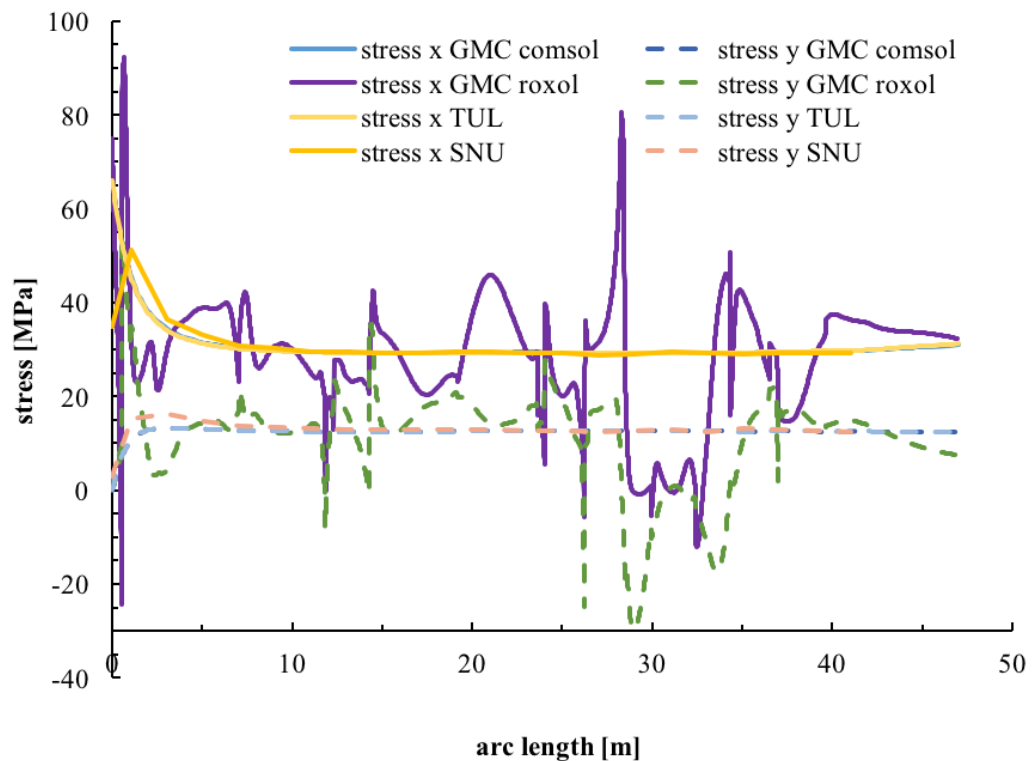


Figure 132. Stress in x- and y-direction along Monitoring Line 2 as derived from different modelling teams.

## 12.6. Discussion and Conclusion

Since TUL-IGN and GMC have been using the same code and the same physical interfaces to model the activities, it is not surprising that their simulations yield almost identical results. Some insignificant deviations occur due to different output intervals along monitoring lines or varying mesh refinement, but, in general, these are negligible. Only in Activity 1.1.3, do the pore pressure distributions show increasing offsets with increasing distance from the start- and end-point of the monitoring lines, i.e., the predefined boundary conditions, which cannot be explained by the aforementioned reasons. Due to this observation both teams re-evaluated their model set-ups and results with the model definitions but the differences in pore pressure could not be resolved. Despite the difference in pore pressure in Activity 1.1.3, the remaining values were almost identical.

The results generated by SNU using UDEC show differences to the other modelling teams' results since the read-out intervals are much coarser and the model domain has been altered to fit the needs of the numerical code. The derivations occur especially for stress and strain and can be observed in Activity 1.1.1 and 1.1.3.

At this point, it is interesting to note that the included fracture networks (DTM and DFN) do not seem to influence the fluid flow results for UDEC. For example, the pore pressure curves with and without fractures are almost identical for the UDEC code (see Figure 133). This is in contrast to the results of the other modelling teams who observed high fluctuations of the pore pressure with and without the fracture network. In particular, a large difference in the fluid flow parameters can be observed when comparing UDEC with roxol results.

roxol produces almost identical results to the COMSOL Multiphysics results in Activity 1.1.1. However, in Activity 1.1.3, high fluctuations in strain, stress, fluid flow, and pore pressure in the vicinity of the fracture networks are generated due to the mesh-size-dependent fracture flow (see pore pressure distribution in Figure 134) and the “smooth”, friction-free fractures (compare with Figure 125 to Figure 132).

From Figure 134 it can also be concluded that percolating fracture networks created by the DTM significantly reduce the pore pressure in the matrix and subsequently increase the affected zone around the tunnel. The amount of the pore pressure reduction also depends on the effective fracture aperture. The greater the fracture aperture, the greater the fluid withdrawal out of the formation towards the tunnel. Hence, it can be argued that fractures created from a drill-and-blast-procedure will not result in a significant reduction of pore pressure within the excavation damage zone since the created fracture will be too short to form a percolating fracture network and too narrow to increase the drainage area of the tunnel.

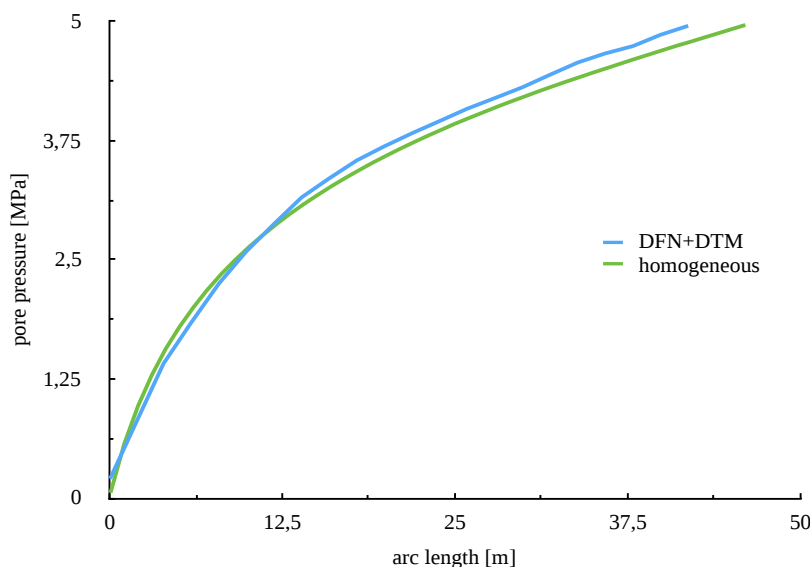


Figure 133. Difference in pore pressure between Activity 1.1.1 and 1.1.3 along monitoring line 1.

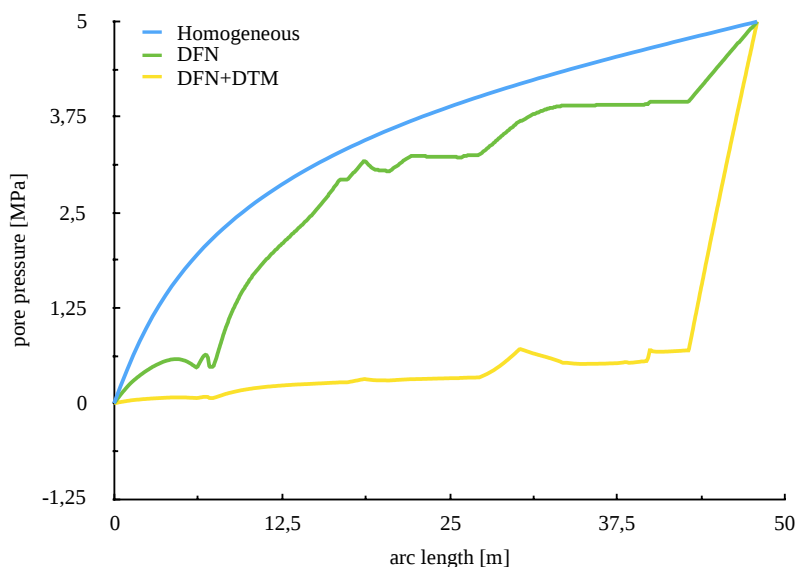


Figure 134. Difference in pore pressure between homogeneous (Activity 1.1.1), discrete, and deterministic + discrete (Activity 1.1.3) fracture networks taken from roxol results.

## 12.7. References

Biot, M.A., 1962. Mechanics of Deformation and Acoustic Propagation in Porous Media, *J. Appl. Phys.*, vol. 33, pp. 1482–1498.

COMSOL MULTIPHYSICS® v. 5.0. COMSOL AB, Stockholm, Sweden.

DECOVALEX-THMC Task D: Long-Term Permeability/Porosity Changes in the EDZ and Near Field due to THM and THC Processes in Volcanic and Crystalline-Bentonite Systems, Status Report October 2005.

Dershowitz, W., Winberg, A., Hermanson, J., Byegård, J., Tullborg, E-L., Andersson, P., and Mazurek, M., 2003. Äspö Hard Rock Laboratory. Äspö Task Force on modelling of groundwater flow and transport of solutes Task 6c: A semi-synthetic model of block scale conductive structures at the Äspö HRL. International Progress Report IPR-03-13, Swedish Nuclear Fuel and Waste Management Co., Stockholm.

Dershowitz, W., Fox, A., Lee, G., Van Fossen, M., and Uchida, M., 2005. Äspö Hard Rock Laboratory. Äspö Task Force on modelling of groundwater flow and transport of solutes: Discrete fracture network flow and transport modelling at the rock block scale: Task 6D, 6E, 6F and 6F2. International Progress Report IPR-06- 22, Swedish Nuclear Fuel and Waste Management Co., Stockholm.

Ericsson, L. O., Brinkhoff, P., Gustafson, G., Kvartsberg, S., 2009. Hydraulic Features of the Excavation Disturbed Zone – Laboratory investigations of samples taken from the Q- and S-tunnels at Äspö HRL. Report R-09-45.

Ericsson, L., Thörn, J., Christiansson, R., Lehtimäki, T., Ittner, H., Hansson, K., Butron, C., Sigurdsson, O., Kinnbom, P., 2015. A demonstration project on controlling and verifying the excavation-damaged zone - Experience from the Äspö Hard Rock Laboratory. Report R-14-30.

Ericsson L.-O., Christiansson R., Butron C., Hansson K., Lehtimäki T. (2014). Characterization of the Excavation Damaged Zone by means of Geological, Geophysical and Hydrogeological Co-interpretation, 8th Asian Rock Mechanics Symposium.

Hjerne, C., Nordqvist, R., and Harrström, J., 2010. Compilation and analyses of results from cross-hole tracer tests with conservative tracers. SKB Report R-09-28, Swedish Nuclear Fuel and Waste Management Co., Stockholm.

Hökmark, H., Lönnqvist, M., Fälth, B., 2010. THM-issues in repository rock. Thermal, mechanical, thermo-mechanical and hydro-mechanical evolution of the rock at the Forsmark and Laxemar sites. Technical Report TR-10-23.

Holzbecher, E., and Oberdorfer, P., 2014. Rock Deformation due to Geothermal Heat Production - a Modelling Study. *Oil Gas European Magazine*, 1, 25–26.

Itasca Consulting Group Inc., 2013. 3DEC User's Guide. Minneapolis, Minnesota.

Ittner H., Lehtimäki T., Christiansson R. (2014). Design and control of the EDZ for a deep repository in crystalline rock. *Rock Engineering and Rock Mechanics: Structures in and on Rock Masses – Alejano, Peruchó, Olalla & Jiménez (Eds)*. 2014 Taylor & Francis Group, London, 978-1-138-00149-7.

Liu Q., Wu Y., Liu B. (2011). Discrete element analysis of effect of stress on equivalent permeability of fractured rockmass, *Yanshilixue Yu Gongcheng Xuebao/Chinese Journal of Rock Mechanics and Engineering*, 30(1), 176-183.

Mas Ivars, D., Veiga Rios, M., Shiu, W., Johansson, F., Fredriksson, A., 2014. Long term stability of rock caverns BMA and BLA of SFR, Forsmark. SKB Report R-13-53, Swedish Nuclear Fuel and Waste Management Co., Stockholm, Sweden.

Meier, T., and Backers, T., 2017. Thermo-hydro-mechanische Simulation des Reservoirverhaltens zur Abschätzung des Potentials induzierter Seismizität bei Förderung und Injektion/Thermal-hydraulic-mechanical Simulation of a Reservoir for Assessing the Potential of Induced Seismicity during Depletion and Injection. *Erdöl, Erdgas, Kohle*, April(4), 1–12.

Min K.-B., Rutqvist J., Tsang C.-F., Jing L. (2004). Stress-dependent permeability of fractured rock masses: a numerical study, *Int J Rock Mech & Min Sci*, Vol. 41(7), p. 1191-1210.

Min K.-B., Rutqvist J., Elsworth D. (2009). Chemically- and mechanically-mediated influences on the transport and mechanical characteristics of rock fractures, *Int J Rock Mech & Min Sci*, Vol. 46(1), p. 80-89.

Öhman J., Niemi A., Tsang C.-F. (2005). Probabilistic estimation of fracture transmissivity from Wellbore hydraulic data accounting for depth-dependent anisotropic rock stress, *Int J Rock Mech & Min Sci*, Vol. 42(5-6), p. 793-804, ISSN 1365-1609.

Rutqvist J., Barr D., Birkholzer J.T., Fujisaki K., Kolditz O., Liu Q.-S., Fujita T., Wang W., Zhang C.-Y. (2009a). A comparative simulation study of coupled THM processes and their effect on fractured rock permeability around nuclear waste repositories, Special Issue: The DECOVALEX-THMC Project (Safety assessment of nuclear waste repositories), *Journal of Environmental Geology*, Vol. 57(6), p. 1347-1360.

Rutqvist J., Börgesson L., Chijimatsu M., Hernelind J., Jing L., Kobayashi A., Nguyen S. (2009b). Modeling of damage, permeability changes and pressure responses during excavation of the TSX tunnel in granitic rock at URL, Canada, Special Issue: The DECOVALEX-THMC Project (Safety assessment of nuclear waste repositories), *Journal of Environmental Geology*, Vol. 57(6), p. 1263-1274.

SKB, 2009a. Underground design Forsmark. Layout D2, SKB R-08-116, the Swedish Nuclear Fuel and Waste Management Co (SKB).

SKB, 2009b. Design premises for a KBS-3V repository based on results from the safety assessment SR-Can and some subsequent analyses. Updated 2013-01, SKB TR-09-22, the Swedish Nuclear Fuel and Waste Management Co (SKB).

SKB 2010. Design, production and initial state of the backfill and plug in deposition tunnels. Technical Report TR-10-16.

SKB, 2011. Long-term safety for the final repository for spent nuclear fuel at Forsmark. Main report of the SR-Site project. Updated 2015-05, SKB TR-11-01, the Swedish Nuclear Fuel and Waste Management Co (SKB).



SSM, 2018. Strålsäkerhet efter slutförvarets förslutning, SSM Report 2018:07 (in Swedish), the Swedish Radiation Safety Authority (SSM).

Wang W., Rutqvist J., Görke U.-J., Birkholzer J.T., Kolditz O. (2011). Non-isothermal flow in low permeable porous media: a comparison of Richards' and two-phase flow approaches, *Environmental Earth Sciences*, Vol. 62(6), p. 1197-1207, DOI:10.1007/s12665-010-0608-1.

Wang, X., 2005. Stereological Interpretation of rock fracture traces on borehole walls and other cylindrical surfaces. Ph.D. Dissertation, Virginia Polytechnic Institute and State University, Blacksburg, Virginia, 113 pp.

## 12.8. Annex

### 12.8.1. Specification of Discrete Fracture Network

The DFN statistical model of the Äspö Task Force (Dershowitz et al., 2003; 2005) consists of two fracture sets: (1) a sub-vertical set with nominally WNW strike, and (2) a moderately dipping set with nominally NNW strike. The fracture poles (normal vectors) for each set are considered to be distributed according to a Fisher distribution with parameters as listed in **Table 30**.

Both fracture sets are considered to have the same distribution of fracture size (i.e. fracture radius, for disc-shaped fractures), which is defined as a lognormal distribution with an arithmetic mean of 2 m and an arithmetic standard deviation of 1 m, truncated such that the minimum radius retained in the model is 2 m and the maximum radius is 50 m.

Fractures are located by a three-dimensional Poisson process, with uniform fracture intensity ( $P_{32}$ ) for a given set. The defining parameters for simulation of geometric aspects of the model, as given in Table 6-1 of Dershowitz et al. (2005) are listed in **Table 30**.

3-D simulations are performed by generating fractures in a cube-shaped volume centered at the origin (0,0,0), with edges of length 150 m, and rotated by 45° from the cardinal directions (North, South, East and West) so that the edges are aligned with the vertical, NW-SE, and NE-SW directions. The size of this simulation volume is chosen to be large enough that truncation effects are negligible for the smaller 100 m cube-shaped volume from which data are used. For the lognormal model as specified, in practice fractures larger than 15 m radius are extremely rare.

**Table 30.** Parameters for generation of fracture sets for Calculation Cases t1 and t1d.

Parameter	Mean Pole Trend (°)	Mean pole plunge (°)	Fisher concentration $\kappa$	$\mu_r$ (m)	$\sigma_r$ (m)	$P_{32}$ (m <sup>2</sup> / m <sup>3</sup> )	$r_{max}$ (m)
Set 1	211.0	0.6	9.4	2.0	1.0	0.16	50
Set 2	250.0	54.0	3.8	2.0	1.0	0.13	50

### 12.8.2. Continuous vs. discrete simulation of fracture orientation distribution

Three different methods have been used for modelling fracture orientations:

- Continuous: Fracture poles in each set are sampled from a continuous Fisher distribution.
- Discrete (default alignment): Fracture poles are sampled from a continuous Fisher distribution, but each pole is then mapped onto the nearest direction in an icosahedral set, which has a fixed, default alignment with respect to standard geographic coordinates.
- Discrete (pole-aligned): Fracture poles are sampled from a continuous Fisher distribution, but each pole is then mapped onto the nearest direction in an icosahedral set which is aligned with the mean pole direction for the given fracture set.

An icosahedral direction set consists of 20 discrete directions that are spaced uniformly on the unit sphere.

The differences in orientations simulated by these three methods can be seen from the stereonet plots in Figure 135. With the continuous method, fractures may intersect at any angle, including angles very close to 0°. The two discrete methods maintain the scatter of orientations in an approximate way, while ensuring that intersections between fractures will not be excessively acute. When the default alignment is used, the solid angle between any two intersecting fractures in 3D is always greater than 41.8°.

When the icosahedral direction set is aligned with the mean pole for each fracture set, the representation of the directions for each fracture set is improved, but more acute intersections can occur depending on the angle between the mean poles of the fracture sets.

### 12.8.3. Variations with respect to fracture intensity

Initial simulations indicated that the Äspö Task Force statistical DFN model does not lead to percolating networks in 2D cross sections. Here a series of increases in the 3D fracture intensity  $P_{32}$  have been tested to determine what degree of increase is needed to produce percolating networks. These were tested in combination with the alternative methods of simulating fracture orientations as summarized in **Table 31**. In each case, the specified  $P_{32}$  for each fracture set was increased by the factor shown in the first column of the table.

**Table 31.** Key to variants evaluated for this delivery.

Fracture intensity factor	Method for simulating orientation distribution		
	Continuous	Discrete (default)	Discrete (pole-aligned)
1	t1_1	t1dd_1	t1dp_1
1.1	–	–	t1xdp_1
1.2	t1z_1	–	t1zdp_1
1.3	t1t_1	–	t1tdp_1
1.5	t1f_1	–	t1fdp_1
1.6	t1s_1	–	t1sdp_1
2.0	t1D_1	–	t1Ddp_1
3.0	t1T_1 t1T_2	–	t1Tdp_1 t1Tdp_2

### 12.8.4. 2D cross-section specification

To extract 2D fracture traces based on the 3D realization of the DFN model, intersections are calculated between fractures and a square cross-section. This cross-section is vertical and aligned in the NE-SW direction (i.e., perpendicular to N45°W). The top edge of the cross-section is at  $z = 50$  m, and the bottom edge is at  $z = -50$  m. In plan view, the cross-section extends from  $(-50/\sqrt{2}$  m,  $-50/\sqrt{2}$  m) to  $(50/\sqrt{2}$  m,  $50/\sqrt{2}$  m) in a coordinate system with x and y aligned with East and North, respectively.

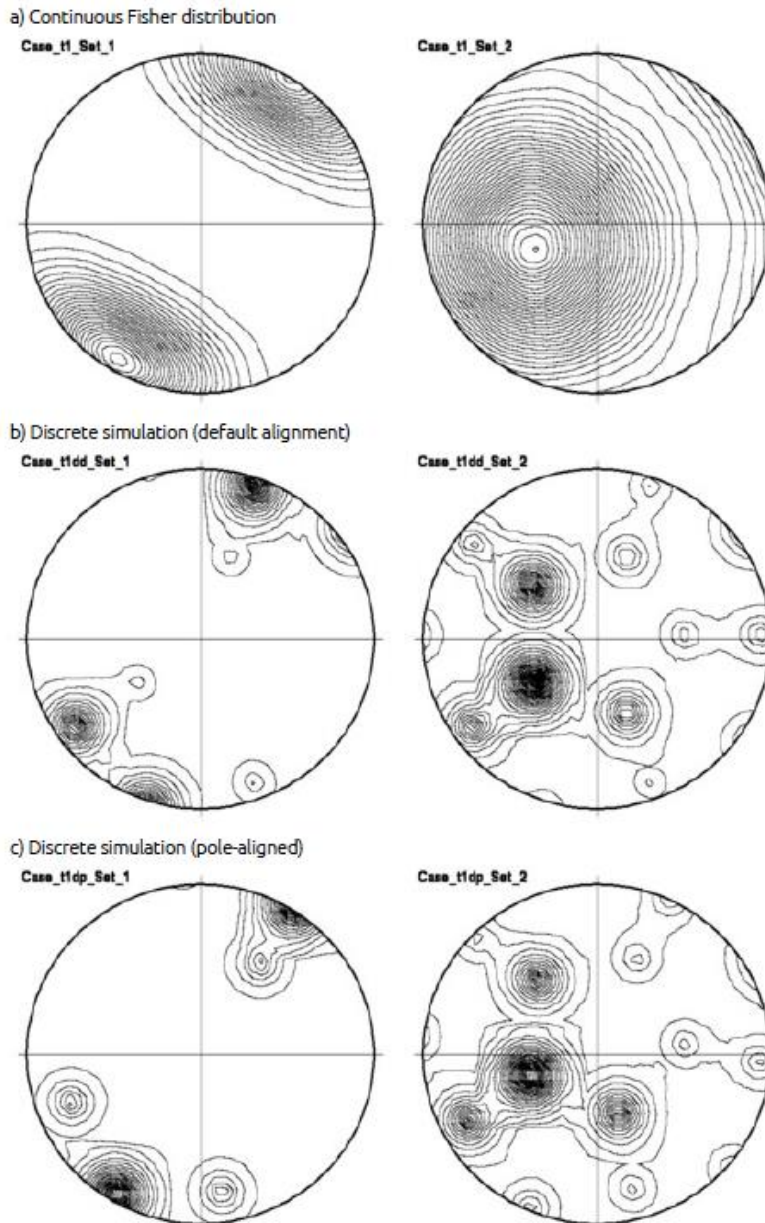


Figure 135. Equal-area plots of fracture poles produced by alternative methods for simulating orientations.

### 12.8.5. Potential influence of 2D cross-section orientation on percolation

The probability of a percolating 2D network being formed by a given cross-section through the 3D fracture population may depend to some extent on the orientation of the cross-section. Percolation is more likely in cross-sections where fractures from both sets have a higher probability of being intersected, so that they form a higher number of 2D traces.

This latter type of probability (of fractures being intersected by a given planar cross-section) is measured by the 2D fracture intensity,  $P_{21}$  (total fracture trace length per unit area). An empirical formula for the ratio of  $P_{21}$  to  $P_{32}$ , for fractures with poles described by a Fisher distribution was developed by Wang (2005). Application of this formula for

the two fracture sets in the Äspö Task Force DFN model yields results for horizontal directions as shown in Figure 136. The highest value of  $P_{21}$  for both fracture sets occurs when the normal vector to the cross-section is in the NW or SE quadrant. The highest total value of  $P_{21}$  (summed over both sets) occurs between N53°W and N54°W, where total  $P_{21} = 0.2627$ . At N45°W (the orientation of the cross section used), total  $P_{21} = 0.2550$ , i.e. 97% of the maximum value. Thus, the chosen orientation is already within 8° to 9° of the horizontal direction that maximizes total  $P_{21}$ . Only a very minor increase would be achieved by adjusting this direction.

Expected  $P_{21}$  fracture intensity on vertical planes as function of normal direction

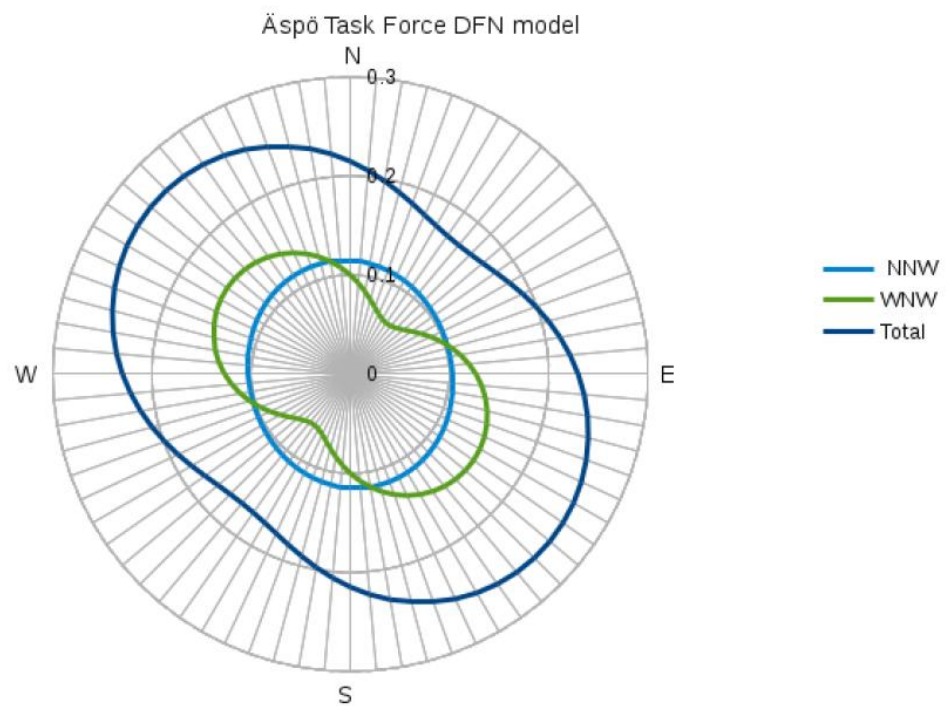


Figure 136. Expected 2D fracture intensity  $P_{21}$  on a vertical sampling plane, plotted as a function of the direction perpendicular to the sampling plane.  $P_{21}$  is plotted for each of the two fracture sets: NNW moderately dipping (Set 2) and WNW subvertical (Set 1) and for the combination of the two fracture sets.

### 12.8.6. Resulting 2D realizations for base case

The 2D cross-section obtained by this method for the Case t1 (base case  $P_{32}$ , continuous Fisher distribution) is plotted in Figure 137. For use in the THM models, the fracture traces were cropped to restrict the fractures to the area at least 5 m from the edges of the 100 m square boundary, and to delete portions of fractures that are inside the tunnel cross-section. The result after cropping according to these specifications is shown in Figure 138 (Case t1) and Figure 139 (Case t1dd). Corresponding detailed-scale plots of the central portion around the tunnel are shown in Figure 140 and Figure 141. Note that these are identical to the datasets previously delivered, except that Case t1d is now called Case t1dd to clarify the type of icosahedral alignment.

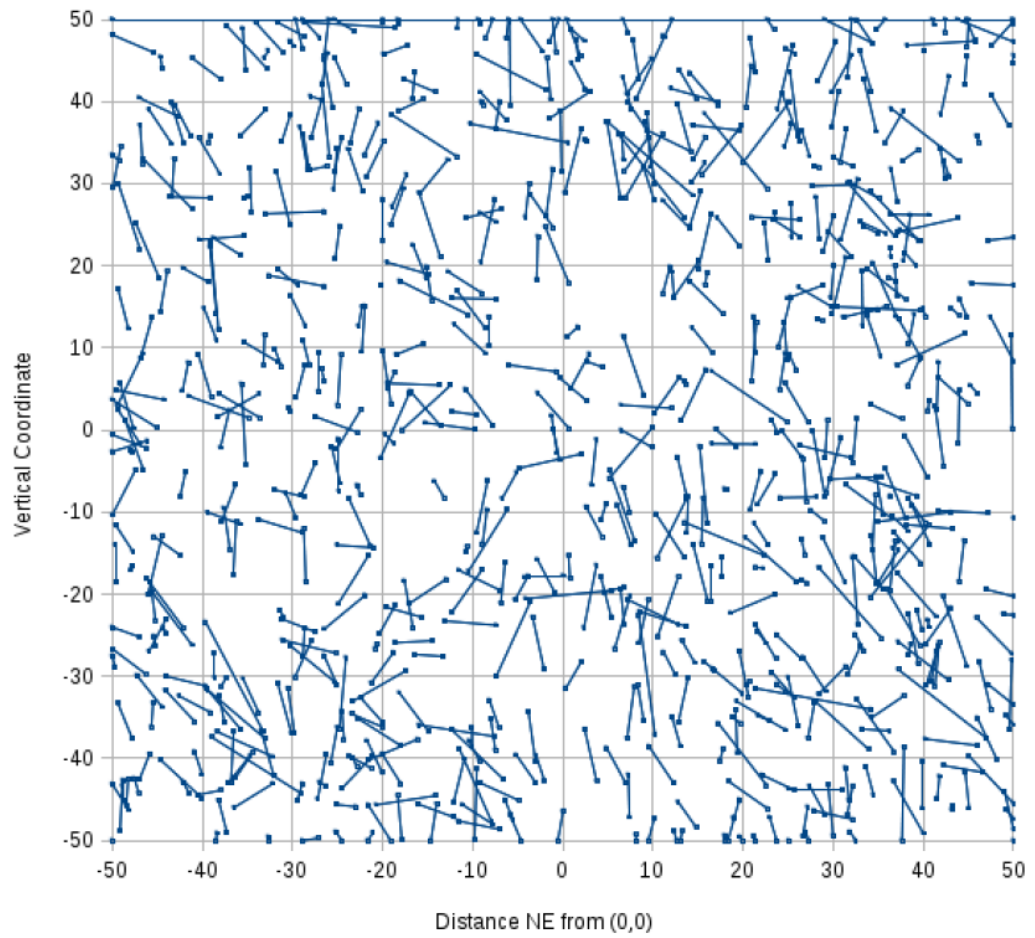


Figure 137. 2D cross-section extracted from 3D realization of the DFN model (Case t1, random seed value = 1), plotted in the plane of the SW-NE cross-section.

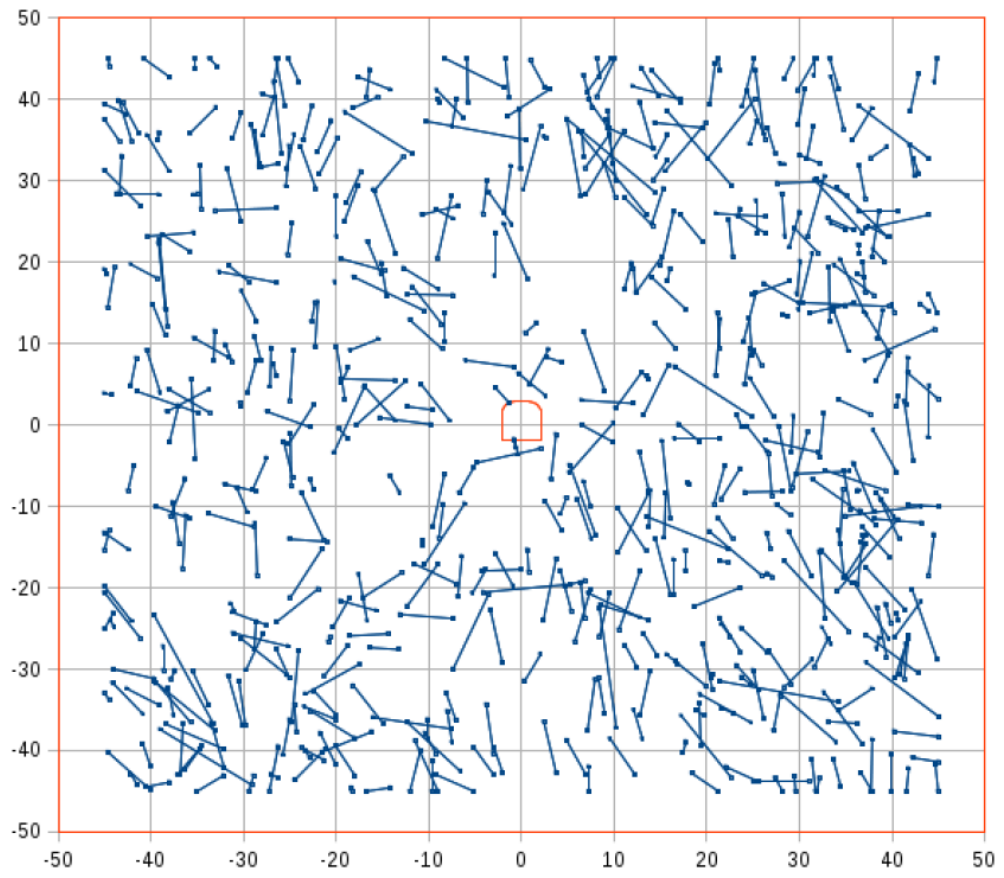


Figure 138. 2D cross-section of the DFN model (Case t1, random seed value = 1), plotted in the plane of the SW-NE cross-section, after cropping fractures inside the tunnel cross-section and within 5 m of the edges of the 2D model area.

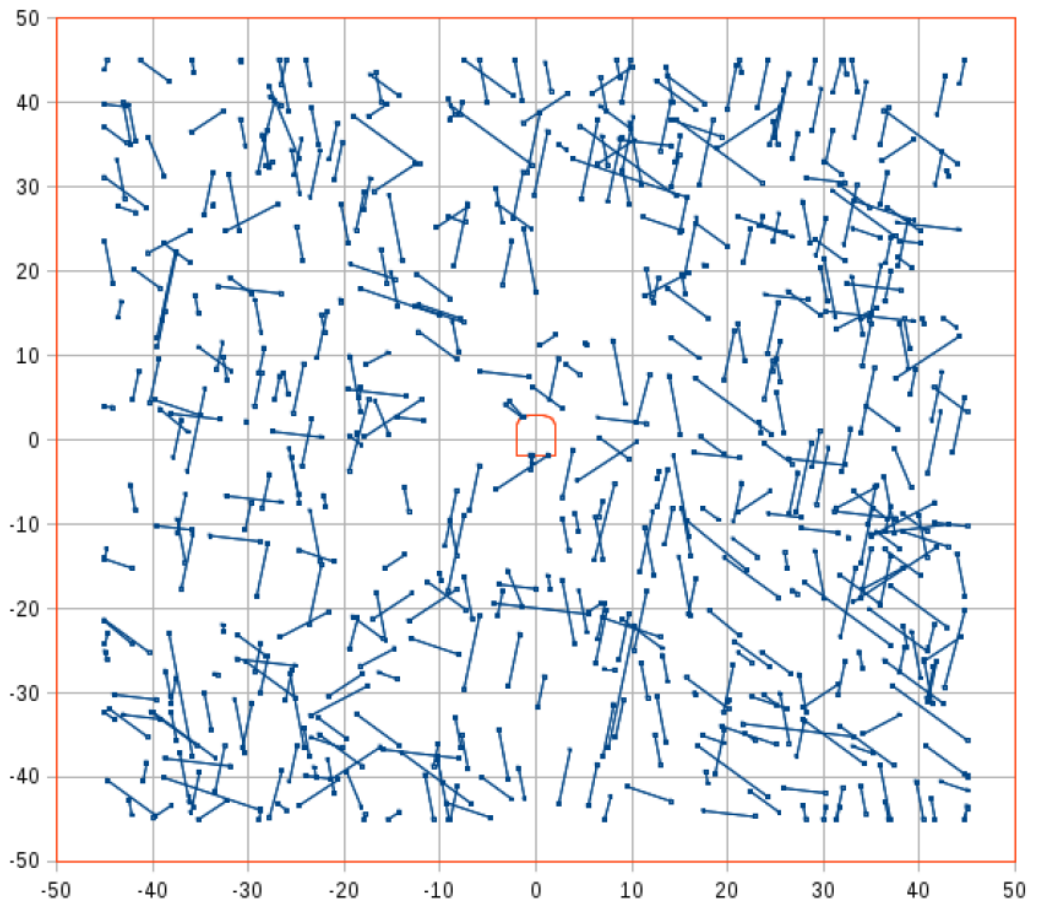


Figure 139. 2D cross-section of the DFN model (Case t1dd, random seed value = 1), plotted in the plane of the SW-NE cross-section, after cropping fractures inside the tunnel cross-section and within 5 m of the edges of the 2D model area.



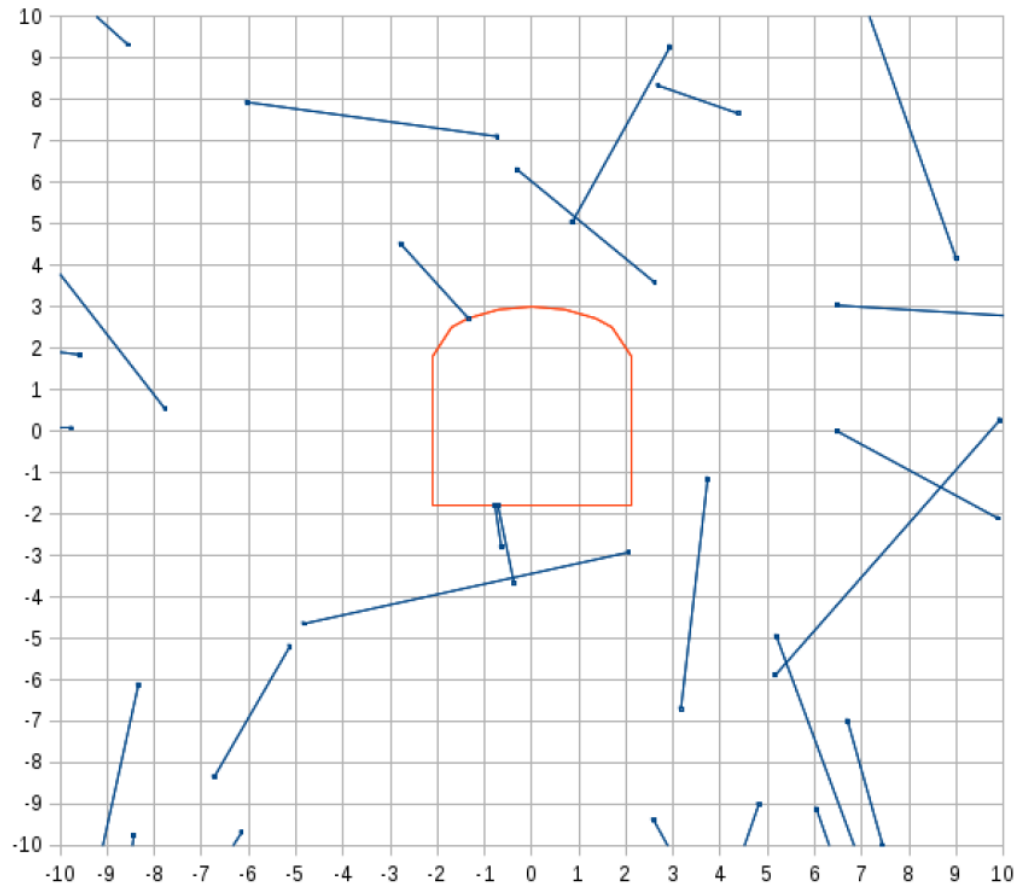


Figure 140. Detailed-scale view of the central portion of the cropped 2D cross-section of the DFN model (Case t1, random seed value = 1). Note that the elliptical roof of the tunnel is approximated by a polyline in this plot, but the cropping algorithm uses the mathematically defined ellipse.

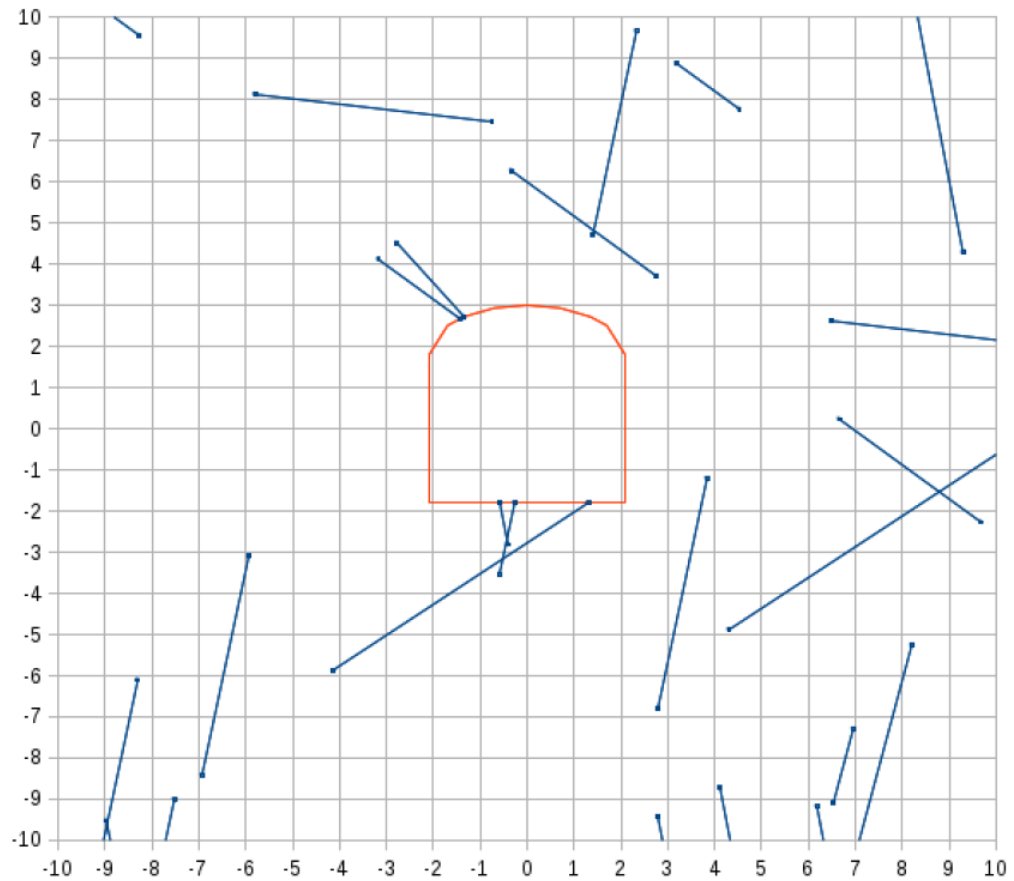


Figure 141. Detailed-scale view of the central portion of the cropped 2D cross-section of the DFN model (Case t1dd, random seed value = 1). Note that the elliptical roof of the tunnel is approximated by a polyline in this plot, but the cropping algorithm uses the mathematically defined ellipse.

### 12.8.7. Effect of intensity and orientation variants on 2D percolation

From Figure 140 and Figure 141, it can be seen that for the base case a few fractures connect to the tunnel perimeter, but these fractures do not belong to networks that reach the effective outer boundary ( $x, y = \pm 45$  m). The effect of increasing  $P_{32}$  on formation of percolating networks on this scale is shown graphically in **Table 32**.

Percolating realizations (i.e. realizations with networks that connect from the tunnel perimeter to the effective outer boundary at  $x, y = \pm 45$  m) are achieved consistently only when  $P_{32}$  is greater than twice the values specified for the base-case model. Realizations of the cases t1T and T1dp, where  $P_{32}$  is three times the values specified for the base-case model, were percolating for both values of the random-number generator seed that were tested.

**Table 32.** Graphical illustration of network connectivity resulting from increasing fracture intensity  $P_{32}$  by a given factor. Percolating realizations (i.e. realizations with networks that connect from the tunnel perimeter to the effective outer boundary at  $x, y = \pm 45$  m, indicated by the yellow line) are highlighted in red. See Table 31 for list of the corresponding model variants. Note that the cases where  $P_{32}$  is scaled by a factor of 2.0 are very close to percolating, but higher-resolution plots show that there are narrow bridges of intact rock.

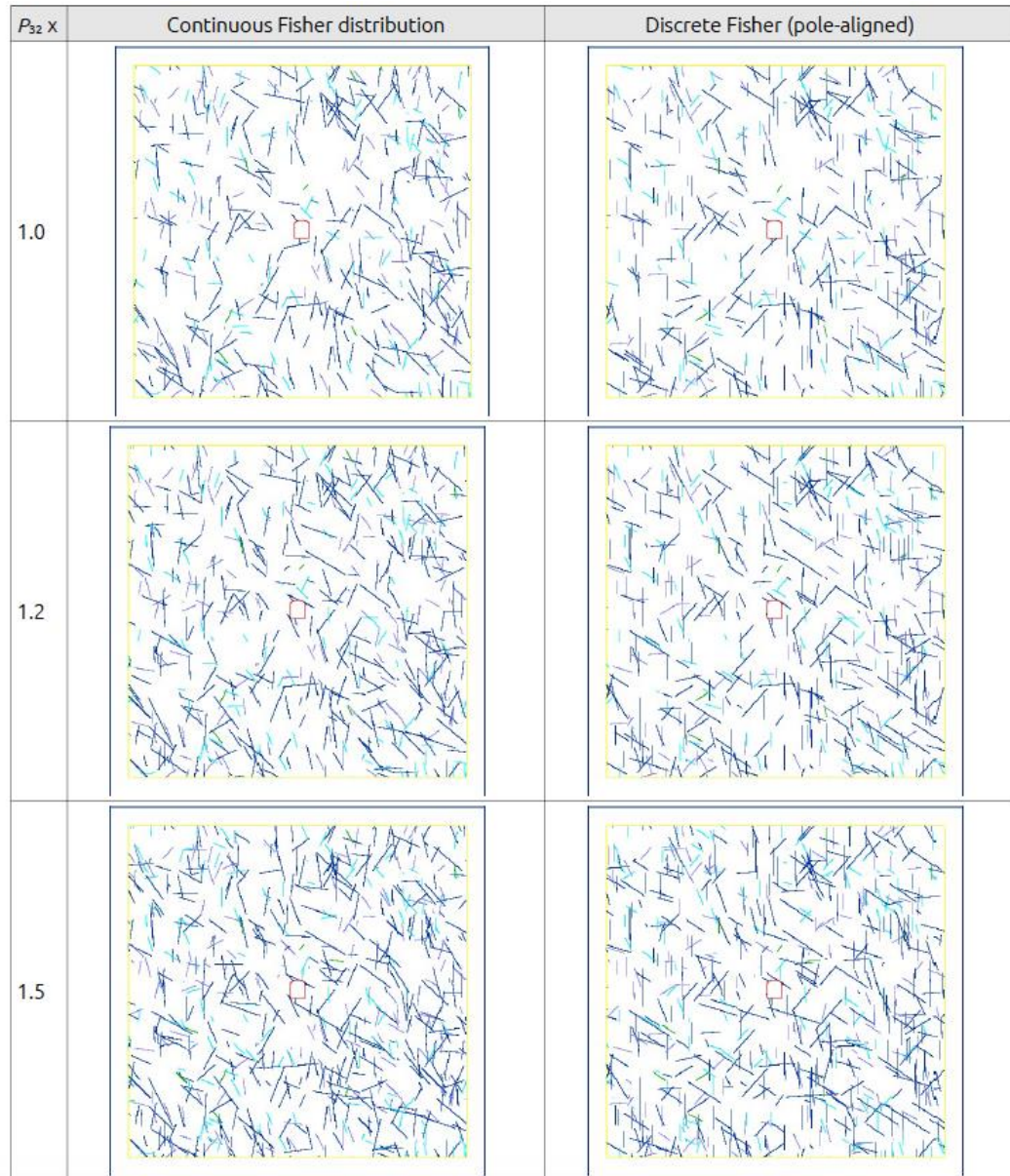
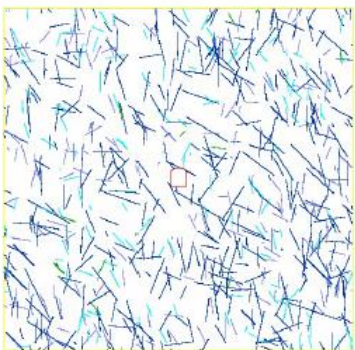


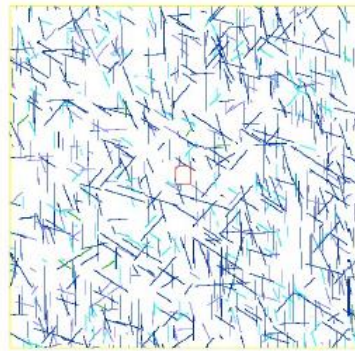
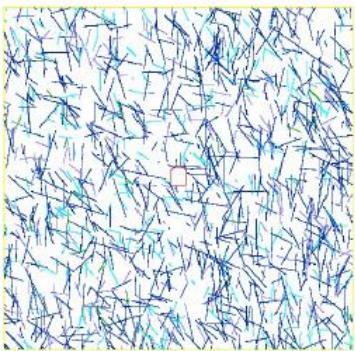



Table 32, ctd.

$P_{32} \times$	Continuous Fisher distribution	Discrete Fisher (pole-aligned)
1.6		
2.0		
3.0		

### 12.8.8. Specification of hydraulic properties in Äspö Task Force model

The DFN statistical model of the Äspö Task Force (Dershowitz et al., 2003; 2005) consists of two fracture sets, both of which have fracture transmissivity values  $T$  (in m<sup>2</sup>/s) that are correlated to fracture length  $L$  (in m) by a relationship of the form:

$$T = T_0 L^{a+bN}$$

$T_0$ ,  $a$ , and  $b$  are empirical constants with the following values:

$$T_0 = 5 \cdot 10^{-10}$$

$$a = 1.386$$

$$b = 0.3$$

and  $N$  is a random value from the standard Gaussian distribution (i.e. normal distribution with zero mean and unit variance).

The definition of  $L$  is not defined precisely by the Äspö Task Force reports, but is here assumed to be the side length of a square fracture that has the same area as a disk with the equivalent radius  $r$ , i.e. such that:

$$L^2 = \pi r^2$$

The size distribution for the fracture sets is defined as a lognormal distribution of  $r$ , with an arithmetic mean  $\mu_r = 2$  m and an arithmetic standard deviation  $\sigma_r = 1$  m, truncated such that the minimum radius retained in the model is  $r_{min} = 2$  m and the maximum radius is  $r_{max} = 50$  m.

Hydraulic aperture  $e_h$  is considered to be correlated to  $T$  according to the empirical relationship:

$$e_h = 0.46\sqrt{T}$$

For fracture storativity, a constant value  $S = 1 \cdot 10^{-6}$  (dimensionless) was recommended. However, Table 6-1 of Dershowitz et al. (2005) notes that storativity does not influence steady-state simulations, so it is not clear whether full consideration was given to this choice of a value, or whether it is based on data. A compilation of data from conservative tracer tests in fractured crystalline rock by Hjerne et al. (2010) includes 27 cases in which estimates of both storativity and transmissivity were obtained. Loglinear regression yields the following fitted model:

$$S = 1.1 \cdot 10^{-3} T^{0.55}$$

as shown in Figure 142.

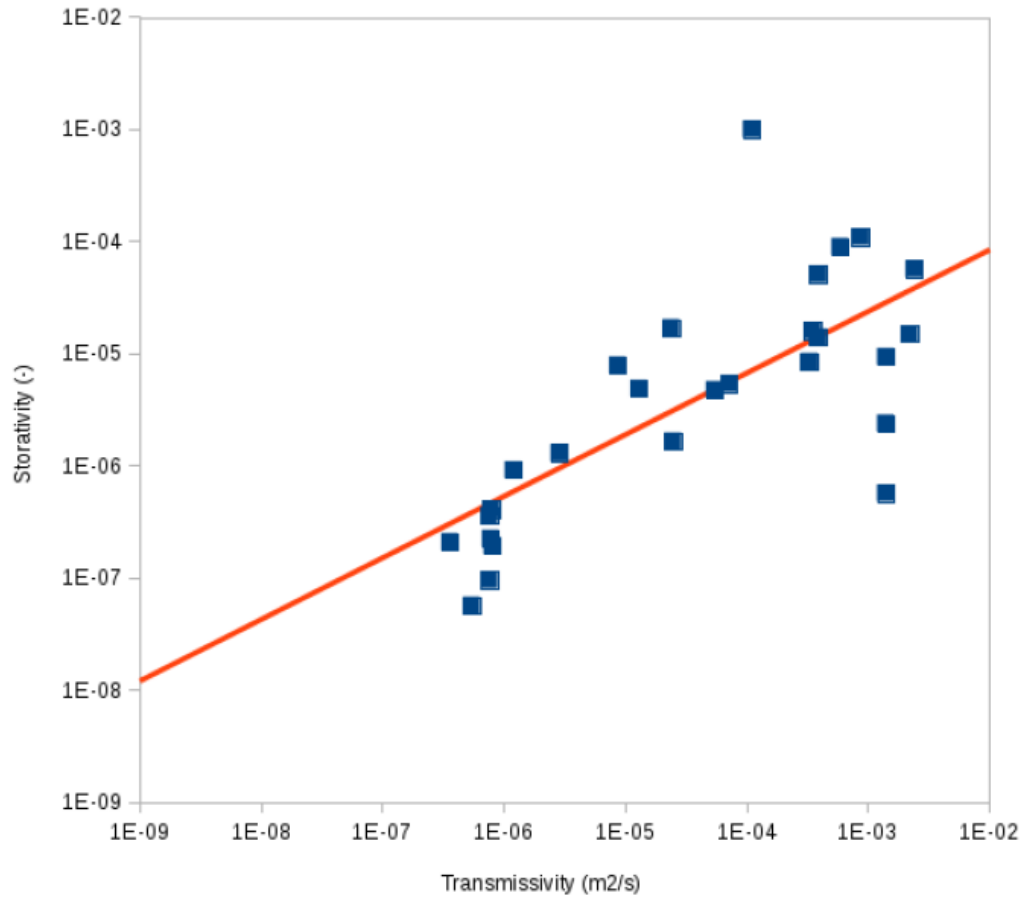


Figure 142. Storativity and transmissivity values from the compilation of Hjerne et al. (2010, Table A1-3) with fitted loglinear model.

### 12.8.9. Recommendations for effective hydraulic properties for 2D DFN datasets

Average values of transmissivity have been calculated by stochastic integration of the specified relationship for transmissivity expressed as a stochastic function of radius:

$$T = T_0(\sqrt{\pi}r)^{a+bN}$$

where  $r$  in turn is a stochastic variable with a truncated lognormal distribution, i.e.:

$$r = e^{\mu_{lnr} + \sigma_{lnr}N} = r_0 e^{\sigma_{lnr}N}, r_{min} \leq r \leq r_{max}$$

where the logarithmic-space parameters of the lognormal distribution corresponding to the arithmetic mean and standard deviation are:

$$\mu_{lnr} = 0.581$$

$$\sigma_{lnr} = 0.472$$

$$r_0 = 1.789 \text{ m}$$



This calculation (carried out in a spreadsheet) yields:

$$T = (5.7 \pm 0.1) \cdot 10^{-9} \text{ m}^2/\text{s}$$

For comparison, the special case of a perfectly correlation between transmissivity and size (i.e. setting  $b = 0$ ) yields a mean value of  $5.0 \cdot 10^{-9} \text{ m}^2/\text{s}$ . For the sake of simplicity, a round value  $T = 5 \cdot 10^{-9} \text{ m}^2/\text{s}$  is therefore suggested for specification of the WP1c calculation case. The corresponding values of fracture storativity, equivalent (cubic-law) aperture, and hydraulic aperture (based on the empirical relationship of Dershowitz et al., 2005) are listed in **Table 33**.

**Table 33.** Hydraulic parameters for 2D DFN model for Activity 1.1.3.

Parameter	Recommended Value	Unit	Basis
Transmissivity	$5 \cdot 10^{-9}$	$\text{m}^2/\text{s}$	See text
Equivalent aperture	$1.8 \cdot 10^{-5}$	m	Cubic law (using fluid density $1000 \text{ kg/m}^3$ and dynamic viscosity $0.001 \text{ Pa}\cdot\text{s}$ ).
Hydraulic aperture	$3.2 \cdot 10^{-5}$	m	Alternative empirical relationship of Dershowitz et al. (2005)
Storativity	$3 \cdot 10^{-8}$	m	Loglinear regression model based on data of Hjerne et al. 2010)

#### 12.8.10. Calculation of Fracture Permeability

The fracture permeability  $k_f$  can be derived from the transmissivity through conductivity by:

$$k_f = \frac{T\mu}{\rho g e_h}$$

For the parameters presented in **Table 27**, **Table 28**, **Table 29** and a gravitational acceleration  $g$  of  $9.81 \text{ m/s}^2$ ,  $k_f$  is  $2.8\text{e-}11 \text{ m}^2$  and  $2.8\text{e-}10 \text{ m}^2$ , respectively.











The Swedish Radiation Safety Authority has a comprehensive responsibility to ensure that society is safe from the effects of radiation. The Authority works from the effects of radiation. The Authority works to achieve radiation safety in a number of areas: nuclear power, medical care as well as commercial products and services. The Authority also works to achieve protection from natural radiation and to increase the level of radiation safety internationally.

The Swedish Radiation Safety Authority works proactively and preventively to protect people and the environment from the harmful effects of radiation, now and in the future. The Authority issues regulations and supervises compliance, while also supporting research, providing training and information, and issuing advice. Often, activities involving radiation require licences issued by the Authority. The Swedish Radiation Safety Authority maintains emergency preparedness around the clock with the aim of limiting the aftermath of radiation accidents and the unintentional spreading of radioactive substances. The Authority participates in international co-operation in order to promote radiation safety and finances projects aiming to raise the level of radiation safety in certain Eastern European countries.

The Authority reports to the Ministry of the Environment and has around 300 employees with competencies in the fields of engineering, natural and behavioral sciences, law, economics and communications. We have received quality, environmental and working environment certification.

Publikationer utgivna av Strålsäkerhetsmyndigheten kan laddas ned via [stralsakerhetsmyndigheten.se](https://stralsakerhetsmyndigheten.se) eller beställas genom att skicka e-post till [registrator@ssm.se](mailto:registrator@ssm.se) om du vill ha broschyren i alternativt format, som punktskrift eller daisy.

**Strålsäkerhetsmyndigheten**  
**Swedish Radiation Safety Authority**  
SE-171 16 Stockholm  
Phone: 08-799 40 00  
Web: [ssm.se](https://ssm.se)  
E-mail: [registrator@ssm.se](mailto:registrator@ssm.se)

©Strålsäkerhetsmyndigheten